

Kinetic Studies of Bio-butanol Oxidation under Low Temperature Combustion Conditions

Samantha Leanne Sime

Submitted in accordance with the requirements for the degree of Doctor of Philosophy

University of Leeds

School of Chemistry

School of Chemical and Process Engineering

November 2019

The candidate confirms that the work submitted is her own and that appropriate credit has been given where reference has been made to the work of others.

This copy has been supplied on the understanding that it is copyright material and that no quotation from the thesis may be published without proper acknowledgement

The right of Samantha Leanne Sime to be identified as Author of this work has been asserted by her in accordance with the Copyright, Designs and Patents Act 1988.

We live in a society where everybody knows everything and it looks like it is a shame to say I don't know.

- Arsene Wenger

Acknowledgements

First of all I'd like to thank Paul, for all of his support and advice over the last three years, and for giving me such a great opportunity in such a fantastic research group. I would also like to thank Mark, for all of the equipment help and wisdom, and the calming presence when things didn't go to plan. Dan, thanks for making my MChem project one I enjoyed so much that I chose to stick around, I wouldn't be here without you. Many thanks also to Alison for the suggestions and advice from an engine perspective, and to Diogo, for all of the Gaussian and MESMER help, even from the other side of the world.

Special thanks to Charlotte W, Zara, Charlotte B, and all other Dainton and HIRAC group friends. You've made the last three years so enjoyable, and I wish you all every success in life. Also, an extra shout out to Katie Greenlees, the world's best MChem student, for your help. An extra special thank you should also be extended to Dave Fogarty, for the endless discussions about football, holidays and cakes, a welcome distraction when I needed a break from kinetics. I would also like to thank all the other Bioenergy CDT students, especially for the weekend break in Settle, a weekend I will honestly never forget for a multitude of reasons. Special thanks to Ella for being the best desk neighbour, and Iram, for knowing what I'm thinking without ever saying it out loud.

I'd like to thank my parents, Steve and Jacqui, the most inspirational people in my life, for their unwavering support in everything I've ever attempted and their endless love and encouragement. I'd also like to thank my Nanny Joyce, your strength and grace are something I will forever admire. Special thanks go to my sister and best friend, Stacey, for always knowing what to say and making me laugh when times are tough, and also to Paul and Fraser for the same reasons. I'd like to extend my warmest thanks to all the Potters and Pascoes, for all of their support over the last few years too.

Lastly, to David, who deserves the biggest thanks of all. Without you, this thesis wouldn't exist. Thank you for your patience, the kinetics discussions while brushing teeth, the excellent vegan food, and for bringing so much light, happiness and love in to my life (and for always asking me for a giant whiteboard to draw our work on). I feel endlessly grateful that we've been allowed to spend so much time together these past six years, and I can't wait for the rest of our lives together.

Abstract

The work presented in this thesis utilises the laser flash photolysis-laser induced fluorescence method to study the reaction kinetics of the four isomers of butanol, potential biofuels, under conditions relevant to low temperature combustion. Prior to the widespread use of these potential alternative fuels, their mechanism of low temperature combustion must be well understood, to ensure the best conditions for these fuels are employed in novel engines.

Chapter 3 describes a detailed experimental study for the reaction of each of the four isomers of butanol (*n*-, *i*-, *s*- and *t*-butanol) with the hydroxyl radical at temperatures between 298 and 714 K, and at pressures between 30 and 130 Torr of nitrogen. This work presents the first temperature dependent study of these reactions at temperatures above 400 K and below 800 K, and has thus assisted in reducing the uncertainty of the bimolecular rate coefficient in this temperature region, which is crucial to low temperature combustion of these alternative fuels in an engine. Temperature dependent modified Arrhenius parameterisations were provided from this work, and also from concatenate fits to this work and high temperature shock tube data from the literature. The temperature dependence for the reaction of each isomer with OH obtained in this work can be described by modified Arrhenius parameterisations (all in units of $\text{cm}^3 \text{ molecule}^{-1} \text{ s}^{-1}$):

$$k_{n\text{-butanol}+\text{OH}} (298 - 715 \text{ K}) = (1.15 \pm 2.62) \times 10^{-19} \times T^{(2.64 \pm 0.31)} \times \exp\left(\frac{7800 \pm 1100}{R \times T}\right)$$

$$k_{i\text{-butanol}+\text{OH}} (298 - 607 \text{ K}) = (2.05 \pm 6.79) \times 10^{-18} \times T^{(2.20 \pm 0.45)} \times \exp\left(\frac{6800 \pm 1600}{R \times T}\right)$$

$$k_{s\text{-butanol}+\text{OH}} (298 - 690 \text{ K}) = (1.38 \pm 2.58) \times 10^{-21} \times T^{(3.22 \pm 0.25)} \times \exp\left(\frac{10330 \pm 970}{R \times T}\right)$$

$$k_{t\text{-butanol}+\text{OH}} (298 - 614 \text{ K}) = (4.50 \pm 23.7) \times 10^{-21} \times T^{(2.99 \pm 0.71)} \times \exp\left(\frac{5200 \pm 2600}{R \times T}\right)$$

These parameterisations are crucial to the improvement of structure-activity relationships, for calculating branching ratios for the reaction of the butanol isomers with OH at temperatures relevant to low temperature combustion. Accurate total bimolecular rate coefficients and branching ratios for the reaction of butanol with OH are vital for modelling of combustion parameters such as ignition delay times, as demonstrated later in Chapter 5.

Chapter 4 presents experimental observations and kinetic measurements of the β -scission decomposition of β -hydroxybutyl radicals above 480 K. The β -site radicals formed through hydrogen abstraction from butanol by OH decompose at these sufficiently high temperatures to produce a butene molecule and an OH radical. The *ab initio* energetic barriers

to decomposition for these radicals have been calculated at the CCSD/aug-cc-pVTZ//M06-2X/aug-cc-pVTZ level. The barriers calculated have also been optimised using master equation solving for β -site radicals derived from all isomers of butanol with the exception of *s*-butanol. The optimised barriers to decomposition of the radical are 103.4 ± 1.3 , 93.0 ± 1.0 and 100.0 ± 2.6 kJ mol⁻¹ for *t*-, *i*- and *n*-butanol respectively. The OH yield obtained in these experiments has also been used as a proxy for abstraction at the beta site of each butanol isomer, and equated to the percentage of OH reaction abstractions occurring at this site.

Chapter 5 presents some unusual observations in which a growth of OH signal was observed at temperatures above 600 K in the presence of oxygen following the photolysis pulse, and some experimental tests were conducted to deduce the source of this behaviour. The bimolecular rate coefficient for the reaction of O (³P) atoms with *n*-butanol was measured at temperatures of 490 – 730 K, and pressures of 40 – 55 Torr, described by the Arrhenius parameterisation: $k_{\text{O}(^3\text{P})+n\text{-butanol}}(490 - 730 \text{ K}) = (1.64 \pm 0.55) \times 10^{-10} \times \exp^{(-18700 \pm 1700/RT)} \text{ cm}^3 \text{ molecule}^{-1} \text{ s}^{-1}$.

Table of Contents

Chapter 1 Introduction.....	1
1.1 Climate Change and the Need for Alternate Fuels	1
1.2 Development of Biofuels	2
1.3 Sustainability	5
1.4 Use of Alcohols from Renewable Resources	6
1.4.1 Properties of Alcohol Fuels	7
1.5 Butanol as a Fuel.....	8
1.5.1 Production of Butanol	9
1.5.2 Butanol Properties	10
1.6 Engine Combustion.....	11
1.6.1 Engine Types	12
1.6.2 Rapid Compression Machines	13
1.6.3 Combustion Reactions.....	14
1.7 Butanol Combustion	17
1.8 Combustion Modelling	20
1.9 Theories of Chemical Reactions	23
1.9.1 Transition state theory	23
1.9.2 Unimolecular decompositions	25
1.10 Thesis overview	29
Chapter 2 Experimental Techniques	31
2.1 Introduction.....	31
2.2 Laser Flash Photolysis – Laser Induced Fluorescence	31
2.3 Lasers	32
2.3.1 Absorption and Emission	33
2.3.2 Population Inversion.....	34
2.3.3 Excimer Laser.....	36
2.3.4 Nd:YAG Lasers	38
2.3.5 Dye lasers	38
2.3.6 Laser Flash Photolysis (LFP)	41
2.3.7 Laser Induced Fluorescence (LIF)	41
2.4 Alternative Initiation Methods.....	44
2.4.1 Discharge Flow.....	44
2.4.2 Shock Tube.....	45

2.4.3	Pulse Radiolysis	47
2.5	Alternative Detection Techniques	48
2.5.1	Resonance Fluorescence.....	48
2.5.2	Absorption Spectroscopy	49
2.5.3	Mass Spectrometry	50
2.6	Relative Rate.....	50
2.7	This work.....	52
2.7.1	Gas Delivery.....	53
2.7.2	Reaction Cell and Laser Set up	58
2.7.3	Temperature and Pressure Measurement	60
2.7.4	Kinetics.....	63
2.7.5	Data Acquisition and Analysis	67
Chapter 3 Temperature Dependent Studies of OH + Butanol Isomers.....		69
3.1	Chapter Summary	69
3.2	Introduction.....	69
3.3	Experimental.....	73
3.4	<i>n</i> -butanol.....	74
3.4.1	<i>n</i> -butanol + OH: Temperature Dependence	76
3.4.2	Conclusion.....	90
3.5	<i>i</i> -butanol.....	92
3.5.1	<i>i</i> -butanol + OH: Temperature Dependence	94
3.5.2	Conclusion.....	104
3.6	<i>s</i> -butanol.....	105
3.6.1	<i>s</i> -butanol + OH: Temperature Dependence.....	107
3.6.2	Conclusion.....	119
3.7	<i>t</i> -butanol.....	119
3.7.1	<i>t</i> -butanol + OH: Temperature Dependence	121
3.7.2	Conclusion.....	131
3.8	Isomer Comparison.....	132
3.9	Summary.....	135
Chapter 4 Unimolecular Decomposition of the β-hydroxy-butyl Isomers Following β-site Abstraction by OH		136
4.1	Chapter Summary	136
4.2	Introduction.....	136
4.3	Experimental.....	140

4.3.1	Kinetics and Analysis	142
4.3.2	Master Equation Analysis	143
4.4	<i>t</i> -Butanol	145
4.4.1	Experimental results	146
4.4.2	<i>Ab initio</i> calculations and Master Equation analysis.....	152
4.4.3	Discussion of Branching Ratios	156
4.4.4	<i>t</i> -butanol + Chlorine	159
4.5	<i>i</i> -Butanol	163
4.5.1	Experimental results	163
4.5.2	<i>Ab initio</i> Calculations and Master Equation Analysis.....	165
4.5.3	Discussion of Branching Ratios	169
4.5.4	<i>i</i> -butanol + Chlorine	173
4.6	<i>n</i> -Butanol	176
4.6.1	Experimental results	176
4.6.2	<i>Ab initio</i> Calculations and Master Equation Analysis.....	178
4.6.3	Discussion of Branching Ratios	183
4.7	<i>s</i> -Butanol.....	186
4.7.1	Experimental results	187
4.7.2	<i>Ab initio</i> Calculations	190
4.7.3	Discussion of Branching Ratios	194
4.8	Isomer Comparison.....	196
4.9	Summary.....	198
Chapter 5 Potential QOOH Decomposition Observation and a Kinetic Study of O (³P) with <i>n</i>-butanol		200
5.1	Chapter Summary	200
5.2	Introduction.....	201
5.3	Experimental.....	203
5.4	<i>t</i> -butanol OH Growth Observation and Modelling.....	204
5.4.1	Observation of OH Signal Growth.....	204
5.4.2	Signal Growth Modelling	210
5.4.3	Sarathy Model Modification	214
5.4.4	Summary of Modelling Work	217
5.5	<i>n</i> -butanol OH Growth Observation and O (³ P) Experiments	218
5.5.1	Observation of OH Signal Growth.....	218
5.5.2	OH Signal Growth Tests	219

5.5.3	Effects of Varying Oxygen on OH Signal Growth	225
5.5.4	O (³ P) + <i>n</i> -butanol Measurements	228
5.5.5	Fitting of OH Growth Signal Traces	234
5.6	Conclusions.....	234
Chapter 6 Conclusions.....		236
6.1	Summary of This Work	236
6.2	Future Work.....	238
References.....		240
Appendices.....		254

List of Figures

Figure 1-1: Processing costs (\$/GJ, i.e. dollars for processing per GJ of energy produced) against feedstock cost (\$/GJ) for a range of biomass and fossil materials, replicated from reference [20].	4
Figure 1-2: Structures of lignocellulosic biomass, showing cellulose, lignin and hemicellulose, with the building blocks of lignin also shown. Replicated from reference [23].	5
Figure 1-3: Schematic diagram of three different types of engine: Spark ignition (SI), Homogeneous Charge Compression Ignition (HCCI) and Compression Ignition (CI). Replicated from [42].	12
Figure 1-4: An example pressure trace obtained from a rapid compression machine (RCM) study. Pressure trace obtained for <i>s</i> -butanol, from the study of Weber and Sung [47], obtained at 15 bar, end compression temperature 827 K, equivalence ratio = 1.13	
Figure 1-5: Simplified sample reaction scheme for low temperature alcohol combustion, replicated from Sarathy <i>et al.</i> [1].	17
Figure 1-6: Possible structures formed during the internal isomerisation of <i>n</i> -butanol, following hydrogen abstraction at the gamma site and subsequent addition of oxygen. "6 m.r" represents isomerisation via a six-membered ring and "5 m.r" represents isomerisations via a five-membered ring.	18
Figure 1-7: Important reactions for low-temperature oxidation pathways for each isomer of butanol, replicated from Sarathy <i>et al.</i> [1].	20
Figure 1-8: A sensitivity analysis conducted by Zhou <i>et al.</i> [58], for the ignition delay times predicted for iso-butene, at 1250 K and pressures between 10 – 50 atm.	22
Figure 1-9: A schematic diagram of a typical reaction energy profile, where ABC [‡] is the transition state species, and E _A is the energy required to overcome the energy barrier.	23
Figure 1-10: Example showing the falloff in the unimolecular rate coefficient, k_{uni} , at lower pressures.	27
Figure 1-11: A schematic potential energy surface for the decomposition of the β -hydroxybutyl radicals formed following abstraction at the beta site of each of the butanol isomers, as described in Chapter 4.	29
Figure 2-1: A simplified schematic diagram of the off-resonant fluorescence set up used in this work, demonstrating the orientation and wavelengths of the lasers involved and other essential equipment.	32
Figure 2-2: Schematic diagram of radiative processes: a) Stimulated absorption, b) Spontaneous emission and c) Stimulated emission.	34
Figure 2-3: Energy levels involved in three- and four-level lasing systems.	35
Figure 2-4: A schematic diagram of a simple laser cavity.	36
Figure 2-5: Energy levels involved in a Krypton Fluoride excimer laser.	37
Figure 2-6: Structure of Rhodamine 6G, and the absorption (solid line) and fluorescence (dashed line) achieved when dissolving Rhodamine 6G in ethanol [64].	39

Figure 2-7: Jablonski diagram of possible fates for an excited molecule in a laser dye.	40
Figure 2-8: Energy level diagram of a) off-resonant and b) on-resonant fluorescence in an OH radical.....	42
Figure 2-9: A schematic diagram of a photomultiplier tube, showing the amplification in the number of electrons released on going between subsequent dynodes in the series [67].	43
Figure 2-10: A schematic diagram of a discharge flow apparatus.....	45
Figure 2-11: A schematic diagram of a shock tube apparatus, showing the relevant high and low pressure sections separated by a diaphragm.	46
Figure 2-12: Resonance fluorescence schematic diagram, where red arrows represent microwave discharge and green arrows represent resonant fluorescence from H atoms.	48
Figure 2-13: An example plot used in the relative rate method, replicated from Andersen <i>et al.</i> [84] for measuring the rate of <i>i</i> -butanol with OH relative to reference compounds of cyclohexane and ethene.	51
Figure 2-14: Schematic diagram of the gas mixing manifold utilised in this work..	53
Figure 2-15: Schematic of mixing manifold in which bubbler method used for reagent delivery.	58
Figure 2-16: Schematic diagram of the cell used in both experimental set ups.	59
Figure 2-17: Off-resonant fluorescence set up temperature calibration curve, for total gas flows of approximately 1000 sccm. Black circles represent corrections required relative to the methane parameterisations of Dunlop and Tully [93], and red triangles for the temperature corrections required relative to the hydrogen parameterisation of Tully and Ravishankara [92]. Solid red line represents concatenate polynomial fit to data, $y = 5.62 + (0.07 \times x) + (-2.5 \times 10^{-4} \times x^2)$	62
Figure 2-18: Example single exponential decay of OH fluorescence signal. Black circles represent data points with red line representing a single exponential decay fit using E 2-26, 298 K, 40 Torr nitrogen, $[n\text{-butanol}] = 2.1 \times 10^{14} \text{ molecule cm}^{-3}$, $k' = (2050 \pm 10) \text{ s}^{-1}$	65
Figure 2-19: Example bimolecular plot obtained for the reaction of <i>t</i> -butanol with OH. Obtained at 298 K and 31 Torr of nitrogen. The slope represents the bimolecular rate coefficient, $k_{t\text{-butanol}+\text{OH}} = (8.86 \pm 0.08) \times 10^{-13} \text{ cm}^3 \text{ molecule}^{-1} \text{ s}^{-1}$. The error bars are the statistical error at the 1σ level, and the red shaded area represents the 95 % confidence limits.....	66
Figure 2-20: Example trace showing laser power fluctuations (purple solid line), raw data signal (red hollow circles and red solid fit line), and normalised data signal (black hollow squares and black fit line). k' obtained from fitting to raw signal = $(1454 \pm 18) \text{ s}^{-1}$ and normalised signal = $(1433 \pm 15) \text{ s}^{-1}$. Uncertainties are statistical at 1σ	67
Figure 3-1: Simplified schematic of low temperature reaction pathways resulting from abstraction at different reactive sites for the four isomers of butanol [1].....	71

- Figure 3-2: Current literature for temperature dependence of the reaction of *n*-butanol with OH, demonstrating gap in the knowledge for experimental data between 400 and 900 K. See Section 3.4.1 for in-depth discussion. 72
- Figure 3-3: Possible abstraction sites from *n*-butanol by OH. Primary abstraction sites in blue, secondary abstraction sites in green, and hydroxyl group abstraction in orange. Carbon positions relative to hydroxyl group labelled in red. 75
- Figure 3-4: Resulting *n*-butyl and *n*-butoxy radicals formed from H atom abstraction by OH at each potential abstraction site. 75
- Figure 3-5: Example kinetic trace for *n*-butanol + OH, with single exponential equation (Equation E 2-28) fit, $k' = (2050 \pm 20) \text{ s}^{-1}$, where the error is the statistical uncertainty at a 1σ level. Obtained at 298 K and 35 Torr, $[n\text{-butanol}] = 2.09 \times 10^{14} \text{ molecule cm}^{-3}$ 76
- Figure 3-6: Example bimolecular plot for OH + *n*-butanol at 35 Torr and 298 K. Plot of pseudo-first order rate constant k' (s^{-1}) against $[n\text{-butanol}]$ (molecule cm^{-3}). $k_{n\text{-butanol}+\text{OH}} = (8.98 \pm 0.16) \times 10^{-12} \text{ cm}^3 \text{ molecule}^{-1} \text{ s}^{-1}$, where the quoted bimolecular error is the 1σ statistical analysis of the linear fit, with the 95 % confidence limits in red filled area. Experimental points as black filled triangles with 1σ error bars from single trace fitting, with instrumental fit to data points. 77
- Figure 3-7: All experimentally obtained $k_{n\text{-butanol}+\text{OH}}$ rate coefficients in this work, with Arrhenius parameterisation and 95 % confidence limits (red shaded region). Filled black circles represent experimental measurements conducted using the bulb method for reagent delivery, and filled red triangles are those utilising the bubbler method. See Table 3-1 for error justification. 80
- Figure 3-8: Rate coefficient data for the *n*-butanol + OH reaction: This work (black triangles, black solid line, 95 % confidence limits in red shaded region). Compared with Pang *et al.* (purple circles, purple solid line and dashed line for extrapolated region), McGillen *et al.* (red inverted triangles and blue diamonds, blue solid line), Yujing *et al.* (light blue pentagons, light blue solid line and dashed line for extrapolated region) experimental data; Sarathy *et al.* (solid pink line), Zhou *et al.* G3 (orange dotted line) and CCSD (lilac dashed line) calculations; SAR of Atkinson (Red dot-dash line) and Bethel *et al.* (green dot-dash line). Data replicated from [78], [111], [73], [55], [112], [114], and [101]. 87
- Figure 3-9: Concatenate fit to rate coefficient data for the *n*-butanol + OH reaction: This work (black triangles, black solid line, 95 % confidence limits in red shaded region), with Arrhenius parameterisation constrained to high temperature data of Pang *et al.* (purple circles, purple solid line and dashed line for extrapolated region). Compared to McGillen *et al.* (red inverted triangles and blue diamonds, blue solid line), Yujing *et al.* (light blue pentagons, light blue solid line and dashed line for extrapolated region) experimental data; Sarathy *et al.* (solid pink line), Zhou *et al.* G3 (orange dotted line) and CCSD (lilac dashed line) calculations; SAR of Atkinson (Red dot-dash line) and Bethel *et al.* (green dot-dash line). Data replicated from [78], [111], [73], [55], [112], [114], and [101]. 89
- Figure 3-10: Possible abstraction sites from *i*-butanol by OH. Primary abstraction sites in blue, secondary abstraction sites in green, tertiary abstraction sites in red and hydroxyl group abstraction in orange. Carbon positions relative to hydroxyl group labelled in red. 93

- Figure 3-11: Resulting *i*-butyl and *i*-butoxy radicals formed from H atom abstraction by OH at each potential abstraction site. 93
- Figure 3-12: All experimentally obtained $k_{i\text{-butanol}+\text{OH}}$ bimolecular rate coefficients in this work, with Arrhenius parameterisation and 95 % confidence limits (red shaded region). See Table 3-4 for error justification. 96
- Figure 3-13: Rate coefficient data for *i*-butanol + OH reaction: This work (black triangles, black solid line, 95 % confidence limits in red shaded region). Compared with Pang *et al.* (purple circles, purple solid line and dashed line for extrapolated region), McGillen *et al.* (blue inverted triangles, blue solid line), Mellouki *et al.* (light blue squares, light blue solid line) experimental data; Sarathy *et al.* (solid pink line) calculation; SAR of Atkinson (Red dot-dash line) and Bethel *et al.* (green dot-dash line). Data replicated from [78], [119], [75], [55], [114], and [101]. 101
- Figure 3-14: Concatenate fit to rate coefficient data for *i*-butanol + OH reaction: This work (black triangles, black solid line, 95 % confidence limits in red shaded region), with the modified Arrhenius parameterisations constrained to the high temperature data from Pang *et al.* (purple circles, purple solid line and dashed line for extrapolated region). Compared with McGillen *et al.* (blue inverted triangles, blue solid line), Mellouki *et al.* (light blue squares, light blue solid line) experimental data; Sarathy *et al.* (solid pink line) calculation; SAR of Atkinson (Red dot-dash line) and Bethel *et al.* (green dot-dash line). Data replicated from [78], [119], [75], [55], [114], and [101]. 103
- Figure 3-15: Possible abstraction sites from *s*-butanol by OH. Primary abstraction sites in blue, secondary abstraction sites in green, tertiary abstraction sites in red and hydroxyl group abstraction in orange. Carbon positions relative to hydroxyl group labelled in red. 106
- Figure 3-16: Resulting *s*-butyl and *s*-butoxy radicals formed from H atom abstraction by OH at each potential abstraction site. 106
- Figure 3-17: Experimentally obtained bimolecular rate coefficients with Arrhenius parameterisation (solid black line) and 95 % confidence limits (red shaded region). Experiments conducted using Hydrogen peroxide/water precursor are filled black shapes (circle for bulb delivery, triangle for bubbler delivery), and experiments conducted using urea hydrogen peroxide are hollow red shapes (circles for bulb delivery, triangles for bubbler delivery and pentagons for thermostatted bubbler). 109
- Figure 3-18: Rate coefficient data for *s*-butanol + OH reaction: This work (black triangles, black solid line, 95 % confidence limits in red shaded region). Compared with Pang *et al.* (purple circles, purple solid line and dashed line for extrapolated region), McGillen *et al.* (blue inverted triangles, blue solid line), Jimenez *et al.* (olive squares, olive solid line with dashed line for extrapolated region) experimental data; Sarathy *et al.* (solid pink line) calculation; SAR of Atkinson (Red dot-dash line) and Bethel *et al.* (green dot-dash line). Data replicated from [78], [123], [74], [55], [114] and [101]. 115

- Figure 3-19: Concatenate fit to rate coefficient data for *s*-butanol + OH reaction: This work (black triangles, black solid line, 95 % confidence limits in red shaded region) with the Arrhenius parameterisations constrained to the high temperature data from Pang *et al.* (purple circles, purple solid line and dashed line for extrapolated region). Compared with McGillen *et al.* (blue inverted triangles, blue solid line), Jimenez *et al.* (olive squares, olive solid line with dashed line for extrapolated region) experimental data; Sarathy *et al.* (solid pink line) calculation; SAR of Atkinson (Red dot-dash line) and Bethel *et al.* (green dot-dash line). Data replicated from [78], [123], [74], [55], [114] and [101]. 117
- Figure 3-20: Possible abstraction sites from *t*-butanol by OH. Primary abstraction sites in blue and hydroxyl group abstraction in orange. Carbon positions relative to hydroxyl group labelled in red. 120
- Figure 3-21: Resulting *t*-butyl and *t*-butoxy radicals formed by H atom abstraction by OH at each potential abstraction site. 120
- Figure 3-22: All experimentally obtained rate coefficient data for the reaction of *t*-butanol with OH, obtained between 30 – 88 Torr. Experimental data measured using bulb method (filled black circles) and bubbler method (filled red triangles) of reagent delivery. 122
- Figure 3-23: Rate coefficient data for *t*-butanol + OH reaction: This work (black triangles, black solid line, 95 % confidence limits in red shaded region). Compared with Stranic *et al.* (purple circles, purple solid line and dashed line for extrapolated region), McGillen *et al.* (blue inverted triangles, blue solid line), Wallington *et al.* (olive hexagons) experimental data; Sarathy *et al.* (solid pink line) calculation; SAR of Atkinson (red dot-dash line), Kwok and Atkinson (orange dot-dash line) and Bethel *et al.* (green dot-dash line). Data replicated from [78], [76], [127], [55], [114], [130] and [101]. 128
- Figure 3-24: Concatenate fit to rate coefficient data for *t*-butanol + OH reaction: This work (black triangles, black solid line, 95 % confidence limits in red shaded region), with the modified Arrhenius parameterisation constrained to the high temperature data of Stranic *et al.* (purple circles, purple solid line and dashed line for extrapolated region). Compared with McGillen *et al.* (blue inverted triangles, blue solid line), Wallington *et al.* (olive hexagons) experimental data; Sarathy *et al.* (solid pink line) calculation; SAR of Atkinson (red dot-dash line), Kwok and Atkinson (orange dot-dash line) and Bethel *et al.* (green dot-dash line). Data replicated from [78], [76], [127], [55], [114], [130] and [101]. 130
- Figure 3-25: Four structures of the butanol isomers: a) *n*-butanol, b) *i*-butanol, c) *s*-butanol and d) *t*-butanol. 132
- Figure 3-26: C–H Bond dissociation energies (kcal mol⁻¹) calculated at CBS-QB3 level of theory, replicated from Sarathy *et al.* [1]. 133
- Figure 3-27: Potential pre-reactive complex structures formed during the reaction of *n*-butanol with OH. a) Five-membered ring system and b) Six-membered-ring system. 134

- Figure 4-1: Experimental OH fluorescence traces obtained by Hess and Tully [134] for the reaction of 2-propanol ((CH₃)₂CHOH) with ¹⁶OH (hollow squares, black solid line) and ¹⁸OH (hollow circles, with red fit line added), obtained at 535 K and 544 K respectively, with radical decomposition mechanism shown for the resulting 2-propanol radical. 137
- Figure 4-2: Potential energy surface calculated for the 2-propanol β -radical by Zádor *et al.*, replicated from [136]. All energies reported in kcal mol⁻¹, relative to the entrance channel of propene + OH..... 139
- Figure 4-3: Representation of a model for Energy Grained Master Equation (EGME) solving for a typical association reaction, replicated from Glowacki *et al.* [144]..... 144
- Figure 4-4: A typical kinetic trace obtained above 480 K, where the red line is the single exponential fit from Section 2.7.4, equation E 2-28, ($k' = (6040 \pm 270) \text{ s}^{-1}$) and the blue line is the biexponential function (E 4-6) ($k'_{\beta\text{-abs}} + k_{\text{non}\beta\text{-abs}} = (9240 \pm 180) \text{ s}^{-1}$, $k_{\text{recycle}} = (870 \pm 50) \text{ s}^{-1}$). The errors obtained are statistical uncertainty at 2σ . The trace was obtained at 535 K, 50 Torr, $[t\text{-butanol}] = 8 \times 10^{15} \text{ molecule cm}^{-3}$. The inset to the figure shows the residual plot of the biexponential equation fitting to trace. 147
- Figure 4-5: Increasing biexponential behaviour observed for increasing temperature. All experiments conducted around 30 Torr with $[t\text{-butanol}] \approx (2\text{-}2.5) \times 10^{14} \text{ molecule cm}^{-3}$ 148
- Figure 4-6: Globally obtained k_{recycle} for *t*-butanol β -hydroxybutyl radical. Parameters shown as a function of temperature and pressure. The errors reported in temperatures are ± 3 K for pressures around 40 Torr and ± 5 K for pressures around 89 Torr, and the errors reported for the experimental k_{recycle} values are the 1σ errors obtained from the biexponential global fit to the experimental traces multiplied by a factor of 4. 149
- Figure 4-7: Graph of OH yield (% , percentage of abstraction reactions that reform OH via the suggested route in Scheme 4-3) against temperature (K), conducted at 40 – 90 Torr. Error bars represent propagated errors of $k'_{\text{R-loss}}$ and $k_{\text{non-OH}}$ obtained from single trace analysis..... 151
- Figure 4-8: Rotations described by hindered rotor approximation (highlighted by red arrows) 153
- Figure 4-9: Potential energy surface for the decomposition of β *t*-hydroxybutyl radical, calculated at CCSD(T)/CBS//M06-2X/aug-cc-pVTZ level. 153
- Figure 4-10: Globally obtained k_{recycle} for *t*-butanol β -hydroxybutyl radical decomposition as a function of temperature and pressure, compared with corresponding MESMER fitted values and MESMER high pressure limit predicted values for decomposition. Decomposition barrier estimated by MESMER = $(103.4 \pm 1.3) \text{ kJ mol}^{-1}$. The errors reported in temperatures are ± 3 K for pressures around 40 Torr and ± 5 K for pressures around 89 Torr, and the errors reported for the experimental k_{recycle} values are the 1σ errors obtained from the biexponential global fit to the experimental traces multiplied by a factor of 4. 155

- Figure 4-11: A graph of yield of OH for *t*-butanol radical decomposition as a function of temperature and pressure, where the error bars represent propagated errors of k_{recycle} and $k_{\text{non-OH}}$ obtained from global analysis. The literature lines represent the branching ratio of *t*-butanol abstraction reactions occurring at the beta site from literature: Sarathy *et al.* (purple dashed line), McGillen *et al.* (blue dashed line) and the SAR of Atkinson (orange short dashed line), the updated SAR of Kwok and Atkinson (Brown dashed line) and the SAR of Bethel *et al.* (red dashed line). Data replicated from: [55], [78], [114], [130], and [101]. 158
- Figure 4-12: Example kinetic traces obtained a) Utilising oxalyl chloride as the radical precursor with *t*-butanol, 640 K, 130 Torr, [*t*-butanol] = 4×10^{15} molecule cm^{-3} and an estimated starting Cl radical concentration of 1×10^{13} molecule cm^{-3} . b) Utilising hydrogen peroxide radical precursor with *t*-butanol, 640 K, 130 Torr, [*t*-butanol] = 4×10^{15} molecule cm^{-3} and an estimated starting OH concentration of 2×10^{12} molecule cm^{-3} 161
- Figure 4-13: Globally obtained k_{recycle} for *i*-hydroxybutyl β -radical decomposition as a function of temperature and pressure, with hollow black squares representing experiments at 37 Torr and hollow red circles for experiments at 82 Torr. The reported error bars represent the 1σ errors obtained from the biexponential global fit to the experimental traces multiplied by a factor of 4. 165
- Figure 4-14: Rotations described by hindered rotors, calculated for *i*-butanol β -hydroxybutyl radical and iso-butene. Bonds described are highlighted by red arrows. 166
- Figure 4-15: Potential energy surface for the decomposition of β *i*-hydroxybutyl radical, calculated at CCSD(T)/aug-cc-pVTZ//M06-2x/aug-cc-pVTZ level. Van der Waals complex not calculated but included based on analogy with *t*-butanol system (shown in orange). 166
- Figure 4-16: Globally obtained k_{recycle} for *i*-butanol β -hydroxybutyl radical decomposition as a function of temperature and pressure, compared with corresponding MESMER fitted values and MESMER high pressure limit predicted values for decomposition. Decomposition barrier estimated by MESMER = (93 ± 1) kJ mol^{-1} . The errors reported in temperatures are ± 3 K for pressures around 37 Torr and ± 5 K for pressures around 82 Torr, and the errors reported for the experimental k_{recycle} values are the 1σ errors obtained from the biexponential global fit to the experimental traces multiplied by a factor of 4. 168
- Figure 4-17: A graph of the MESMER predicted values for *i*-butanol radical decomposition compared to the experimentally obtained recycling parameters, with a linear fit (red solid line). A perfect 1:1 fit (black solid line) has also been fit. 169
- Figure 4-18: A graph of yield of OH for *i*-butanol radical decomposition as a function of temperature and pressure, where the error bars represent propagated errors of k_{recycle} and $k_{\text{non-OH}}$ obtained from global analysis. The literature lines represent the branching ratio of *i*-butanol abstraction reactions occurring at the beta site from literature: Sarathy *et al.* (purple dashed line), McGillen *et al.* (blue dashed line) and the SAR of Atkinson (green dashed line), the updated SAR of Kwok and Atkinson (red dashed line) and SAR of Bethel *et al.* (orange dashed line). Data replicated from: [55], [78], [114], [130], and [101]. 170

- Figure 4-19: Example kinetic traces obtained a) Utilising oxalyl chloride as the radical precursor with *i*-butanol, 640 K, 130 Torr, [*i*-butanol] = 9.8×10^{14} molecule cm^{-3} and an estimated starting Cl concentration of 1×10^{13} molecule cm^{-3} . b) Utilising hydrogen peroxide radical precursor with *i*-butanol, 640 K, 130 Torr, [*i*-butanol] = 9.8×10^{14} molecule cm^{-3} and an estimated starting OH concentration of 2×10^{12} molecule cm^{-3} .
..... 174
- Figure 4-20: Globally obtained k_{recycle} for *n*-butanol β -hydroxybutyl radical decomposition, as a function of temperature and pressure. The reported error bars represent the 1σ errors obtained from the biexponential global fit to the experimental traces multiplied by a factor of 4. 177
- Figure 4-21: Rotations described by hindered rotors, calculated for the *n*-butanol β -hydroxybutyl radical and *n*-butene. Bonds described are highlighted by red arrows.
..... 179
- Figure 4-22: Potential energy surface for the decomposition of β *n*-hydroxybutyl radical, calculated at CCSD(T)/aug-cc-pVTZ//M06-2X/aug-cc-pVTZ level. Van der Waals complex not calculated but included based on analogy with *t*-butanol system (shown in orange). 179
- Figure 4-23: Globally obtained k_{recycle} for *n*-butanol β -hydroxybutyl radical decomposition as a function of temperature and pressure, compared with corresponding MESMER fitted values and MESMER high pressure limit predicted values for decomposition. Decomposition barrier estimated by MESMER = (100 ± 2.6) kJ mol^{-1} . The errors reported in temperatures are ± 3 K for pressures around 37 Torr and ± 5 K for pressures around 82 Torr, and the errors reported for the experimental k_{recycle} values are the 1σ errors obtained from the biexponential global fit to the experimental traces multiplied by a factor of 4. 181
- Figure 4-24: A graph of the MESMER predicted values for *n*-butanol radical decomposition compared to the experimentally obtained recycling parameters, with a linear fit (red solid line). A perfect 1:1 fit (black solid line) has also been fit. 182
- Figure 4-25: A graph of yield of OH for *n*-butanol radical decomposition as a function of temperature and pressure, where the error bars represent propagated errors of k_{recycle} and $k_{\text{non-OH}}$ obtained from global analysis. The literature lines represent the branching ratio of *n*-butanol abstraction reactions occurring at the beta site from literature: Sarathy *et al.* (purple dashed line), McGillen *et al.* (blue dashed line) and the SAR of Atkinson (green dashed line), the updated SAR of Kwok and Atkinson (red dashed line) and the SAR of Bethel *et al.* (orange dashed line). Data replicated from: [55], [78], [114], [130], and [101]. 185
- Figure 4-26: Example kinetic traces obtained for *s*-butanol above 490 K using different OH radical precursors. a) Hydrogen peroxide/water precursor, 112 Torr, 560 K, 1.4×10^{15} molecule cm^{-3} . b) Urea hydrogen peroxide precursor, 37 Torr, 550 K, 1.05×10^{15} molecule cm^{-3} . Insets to each trace show residual from fit of biexponential equation to data. 188
- Figure 4-27: Globally obtained k_{recycle} for *s*-butanol β -hydroxybutyl radical decomposition, as a function of temperature and pressure. Open shapes represent parameters obtained using hydrogen peroxide precursor and filled shapes represent those obtained using the urea hydrogen peroxide (UHP) precursor. 189

- Figure 4-28: A graph of yield of OH as a function of temperature and pressure for *s*-butanol, where the error bars represent propagated errors of k_{recycle} and $k_{\text{non-OH}}$ obtained from global analysis..... 190
- Figure 4-29: Potential energy surface for the decomposition of the two β *s*-hydroxybutyl radicals, calculated at CCSD(T)/aug-cc-pVTZ//M06-2X/aug-cc-pVTZ level. Water has been omitted as a product from the initial abstraction reaction. Van der Waals complexes not calculated but included based on analogy with *t*-butanol system (shown in orange). 191
- Figure 4-30: C3 radical, transition states, and both cis and trans-2-butene products energies in kcal mol⁻¹, defined relative to trans-2-butene + OH. Plain black font represents *ab initio* calculated barriers (CCSD(T)-F12a/cc-pVTZ-F12//M06-2X/6-311++G(d,p)) and bold black font represents master equation adjusted values, both from Antonov [142], compared with *ab initio* calculated energies from this work in red italics (CCSD/aug-cc-pVTZ//M06-2X/aug-cc-pVTZ). *Value not adjusted in master-equation calculation. 193
- Figure 4-31: A graph of yield of OH for *s*-butanol radical decomposition as a function of temperature and pressure, where the error bars represent propagated errors of k_{recycle} and $k_{\text{non-OH}}$ obtained from global analysis. The literature lines represent the branching ratio of *s*-butanol abstraction reactions occurring at the beta site from literature: Sarathy *et al.* (purple dashed line), McGillen *et al.* (blue dashed line) and the SAR of Atkinson (green dashed line), the updated SAR of Kwok and Atkinson (red dashed line) and the SAR of Bethel *et al.* (orange dashed line). * McGillen *et al.* parameterisation only represents the secondary beta site, as the primary beta site was reported as a total of the primary beta and primary delta sites, and cannot be added. Data replicated from: [55], [78], [114], [130], and [101]. 194
- Figure 5-1: Sarathy *et al.* combustion model reaction path analysis for *n*-butanol combustion at 800 K, 1 atm and $\phi = 1.0$, replicated from [55]. The reaction fluxes are given for 20 % fuel consumption. 202
- Figure 5-2: An example kinetic trace obtained under biexponential conditions in the absence of added oxygen. Trace obtained at 613 K, 36 Torr N₂, $[t\text{-butanol}] = 1.6 \times 10^{16}$ molecule cm⁻³. The red line represents a biexponential fit (Equation E 4-6) $k_a = (31400 \pm 1100)$ s⁻¹, $k_{\text{recycle}} = (5980 \pm 210)$ s⁻¹, $k_{\text{non-OH}} = (1420 \pm 50)$ s⁻¹. The quoted errors are statistical at the 1 σ level. 204
- Figure 5-3: Example traces obtained at 500 K, 34 Torr, both with (hollow red triangles) and without (hollow black circles) the addition of significant amounts of oxygen, where added $[O_2] = 1.76 \times 10^{17}$ molecule cm⁻³. 205
- Figure 5-4: Example trace obtained at 580 K, 34 Torr, both with (hollow red triangles) and without (hollow black circles) the addition of significant amounts of oxygen, where added $[O_2] = 1.76 \times 10^{17}$ molecule cm⁻³. 206
- Figure 5-5: A graph of increasing biexponential behaviour as a function of varying oxygen (molecule cm⁻³). All traces were obtained at 587 K, approximately 82 Torr, with $[t\text{-butanol}] = 1.1 \times 10^{16}$ molecule cm⁻³. All experimental traces have been rescaled to 1 at point of photolysis for ease of comparison. 207

- Figure 5-6: Experimental traces showing slight growth of OH signal on addition of varying amounts of oxygen to the system. All traces obtained at approximately 590 K, 45 Torr, $[t\text{-butanol}] = 5.7 \times 10^{14}$ molecule cm^{-3} 208
- Figure 5-7: An example set of experimental traces obtained with and without the addition of oxygen at 620 K, where addition of oxygen resulted in instantaneous growth of signal following photolysis pulse. Experiments conducted at 45 Torr, $[t\text{-butanol}] = 5.3 - 6.0 \times 10^{14}$ molecule cm^{-3} , added $[\text{O}_2] = 0 - 3.1 \times 10^{17}$ molecule cm^{-3} 209
- Figure 5-8: Simulations obtained from running *t*-butanol submechanism in kinetic modelling, as a function of oxygen. All simulations run at 620 K, with starting concentration of *t*-butanol = 5.5×10^{14} molecule cm^{-3} . Filled symbols represent OH simulation data and open symbols represent CH_3COCH_3 simulation data (chosen as a marker of $\text{RO}_2 \rightarrow \text{Products}$). 212
- Figure 5-9: Potential energy surface for rearrangement and decompositions of the $\text{C}_4\text{H}_8\text{OH}-\text{O}_2(\text{RO}_2)$ species formed following β -site abstraction of *t*-butanol calculated by Sun *et al.*, replicated from reference [152]. Energies calculated at the CBS-Q/B3LYP level, reported in kcal mol^{-1} 213
- Figure 5-10: Ignition delay time data from Weber and Sung [47] obtained at 15 bar and $\Phi = 1$. Simulations using the Sarathy *et al.* [55] base combustion mechanism shown as red hollow circles, with subsequent updates: Purple squares: Updating total bimolecular $\text{OH} + t\text{-butanol}$ reactivity. Blue diamonds: Separating of $\text{RO}_2 \rightarrow \text{QOOH} \rightarrow \text{Product}$ reactions based on recommended rates of Sun, *et al.* Green triangles: Addition of pressure dependence to RO_2 separated reactions based on recommendations of Sun *et al.* 216
- Figure 5-11: An example set of experimental series of traces obtained at high temperatures following addition of oxygen. Traces obtained at 720 K, 130 Torr N_2 , $[n\text{-butanol}] = 1.6 \times 10^{15}$ molecule cm^{-3} , as a function of O_2 . Range of added $[\text{O}_2] = 0 - 2.7 \times 10^{17}$ molecule cm^{-3} 218
- Figure 5-12: OH Fluorescence traces obtained when varying photolysis laser repetition rate. Traces obtained at 760 K, 130 Torr total pressure N_2 , $[n\text{-butanol}] = 2.5 \times 10^{15}$ molecule cm^{-3} and added $[\text{O}_2] = 2.5 \times 10^{16}$ molecule cm^{-3} 220
- Figure 5-13: Example trace obtained at temperatures above 650 K in the absence of hydrogen peroxide precursor. $[n\text{-butanol}] = 1.86 \times 10^{14}$ molecule cm^{-3} , $[\text{O}_2] = 4.1 \times 10^{16}$ molecule cm^{-3} . Experimental trace was obtained at 682 K, in 35 Torr N_2 . 221
- Figure 5-14: Trace obtained in the absence of hydrogen peroxide precursor, with (hollow red triangles) and without (hollow black circles) the photolysis laser. $[n\text{-butanol}] = 7 \times 10^{14}$ molecule cm^{-3} , added $[\text{O}_2] = 8.3 \times 10^{16}$ molecule cm^{-3} . Experimental trace was obtained at 600 K, in 95 Torr N_2 222
- Figure 5-15: Trace obtained in the absence of hydrogen peroxide precursor and oxygen, with (hollow red triangles) and without (hollow black circles) the photolysis laser. $[n\text{-butanol}] = 7 \times 10^{14}$ molecule cm^{-3} . Experimental trace was obtained at 600 K, in 95 Torr N_2 223
- Figure 5-16: Trace obtained in the absence of hydrogen peroxide precursor, with (hollow red triangles) and without (hollow black circles) the addition of 8.3×10^{16} molecule cm^{-3} of oxygen. $[n\text{-butanol}] = 7 \times 10^{14}$ molecule cm^{-3} . Experimental trace was obtained at 600 K, in 95 Torr N_2 224

- Figure 5-17: Unnormalised OH fluorescence traces for series of *n*-butanol (approximately 7×10^{14} molecule cm^{-3}) in the absence of hydrogen peroxide, as a function of oxygen (varied from $0.8 - 3.8 \times 10^{17}$ molecule cm^{-3}), obtained at 610 K and 94 Torr N_2 226
- Figure 5-18: Unnormalised OH fluorescence traces for series of *n*-butanol (approximately 7×10^{14} molecule cm^{-3}) experiments in the absence of hydrogen peroxide. Traces obtained as a function of oxygen (varied from $0.8 - 3.8 \times 10^{17}$ molecule cm^{-3}), showing increase in baseline pre-photolysis laser pulse. Traces obtained at 683 K and 94 Torr N_2 . Solid lines are line of best fit with fixed gradient of 0. 227
- Figure 5-19: Example OH fluorescence kinetic trace obtained for reactions of O (^3P) with *n*-butanol. Experimental trace was obtained at 620 K, in 47 Torr N_2 , with [*n*-butanol] = 2.7×10^{14} molecule cm^{-3} 230
- Figure 5-20: Example global fitting results from fitting to multiple OH fluorescence signal traces obtained from reactions of O with *n*-butanol. Traces were obtained at 45 – 48 Torr N_2 and 620 K. Concentration of alcohol reagent: [*n*-butanol] = $2.7 - 8.4 \times 10^{14}$ molecule cm^{-3} 231
- Figure 5-21: All experimentally obtained $k_{\text{O}(^3\text{P})+n\text{-butanol}}$ rate coefficients from this work (hollow black circles with black error bars, representing a 10 % error), with Arrhenius parameterisation and 95 % confidence limits (solid red line, filled red area). Compared with Roscoe *et al.* [154] (blue filled circles calculated from Arrhenius parameterisation fit to data, blue dashed line is Arrhenius parameterisation and filled blue area represents reported errors). 233

List of Tables

Table 1-1: Skeletal structures of the four isomers of butanol.....	8
Table 1-2: Properties of the different isomers of butanol compared to an average gasoline structure and an alternate alcohol fuel, ethanol. Adapted from [1].	10
Table 2-1: Potential excimer complexes and their corresponding wavelengths and energies.	36
Table 2-2: Antoine parameters for alcohols studied in this work [90].	57
Table 3-1 : Summary of experimental conditions and bimolecular rate coefficients (k) obtained in this work for the n -butanol and OH reaction.	79
Table 3-2: Measured $k_{n\text{-butanol}+\text{OH}}$ (298 K) for this work with all previous literature values.	82
Table 3-3: Arrhenius parameterisation for the OH + n -butanol reaction from previous literature and this study.....	85
Table 3-4: Summary of experimental conditions and bimolecular rate coefficients (k) obtained for the reaction of i -butanol and OH.	95
Table 3-5: Measured $k_{\text{OH}+i\text{-butanol}}$ (298 K) for this work with all previous literature values.	97
Table 3-6: Arrhenius parameterisation for the OH + i -butanol reaction from previous literature and this study.....	100
Table 3-7: Summary of experimental conditions and bimolecular rate coefficients (k) obtained in this work for the s -butanol and OH reaction.....	108
Table 3-8: Measured $k_{s\text{-butanol}+\text{OH}}$ (298 K) for this work with all previous literature values	111
Table 3-9: Arrhenius parameterisation for the OH + s -butanol reaction from previous literature and this study.....	114
Table 3-10: Summary of experimental conditions and bimolecular rate coefficients (k) obtained for the t -butanol and OH reaction.	123
Table 3-11: Summary of previous studies on $k_{t\text{-butanol}+\text{OH}}$ conducted in literature compared with this work.	125
Table 3-12: Arrhenius parameterisation for the OH + t -butanol reaction from previous literature and this study.....	127
Table 4-1: Summary of experimental conditions and obtained OH recycling parameter k_{recycle} for t -butanol.....	150
Table 4-2: Fraction of OH abstractions occurring at beta site of t -butanol, according to branching ratios from literature.	157
Table 4-3: Summary of experimental conditions for comparable experiments conducted using hydrogen peroxide and oxalyl chloride at high temperatures with t -butanol.	162
Table 4-4: Summary of experimental conditions and obtained OH recycling parameter k_{recycle} for i -butanol.....	164

Table 4-5: Fraction of OH abstractions occurring at beta site of <i>i</i> -butanol, according to branching ratios from literature.	172
Table 4-6: Kinetic parameters (all in s ⁻¹) obtained from fitting to traces obtained at 640 K and 130 Torr, utilising either hydrogen peroxide or oxalyl chloride as an initiating radical source.	175
Table 4-7: Summary of experimental conditions and obtained OH recycling parameter k_{recycle} for <i>n</i> -butanol.....	178
Table 4-8: Fraction of OH abstractions occurring at beta site of <i>n</i> -butanol, according to branching ratios from literature.	183
Table 4-9: Summary of experimental conditions and obtained OH recycling parameter k_{recycle} for <i>s</i> -butanol.....	187
Table 4-10: Fraction of OH abstractions occurring at beta sites of <i>s</i> -butanol, according to branching ratios from literature.	195
Table 4-11: <i>Ab initio</i> calculated barriers at the CCSD/aug-cc-pVTZ//M06-2X/aug-cc-pVTZ level, compared with optimised barriers obtained from MESMER fitting, and radical structure diagrams. *Errors reported only represent the error calculated by MESMER. An error for each barrier including the systematic errors of the system is assumed to be 4 kJ mol ⁻¹	197
Table 5-1: Reduced model used for kinetic simulations of OH species profiles, constructed from experimental measurements in this work and the butanol combustion model of Sarathy <i>et al.</i> [55]......	211
Table 5-2: Summary table of the tests conducted to attempt to deduce the source of OH fluorescence growth signal. Key: green filled box indicates present, red filled box indicates absent.	225
Table 5-3: Parameters obtained from global fitting to series of O (³ P) + <i>n</i> -butanol traces obtained at 45 – 48 Torr pressure, 620 K, where [<i>n</i> -butanol] was varied across the range [<i>n</i> -butanol] = 2.7 – 8.4 × 10 ¹⁴ molecule cm ⁻³	232

List of Abbreviations

ABE	Acetone-butanol-ethanol
CI	Compression Ignition
DF	Discharge Flow
DFST	Diaphragmless Shock Tube
DFT	Density functional theory
EGME	Energy grained master equation
FP	Flash Photolysis
GC	Gas chromatography
HCCI	Homogeneous charge compression ignition
IDT	Ignition delay time
IPCC	Intergovernmental Panel on Climate Change
IR	Infrared
IUPAC	International Union of Pure and Applied Chemistry
LASER	Light amplification by stimulated emission of radiation
LFP	Laser flash photolysis
LHV	Lower heating value
LIF	Laser-induced fluorescence
MESMER	Master Equation Solver for Multi-Energy well Reactions
MFC	Mass flow controller
PES	Potential energy surface
PMT	Photomultiplier tube
PR	Pulse radiolysis
RCM	Rapid compression machine
RF	Resonance Fluorescence

RR	Relative Rate
RRKM	Rice-Ramsperger-Kassel-Marcus
SAR	Structure-activity relationship
SI	Spark ignition
ST	Shock tube
ST-CM	Shock tube-combustion modelling
TST	Transition state theory
UHP	Urea hydrogen peroxide
UV	Ultraviolet
YAG	Yttrium Aluminium Garnet
ZPE	Zero point energy

Chapter 1 Introduction

1.1 Climate Change and the Need for Alternate Fuels

As a result of an ever increasing global population and the associated growth in energy usage, the need for a renewable, clean energy strategy is of paramount importance [1]. Predictions suggest the global population could reach 9 – 10 billion people by the year 2050, resulting in severe challenges associated with feeding a growing population and competition for water and energy [2].

A recent report from the Intergovernmental Panel on Climate Change (IPCC) stated that the ‘human influence on the climate system is clear’ and that the atmospheric levels of carbon dioxide, methane and nitrous oxide have all increased since 1750 as a result of human impact [3]. Since the publication of the IPCC report, a significant milestone was reached in global climate change mitigation: the Paris Agreement of 2016 [4]. The agreement states that all countries involved will aim to hold the increase in global average temperature to well below 2 °C compared to pre-industrial levels, acknowledging that this would significantly reduce the risks and impacts of climate change. For this to be implemented, substantial policy and societal change must be employed, including the progression to a low carbon society that is less reliant on fossil fuels.

In excess of 80 % of the world’s primary energy consumption came from fossil fuels in 2018, according to the most recent BP statistical review of world energy, with oil remaining the dominant fuel of the energy mix [5]. Reserves for these conventional energy sources are being rapidly consumed, with some estimates predicting that resources will be used up by 2050 [6]. The combustion of fossil fuels is associated with substantial greenhouse gas emissions, and has thus been acknowledged as a significant contributor to climate change [1]. Carbon dioxide (CO₂) emissions from fossil fuels and industry represent 78 % of the total greenhouse gas emissions increase between 1970 and 2010, and are continuing to rise [7]. Alongside greenhouse gas emissions, the combustion of fossil petroleum also leads to the formation of pollutants, such as carbon monoxide and nitrogen oxides (NO_x), which can have detrimental effects on human health [1].

Whilst renewable alternatives to fossil fuels are being developed for power generation (such as solar and wind energy), there still exists a need for alternate liquid or gaseous fuels for transport [1], as conventional fuels currently account for more than 96 %

of energy for transport in the UK [8]. Renewable liquid alcohol fuels possess the important advantage of having a high energy density, compared to other possible alternate fuels such as hydrogen, which faces the difficult challenge of high density storage for transport vehicles [9]. For example, the energy density of liquid *n*-butanol fuel is 26.9 MJ L⁻¹ [10], compared to that of 8 MJ L⁻¹ for condensed liquid hydrogen fuels [9].

Alongside the climate change implications of the carbon dioxide emissions from vehicles (exhaust emissions from automobiles represent around 27 % of EU CO₂ emissions [11]), the detrimental effects on local air pollution and the dwindling resources of fossil fuels all point towards the need for the development of alternate, cleaner transport fuels.

1.2 Development of Biofuels

One alternative to fossil fuel energy generation is the use of biofuels from renewable biomass. The development of biofuels has received significant interest on a global scale as the need for a secure energy source becomes more apparent, following dwindling fossil fuel resources and unstable oil prices [12]. Biomass is seen as a viable alternative as it can be used or converted to fuel for almost all energy sectors, such as direct combustion to produce heat, and conversion into liquid fuels for replacement of fossil fuel equivalents [13].

A biofuel is any solid, liquid or gas fuel primarily derived from a biomass resource [14]. They can be readily produced from a range of feedstocks and display several key advantages over fossil fuels, such as coming from biodegradable resources, and providing a method of energy production that releases less greenhouse gas emissions than fossil fuel energy generation [15]. The use of biofuels is largely considered carbon neutral, as during growth, the crop absorbs carbon dioxide from the atmosphere, which balances with the CO₂ that is subsequently released on combustion of the fuel, however some controversy surrounds this concept (see Section 1.3) [16]. The benefits of biofuels over traditional fossil fuels can be further enhanced by sequestering the processed biomass into soil, such as the biochar that is produced during biomass pyrolysis, which can render the overall process carbon negative.

Types of biofuel can be separated into so called ‘generations’ depending on the type of feedstock used to make them. First generation biofuels are those that originate

from sources such as corn and oilseed, from which significant amounts of biofuels such as bioethanol can be produced [17]. These biofuels resulting from food crops however pose multiple issues for sustainability and food security. If favourable land that is currently used for food production is converted to produce biomass for biofuels, this results in direct competition for the grain from the crops, and could result in increased global prices of food [13]. Alongside this, biofuel crop growth can also result in competition for commodities such as water and fertiliser, which could similarly drive up the cost of food. Whilst the requirements for growing biomass crops can differ greatly by region, a recent study suggested that 70 % of ethanol from corn in the US requires 10 – 17 litres of water per litre of ethanol produced, compared with the 2.8 – 6.6 litres of water per litre of gasoline produced for most of the crude oil obtained onshore in the US [18].

Second generation biofuels are fuels made from lignocellulosic biomass, and from crops that are not used as food [17]. This can also include waste from various industry sectors such as forest and agricultural waste [19]. The negative effects of first generation crops on food prices are therefore not seen with the second generation crops, as they do not directly compete with food supplies [13]. Lignocellulosic material can also be grown rapidly with lower associated costs when compared to biomass grown for food consumption, which provides another advantage over first generation biomass [19]. Despite the relatively lower cost of lignocellulosic material (\$34 – 70/T dry material) compared to other biomass derived fuels such as vegetable oils (\$500 – 700/T), the conversion costs can be much higher. This is illustrated by Figure 1-1, in which production costs per GJ are compared to feedstock cost per GJ. The diagonal lines represent the overall production costs of fuels, with those for biofuels usually falling in the range of \$15 – 25/GJ, compared to the lower cost of \$5 – 15/GJ for fossil derived fuels. This figure portrays the urgent need for an improvement in the processing costs of lignocellulosic materials to bring down the total production cost to a level more comparable with that of fossil fuels.

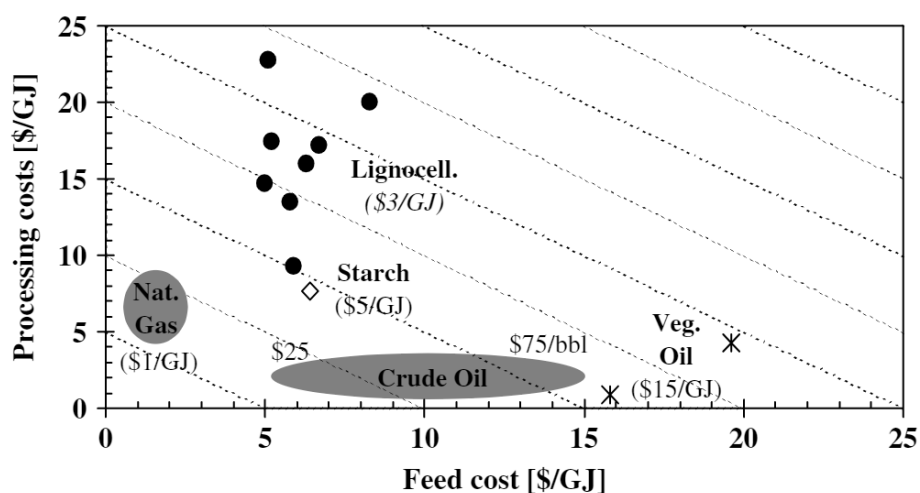


Figure 1-1: Processing costs (\$/GJ, i.e. dollars for processing per GJ of energy produced) against feedstock cost (\$/GJ) for a range of biomass and fossil materials, replicated from reference [20].

The conversion of this non-edible biomass is difficult, and as a result, the costs of processing to produce the resulting fuel are high [19]. Lignocellulosic biomass contains three main components: cellulose (40 – 50 %), hemicellulose (25 – 35 %) and lignin (15 – 20 %) [21], the structures of which can be seen in Figure 1-2. As cellulose is a long polymer constructed of glucose units, hydrogen bonding between the cellulose chains results in a rigid structure that is resistant to degradation. Alongside this, hemicellulose and lignin also provide extra strength to the lignocellulose. The decomposition of this rigidity provides a significant technological and economical barrier to the use of lignocellulose for biofuel production.

The third generation of biofuels is largely focused on species such as microalgae [14]. Algae are simple plants that absorb carbon dioxide and sunlight, and from this, form substantial amounts of oil which can be converted into biodiesel. As the algae have low levels of hemicellulose and little to no lignin, the processing of the biomass is substantially easier, and is therefore cheaper to carry out [22].

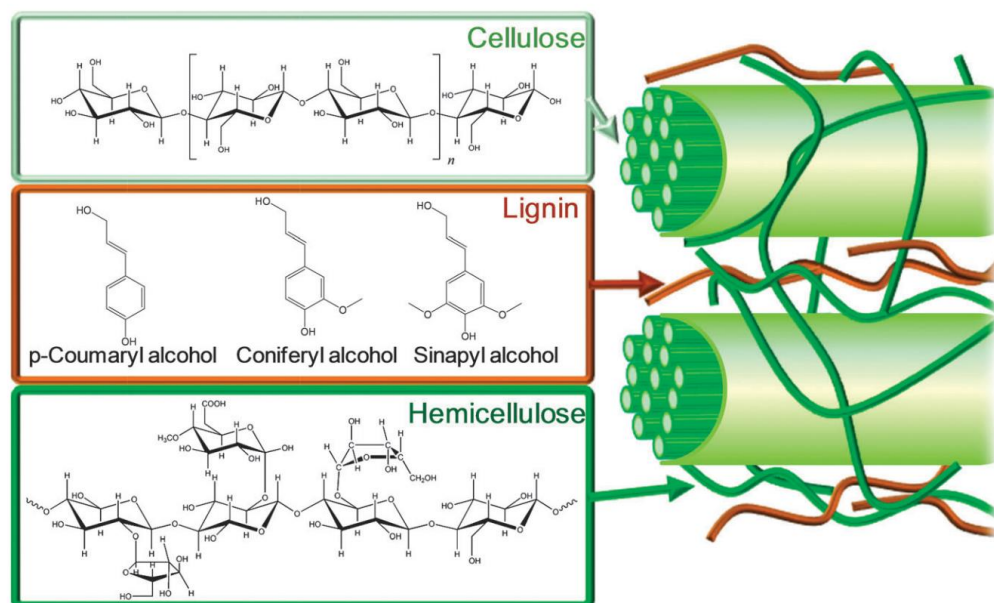


Figure 1-2: Structures of lignocellulosic biomass, showing cellulose, lignin and hemicellulose, with the building blocks of lignin also shown. Replicated from reference [23].

1.3 Sustainability

For a renewable source of energy to be considered a suitable replacement for fossil fuels, it should be evenly distributed across the globe, and demonstrate a reduction in the amount of greenhouse gas emissions it releases on production and use compared to fossil fuels [19]. Biomass and biofuels can act as a low carbon source of energy, but only if they are grown and sourced sustainably [24].

The growth of first generation biofuel food crops for energy can lead to direct and indirect land use change [25]. In areas where direct land use change is a problem, such as Brazil and Southeast Asia, rainforests and grasslands are being cleared and converted into fields for energy crop growth [24]. By doing so, a ‘carbon debt’ is created, in which up to 420 times the amount of carbon dioxide that would be saved by using the land for biofuel crops can be effectively released [24], negating any possible greenhouse gas reductions that would be achieved through using renewable biofuels. Indirect land use change can result from favourable land in one part of the world growing food crops for bioenergy instead of for human consumption, leading to farmers in another part of the world clearing an area of natural habitat to produce crops to replace this food deficit [25]. Not only can direct and indirect land use change cause elevated greenhouse gas emissions

compared to the potential savings, but it can also affect the price of food crops and reduce biodiversity as a result of habitat loss [26].

If biomass for biofuels could be developed on marginal land rather than favourable farm lands, this would pose a substantial advantage for the biofuel industry and sustainability. The use of lignocellulosic material as a resource demonstrates a significantly reduced carbon footprint compared to that of food crops, as they require much less energy intensive cultivation methods, alongside lower chemical requirements [1]. The development of processing methods for forming biofuels from leftover agricultural residue and forest residue would also be a significant milestone for the renewables industry, as it involves the use of material that would otherwise be going to waste.

1.4 Use of Alcohols from Renewable Resources

Alcohols developed from biomass sources represent a significant portion of the biofuel industry, with approximately 60 billion litres of ethanol produced from corn in the US alone in 2012 [22]. The use of ethanol as a fuel is not a new concept, with Henry Ford expecting ethanol to be the fuel of choice for his Model T car, but widespread use was not seen until the 1970s [27]. Bioethanol is now an established fuel additive in several countries, and is commonly blended in small concentrations of 5 – 10 % by volume, lending to the names E5 and E10 [19]. Some countries such as Brazil and Sweden use blends up to 85 %, although this is not commonplace due to requiring alternate specialised engines compared to those used in conventional vehicles.

Bioethanol is typically obtained from the fermentation of a range of biomass sugars [28] by microorganisms such as bacteria and yeast [19]. In the USA, it is predominantly produced from corn, and in Brazil it is largely derived from sugar-cane. As a result, bioethanol is primarily seen as a ‘first generation biofuel’ as it is produced mainly from food crops. This has led to significant concern surrounding the sustainability and viability of this method of bioethanol generation as an alternative energy source to replace traditional gasoline (see Section 1.3) [1]. Bioethanol can also be made from second generation feedstocks such as miscanthus grass and lignocellulosic crop residues, although the breakdown of this type of material provides a significant economic barrier [1]. It is therefore widely acknowledged that producing and improving the efficiency of production of biofuels from alternate sources such as waste and lignocellulosic materials are key areas of research for progressing the biofuel market [29].

1.4.1 Properties of Alcohol Fuels

Alcohols for use as potential biofuels have received attention from researchers as a result of their useful properties. Their largest advantage is that they have high octane ratings, which means they are less prone to knocking in engines (see Section 1.6.1), and allow the engine to operate at higher compression ratios [1]. Some alcohols such as methanol and ethanol are already established as common fuel additives which are used to increase the octane rating of gasoline. Butanol and longer chain alcohols have octane numbers that are closer to that of gasoline and can often decrease the octane number of the overall blend, resulting in increased engine knock. These fuels however have an increased cetane number, making them easier to ignite, and therefore are better suited to compression ignition engines.

The addition of alcohols to traditional fuels can result in improved fuel combustion in engines, and lead to a reduction in harmful pollutants [14]. The presence of oxygen in the alcohol results in more oxygen being available during combustion, leading to a reduction in smoke production in the engine [30]. The combustion of alcohols also demonstrates reduced emissions of species such as carbon monoxide and nitrogen oxides, but can demonstrate an increase in aldehyde emissions, which can ultimately lead to photochemical smog formation in the atmosphere [27].

Bioalcohols also demonstrate some disadvantages. For example, the latent heat of vaporisation of alcohols (approximately 700 kJ/kg for butanol at 25 °C) is much higher than that of traditional gasoline (approximately 350 kJ/kg at 25 °C) [31], which results in difficulty when trying to start the engine in cold conditions [1]. Another issue associated with the use of ethanol is that it can be damaging to existing infrastructure for delivering fuel. Ethanol can result in three types of corrosion: wet corrosion, dry corrosion and general corrosion [27]. General corrosion by ethanol is attributed to ionic impurities such as chloride ions. Dry corrosion is thought to be caused by the polarity of the ethanol molecule, and wet corrosion occurs as a result of water absorbed by the ethanol [12]. The extent of corrosion caused by the ethanol is linked to the quality of fuel produced, and how recently the fuel has been produced [27]. If dry ethanol is left in a tank for a prolonged period of time, it is possible that the ethanol can absorb water from the atmosphere, thus making it more corrosive.

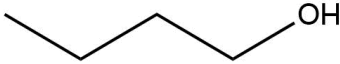
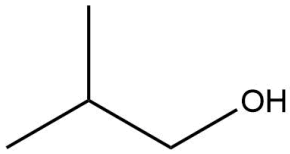
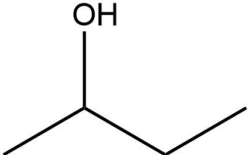
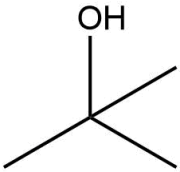
One set back of the shorter alcohol chains (C1 – C3) is that they possess significantly reduced lower heating values (LHV) when compared to gasoline [1]. As a result, one of the main barriers to bio-ethanol's widespread use is that it has a significantly

lower energy density than traditional gasoline [28], and therefore causes a decline in fuel economy. From this, attention has turned to alcohols with longer carbon chains such as butanol to provide an alternative.

1.5 Butanol as a Fuel

Butanol is a saturated four carbon alcohol that can exist as four different isomers (the structures of which can be seen below in Table 1-1): normal-butanol (*n*-butanol), iso-butanol (*i*-butanol), secondary butanol (*s*-butanol), and tertiary butanol (*t*-butanol). As it contains more hydrogen and carbon atoms relative to ethanol, it is easier to blend with other fuels such as gasoline [14]. Butanol can be made from fermentation methods (bio-butanol) and can also be derived from petro-chemical sources (petro-butanol) (see Section 1.5.1) [32]. Bio-butanol contains a higher energy density compared to that of bioethanol and other shorter chain alcohols, and thus has a LHV that is similar to that of traditional gasoline [28], and is considered a potential alternative fuel.

Table 1-1: Skeletal structures of the four isomers of butanol.

Name	Structure
<i>n</i> -butanol	
<i>i</i> -butanol	
<i>s</i> -butanol	
<i>t</i> -butanol	

1.5.1 Production of Butanol

The first noted production of butanol from biomass was in 1861, when Louis Pasteur first observed that *n*-butanol was formed from the fermentation of sugars [1]. This was followed in the early 1900s by the development of the acetone-butanol-ethanol (ABE) fermentation process by Chaim Weizmann, which used the *Clostridium acetobutylicum* strain of bacterium to breakdown sugars into acetone, *n*-butanol and ethanol in the ratio 3:6:1. This popular method of fermentation was used throughout the Second World War [33] to produce the acetone needed for ammunition manufacture [34], and at the time was the second most popular fermentation method after ethanol production from yeast [35]. Synthesis of butanol via the ABE fermentation method declined in popularity during the 1960s, in favour of the more economical petrochemical route, which was further accelerated by the increasing price of the fermentation substrate [35]. Recent interest in the use of bio-butanol as a replacement fuel for gasoline has sparked renewed interest in improving the ABE fermentation and other production methods that do not rely on petro-chemical sources.

Currently, a significant portion of butanol produced is further processed to form chemical derivatives that are used in enamels and surface coatings, and other useful chemicals such as butyl glycol ether [36]. The three most common methods for producing butanol at present are the Oxo synthesis, Reppe synthesis and crotonaldehyde hydrogenation. Both the Oxo and Reppe synthesis methods start from propylene from petrochemical sources, and thus would not be appropriate for the production of bio-butanol from renewable biomass sources.

A review by Nigam and Singh [14] stated that three isomers, *n*-butanol, *i*-butanol and *s*-butanol, can be produced through biological methods, and that the fourth isomer, *t*-butanol, can only be produced by petro-chemical means [1]. The most common fermentation method used for producing butanol is the ABE fermentation process mentioned earlier. This fermentation method can be used on a range of low cost feedstocks such as wheat straw and switchgrass [37]. As butanol can also be produced from the same feedstocks as bioethanol, existing ethanol plants can be cost-effectively retrofitted and converted to produce biobutanol [12]. There are however several challenges associated with this method of production, such as low product yields and potentially high feedstock costs [34]. In terms of reducing this cost, a transition across to cheaper waste feedstocks such as agricultural residues would have a substantial effect.

The use of waste material would also improve the sustainability and reduce the environmental impact of the fuel production.

The use of ABE fermentation for bio-butanol production poses multiple drawbacks that provide economic barriers to its widespread use. One such problem is that the yield from the process is limited by the toxicity of the resulting solvents to the bacteria [12]. As a result, metabolic engineering of the bacteria strain is a key area of research, which is essential for improving the overall yield of the process. Another issue lies with the expensive cost of recovering the butanol from the fermentation liquid. This has been improved through the development of methods such as supercritical extraction and gas stripping [30], which can also be performed during the fermentation process, alleviating some of the issues with toxicity, as the butanol is removed *in situ* [12].

1.5.2 Butanol Properties

A summary table of some of the physical properties of the four isomers of butanol can be seen below in Table 1-2.

Table 1-2: Properties of the different isomers of butanol compared to an average gasoline structure and an alternate alcohol fuel, ethanol. Adapted from [1].

Fuel	Wt %	Lower heating	Boiling Point	ΔH_{vap} (kJ/kg at 25
	O	value (MJ/L)	(°C)	°C)
Ethanol	0.35	21.4	78	919.6
<i>n</i> -butanol	0.22	26.9	118	707.9
<i>s</i> -butanol	0.22	26.7	99	671.1
<i>i</i> -butanol	0.22	26.6	108	686.4
<i>t</i> -butanol	0.22	25.7	83	629.9
Gasoline (Average C ₈ H ₁₅)	0	30 – 33	27 – 225	351

Biobutanol poses several advantages over the other potential bioalcohols. Compared to ethanol, butanol contains twice as many carbon atoms, and as a result contains more energy and has an increased lower heating value [12]. Consequently, butanol demonstrates a higher fuel economy and results in a reduced fuel consumption compared to ethanol. The cetane number of butanol has been reported to be as high as 25, much higher than the other suggested bioalcohols, making it more suitable for auto-ignition in certain engines [30]. The heat of vaporisation of butanol is significantly lower than that of ethanol, and consequently would be easier to start in cold weather conditions [12].

As butanol does not evaporate as easily as gasoline, it releases fewer volatile organic compound emissions, and is safer to use [33]. It also possesses a high flash point, which is another important safety aspect [12]. Butanol is more suitable than ethanol for long term storage, as it has an increased resistance to water contamination. Following from this, if butanol is to be used as a fuel additive, it is less likely to separate from the main component of the blend if contaminated with water.

Butanol is currently considered as a ‘drop-in’ fuel, as it can be added to the current infrastructure and fuel supply [28], such as in storage tanks and fuel stations [14]. As discussed previously, ethanol is highly corrosive to pipework and therefore needs to be transported via other methods such as rail or truck. Butanol is much less corrosive than ethanol, and is therefore easier to transport and is suitable for existing pipework infrastructure [12, 32].

Butanol contains more oxygen than other alternative fuels such as biodiesel, and as a result of this, when used in an engine, it can demonstrate a reduction in the levels of soot produced compared to traditional gasoline combustion [12]. As butanol has a higher heat of evaporation than gasoline, the temperature of the combustion would consequently be lower in the engine, which can also lead to reduced NO_x emissions [12].

1.6 Engine Combustion

Combustion represents a series of central reactions for producing energy in an engine. The oxidation pathway of new potential biofuels in combustion is linked with their widely varying chemical structures, and in order to assess the suitability of a fuel, an extensive understanding of the combustion mechanism is required [38]. The development of this understanding is also crucial for the advancement of cleaner, more efficient internal combustion engines [39].

1.6.1 Engine Types

In a spark ignition (SI) engine, air and fuel are injected into a cylinder, which is compressed and ignited using a spark, resulting in a flame that is propagated evenly through the fuel-air mixture [40]. However, under some conditions, unwanted spontaneous ignition of the fuel ahead of the flame front or in the absence of a spark can occur, in a process known as ‘knocking’ [41]. This can cause audible ringing noises, and can cause serious damage to the engine. The ignition process in a SI engine is different to that of a diesel engine, in which only air is initially contained and compressed in the engine cylinder (compression ignition, CI), and following the injection of the fuel, the droplets disperse in the hot air and spontaneously burn.

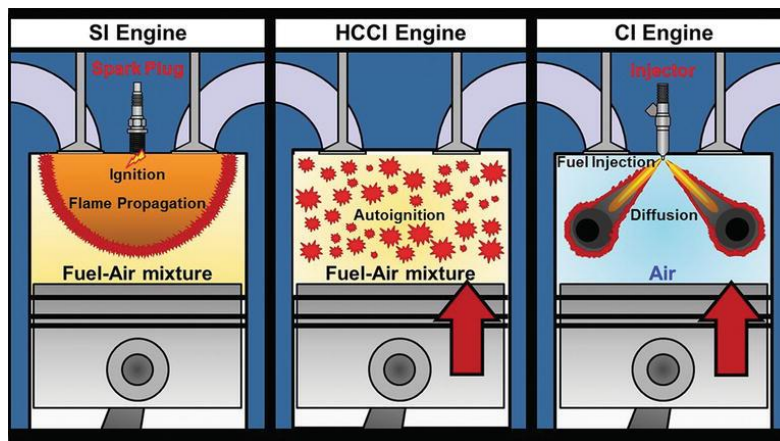


Figure 1-3: Schematic diagram of three different types of engine: Spark ignition (SI), Homogeneous Charge Compression Ignition (HCCI) and Compression Ignition (CI). Replicated from [42].

The development of the Homogeneous Charge Compression Ignition (HCCI) engine, which combines features of spark ignition engines and diesel engines, has proven to be a significant milestone in engine development [43]. A schematic diagram showing the differences between the three different types of engine is shown in Figure 1-3. HCCI uses a fuel-air mixture similar to that of a spark ignition engine with the compression-ignition method used by diesel engines. By doing so, the fuel consumption of an engine can be reduced, improving the fuel economy. As HCCI combustion occurs entirely in the gas phase using premixed fuel and air mixtures, the amount of soot produced by the engine is reduced [44]. The emissions of oxides of nitrogen (NO_x) are also reduced [45], largely resulting from the lower temperature combustion [43]. One downside of HCCI

engines however is that they often result in significant emissions of carbon monoxide (CO) and unburnt hydrocarbons [44]. Ignition within a HCCI engine is largely dependent on the chemical kinetics of the reactive species, and therefore, accurate measurements of these rates must be obtained to ensure the engine is run at optimal conditions [46].

1.6.2 Rapid Compression Machines

To test the suitability of a potential fuel, experimental measurements using equipment such as rapid compression machines (RCM) are carried out. In these, a full engine cycle in an HCCI engine is mimicked in an experimental scenario, in which the fuel-air mix is contained within a vessel, and rapidly compressed, elevating the pressure and thus the temperature. The time between this compression stroke and time for the fuel to auto-ignite is measured, and is known as the ‘ignition delay time’ (IDT). An example pressure trace obtained from the study of Weber and Sung [47] is shown in Figure 1-4, for a rapid compression machine (RCM) study of *s*-butanol.

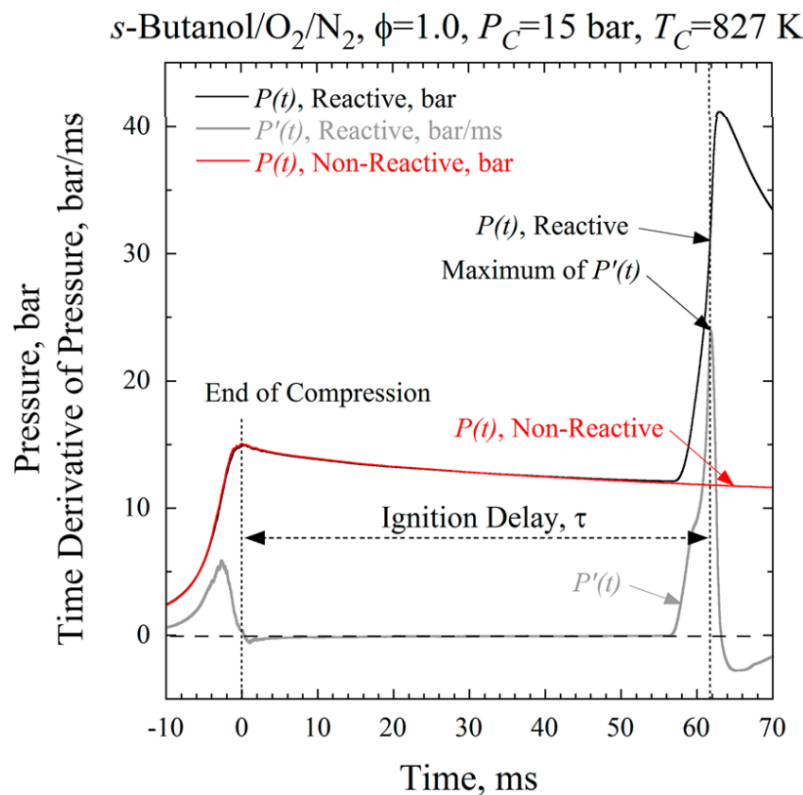


Figure 1-4: An example pressure trace obtained from a rapid compression machine (RCM) study. Pressure trace obtained for *s*-butanol, from the study of Weber and Sung [47], obtained at 15 bar, end compression temperature 827 K, equivalence ratio = 1.

The results from these experimental studies using RCMs are then modelled using combustion modelling (as described in Section 1.8), to test the understanding of the processes driving the autoignition process observed. If good agreement is obtained between the simulations and the experimentally measured parameters, then the rate constants described within the model are assumed to be a reasonably accurate representation of the combustion process occurring. Good agreement is not always obtained however, and this is often a consequence of incorrect rate constants and descriptions being used in the combustion model. Section 1.8 discusses the use of sensitivity analysis to deduce the reactions that control the reactivity of the system, and how to identify where model improvements must be made.

Rapid compression machines can be operated across a range of high temperatures and pressures, from 600 – 1200 K and 5 – 80 bar [48]. Another experimental parameter that can be varied in these tests is the fuel-air equivalence ratio, ϕ . This allows the ignition delay time to be measured under conditions ranging from fuel rich (equivalence ratio > 1) to fuel lean (equivalence ratio < 1), to investigate the effects of these different conditions on the reactivity of the fuel. Further discussions of the reactions involved in these modelling simulations are described in the next section, Section 1.6.3, and applied specifically to the isomers of butanol in Section 1.7.

1.6.3 Combustion Reactions

The combustion of a fuel is a complicated process with many reaction steps, with the importance and the rate of each reaction depending on the temperature in the engine [49]. Combustion processes can be split between low temperature combustion (that which occurs at less than 1000 K) and high temperature combustion (combustion above 1000 K) [41].

There are several types of chain reaction which are crucial to combustion: initiation, chain propagation, chain branching and chain termination [40]. Highly complicated reaction schemes for different hydrocarbons and fuel species can be built up from subsets of mechanisms of smaller molecules, that are comprised of each of these types of chain reaction [50].

1.6.3.1 Low Temperature Hydrocarbon Oxidation

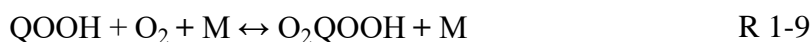
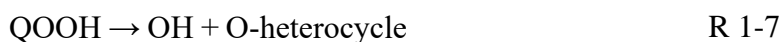
The first step in hydrocarbon fuel oxidation is the formation of a radical from the initial reactive fuel species, which can be formed by reaction with a radical species (X), as outlined below in reaction R 1-1. Reaction R 1-2 highlights the fastest possible reaction for the initial fuel species, in which an OH radical abstracts a hydrogen to form a water and leaves the alkyl radical R [51].

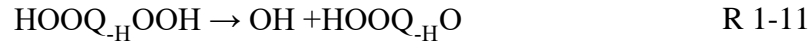


Following this, the alkyl radical R formed then goes on to react with molecular oxygen (as seen in reactions R 1-3 and R 1-4), to form an alkene and HO₂ radical species, or the alkyl peroxy radical, RO₂.



The RO₂ radical species then goes on to form an alkene and HO₂ species (R 1-5), or undergoes an internal rearrangement to form the QOOH hydroperoxyalkyl radical (R 1-6) [52]. The QOOH species can then fall apart to form a highly reactive OH radical and an O-heterocycle (R 1-7), resulting in chain propagation, or again fall apart in the same manner as the RO₂ species to form HO₂ and an alkene (R 1-8). QOOH can also undergo addition of a second O₂ to form O₂QOOH (R 1-9), which in turn undergoes an internal abstraction of an H atom (R 1-10), and could ultimately lead to the formation of two OH reactive radicals, resulting in a chain branching reaction (R 1-11 and R 1-12).





1.6.3.2 High Temperature Hydrocarbon Oxidation

At high temperatures (> 1000 K), the thermal decomposition of the fuel species to produce the reactive radical R becomes an important chain initiation step (R 1-13) [51]. This initiation leads to formation of reactive radicals, such as the CH_3 radical, which in turn leads to a series of reactions allowing a source of OH, O and H radicals to be built up. Following this build up, reaction R 1-14 occurs, where X represents any of a number of radical species, in which hydrogen is abstracted from the starting fuel.



Depending on the conditions within the engine, the resulting fuel radical species can potentially recombine to form longer hydrocarbon species, which acts in competition with other degradation reactions [41]. At these high temperatures, the rate of reaction is controlled by several reactions, which govern the total radical concentration. These chain branching reactions involved are not fuel specific, as they involve simple, small radical species that are generated from all hydrocarbon oxidation mechanisms [41].



Reaction R 1-15 is of significance as it produces the H radicals, which ultimately lead to the chain branching seen in reaction R 1-16. Reaction R 1-16 represents the major chain branching step seen in high temperature oxidation, resulting in the production of both O and OH radicals.

1.7 Butanol Combustion

A general simplified reaction scheme for the oxidation of alcohol fuels is shown below in Figure 1-5, replicated from [1]. From this diagram, it can be seen that an initial reaction between the fuel RH and a radical removes an H atom from the fuel, to form the fuel radical species R. This radical species then undergoes a rapid addition with oxygen to form the RO₂ radical, which undergoes an internal rearrangement to form the species QOOH in a similar manner to that seen in Section 1.6.2 for hydrocarbon oxidation.

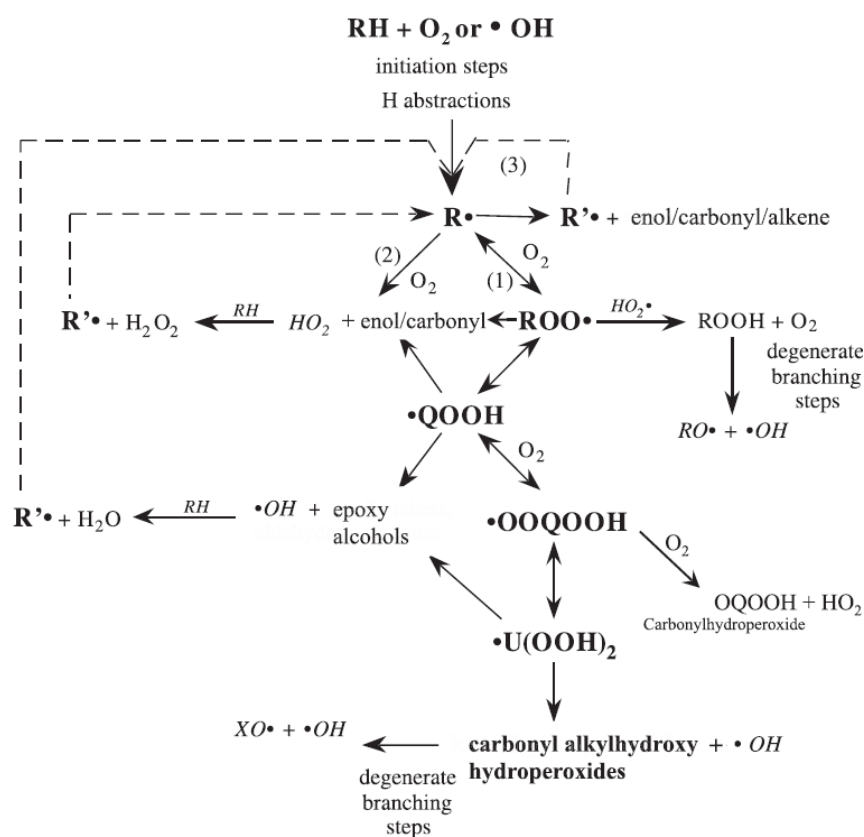


Figure 1-5: Simplified sample reaction scheme for low temperature alcohol combustion, replicated from Sarathy *et al.* [1].

At low and intermediate temperatures, the most important radical for hydrogen abstraction from alcohols is OH. The hydrogen found in the hydroxyl group of the butanol isomers is the hardest to abstract, and tertiary bonded H atoms are the easiest [1]. From Figure 1-5, it can be seen that carbonyls and enols are formed through multiple possible channels in the oxidation of alcohols. At low temperatures, the addition of molecular oxygen to hydroxyalkyl radicals can lead to the formation of stabilised peroxy radicals

(RO₂), the first stage in the chain branching process [1]. Following the addition of oxygen, an internal hydrogen abstraction to form the QOOH hydroxyalkyl hydroperoxy radical occurs, usually via 5-membered, 6-membered or 7-membered transition state rings (R 1-17). This isomerisation is in competition with the elimination reaction to produce an enol and HO₂ from the RO₂ species (R 1-18).

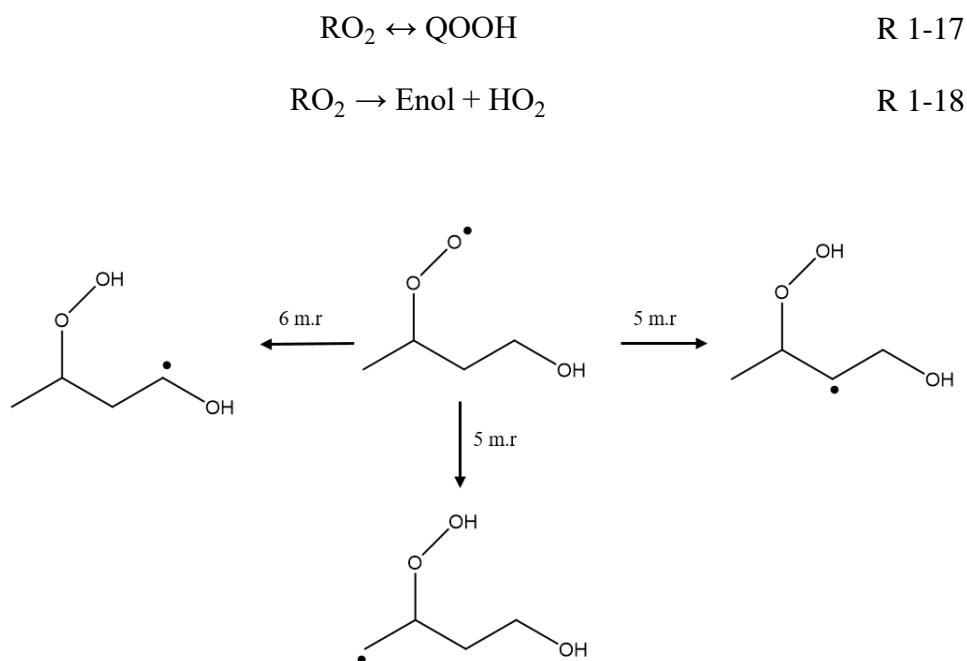
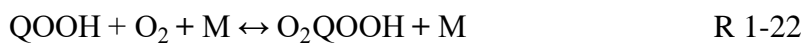
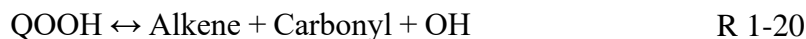
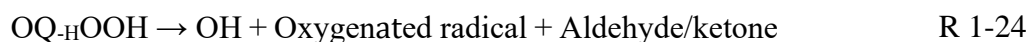
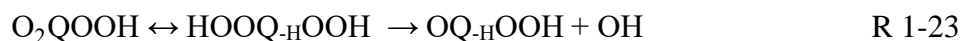


Figure 1-6: Possible structures formed during the internal isomerisation of *n*-butanol, following hydrogen abstraction at the gamma site and subsequent addition of oxygen. “6 m.r.” represents isomerisation via a six-membered ring and “5 m.r.” represents isomerisations via a five-membered ring.

An example of potential QOOH structures formed from the isomerisation of the *n*-butanol radical is shown in Figure 1-6. This QOOH species can then react in one of several ways, depending on the position of the radical site. It can decompose to give an enol and HO₂ species (R 1-19) if the radical is in the beta position to the OOH group, or an alkene, carbonyl and OH radical (R 1-20) if the radical is in the gamma position. The QOOH can also cyclise and form an epoxy alcohol plus an OH radical (R 1-21), but this is thought to be a minor channel [1]. Each of these decompositions are in competition with low temperature chain branching channel of (R 1-22), in which another molecular oxygen is added to the QOOH species.



The addition of O_2 to the QOOH species is thought to be one of the most important steps in the low temperature chain branching mechanism [46]. Following this addition, subsequent isomerisation of the O_2QOOH species formed in reaction R 1-22 leads to the formation of HOOQ-HOOH ($\text{U}(\text{OOH})_2$ in Figure 1-5) in a reversible process. The HOOQ-HOOH species then decomposes into a carbonyl hydroxyalkyl hydroperoxide species (OQ-HOOH) and an OH radical. This is followed by the decomposition of the carbonyl hydroxyalkyl hydroperoxide to form an OH radical, another oxygenated radical and a stable species such as an aldehyde or ketone.



This general alcohol low temperature combustion mechanism can be applied to the four different isomers of butanol, as shown below in Figure 1-7. This shows the different reaction pathways depending on the site of the H abstraction, and demonstrates the pathways that ultimately lead to chain branching at low temperatures.

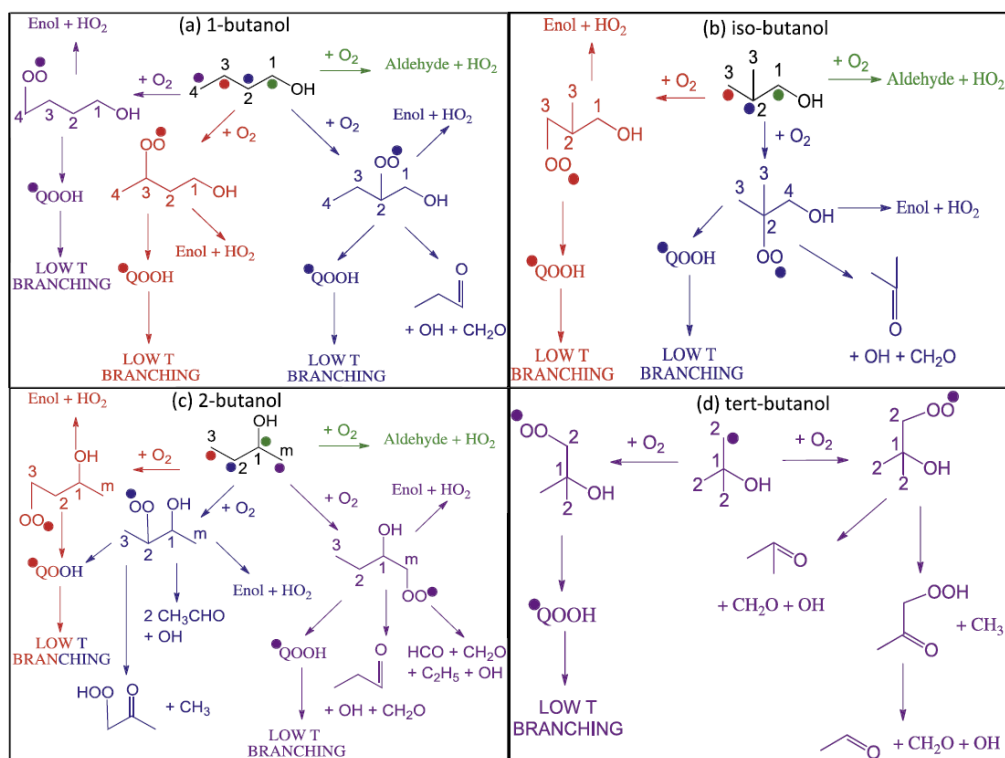


Figure 1-7: Important reactions for low-temperature oxidation pathways for each isomer of butanol, replicated from Sarathy *et al.* [1].

From the reactions described in this section and Figure 1-7, substantial combustion models can be built to describe the low temperature oxidation of fuels. These models are vital for improving our understanding of the combustion process, and for the development of technology that best utilises novel fuels. The next section will explain these combustion models in further detail, and explain some of the limitations encountered when using them to model experimental parameters.

1.8 Combustion Modelling

As mentioned in Section 1.6, for widespread use of alternative fuels such as the bio-butanol to be adopted, a thorough understanding of the kinetics and reactions which occur during the combustion process is required. This comprises an understanding of phenomena such as autoignition behaviour across different engine conditions, including when blended with gasoline [53]. One way to test this understanding is through combustion modelling of experimental parameters, for example ignition delay times (described in Section 1.6.2), flame speed measurements and key species concentrations

[54]. Consequently, significant research and development of chemical kinetic models has been conducted for the butanol isomers and other potential fuels.

From the example reaction pathways described in Section 1.7 and Figure 1-7, substantial combustion models can be constructed, containing large amounts of species and reactions. For example, in the combustion model for the four butanol isomers constructed by Sarathy *et al.* [55], there are 426 species and 2335 reactions. Combustion models are usually developed in conjunction with some validation against experimental measurements [56], and are built upon previous submechanisms for smaller species, such as the H₂/CO/O₂ submechanism of Ó Conaire *et al.* [57].

Combustion models are often built comprising of multiple reaction classes that can be divided into those relevant to high temperature combustion and low temperature combustion. Those at high temperature are usually related to unimolecular fuel decomposition, H-atom abstraction and fuel radical isomerisation and decomposition. The reaction classes involved in low temperature combustion are those typically described by the pathways shown in Figure 1-7, such as the addition of O₂ to fuel radicals and isomerisation of the subsequent RO₂ species. The rates of these reactions found in the combustion models are often based on experimental measurement, theoretical calculation or estimation based on analogous species [54].

When validating combustion models and comparing with experimental measurement, good agreement is not always obtained. This is due to some reaction classes and reaction rates in the input model possessing significant associated uncertainties, owing to being estimates based on similar structures. One method of classifying which aspects of the combustion models have the most significant effect on the output parameter is to conduct a sensitivity analysis. In this method, the relationship between an input value in a model and its effect on the predicted output is examined, to determine which inputs have the largest influence on the output parameter. This allows a prioritisation of which reactions rates in the model require further investigation for improvement. An example sensitivity analysis conducted by Zhou *et al.* [58] for iso-butene is shown in Figure 1-8, where a negative sensitivity index means an increase in the simulated ignition delay time, and a positive sensitivity index means a decrease in the simulated ignition delay time.

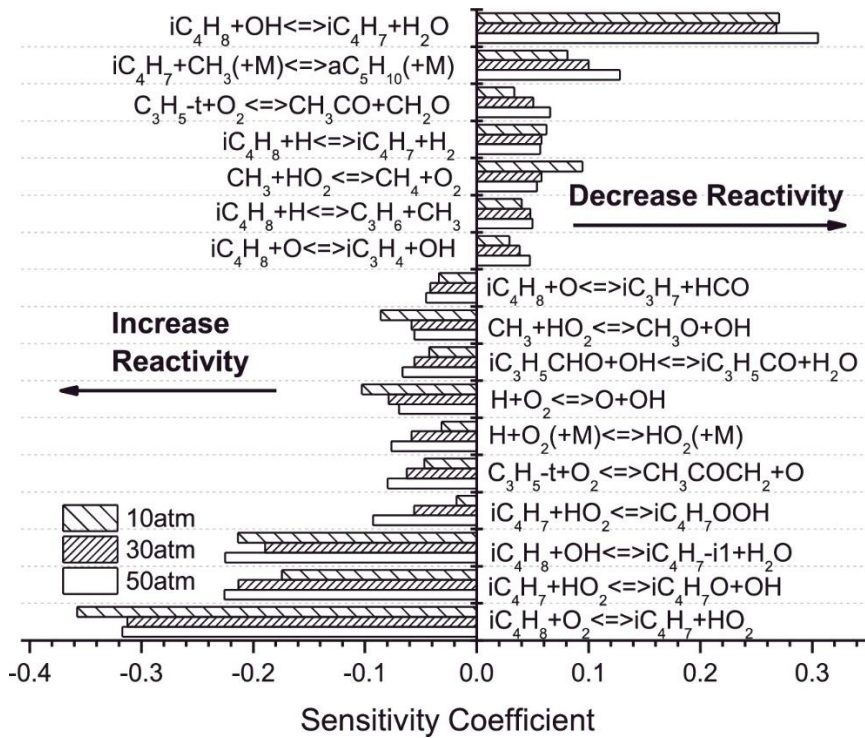


Figure 1-8: A sensitivity analysis conducted by Zhou *et al.* [58], for the ignition delay times predicted for iso-butene, at 1250 K and pressures between 10 – 50 atm.

A sensitivity analysis is usually conducted within the uncertainty bounds provided by those that conducted the initial study into the parameter being tested (i.e., the uncertainty bounds provided from the experimental kinetic measurement of the rate constant). This therefore assumes that the rate constant and uncertainty provided are an accurate measurement or estimate. If the starting value for a particular rate is inaccurate, it may result in a lack of sensitivity shown during a local sensitivity analysis to a reaction that may in fact influence the reactivity. It is therefore important to conduct global sensitivity analysis on the rate constants found within combustion models, as this accounts for interactions between the rate constants, and gives a better overall understanding of the contributions of each rate to the output parameter to be modelled [59].

Agbro *et al.* [60] recently conducted a global sensitivity analysis into the reactions governing the ignition delay times of the butanol isomer *n*-butanol under conditions relevant to low temperature combustion. In their work, it was highlighted that the H atom abstraction reactions by OH are important for accurate predictions in the context of ignition delay times, and that under fuel rich conditions, the reactions of the R radical with O₂ were of equal importance. Sarathy *et al.* [1] also recently conducted a review of

alcohol combustion chemistry, highlighting the need for chemical kinetic model development for reducing uncertainties, and measurements of reaction kinetics at temperatures relevant to low temperature conditions. This thesis will therefore present the investigation of several reactions of the four butanol isomers relevant to low temperature combustion conditions, to assist in the reduction of these uncertainties in future when developing models for simulations under these conditions.

1.9 Theories of Chemical Reactions

The study of chemical kinetics is of fundamental importance for understanding the reactions which drive reactivity in complex systems, such as those occurring in combustion. This section describes in brief some of the theory used for the reaction kinetics studied in this thesis.

1.9.1 Transition state theory

Transition state theory (TST) can be primarily used to understand how reactions take place, by taking account of an activated complex species between the reactants and the products, known as a transition state (ABC^\ddagger in Figure 1-9).

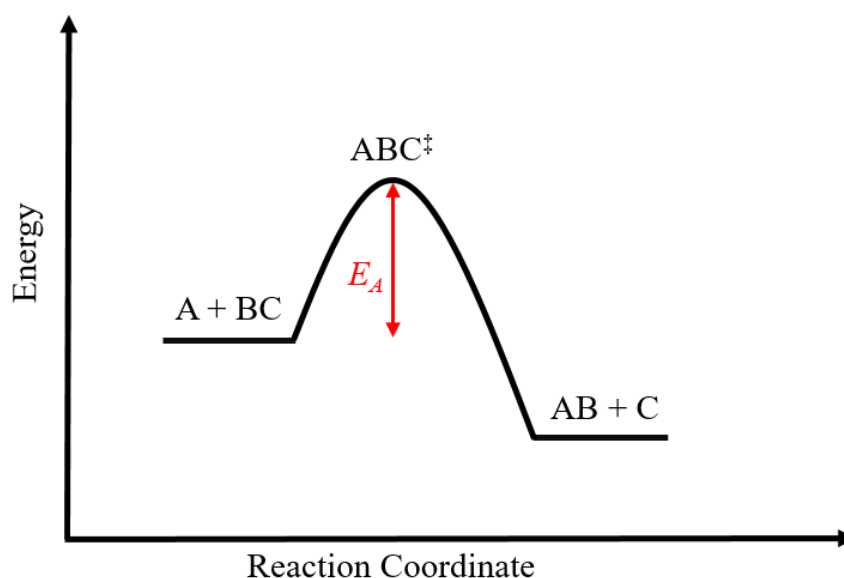


Figure 1-9: A schematic diagram of a typical reaction energy profile, where ABC^\ddagger is the transition state species, and E_A is the energy required to overcome the energy barrier.

The transition state is located at the highest energy point along the reaction coordinate, prior to decomposition to the reaction products. The following elementary

reactions R 1-25 and R 1-26 can be used to describe the system shown in Figure 1-9, with E 1-1 describing the experimentally observed rate of formation of the products AB.



$$\frac{d[AB]}{dt} = k_r [A][BC] \quad \text{E 1-1}$$

where k_r is the reaction rate coefficient. Transition state theory assumes that the transition state ABC^\ddagger is in equilibrium with the reactants A and BC, and thus the concentration $[ABC^\ddagger]$ can be described by equation E 1-2:

$$[ABC^\ddagger] = K^\ddagger [A][BC] \quad \text{E 1-2}$$

where K^\ddagger is the equilibrium constant for the formation of ABC^\ddagger from A and BC:

$$K^\ddagger = \frac{[ABC^\ddagger]}{[A][BC]} \quad \text{E 1-3}$$

The overall rate of forming products is described by:

$$\frac{d[AB]}{dt} = k^\ddagger [ABC^\ddagger] \quad \text{E 1-4}$$

where k^\ddagger is the first order rate coefficient for decomposition of ABC^\ddagger to products. Combining equations E 1-1, E 1-2 and E 1-4, the following equation can be derived:

$$k_r = k^\ddagger K^\ddagger \quad \text{E 1-5}$$

The equilibrium constant K^\ddagger can be defined by the expression shown in equation E 1-6:

$$K^\ddagger = \frac{Q_{ABC}}{Q_A Q_{BC}} \exp^{-\Delta\varepsilon_0/RT} \quad \text{E 1-6}$$

where Q_i is the partition function for species i per unit volume, and $\Delta\varepsilon_0$ is the energy difference between the reactants and the transition state. The partition function for the activated complex Q_{ABC} can then be separated into two components – the component q_{ABC} for the contribution from the stretching mode that leads to dissociation, and the remaining partition function Q_{ABC}^\ddagger . The partition function q_{ABC} can be approximated by:

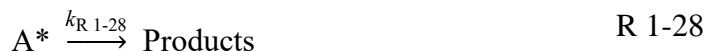
$$q_{ABC} \approx \frac{k_B T}{h\nu} \quad \text{E 1-7}$$

where ν is the vibrational frequency of the reactive vibration. At this point, a transmission coefficient, κ , is also introduced, to account for the fraction of reactant vibrations that lead to the formation of products. Factoring in equations E 1-5 – E 1-7 as described above, the overall rate coefficient k_r can be described by equation E 1-8:

$$k_r = \frac{\kappa k_B T}{h} \frac{Q_{ABC}^\ddagger}{Q_A Q_{BC}} \exp^{-\Delta\varepsilon_0/RT} \quad \text{E 1-8}$$

1.9.2 Unimolecular decompositions

The development of the Lindemann mechanism provided a mechanism for the unimolecular decomposition of a species A, described by reactions R 1-27 and R 1-28 below. A species A can be excited following collision with a third body M, which can be another A molecule or a bath gas molecule. Following this excitation, the excited species A* can be collisionally deactivated again (reaction R 1-27), or can go on to form products.



Reaction R 1-28 shows that the formation of products is equal to $k_{1-28} [A^*]$, and therefore an equation describing $[A^*]$ must be formulated. The rates for formation and removal of A* are described in equation E 1-9.

$$\frac{d[A^*]}{dt} = k_{1-27}[A][M] - k_{-1-27}[A^*][M] - k_{1-28}[A^*] \quad \text{E 1-9}$$

As A^* has a short lifetime, after a short period of accumulation, the concentration of A^* remains at a steady concentration. Using E 1-9, the steady-state approximation can be applied to $[A^*]$, and it can be assumed that $d[A^*]/dt \approx 0$, therefore:

$$k_{1-27}[A][M] = k_{-1-27}[A^*][M] + k_{1-28}[A^*] \quad \text{E 1-10}$$

Rearrangement of equation E 1-10 for $[A^*]$ gives equation E 1-11:

$$[A^*] = \frac{k_{1-27}[A][M]}{k_{-1-27}[M] + k_{1-28}} \quad \text{E 1-11}$$

Substituting equation E 1-11 into the equation for the formation of products $d[P]/dt$ obtains equation E 1-12:

$$\frac{d[P]}{dt} = k_{1-28}[A^*] = \frac{k_{1-27}k_{1-28}[A][M]}{k_{-1-27}[M] + k_{1-28}} \quad \text{E 1-12}$$

If equation E 1-12 is rewritten as $d[P]/dt = k_{\text{uni}}[A]$, where k_{uni} represents the formal unimolecular rate constant:

$$k_{\text{uni}} = \frac{k_{1-27}k_{1-28}[M]}{k_{-1-27}[M] + k_{1-28}} \quad \text{E 1-13}$$

it becomes clear that k_{uni} is a pressure dependent function. This results in two distinct pressure dependent regions of the unimolecular rate constant k_{uni} , as described in Figure 1-10. At low pressures, the rate determining step is the bimolecular excitation reaction described by the forward reaction of R 1-27. Following excitation, formation of products is more likely than deactivation at low pressures, therefore $k_{1-28} \gg k_{-1-27}[M]$, and k_{uni} reduces to $k_{\text{uni}} = k_{1-27}[M]$, resulting in a pressure dependence at low pressures.

At high pressures, the rate of collisional deactivation is much faster than that of the unimolecular reaction of A^* forming products, $k_{-1-27}[M] \gg k_{1-28}$. This reduces the unimolecular rate constant k_{uni} to $k_{uni} = k_{1-28} k_{1-27} / k_{-1-27}$, i.e. it is independent of pressure.

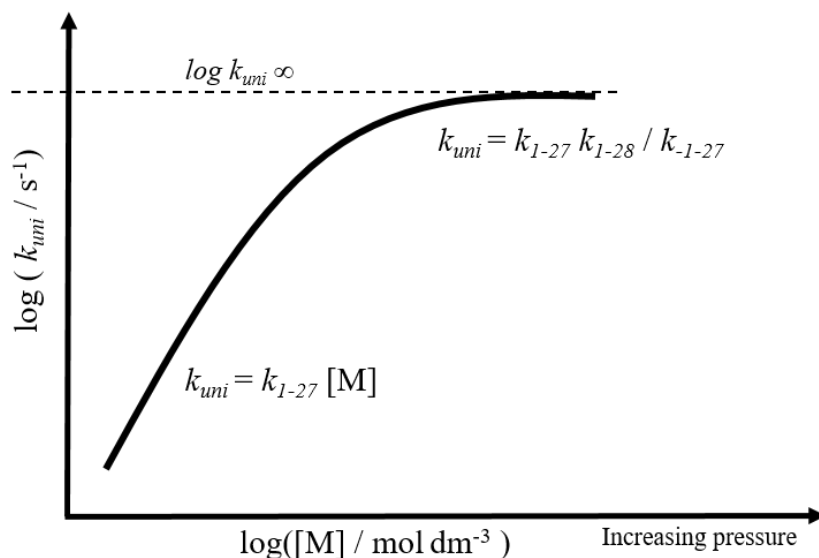


Figure 1-10: Example showing the falloff in the unimolecular rate coefficient, k_{uni} , at lower pressures.

The Lindemann mechanism does however have some failures, and cannot always accurately describe experimentally measured reaction kinetics. Primarily, Lindemann theory breaks down as it does not consider the energy dependence of the activation reaction, and ignores the internal degrees of freedom of the molecule.

For a unimolecular decomposition to occur, the energy for the reaction must be localised within the relevant form of motion. Previously, only the general method of excitation of the molecule has been considered. In order to describe this conversion of the generally excited molecule A^* to the specifically excited molecule A^\ddagger (the activated complex), the introduction of a further reaction step is required, as described by reaction R 1-29 and equation E 1-14.



$$k^* = \frac{k^\ddagger [A^\ddagger]}{[A^*]} \quad \text{E 1-14}$$

k^\ddagger is typically much larger than that of k^* , and therefore the conversion of A^* into the activated complex is typically the rate determining step. As the concentration of A^\ddagger is small (due to $k^* \ll k^\ddagger$), application of the steady state approximation, $d[A^\ddagger]/dt = 0$ obtains equation E 1-14. The first improvement to Lindemann theory centred on this aspect was conducted by Rice and Ramsperger, and later developed by Kassel (RRK Theory), based on the assumption that energy can flow freely from one vibrational mode to another.

Further developments by Marcus, resulting in the development of Rice-Ramsperger-Kassel-Marcus (RRKM) theory, has resulted in better overall agreement between experimental observations and calculated rates, through the inclusion of transition state theory (TST). RRKM is a microcanonical transition state theory, which forms the basis of the master equation calculations conducted in Chapter 4, and is described in more detail in Section 4.3.2 .

The Lindemann mechanism and the further developments that followed are crucial for explaining the kinetics involved in unimolecular decomposition reactions, such as the unimolecular decomposition of the β -hydroxybutyl radicals described in Chapter 4. A schematic potential energy surface of this decomposition is shown in Figure 1-11, showing the potential reactions occurring following formation of the β -hydroxybutyl radical. The need for collisions to form the excited species is shown, highlighting the pressure dependent aspect of the mechanism as described previously, and emphasising why the unimolecular decomposition of this species is dependent on the concentration of bath gas molecules M .

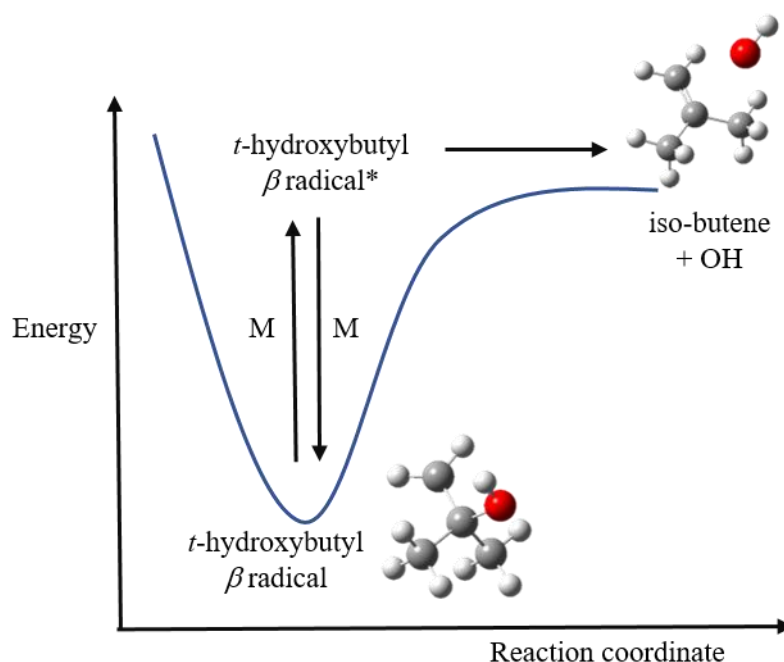


Figure 1-11: A schematic potential energy surface for the decomposition of the β -hydroxybutyl radicals formed following abstraction at the beta site of each of the butanol isomers, as described in Chapter 4.

1.10 Thesis overview

Chapter 2 provides an overview of the experimental methods used to study gas phase kinetic reactions, and gives a detailed account of the laser flash photolysis – laser-induced fluorescence method and apparatus used in this thesis.

Chapter 3 presents a detailed experimental investigation of the reaction of the four isomers of butanol with the hydroxyl radical, an important initiation reaction for the low temperature oxidation of these potential biofuels in an engine. Experimental data is presented from room temperature to approximately 700 K, significantly reducing the gap in the literature for these reactions.

Chapter 4 investigates the unimolecular decomposition of β -hydroxybutyl radicals formed following hydrogen abstraction at the beta site, to form a butene molecule and an OH radical. Experimental observations of the unimolecular decomposition rate constants have been made as a function of temperature and pressure, and used in conjunction with *ab initio* calculated barriers and master equation solving to obtain optimised energetic barriers to this decomposition.

Chapter 5 highlights some unusual OH regeneration observed in this work at high temperatures (> 600 K) and in the presence of oxygen. Experimental tests were conducted to deduce the source of this unusual behaviour, with one hypothesis suggesting the reaction of O (3P) atoms with alcohol reagent to form OH radicals. A temperature dependent study of *n*-butanol with O (3P) atoms has been conducted between 490 – 732 K, at pressures of 40 – 50 Torr nitrogen.

Chapter 6 presents a summary of the findings in this work, and highlights areas of potential future work.

Chapter 2 Experimental Techniques

2.1 Introduction

To measure the kinetics of gas phase radical reactions, a range of experimental techniques can be used. The development of new experimental techniques has been vital for measurement of reactions key to the combustion process, and to building combustion models for verifying understanding.

This chapter covers the details of the main experimental technique used in this work: the Laser Flash Photolysis – Laser Induced Fluorescence (LFP-LIF) method. The basic principles of laser action are also covered, alongside the fundamentals of other methods used for initiating and studying gas-phase reaction kinetics, such as discharge flow, the relative rate method, pulse radiolysis and resonance fluorescence. The final section of this chapter will cover the finer details of the experimental setup used in this work.

2.2 Laser Flash Photolysis – Laser Induced Fluorescence

The coupling of laser flash photolysis to laser induced fluorescence results in a widely adopted method for monitoring the kinetics of reactions in the gas phase (LFP-LIF). For LFP-LIF, a ‘pump-probe’ system is used, which uses two pulses of light: one to generate the reactive species of interest for monitoring, and another to ‘probe’ the system at a series of different time delays after the initial ‘pump’ light flash. The time at which the photolysis ‘pump’ laser flashes to initiate the reaction is defined as $t = 0$, and the second probe laser is fired at a set time after this, to excite the radical species formed and the subsequent fluorescence is then monitored [41]. By altering the time between the photolysis laser flash and the probe laser flash, a decay signal of the fluorescence over time can be obtained. Analysis of this decay trace can then provide kinetic data regarding the reaction of the reagent of interest with the radical species generated by the photolysis laser.

A schematic diagram of the orientation of the experimental set up used in this work is shown in Figure 2-1. It shows the intersection of the two lasers perpendicular to each other, with the fluorescence collected by the photomultiplier tube (PMT) above this intersection. By collecting the fluorescence from the species of interest perpendicular to the intersection of the photolysis and probe laser beams, the amount of unwanted scattered

light measured is minimised. Alongside this arrangement, a filter at a suitable wavelength for the fluorescence being measured is used, also assisting in reducing the amount of scattered light collected by the PMT.

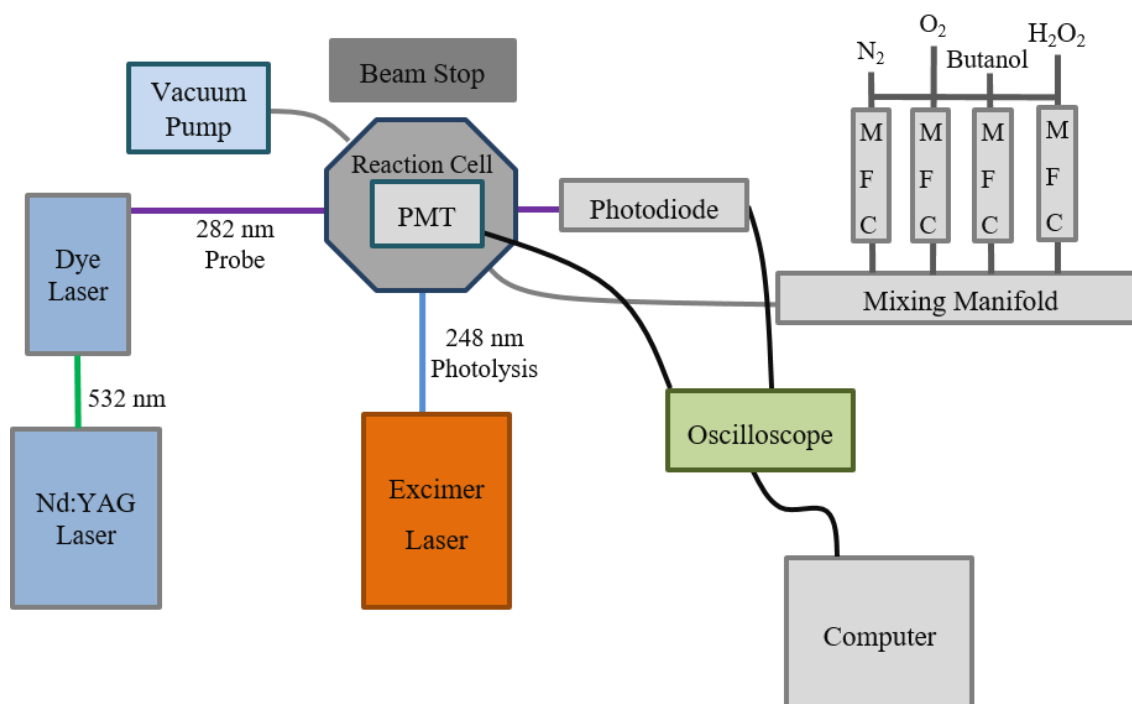


Figure 2-1: A simplified schematic diagram of the off-resonant fluorescence set up used in this work, demonstrating the orientation and wavelengths of the lasers involved and other essential equipment.

The basic principles explaining the functioning of lasers and their use in this work are explained in Section 2.3, and a further description of the experimental set up used in this thesis can be found in Section 2.7.

2.3 Lasers

A range of experimental and analytical techniques have been significantly advanced by the development of lasers (Light Amplification by Stimulated Emission of Radiation), by assisting the monitoring of rapid reactions that may not have been previously possible [61]. Pulsed lasers can produce extremely short bursts of light to initiate reactions, which can then be monitored by a number of different methods such as laser induced fluorescence (see Section 2.3.7).

2.3.1 Absorption and Emission

In accordance with quantum theory, atoms and molecules possess discrete energy levels, over which the energy of the system is distributed. The relative populations of these states at equilibrium at a given temperature, T , can be described using the Boltzmann distribution:

$$N_n/N_m = \exp^{-\Delta E/k_B T} \quad \text{E 2-1}$$

where N_n and N_m are the populations of the higher and lower energy levels respectively, separated by an energy gap ΔE , and k_B is the Boltzmann constant ($k_B = 1.381 \times 10^{-23} \text{ J K}^{-1}$). In order to promote a molecule from its ground state to an excited state, absorption of a photon of energy that exactly matches the energy gap between the two levels must occur. The absorbed photon energy, E , is related to its frequency, ν , by the equation $E = h\nu$, where h is Planck's constant ($6.63 \times 10^{-34} \text{ J s}$). As only discrete energy levels exist in molecules, this results in selectivity in the frequency of light that can be involved in this absorption process.

A species in an excited state can then undergo spontaneous emission, relaxing back to the ground state, and releasing a photon of energy corresponding to the energy gap between the two levels. This spontaneous emission can occur in any direction. A species in the excited state can also relax back to the ground state in a stimulated emission process, in which an incident photon of a given frequency stimulates the emission of a photon of the same frequency from the excited species. This stimulated emission occurs preferentially in the direction of the applied light beam, resulting in an amplification in intensity. The radiative processes described here are illustrated in Figure 2-2, between lower (E_1) and higher (E_2) energetic states.

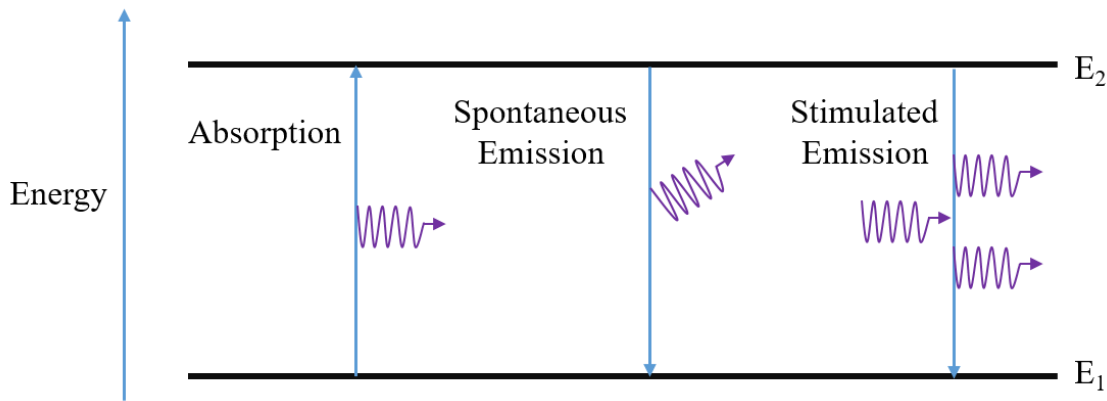


Figure 2-2: Schematic diagram of radiative processes: a) Stimulated absorption, b) Spontaneous emission and c) Stimulated emission.

In order to achieve laser action, a deviation from thermal equilibrium is required, such that the population of the higher energy level E_2 is greater than that of the lower energy state E_1 . This non-equilibrium behavior is known as a population inversion, described in more detail below.

2.3.2 Population Inversion

A population inversion is not usually possible with the simple two-level model described previously. Optical pumping of the lower state, N_m , increases the population of the excited state, N_n , but eventually an equilibrium between the two states will be established where $N_m = N_n$ as a result of the increase in stimulated emission.

For a population inversion to be established, a three- or four-level laser system is often used, as outlined in Figure 2-3. For a three-level laser, a suitable pumping method is required to excite from the ground state E_1 to the second excited state E_3 . Following this, a fast transition from E_3 to the first excited state E_2 occurs, populating this energy level. The transition from level E_3 to E_2 must be faster than that of the transition from level E_2 to E_1 , as this allows the population of level E_2 to build up whilst the population of E_1 decreases during subsequent pumping, thus creating the population inversion required [62]. However, the lasing transition populates the ground state energy level, and in doing so, disrupts the population inversion. This issue can be avoided through the introduction of a fourth level to the system.

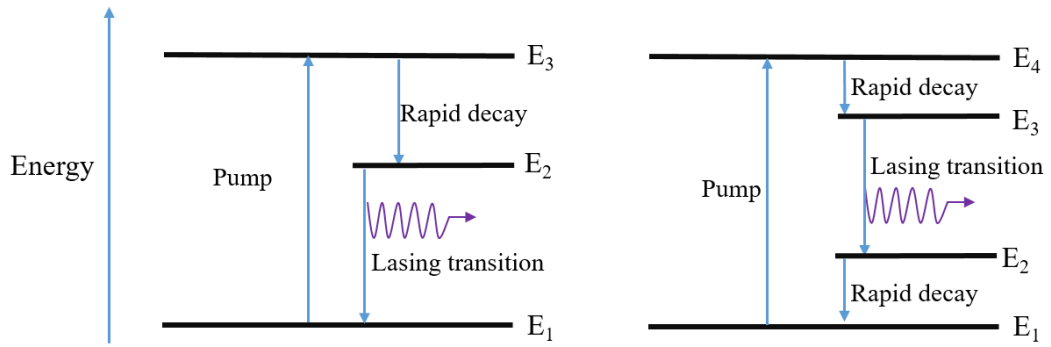


Figure 2-3: Energy levels involved in three- and four-level lasing systems.

In a four-level laser, the transition in which lasing occurs is between excited levels E_3 and E_2 , and not to ground state E_1 , and thus the population inversion is required between the E_3 and E_2 energy levels. The pumping process occurs from the ground state level E_1 to the third excited state E_4 , which then leads to rapid transitions from E_4 to E_3 . The rate at which this transfer occurs must be faster than that of the lasing transition, similar to that of the three level laser. As the lasing emission is not to the ground state E_1 , a further rapid transition from E_2 to E_1 occurs, which depletes the population of level E_2 and helps to maintain the population inversion between levels E_3 and E_2 . There are other ways of generating a population inversion than electromagnetic radiation absorption, such as electric discharge and chemical excitation [63], the mechanism for which can contain many energy levels and can rapidly become very complicated. In this work, two four-level laser systems will be used: a Nd:YAG laser and a dye laser. Both are described in more detail in Sections 2.3.4 and 2.3.5 respectively.

The system in which the population inversion is created is the active medium, and comes in gas, liquid or solid form. The type of active medium used in the laser depends on what frequency of light is required, as each substance has its own set of energy levels. To amplify the intensity of the laser light, the active medium is placed in an optical cavity, consisting of two mirrors positioned parallel to each other at either end of the active medium. By trapping the light between the two mirrors, the light then reflects back and forth, growing in intensity. Only photons that are emitted perpendicular to the two mirrors are reflected, with those emitted in random directions passing out of the active medium, resulting in highly directional amplified light. As demonstrated in Figure 2-4, one of the mirrors is fully reflective, whilst the other is partially transmissive to allow the laser beam to exit the cavity.

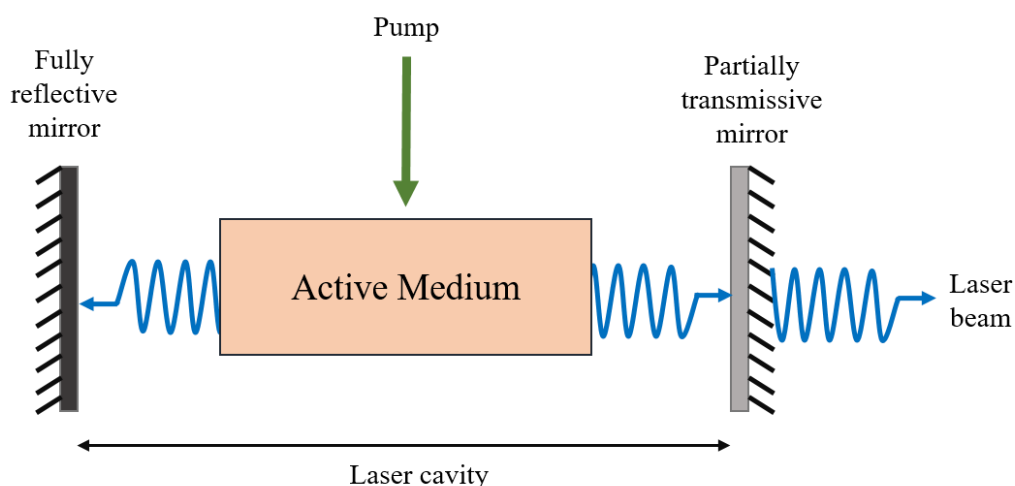


Figure 2-4: A schematic diagram of a simple laser cavity.

2.3.3 Excimer Laser

Excimer (also known as exciplex) lasers rely on the generation of an electronically excited diatomic complex, formed from passing a high voltage electrical discharge through a high-pressure gas mixture containing three components: a noble gas, a halogen and a buffer gas. Different wavelengths and energies are achieved by combining different noble and halogen gases, as outlined in Table 2-1.

Table 2-1: Potential excimer complexes and their corresponding wavelengths and energies.

Exciplex	Wavelength / nm	Photon Energy / kJ mol ⁻¹
ArF	193	621
KrCl	222	540
KrF	248	483
XeCl	308	389
XeF	351	342

In this work, a KrF excimer system was employed, using a gas mixture of krypton, fluorine and neon, to generate a laser wavelength of 248 nm. An electrical discharge is passed through the gas mixture, and results in the formation of Kr⁺ and F⁻ ions, forming the complex according to the following reactions:



The excited complex KrF^* has a short lifetime (2.5 ns), and decays by photon emission to the ground state, where the complex rapidly dissociates to its constituent atoms due to the repulsive forces between the ground state atoms. As a result of this rapid dissociation, the ground state does not obtain a significant population, and thus a population inversion is maintained between the excited exciplex and the ground state, despite being a two level system. The energy levels involved in this lasing transition are highlighted in Figure 2-5.

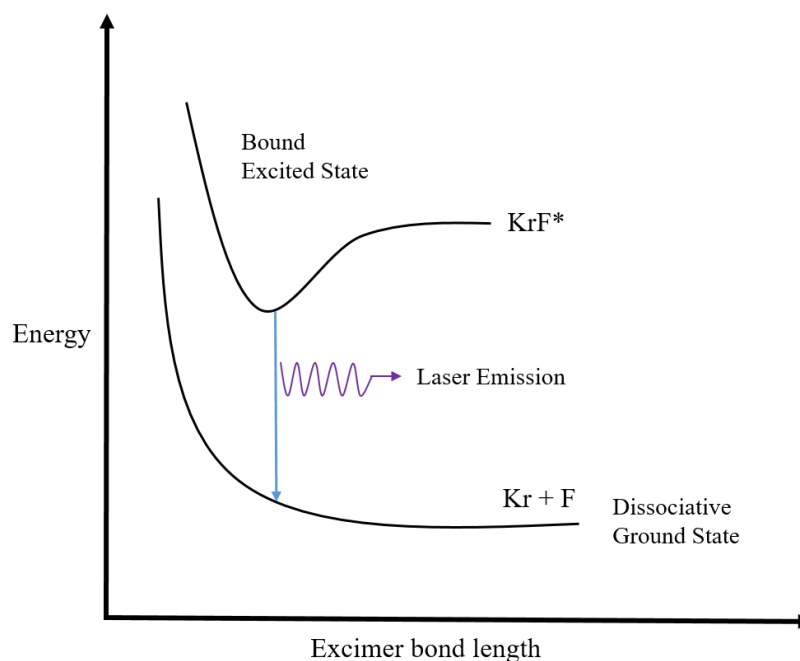


Figure 2-5: Energy levels involved in a Krypton Fluoride excimer laser.

Due to the high energy of the photons generated by an excimer laser, they are typically employed in kinetic studies for the cleavage of bonds in a stable reaction precursor to generate reactive radical species. For example, in this work, the photolysis of hydrogen peroxide precursor using the 248 nm laser output from a KrF excimer laser

was used to generate the OH radical species, which in turn was monitored using laser induced fluorescence (see Section 2.3.7).

2.3.4 Nd:YAG Lasers

A Nd:YAG laser is a solid state laser, that utilises a yttrium aluminium garnet (YAG) crystal lattice, with embedded neodymium ions. The Nd^{3+} ions form a four energy level lasing system when placed within the crystal, as the usually degenerate energy levels are split due to interaction with the crystal field. This four level system is responsible for the lasing action of this active medium. In order to achieve the population inversion required, flashlamps are used to excite the Nd^{3+} from the ground state. Following excitation, non-radiative decay occurs to populate the ${}^4\text{F}_{3/2}$ level. From here, the lasing transition occurs to the ${}^4\text{I}_{11/2}$, resulting in 1064 nm photon emission. As this level exists at a higher energy than the ${}^4\text{I}_{9/2}$ ground state, these energy levels act essentially as a four-level system.

A Nd:YAG laser is particularly useful for dye laser pumping due to its high power, pulsed light, with energies of up to 100 J. As the efficiency of a dye laser is often around 5 %, the use of a Nd:YAG pumping source ensures that the highest powers possible are generated from the dye laser. In this thesis, the output of a Nd:YAG laser, frequency doubled to 532 nm, has been employed to pump the dye laser used for probing of OH radicals (discussed in Section 2.3.5).

2.3.5 Dye lasers

Dye lasers use a solution of an organic dye dissolved in a suitable solvent such as methanol as the active laser medium. They utilise organic compounds that are typically highly conjugated systems, which absorb strongly at visible wavelengths and result in a broad fluorescence spectrum. A common organic dye utilised is Rhodamine 6G, the structure of which is shown in Figure 2-6, alongside the broad band absorption and fluorescence achieved when dissolving Rhodamine 6G in ethanol.

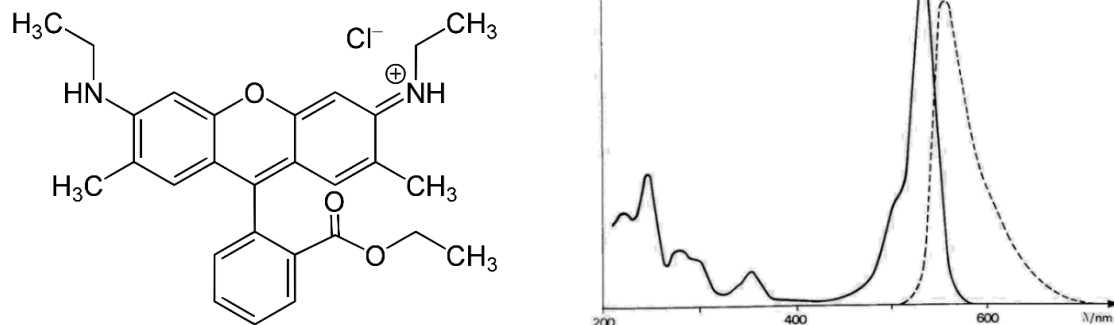


Figure 2-6: Structure of Rhodamine 6G, and the absorption (solid line) and fluorescence (dashed line) achieved when dissolving Rhodamine 6G in ethanol [64].

The energy levels within the dye molecule are broadened due to strong intramolecular interactions, and thus an energy continuum is formed for each electronic state, resulting in broad band absorption and fluorescence. The absorption of visible light typically results in excitation from the ground state level S_0 to the excited singlet state S_1 energy continuum (solid line in Figure 2-6). Rapid radiationless decay then occurs to the lowest energy level in the S_1 excited state. From here, fluorescent emission occurs down to the S_0 continuum, where further radiationless decay occurs. Due to the rapid radiationless decay processes in both states, a four-level laser is essentially established. Also as a consequence of the radiationless decay processes, the photon emitted during fluorescence is of a lower energy than the initial excitation, and therefore occurs at a longer wavelength (as demonstrated by the dashed line in Figure 2-6).

The fluorescence process is in competition with several other processes, described in Figure 2-7. One important other process is the spin-forbidden intersystem crossing to the triplet state T_1 . This state is depopulated by slow phosphorescence down to the ground state S_0 . Another important process is internal conversion, where the molecule can undergo a radiationless transition from the excited state S_1 to S_0 . Both processes described here contribute to the depopulation of the level S_1 , and result in a reduction of the overall output intensity of fluorescence, and a decrease in efficiency. The heat released during non-radiative decay transitions results in degradation of the dye, and therefore the dye is usually pumped through a circulator continuously whilst operating, to ensure fresh dye is used for each laser pulse and to allow some cooling of the dye.

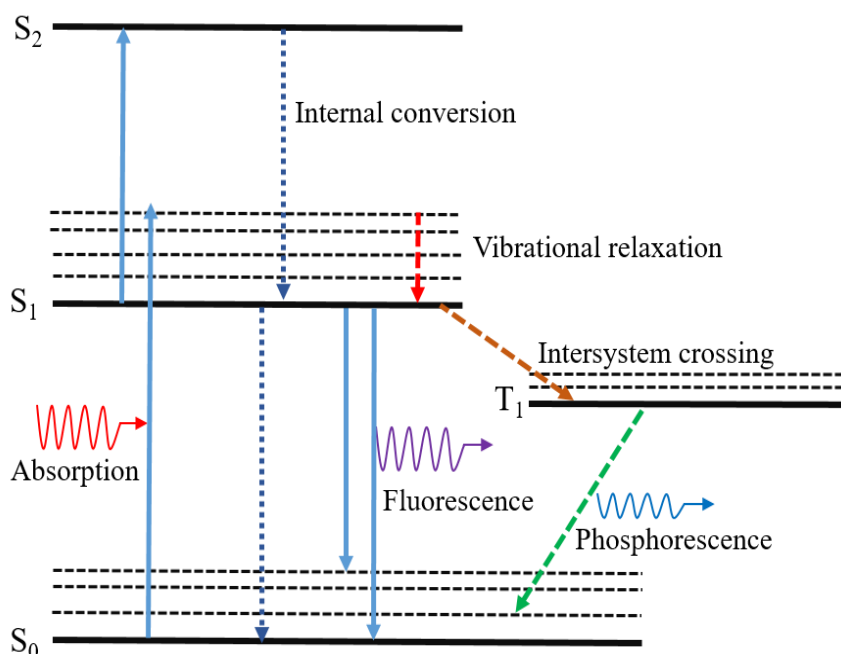


Figure 2-7: Jablonski diagram of possible fates for an excited molecule in a laser dye.

As fluorescence occurs over a range of wavelengths as a consequence of the continuum of energy states, dye lasers provide a broad spectrum of fluorescence as described previously, and can be described as a tuneable source of laser emission. A diffraction grating is therefore required to generate a monochromatic laser emission from this broad fluorescence output. Rotation of the diffraction grating element changes the wavelength that is amplified between the two end mirrors of the dye laser cavity, resulting in the tuneable aspect of the laser. This tuneable characteristic makes dye lasers particularly favourable for spectroscopic purposes, as they result in high selectivity of specific transitions in the species that is to be observed.

In this thesis, to generate fluorescent emission from the dye, the input beam from the Nd:YAG pump was split into two components by a beam splitter, and a portion of the beam (10 – 20 %) was used to excite the dye found in the oscillator cell, while the rest was used to stimulate the dye contained within the amplifier cell. A diffraction grating was used to select the precise wavelength required as described previously, and reflect the light back into the oscillator. The output from the oscillator cell was then amplified in the amplifier dye cell, before exiting the dye laser at the chosen wavelength. The dyes used in this work were Rhodamine 6G and DCM special dye, both dissolved in methanol, to achieve wavelengths of 564 nm and 616 nm respectively. The dye laser output was then doubled to 282 nm and 308 nm using a potassium dihydrogen phosphate (KDP)

crystal, for off- and on-resonant fluorescence respectively. The orientation of this crystal was tuned manually at regular intervals, as the refractive index of the crystal is temperature sensitive, and therefore was sensitive to the temperature fluctuations of the laboratory.

2.3.6 Laser Flash Photolysis (LFP)

Norrish and Porter first developed flash photolysis in 1949, when it was discovered that species with lifetimes of less than a few milliseconds could be monitored and analysed [61]. In this original work of Norrish and Porter, high voltage flash lamps were used as the light source. As the length of time of the light pulse must be shorter than the lifetime of the species being monitored, this limited the timescale of the experimental measurements possible to several milliseconds. Following the development of the laser in 1960, monitoring experiments on the nanosecond timescale became possible, due to the much shorter pulses of light produced.

In this method, the required reagents are premixed in the reaction cell, and a pulse of high energy laser light is used to form a radical or excited state molecule through photolysis *in situ*, the concentration of which is monitored over time using a suitable detection method [41]. Operating the photolysis laser at a high repetition rate enables the data to be acquired rapidly, with the only limitation being that it must be ensured the gas within the photolysis zone is a fresh sample of gas, to avoid secondary photolysis effects. The use of a laser in the flash photolysis method demonstrates several benefits over the original flash lamps used by Norrish and Porter. Lasers can be used to produce much shorter bursts of highly directional, monochromatic light (on the timescale of milliseconds to femtoseconds and beyond [65]) at high energies. Also as a result of the high pulse energies, low precursor concentrations can be used, reducing the contribution of unwanted precursor reactions.

2.3.7 Laser Induced Fluorescence (LIF)

Laser induced fluorescence involves the excitation of a species from its ground electronic state to an excited state by the absorption of a photon of particular wavelength, and subsequent relaxation back to the ground electronic state accompanied by the emission of a photon [61]. For this excitation, dye lasers are typically used, as the frequency can be finely tuned to a particular transition within the species that is to be monitored, resulting in a highly selective technique [41].

Following excitation, the molecule then relaxes back to the ground electronic state either by on-resonant or off-resonant fluorescence, highlighted by the schematic diagram of OH fluorescence in Figure 2-8. In on-resonant fluorescence (b) in Figure 2-8), both the photon used for exciting the molecule and the photon released during subsequent fluorescence are of the same wavelength (308 nm). In off resonant fluorescence (a) in Figure 2-8), vibrational relaxation of the excited molecule can occur (i.e. to $v' = 0$), and the fluorescence then occurs at a longer wavelength (282 nm). At lower pressures, off-resonant fluorescence can also occur from the $v' = 1$ level. In this work, LIF monitoring of the OH radical was used, probing the transition $A^2\Sigma(v'=1) \leftarrow X^2\Pi(v''=0)$. Following this excitation, the fluorescence was monitored by both on- and off-resonant fluorescence, as detailed in the scheme in Figure 2-8.

As well as fluorescence, excited molecules can undergo other processes, such as collisional quenching, in which the molecule decays to the ground state via a radiationless transition. This process can be reduced by reducing the total pressure of the system in which the fluorescence is occurring, reducing the number of collisions with the bath gas.

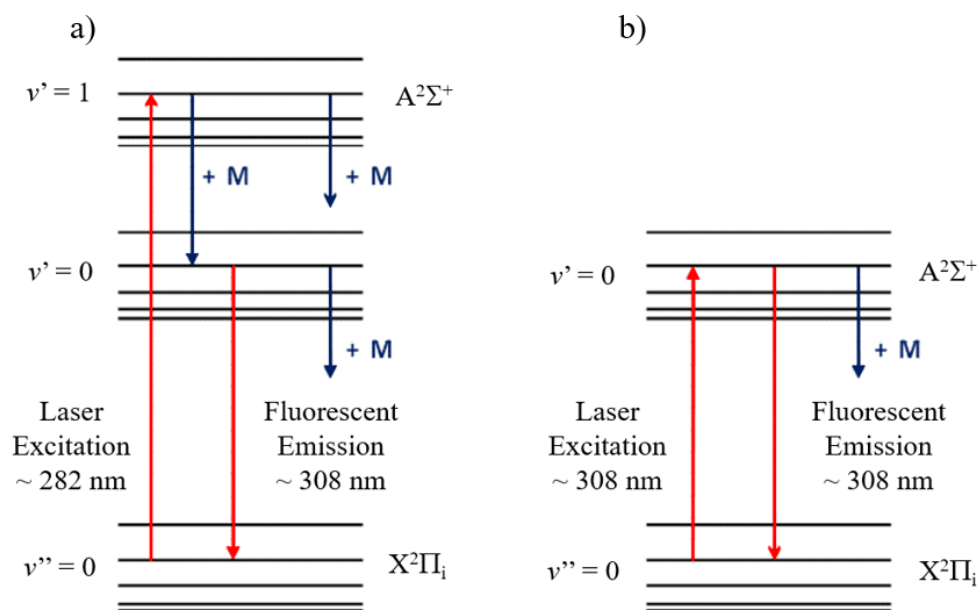


Figure 2-8: Energy level diagram of a) off-resonant and b) on-resonant fluorescence in an OH radical.

By using tuneable dye lasers, it is possible to pick specific excitation wavelengths that match to particular transitions in different species, ensuring only the chosen species is monitored during the experiment. As an example, this can be of benefit in experimental mechanisms where OH recycling is thought to occur. The probe laser can be easily

changed between the wavelength for the above OH radical transition (282 nm) to the wavelength for the same OD radical transition (287 nm) [66], and due to the specificity of the laser-induced fluorescence method, only one of OH or OD will be monitored. This allows comparative experiments between OH and OD to be conducted where regenerated OH is not observed when the dye laser has been tuned to the OD transition, and different pseudo-first order rate constants should be obtained as a result.

A photomultiplier tube (PMT) is used to detect light or fluorescence, and significantly amplify the measured signal. The fluorescence is detected and hits a photosensitive cathode, which emits electrons that are then directed towards a series of dynodes by focusing electrodes. By increasing the voltage at each dynode in the series, an increasing number of electrons are released at each stage, creating a positive feedback effect in which large numbers of electrons are directed towards the final anode plate where it is detected.

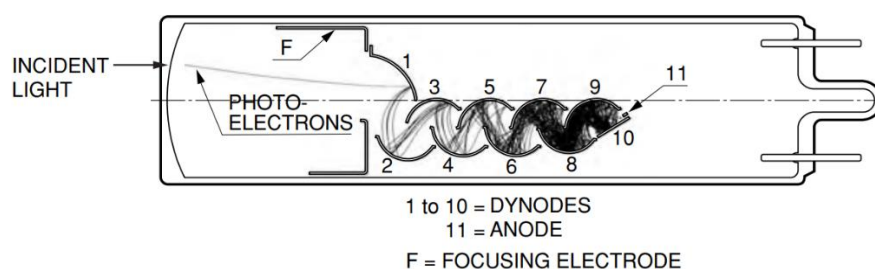


Figure 2-9: A schematic diagram of a photomultiplier tube, showing the amplification in the number of electrons released on going between subsequent dynodes in the series [67].

The main limitation of the laser-induced fluorescence method is that it can only be used on species which are capable of fluorescence, and thus is not suitable for compounds such as large conjugated systems, in which rapid radiation-less transitions occur. The amount of fluorescence measured from a molecule capable of laser-induced fluorescence is dependent upon several factors independent to the individual species, such as the cross section at the particular wavelength and the concentration present in the system. The amount of fluorescence is also dependent upon the laser power of the probe laser used, and the quantum yield (described by Equation E 2-2). Whilst fluorescence is often used for providing relative amounts of the species present, it can be used to provide absolute concentrations if a series of calibrations are carried out.

$$\Phi = \frac{\text{number of molecules undergoing fluorescence}}{\text{number of photons absorbed}} \quad \text{E 2-2}$$

2.4 Alternative Initiation Methods

2.4.1 Discharge Flow

The discharge flow method is commonly used to study gas phase reaction kinetics on the timescale of seconds to milliseconds. Discharge flow experiments are often conducted at pressures of several Torr [68] (up to approximately 20 Torr), however recent developments, such as those discussed by Percival *et al.*[69], have facilitated the conducting of experiments up to pressures of several hundred Torr. In this method, high frequency microwave discharges are used to generate atoms from molecular gas, which are subsequently pumped along a flow tube. A moveable injector is used to inject a co-reactant at varying distances along the tube, as demonstrated in Figure 2-10. The reaction progress is monitored using a suitable detection method, such as laser induced fluorescence or resonance fluorescence (see Sections 2.3.7 and 2.5.1), using a detector placed at a known distance from the injector [41]. As the distance (z) between the moveable injector and the detection point is known, the time t taken between the reaction initiation and reaction monitoring can be calculated using the distance and the flow velocity of the gas mixture v , as outlined in E 2-3.

$$t = z/v \quad \text{E 2-3}$$

By varying the distance of the injector from the detection point, a profile of the detected signal as a function of injection position can be built up. As the reaction time is a function of the injection position, a profile of the signal against time can be also produced for analysis. If the experiments are carried out with the co-reactant in excess of the reactive species, pseudo-first-order conditions can be assumed (see Section 2.7.4), and the signal against time for the reactive species will appear as a single exponential decay curve [41].

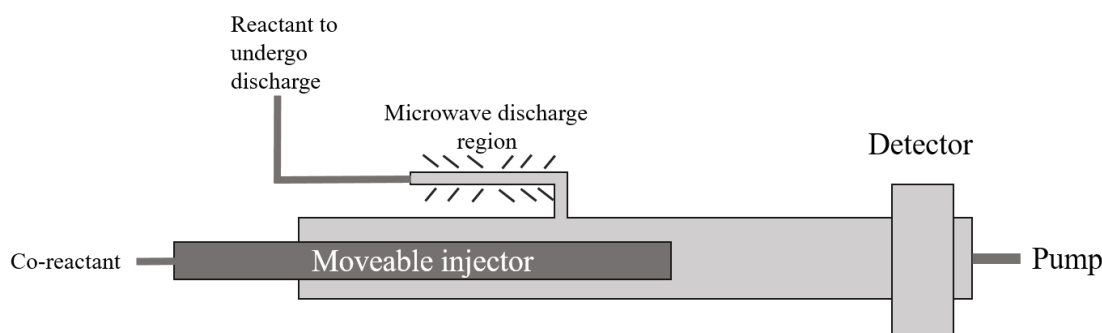


Figure 2-10: A schematic diagram of a discharge flow apparatus.

When measuring the relative concentration of the radical species that is to be detected, a range of detection techniques can be adopted, as a result of the moveable injector for injecting the co-reactant. As the movement of this injector to known distances provides the time resolved aspect of the discharge flow method through equation E 2-3, provided an accurate measurement of this distance is conducted, detection methods that are not time-resolved can be used, such as absorption spectroscopy. This can lead to an improved signal-noise ratio, as the detected signal at the selected distance can be measured until the data quality is of an appropriate standard, before moving to another set distance for the next measurement. This is in contrast to the LFP-LIF method, in which the time resolution between laser flashes must be maintained precisely by a computer, to ensure an accurate measure of the reaction kinetics.

The main limitations for the discharge flow method are the required mixing time for the two reactants and the formation of concentration gradients within the flow. The development of concentration gradients can be overcome by operating the experiment ideally at low pressures, and by reducing the amount of reactions that take place at the wall by providing a wall coating [70]. For reactions in which the mixing time of the reactants is slower than that of the rate of reaction, a uniform concentration will not be obtained by the time the reaction is complete, which limits the timescale of these reactions to at minimum, a few milliseconds [41].

2.4.2 Shock Tube

The use of shock tubes to study reaction kinetics is typically employed for reactions under conditions relevant to combustion, such as high temperatures (> 900 K) and pressures, complementing the work conducted by low temperature kinetic studies

such as those found in this thesis. In a shock tube set up, a low-pressure region containing the dilute reactive gas mixture is separated from a high pressure, inert gas region by a diaphragm. The two regions are referred to as the driven and driver gas respectively. The diaphragm separating the two regions is then rapidly burst, causing a shock wave which propagates the inert driver gas along the length of the shock tube, through the low pressure region. This shockwave causes rapid elevation of temperature and pressure in the reactant gas mixture, initiating chemical reactions which can then be monitored through a range of techniques, such as UV absorption spectroscopy.

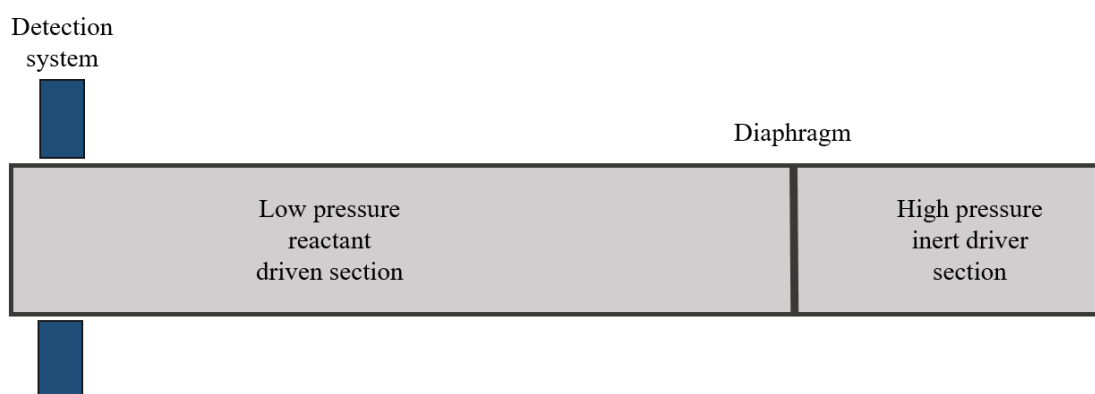


Figure 2-11: A schematic diagram of a shock tube apparatus, showing the relevant high and low pressure sections separated by a diaphragm.

The duration of an experiment conducted using shock tube apparatus is limited by the time it takes for the reflected shockwave to reach the end of the tube, and reflect back towards the incident shockwave travelling in the opposite direction. Consequently, the length of the driven section can be increased significantly to be much longer than that of the driver section, giving a longer time resolution for monitoring the experiments. Each experiment only obtains one kinetic trace, and thus each experiment is considered an individual event. For each of these experiments, significant amounts of gas (both reactant and inert driver gas) are required, which results in a high cost for these experiments compared to other techniques.

In order to fit the experimental data obtained from shock tube experiments, a model is usually constructed, factoring in both the reactions of interest to be studied and any side reactions that occur from the generation of radical species during the course of the experiment. These models can become very complicated, and thus are subject to large uncertainties when a significant number of reactions are involved.

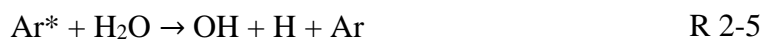
Recent experimental advances published by Tranter *et al.* have demonstrated a range of improvements to the traditional shock tube technique. The development of a diaphragmless shock tube (DFST) has resulted in the demonstration of reproducible shock waves, such that each experiment no longer needs to be considered an individual incident [71]. Due to this reproducibility, multiple experiments can be conducted and averaged to improve the signal-noise ratio obtained [72].

For each of the four butanol isomers studied in this work, research has been conducted using shock tubes to examine the bimolecular reaction of butanol with OH at temperatures that cannot be reached in the LFP-LIF set up used in this work [73-76]. These shock tube experiments provide kinetic measurements of the reactions of OH with the butanol isomers for temperatures relevant to low temperature combustion in the region 800 – 1000 K. As mentioned previously, this lends to a significant gap in the literature for these important reactions between approximately 400 K (conducted by atmospheric research groups [77, 78]) and 800 K. Further discussion of the results for each isomer can be found in the relevant results sections in Chapter 3.

2.4.3 Pulse Radiolysis

Alongside laser flash photolysis, pulse radiolysis can be used as a method for initiating fast reactions. The two methods are based on similar principles, however in pulse radiolysis, a single pulse of high energy radiation is used in place of the laser flash used in laser flash photolysis [79]. The short pulse (10^{-9} to 10^{-6} s) of high energy electrons can be generated from a source such as a linear generator, to produce reaction intermediates that can be monitored using an appropriate detection method on short timescales, such as fluorescence emission [41].

Nelson *et al.* [80] made use of the pulse radiolysis method by generating OH radicals from the pulse radiolysis of argon in water (R 2-4 – R 2-5), generating concentrations of OH radicals typically on the magnitude of 10^{13} molecules cm^{-3} .



In this example, the radiolysis pulse is used to generate excited state argon, which leads to rapid formation of OH radicals. This OH radical is then monitored using a suitable detection method over the course of a reaction for deducing reaction kinetics.

2.5 Alternative Detection Techniques

2.5.1 Resonance Fluorescence

Resonance fluorescence is a detection method mainly used in the detection of atomic species such as H and O [41]. As a technique, it has generally been superseded by laser induced fluorescence, but has been used in other work relevant to this study, such as by Wallington *et al.* [77] who coupled the resonance fluorescence detection method to a flash photolysis initiation.

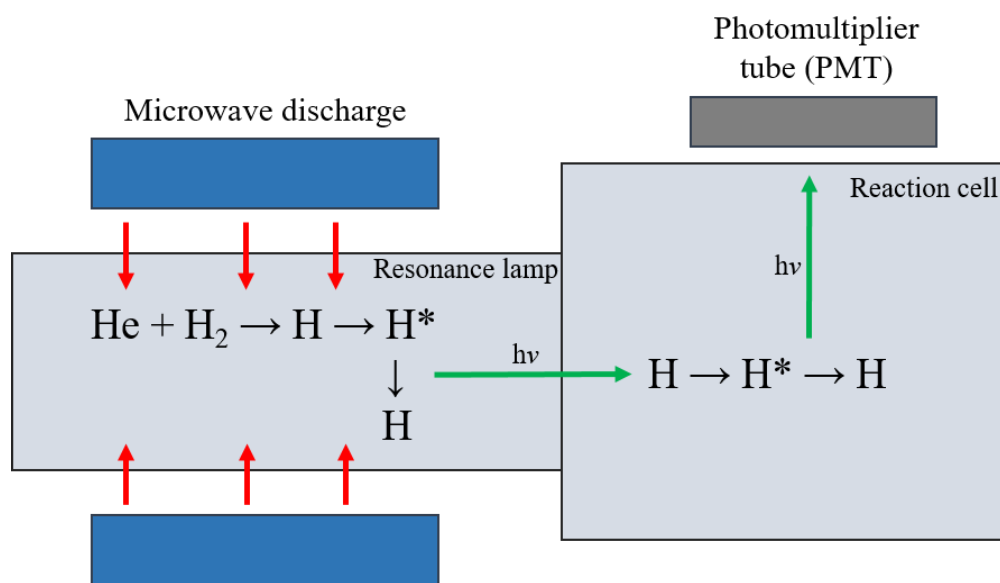


Figure 2-12: Resonance fluorescence schematic diagram, where red arrows represent microwave discharge and green arrows represent resonant fluorescence from H atoms.

In resonance fluorescence, the wavelength of the emitted fluorescence matches that of the wavelength of the excitation radiation [81]. A carrier gas such as helium containing a small amount of precursor (e.g. H_2) is flowed through a microwave discharge source, generating dissociated atoms of the molecular precursor when discharged [41]. These atoms then undergo collisional excitation to generate excited state atoms, which

subsequently relax through fluorescence, releasing a photon of light. This emitted light is then directed into the reaction cell in which the reaction precursors can be found, and atoms of the same species are able to absorb these emitted photons, thus becoming excited, as seen in Figure 2-12. When the atoms contained within the reaction cell relax back to the ground state via fluorescence, the emitted light can be detected by a photomultiplier tube, and is proportional to the atomic concentration within the cell.

2.5.2 Absorption Spectroscopy

Absorption spectroscopy can be used for detection of a species, by probing a reaction cell with light of a particular wavelength in the UV/visible spectrum, and detecting the amount of light that is transmitted through the cell. The absorption process is related to concentration through equation E 2-4 the Beer-Lambert law:

$$\ln\left(\frac{I_T}{I_0}\right) = -\epsilon cl \quad \text{E 2-4}$$

where I_T is the intensity of light transmitted, I_0 is the incident light intensity, c is the concentration of the absorbing species, l represents the path length and ϵ is the absorption coefficient. Provided the absorption coefficient and the path length are known accurately, absorption spectroscopy can be used to measure absolute amounts of species. If these two parameters are not known however, the ratio of transmitted light to incident light can be measured as a function of time, and can give the relative change in concentration of a species over the duration of a reaction.

The sensitivity of the absorption spectroscopy technique can be improved by the use of highly reflective mirrors around the reaction cell, which can result in long path lengths of several meters [82]. However, potential issues arise when using absorption spectroscopy if multiple species present in the reaction cell absorb at the same wavelengths. One way to overcome this issue is to use tuneable lasers, which can selectively probe specific absorption wavelengths, greatly enhancing the selectivity of the absorption spectroscopy method.

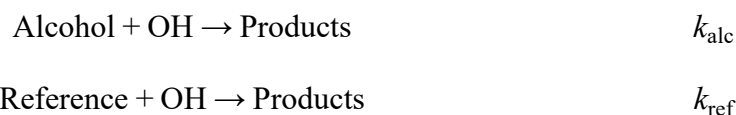
2.5.3 Mass Spectrometry

Mass spectrometry is a detection technique which can be used for highly complex reaction systems, as it is capable of identifying any species that can undergo ionisation [83]. In mass spectrometry, the first stage occurring is ionisation, which results in the formation of charged species. Following ionisation, the charged species are accelerated, and are deflected by magnetic fields, resulting in separation based on their mass-to-charge ratios (m/z).

The separation of the species is analysed using a mass analyser, with the two most common analysers being the quadrupole detector and the time-of-flight mass spectrometer. A quadrupole analyser effectively works as a filter, by detecting only one particular mass-to-charge ratio, and filtering out species that do not possess the correct m/z ratio. In a time-of-flight mass spectrometer, all ionised species are accelerated towards the detector, and the speed at which they accelerate is dependent upon the mass of the individual species. The speed of the ion is therefore dependent on the mass of the species, and results in separation of the species, such that the lightest ions arrive first at the detector. This method is advantageous over the quadrupole detector, as it allows all ions generated to be detected following an experimental reaction in principle.

2.6 Relative Rate

The relative rate method is used in conjunction with analysis such as gas chromatography (GC) to deduce the rate of reaction of a reactant with a radical species, such as OH, when real time monitoring of a reaction may not be possible [41]. The method can be explained through the following kinetic expressions,



Assuming that the reaction of the alcohol and reference compound with OH are the only significant loss processes, the bimolecular rate constant for a chosen alcohol with OH can be deduced from the following equations, E 2-5 – E 2-6.

$$\frac{k_{\text{alc}}}{k_{\text{ref}}} = \frac{\ln\left(\frac{[\text{alcohol}]_0}{[\text{alcohol}]_t}\right)}{\ln\left(\frac{[\text{ref}]_0}{[\text{ref}]_t}\right)} \quad \text{E 2-5}$$

$$\ln\left(\frac{[\text{ref}]_0}{[\text{ref}]_t}\right) \frac{k_{\text{alc}}}{k_{\text{ref}}} = \ln\left(\frac{[\text{alcohol}]_0}{[\text{alcohol}]_t}\right) \quad \text{E 2-6}$$

From a plot of $\ln([\text{alcohol}]_0/[\text{alcohol}]_t)$ against $\ln([\text{ref}]_0/[\text{ref}]_t)$, a straight line plot should be obtained which passes through the origin, and the gradient of which represents the ratio of $k_{\text{alc}}/k_{\text{ref}}$. By using a well-documented literature reference rate constant, k_{ref} , a value for the rate constant k_{alc} can be obtained. An example plot described by the equations above is shown in Figure 2-13, replicated from Andersen *et al.* [84] for measuring the rate of reaction for *i*-butanol with OH relative to a reference compound of cyclohexane.

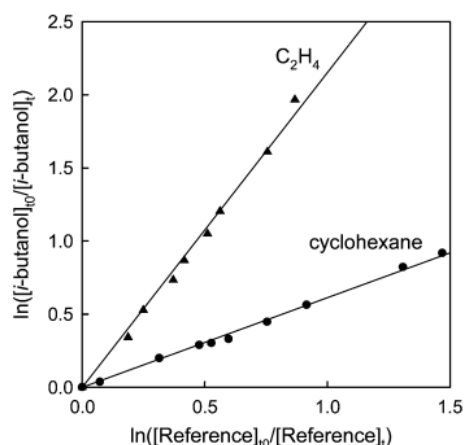


Figure 2-13: An example plot used in the relative rate method, replicated from Andersen *et al.* [84] for measuring the rate of *i*-butanol with OH relative to reference compounds of cyclohexane and ethene.

One significant assumption made for the relative rate method is that the removal of the alcohol reagent only occurs through reaction with OH, and not through any other side reactions. As the alcohol reagent is monitored directly (via GC or some other detection method), any other removal reaction for the alcohol reagent would make the reaction with OH appear faster than it truly is, altering the measured kinetics. This makes the relative rate method sensitive to other side removal reactions, an issue that would not

have a significant effect on LFP-LIF. In LFP-LIF, the alcohol reagent is in large excess of the OH radical, such that small amounts of side removal reactions with other radical species would not significantly alter the measured kinetics of the reaction of alcohol with OH.

However, in LFP-LIF, the presence of significant impurities in the alcohol reagent would alter the measured kinetics, if the impurity present reacts with OH. As the hydroxyl radical is the species measured in LFP-LIF, the presence of another species that reacts with OH would alter the removal kinetics measured. This is an issue that would not be encountered in the relative rate method, as the removal of the alcohol reagent would not be affected by the presence of impurity, and direct measurement of the alcohol reagent would remain the same.

The relative rate method for measuring OH reaction kinetics has been used extensively in the literature for all four isomers of butanol, using a range of relative reference rates. A common reference rate compound used in the literature for studying the butanol isomers is cyclohexane, with a reference rate of $k_{\text{cyclohexane+OH}} = 7.49 \times 10^{-12} \text{ cm}^3 \text{ molecule}^{-1} \text{ s}^{-1}$, as recommended by Atkinson in 1994 [85]. Since the publication of work using this recommended reference rate, e.g. that of Nelson *et al.* for studying *n*-butanol [80] and Chew *et al.* for studying *s*-butanol [86], an updated value for the reference rate compound has been recommended by Atkinson *et al.* in 2003 [87] of $k_{\text{cyclohexane+OH}} = 6.97 \times 10^{-12} \text{ cm}^3 \text{ molecule}^{-1} \text{ s}^{-1}$. Using this updated reference compound rate constant decreases the measured bimolecular rate coefficient for the reaction of butanol with OH by approximately 7 % in both the literature studies of Nelson and Chew, demonstrating the sensitivity of the relative rate method to the reference compound rate. A useful aspect of relative rate is the reporting of the ratio of rate constants, as this allows the calculated rate to be easily updated when new recommendations are provided for the reference rate constant. Further discussion of updating the reference rate constants used in the relative rate studies can be found in Chapter 3.

2.7 This work

This section describes the two experimental set-ups used in the majority of this work, with the specific experimental details, such as exact temperatures and pressures, found in each relevant results chapter. Slight differences between the two experimental

rigs, (utilising either off-resonant fluorescence or on-resonant fluorescence) have been highlighted where appropriate.

2.7.1 Gas Delivery

A schematic diagram of the gas manifold system used is shown in Figure 2-14. The flow rates of the gases required were controlled by calibrated mass flow controllers (MFC), with gases flowing into a mixing manifold, prior to introduction to the reaction cell. Gas lines for the different gases were separated by multiway taps, on which regular leak testing was carried out to ensure small leaks either into or out of the gas line were kept to a minimum. Gas flow was typically maintained at 1000 sccm or 2000 sccm, to ensure the accuracy of the temperature calibration (see Section 2.7.3.1).

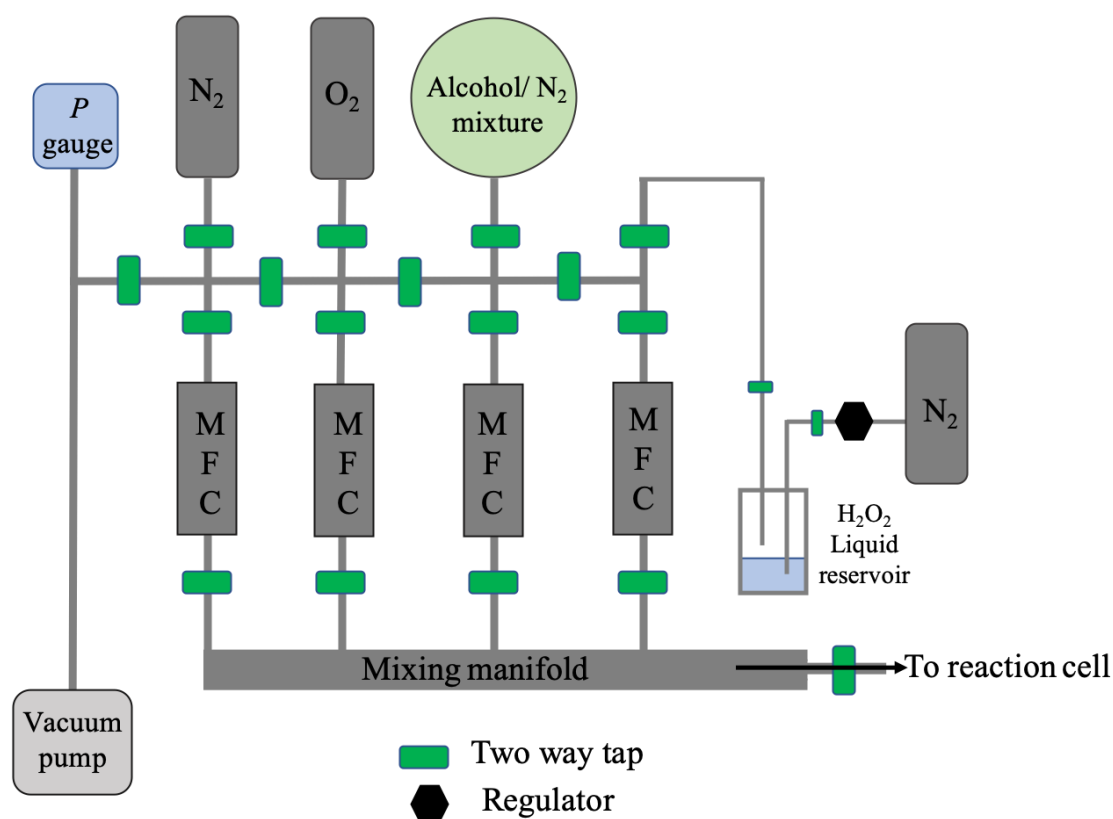


Figure 2-14: Schematic diagram of the gas mixing manifold utilised in this work.

To calibrate the mass flow controllers before use, calibration graphs were obtained using a bubble meter to measure the time taken for a bubble of gas to flow through a known volume for a given MFC digital readout. This graph was then analysed using a linear fit, the equation of which can be used during experiments to calculate the accurate flow delivered from the readout provided. Correction factors were required when flowing a mixture of gases through the MFC, depending on the ratio of the mixture and the relative

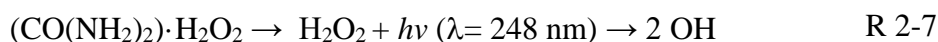
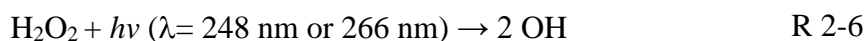
heat capacities. A correction factor was therefore required for mass flow controllers delivering the alcohol reagent diluted in nitrogen bath gas, and was calculated using the following equation, E 2-7:

$$\frac{[\text{Alcohol}]}{\alpha} + \frac{100 - [\text{Alcohol}]}{1} \quad \text{E 2-7}$$

The correction factor, α , varies depending on the species and its heat capacity, and was obtained from the user manual provided with the MFCs. The correction factor estimated for all of the butanol isomers was 0.3, based on the recommended correction factor for *n*-butanol. Due to the low strength bulbs used in this work, this correction factor was usually less than 1 %. When the bubbler method (described in 2.7.1.3) was used for alcohol reagent delivery, this correction factor was at most 5 %.

2.7.1.1 OH Radical Precursors

The majority of experiments conducted in this work utilised hydrogen peroxide (H_2O_2) precursor as an OH radical source, with some experiments using urea hydrogen peroxide (UHP, $(\text{CO}(\text{NH}_2)_2) \cdot \text{H}_2\text{O}_2$). The reaction sources involved are described by reactions R 2-6 and R 2-7.



Hydrogen peroxide was delivered via a flow of nitrogen over a reservoir of liquid hydrogen peroxide in a pressurised bubbler, positioned upstream of the mass flow controller (MFC). Urea hydrogen peroxide (UHP) was introduced by flowing a steady stream of nitrogen over the top of a small amount of solid urea hydrogen peroxide, placed in the bottom of a pressurised bubbler. As the hydrogen peroxide is vapourised from the surface of the solid UHP, the nitrogen acts as a carrier gas to carry this into the reaction cell. The bubbler was placed in a water bath maintained at 298 K to ensure a stable amount of hydrogen peroxide was released from the solid precursor.

One concern of note when using hydrogen peroxide as a radical precursor is that some decomposition occurs when H_2O_2 makes contact with the inside of mass flow controllers and/or the stainless steel delivery lines, producing oxygen which is then in turn delivered to the reaction cell. The amount of oxygen varies depending on the amount of hydrogen peroxide delivered to the reaction cell. The flow of nitrogen/hydrogen peroxide was typically maintained as low as possible to ensure radical-radical reactions were minimised, while preserving good OH fluorescence signal (typically, a flow of less than 400 sccm resulted in signal too noisy for use). Using the method of Potter *et al.* [88], the amount of residual oxygen estimated to be in the system has been calculated as 2.0×10^{14} molecule cm^{-3} for experiments at total cell pressures around 40 Torr at 298 K, and 2.4×10^{14} molecule cm^{-3} for experimental pressures around 90 Torr at 298 K.

2.7.1.2 OH Radical Starting Concentration Estimation

To estimate the starting amount of OH radicals formed from the photolysis laser pulse, $[\text{OH}]_0$, several parameters must be known. Firstly, the number of photons of a given energy in the photolysis pulse must be calculated, according to equations E 2-8 and E 2-9:

$$E_{\text{photon}} = \frac{h \times c}{\lambda} = \frac{6.63 \times 10^{-34} \times 3.00 \times 10^8}{2.48 \times 10^{-7}} = 8.01 \times 10^{-19} \text{ J} \quad \text{E 2-8}$$

$$\text{P. D} = \frac{E_{\text{laser}}}{E_{\text{photon}}} = \frac{0.09}{8.01 \times 10^{-19}} = 1.1 \times 10^{17} \text{ photons cm}^{-2} \quad \text{E 2-9}$$

where h and c are Planck's constant and the speed of light respectively. Assuming a laser energy (E_{laser}) of 0.09 J cm^{-2} at a wavelength of 248 nm (λ), generated by the KrF excimer laser, the photon density (P.D) of photons with energy (E_{photon}) generated is approximately 1×10^{17} photons cm^{-2} . Using the amount of photons calculated, the initial amount of hydrogen peroxide reagent must then be estimated. The initial concentration can be calculated using the bimolecular rate coefficient for the reaction of H_2O_2 with OH, $k_{\text{H}_2\text{O}_2+\text{OH}}$, estimated as $1.7 \times 10^{-12} \text{ cm}^3 \text{ molecule}^{-1} \text{ s}^{-1}$ from the Arrhenius parameterisation of Atkinson *et al.* [89], and a measurement of the pseudo-first-order rate coefficient, k' , obtained from an OH fluorescence decay trace measured in the absence of any alcohol reagent. A typical value measured in this work for k' is approximately 150 s^{-1} . This measurement however is also a measure of the diffusive losses of OH out of the detection

zone, and thus the calculation of equation E 2-10 represents an upper limit to the amount of H₂O₂ in the reaction cell.

$$[\text{H}_2\text{O}_2] = \frac{k'}{k_{\text{H}_2\text{O}_2+\text{OH}}} = \frac{150}{1.7 \times 10^{-12}} = 8.85 \times 10^{13} \text{ molecule cm}^{-3} \quad \text{E 2-10}$$

This estimate of the starting amount of hydrogen peroxide can then be used in equation E 2-11, with an assumed cross section, σ , for hydrogen peroxide of $8.5 \times 10^{-20} \text{ cm}^2 \text{ molecule}^{-1}$ at 248 nm [89] and the number of photons calculated in equation E 2-9.

$$\text{P.D} \times \sigma \times [\text{H}_2\text{O}_2] \times 2 = 1.7 \times 10^{12} \text{ molecule cm}^{-3} \quad \text{E 2-11}$$

As the photolysis of hydrogen peroxide produces two OH radicals, this must then be multiplied by two. This gives an upper limit to the starting concentration of OH radicals at time zero of $1.7 \times 10^{12} \text{ molecule cm}^{-3}$.

2.7.1.3 Alcohol Reagent Delivery

Glass bulbs of reagent were made up using a glass gas manifold, to ensure the accuracy of the concentration of the bulb. To calculate the percentage concentration of the bulb, an accurate measurement of the vapour pressure of reagent delivered to the evacuated bulb was required, together with the final total pressure of nitrogen added. Bulb strength was typically around 0.5 – 1.5 %, in a total pressure of around 1400 Torr.

Experiments conducted at temperatures above approximately 500 K required higher amounts of alcohol reagent compared to those at lower temperatures, to allow sufficient separation of the reaction kinetics measured, and therefore a bubbler method of reagent delivery was used. In this method, a glass bubbler with a 1 – 2 cm deep liquid reservoir of alcohol reagent is pressurised using a backing pressure of nitrogen, and the flow of this nitrogen over the reservoir introduces the reagent to the cell. The strength of the bubbler is calculated using the vapour pressure of the liquid reagent and the total pressure of nitrogen applied to the bubbler, and from these parameters, the amount of

alcohol delivered to the reaction cell can be calculated. For calculating the bubbler concentration, the Antoine parameters for each alcohol, summarised in Table 2-2 (obtained from [90]), were used to estimate the vapour pressure of the liquid reservoir, according to the following equation:

$$\log_{10}(P)=A - \frac{B}{T+C} \quad \text{E 2-12}$$

Table 2-2: Antoine parameters for alcohols studied in this work [90].

	A	B	C
<i>n</i>-butanol	4.55	1351.56	– 93.34
<i>i</i>-butanol	4.43	1236.99	–101.53
<i>s</i>-butanol	4.33	1158.67	– 104.68
<i>t</i>-butanol	4.50	1174.87	– 93.92

The Antoine equation is a parameterisation used to describe the relation between vapour pressure and temperature for a given substance, and is obtained from parameterising experimental measurements of the vapour pressure at different temperatures, as demonstrated in the work of Kemme and Kreps [91].

The use of the Antoine equation allows the vapour pressure to be calculated for a given temperature, and therefore also requires a measurement of the temperature of the liquid reservoir, which was estimated prior to each kinetic trace via a thermocouple placed near to the exterior of the glass bubbler, as the temperature within the bubbler itself could not be measured. The bubbler was then pressurised using a high backing pressure of nitrogen, with the total pressure in the bubbler measured using a capacitance manometer (MKS Baratron, 0 – 1000 Torr) positioned on the stainless steel manifold next to the bubbler inlet, demonstrated in Figure 2-15.

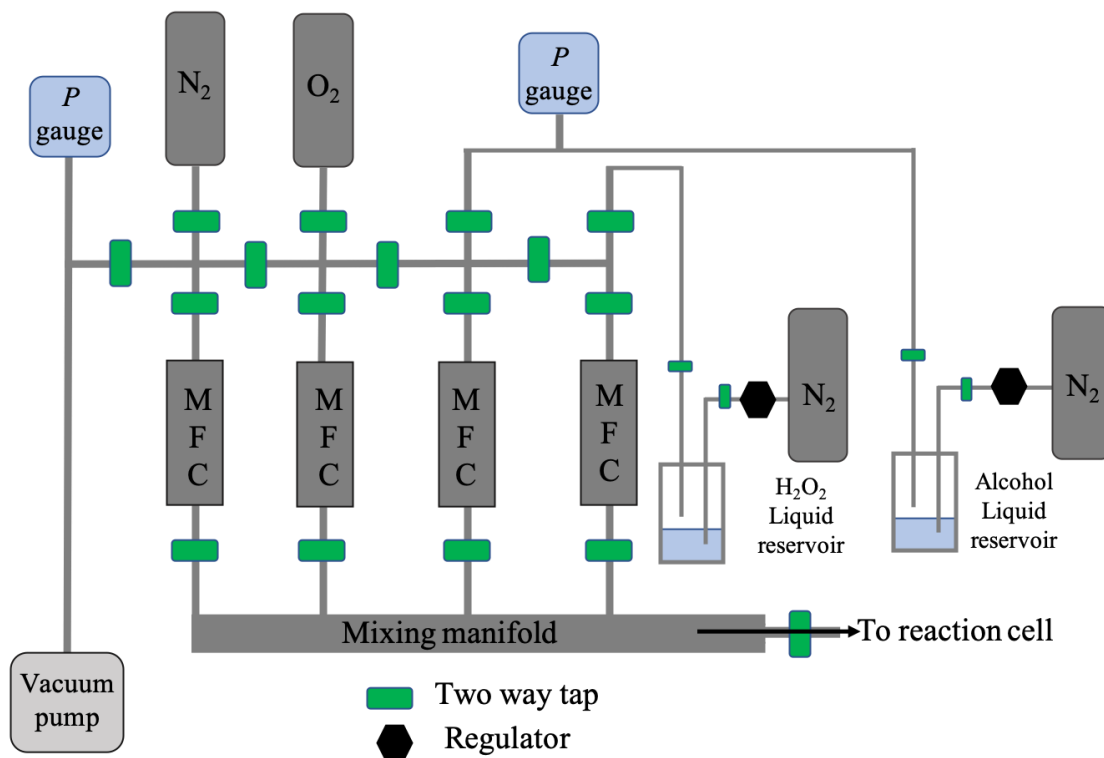


Figure 2-15: Schematic of mixing manifold in which bubbler method used for reagent delivery.

2.7.2 Reaction Cell and Laser Set up

This section describes the practicalities of conducting experiments, including the orientation of the reaction cell and the laser set up involved. This work utilised a two-laser system in a pulsed laser photolysis – laser-induced fluorescence method.

2.7.2.1 Lasers

In this work, both on-resonant and off-resonant fluorescence were used for the monitoring of OH radicals (see Section 2.3.7). On-resonant fluorescence utilised a Nd:YAG (Continuum Powerlite 8010) pumped dye laser (Spectra Physics PDL-3), operating using DCM special dye to obtain a probe laser wavelength of approximately 308 nm. The off-resonant fluorescence system also utilised a Nd:YAG pumped dye laser, however the dye in this case was Rhodamine 6G dissolved in ethanol to generate a probe wavelength of 282 nm.

Both experimental set ups used an excimer laser (KrF, Lambda Physik LPX 200) at 248 nm for photolysis of OH precursor. The photolysis laser was usually operated at 10 Hz, with a typical pulse energy of 50 – 120 mJ pulse⁻¹. Experiments were also conducted where necessary at 2 Hz and 5 Hz for repetition rate dependent investigations,

to investigate if the photolysis laser was influencing the measured kinetics in any way. If there was any secondary photolysis of the reagents or products from the reaction, this could act to either increase or decrease the kinetics measured, affecting experimental results. Some experiments were also conducted using the 4th harmonic of a Nd:YAG laser to generate a photolysis wavelength of 266 nm, also operated at 10 Hz. This was achieved by frequency doubling the initial 1064 nm wavelength light generated from the Nd:YAG laser first by a lithium borate crystal to generate 532 nm, followed by doubling again by a barium metaborate crystal to 266 nm.

2.7.2.2 Reaction Cell

Reactants entered a stainless steel mixing manifold prior to entering the six-way cross reaction cell, also constructed of stainless steel, with a total volume of approximately 1000 cm³. The reaction cell was connected to a vacuum pump via a needle valve, which was used to control the total pressure and gas flow through the reaction cell. A schematic diagram of the reaction cell utilised in both set ups for this work is shown in Figure 2-16.

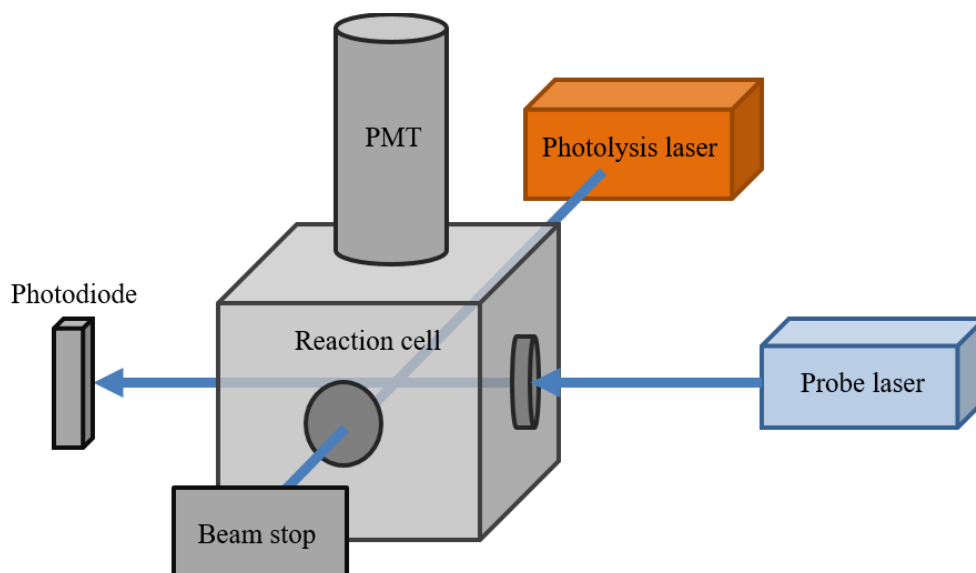


Figure 2-16: Schematic diagram of the cell used in both experimental set ups.

2.7.2.3 Photomultiplier Tube and Orientation

A linear focused photomultiplier tube (schematic diagram shown in Figure 2-9) (PMT) (Electron tubes) was used for detection of the emitted fluorescence during the

reaction. The absolute value of the fluorescence measured is not required, but the voltage applied to the PMT must be kept low to ensure linear response to fluorescence measured (see Section 2.3.7). Increasing the voltage applied increases the noise detected by the PMT, so keeping this applied voltage low (around 1 kV) acts to reduce signal noise. Fluctuations in the probe laser power over the duration of a kinetic trace also required the use of a photodiode, which was positioned on the opposite side of the reaction cell to the probe laser and to provide a measurement of these fluctuations. By measuring the fluctuations, the fluorescence signal can be normalised, removing some of the signal noise caused by fluctuations in the power occurring between laser shots.

The photolysis and probe dye laser beams enter in to the reaction cell at right angles to each other, with the PMT orientated perpendicular to the intersection of the laser beams. As the fluorescent emission from the species of interest occurs in a random direction, this positioning helps to distinguish the fluorescence from scattered background light from the probe laser. An interference filter (308 ± 5 nm) was also positioned between the cell and the PMT, to remove scattered light outside of this wavelength threshold region.

2.7.3 Temperature and Pressure Measurement

The total concentrations of reagents present in the reaction cell were calculated based on the total pressure and temperature of the reaction cell, and thus accurate measurements of these parameters were required.

The total pressure in the cell for the off-resonant fluorescence system was measured by a capacitance manometer (MKS Baratron), capable of measuring to 0.01 Torr and was used for pressures up to 80 Torr. For the on-resonant fluorescence system, a capacitance manometer was also used, measuring to 0.1 Torr for pressures up to 130 Torr. The total pressure within the cell for both setups were maintained by a vacuum pump (Edwards RV 5), controlled by a main valve and a needle valve for fine tuning. For making up of glass reagent bulbs using the glass vacuum line, a Pirani thermal-conductivity type low pressure gauge capable of measuring in mTorr was used, with a vacuum pump controlled by a main valve and a needle valve as before. This ensured precise measurement of the zero pressure of the evacuated bulb and the vapour pressure of reagent delivered, and thus allowed accurate calculation of the concentration of the filled bulb after nitrogen addition.

For temperature measurement, calibrated K type thermocouples were used, placed close to the centre of the reaction cell but not at the intersection of the lasers. For heating the reaction cell in the off-resonant fluorescence system, the temperature required was set on an external heater controller. The heating was achieved by applying a current to a series of cartridge heaters surrounding the reaction cell until the temperature measured by the thermocouple matched the pre-set temperature on the heater controller, and was then maintained at this set temperature by the external controller. For heating the reaction cell in the on-resonant fluorescence system, the temperature is set by controlling the voltage applied to the heaters surrounding the cell, using a Variac voltage controller. After supplying the voltage to the surrounding heaters, the temperature is established and is then left to stabilise for several hours to ensure the system was evenly heated, and is measured using the thermocouples placed within the reaction cell.

2.7.3.1 Temperature Corrections

For both experimental setups, a series of temperature calibrations were required to correct the temperature reported by the thermocouple to the actual temperature of the reaction zone. This correction was done by measuring a well-known reaction rate constant at a series of set temperatures, in order to calculate the true value of the temperature in the reaction zone. The measured value for the rate constant at a given temperature setting was then corrected to the known value from the literature, by iterating the temperature and thus the concentration of reagent in the cell, until the experimental value of the rate constant matched that of the literature. This process gave an actual temperature of the reaction zone, which was noted and compared to the readout provided by the thermocouple. By carrying out this correction across a range of thermocouple readings, a temperature calibration curve could be constructed, and used to apply a correction whilst the experiments are being conducted.

For the off-resonant fluorescence experimental set up, this temperature correction did not appear to be dependent on the total flow of gas into the system, and therefore the temperature calibration curve was parameterised based solely on the thermocouple readout. Temperature calibration experiments were conducted for the reactions of both hydrogen and methane with the hydroxyl radical, and corrected to the studies of Tully and Ravishankara [92] and Dunlop and Tully [93] respectively. The temperature correction data obtained for a 1000 sccm flow is represented graphically in Figure 2-17, with the other flows omitted for clarity. The black circles represent the corrections

required relative to the methane parameterisations of Dunlop and Tully, and red triangles for the temperature corrections required relative to the hydrogen parameterisation of Tully and Ravishankara.

For the on-resonant fluorescence set-up, separate calibration curves were constructed for total flows of 1000, 2000 and 4000 sccm, which were then applied depending on the total flow of gas during the experiments. Extensive temperature correction experiments were conducted on the on-resonant fluorescence setup with corrections applied relative to the study of methane with OH, conducted by Dunlop and Tully as before [93].

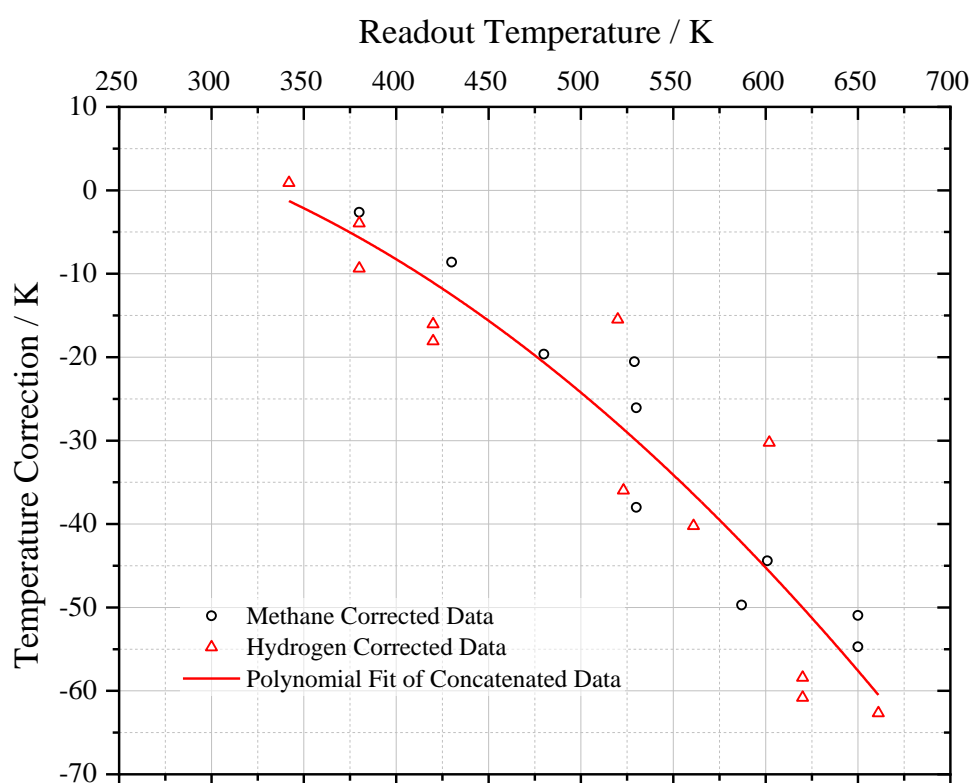


Figure 2-17: Off-resonant fluorescence set up temperature calibration curve, for total gas flows of approximately 1000 sccm. Black circles represent corrections required relative to the methane parameterisations of Dunlop and Tully [93], and red triangles for the temperature corrections required relative to the hydrogen parameterisation of Tully and Ravishankara [92]. Solid red line represents concatenate polynomial fit to data, $y = 5.62 + (0.07 \times x) + (-2.5 \times 10^{-4} \times x^2)$.

2.7.4 Kinetics

If more than one reactant is involved in the reaction of interest being monitored in a kinetic study, solving the reaction kinetics can become complicated. In this situation, it is common to ‘isolate’ one of the reagents, by putting all other reactants in such a large excess that they are effectively considered constant for the time of the reaction [41]. This is known as pseudo-first-order kinetics and was utilised throughout this work. For the bimolecular elementary reaction:



The differential rate law can be written as follows:

$$\frac{-d[B]}{dt} = k [A][B] \quad \text{E 2-14}$$

If the concentration of species A is much greater than that of species B (i.e. $[A] \gg [B]$), then the rate law can be reduced to:

$$\frac{-d[B]}{dt} = k' [B] \quad \text{E 2-15}$$

$$k' = k [A] \quad \text{E 2-16}$$

Integration of equation E 2-15 between time zero and time t with subsequent rearrangement gives:

$$\ln \left(\frac{[B]_t}{[B]_0} \right) = -k't \quad \text{E 2-17}$$

$$[B]_t = [B]_0 e^{-k't} \quad \text{E 2-18}$$

where $[B]_t$ is the concentration of species B at time t , and $[B]_0$ is the concentration of B at time zero [94]. Equation E 2-18 shows that the concentration of B will decrease exponentially with time at a rate determined by k' , the pseudo-first-order rate constant.

By varying the concentration of the species A, a range of pseudo-first-order rate constants can be obtained. When plotting these measured rate constants against

concentration of A, a straight line plot of gradient k is produced, which corresponds to the bimolecular rate constant. Application of this theory to the experimental carried out in this work, the following equations are obtained:



$$\frac{-d[\text{OH}]}{dt} = k [\text{OH}][\text{Butanol}] \quad \text{E 2-20}$$

Assuming $[\text{Butanol}] \gg [\text{OH}]$, and therefore $[\text{Butanol}]$ remains constant throughout the reaction time:

$$\frac{-d[\text{OH}]}{dt} = k' [\text{OH}] \quad \text{E 2-21}$$

$$k' = k_{\text{bim}}[\text{Butanol}] + k_{\text{OH}}[\text{H}_2\text{O}_2] + k_{\text{diff}} \quad \text{E 2-22}$$

$$\int_{[\text{OH}]_0}^{[\text{OH}]_t} \frac{d[\text{OH}]}{[\text{OH}]} = -k' \int_0^t dt \quad \text{E 2-23}$$

$$\ln \left(\frac{[\text{OH}]_t}{[\text{OH}]_0} \right) = -k't \quad \text{E 2-24}$$

$$[\text{OH}]_t = [\text{OH}]_0 e^{-k't} \quad \text{E 2-25}$$

For the experiments conducted in this work, the pseudo-first-order rate constant k' represents several different removal mechanisms for the OH radicals produced in the photolysis pulse, as described in equation E 2-22. These are: the bimolecular reaction of OH with the alcohol reagent (k_{bim}), reaction of OH with the hydrogen peroxide precursor (k_{OH}) and diffusion out of the reactive zone (k_{diff}). From the relationship described by equation E 2-22, a plot of the pseudo-first-order rate coefficients against concentration of butanol reagent will yield a bimolecular plot, where the gradient is the bimolecular rate coefficient for the reaction of butanol with OH, and the intercept represents some combination of the diffusive losses and reaction with precursor (k_{diff} and k_{OH}).

As the concentration of the OH radical is directly proportional to fluorescence signal, equation E 2-25 can be altered to the form seen in E 2-26 where S_t is the

fluorescence signal at time t , and S_0 is the fluorescence at time zero. The modified version also incorporates a background signal value 'bg'.

$$S_t = S_0 e^{-kt} + \text{bg} \quad \text{E 2-26}$$

This equation E 2-26 can then be used to fit experimental kinetic traces obtained in this work, as shown in Figure 2-18, to obtain the pseudo-first-order rate constant.

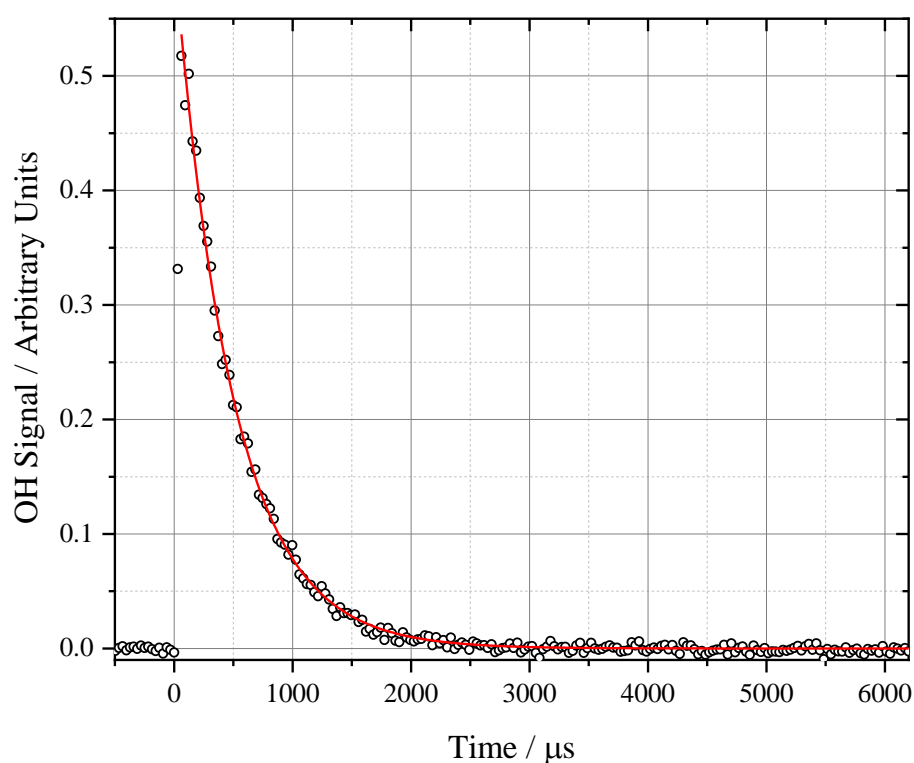


Figure 2-18: Example single exponential decay of OH fluorescence signal. Black circles represent data points with red line representing a single exponential decay fit using E 2-26, 298 K, 40 Torr nitrogen, $[n\text{-butanol}] = 2.1 \times 10^{14}$ molecule cm^{-3} , $k' = (2050 \pm 10) \text{ s}^{-1}$.

An example exponential decay is shown in Figure 2-18, with the solid red line through the data points representing the single exponential decay equation outlined in equation E 2-26. Approximately 20 pre-time zero points are taken to calculate an average background signal which is subtracted from all data points, allowing the baseline to be

fixed at zero when fitting experimental traces. By repeating this process across a range of butanol reagent concentrations, a bimolecular plot could be obtained, in order to calculate the bimolecular rate coefficient. An example bimolecular plot is shown in Figure 2-19.

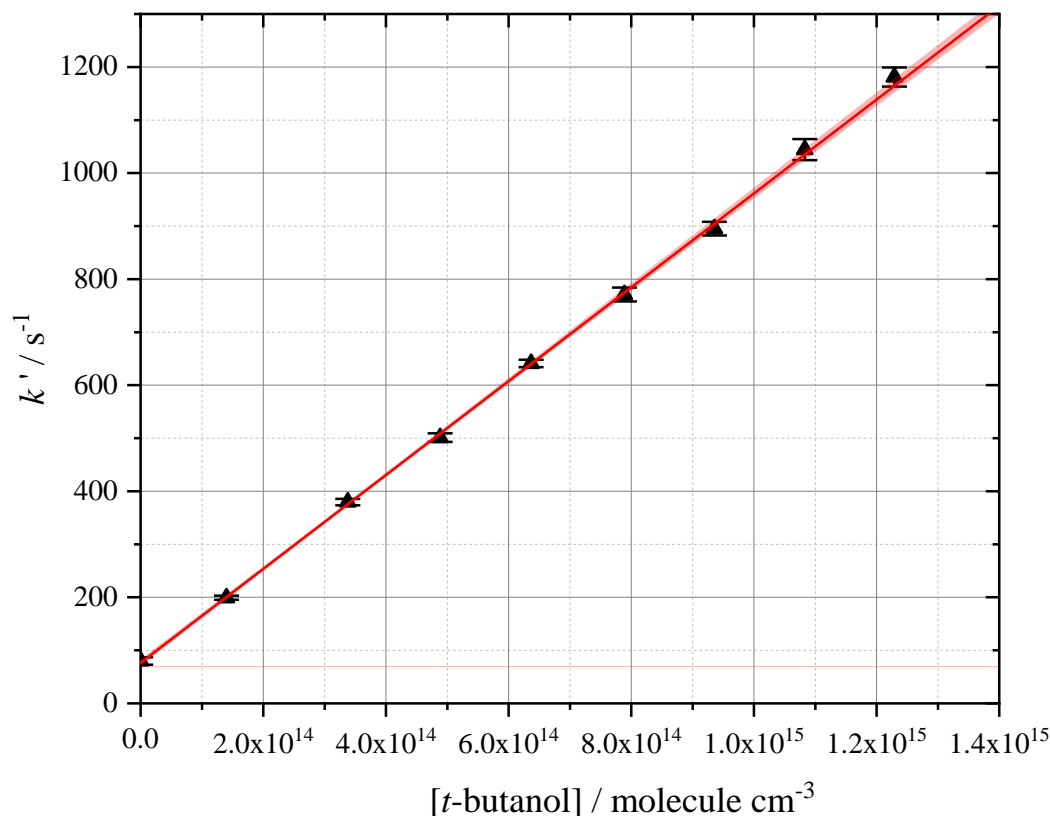


Figure 2-19: Example bimolecular plot obtained for the reaction of *t*-butanol with OH. Obtained at 298 K and 31 Torr of nitrogen. The slope represents the bimolecular rate coefficient, $k_{t\text{-butanol}+\text{OH}} = (8.86 \pm 0.08) \times 10^{-13} \text{ cm}^3 \text{ molecule}^{-1} \text{ s}^{-1}$. The error bars are the statistical error at the 1σ level, and the red shaded area represents the 95 % confidence limits.

Some experiments conducted did not produce simple single exponential decay curves, and where relevant, these have been explained in their respective results chapters. The full fitting equation for the biexponential traces utilising OH radical precursor is provided in Section 4.3.1. The fitting equation for traces that utilise oxalyl chloride precursor has been provided in Appendix A, and in Appendix E for SO_2 precursor experiments.

2.7.5 Data Acquisition and Analysis

An example of the raw fluorescence data obtained from a single experimental trace can be seen in Figure 2-20, alongside the signal measuring the fluctuations of the probe laser power and the normalised data. In this, the purple line represents the relative fluctuations of the probe laser power, observed *via* the photodiode. The absolute power measurement is not important. The data points represented in red are the raw fluorescence data points measured during the kinetic trace, averaged for between 8 – 15 scans. Square black points represent this raw data after being normalised for the probe laser power. As seen in Figure 2-20, this can reduce the noise observed in the data, and provides a means to account for the random fluctuations in laser power. Accounting for the fluctuations in laser power also assists in reducing the uncertainty by removing some of the signal noise, however as highlighted in Figure 2-20, the power remained relatively stable throughout the course of an experimental trace, and thus did not have a great effect on reducing the uncertainty in the obtained kinetic parameter k' . Between 15 – 25 data points prior to the photolysis laser pulse are also measured, as mentioned previously, which provide a measure of the background scattered light observed by the PMT.

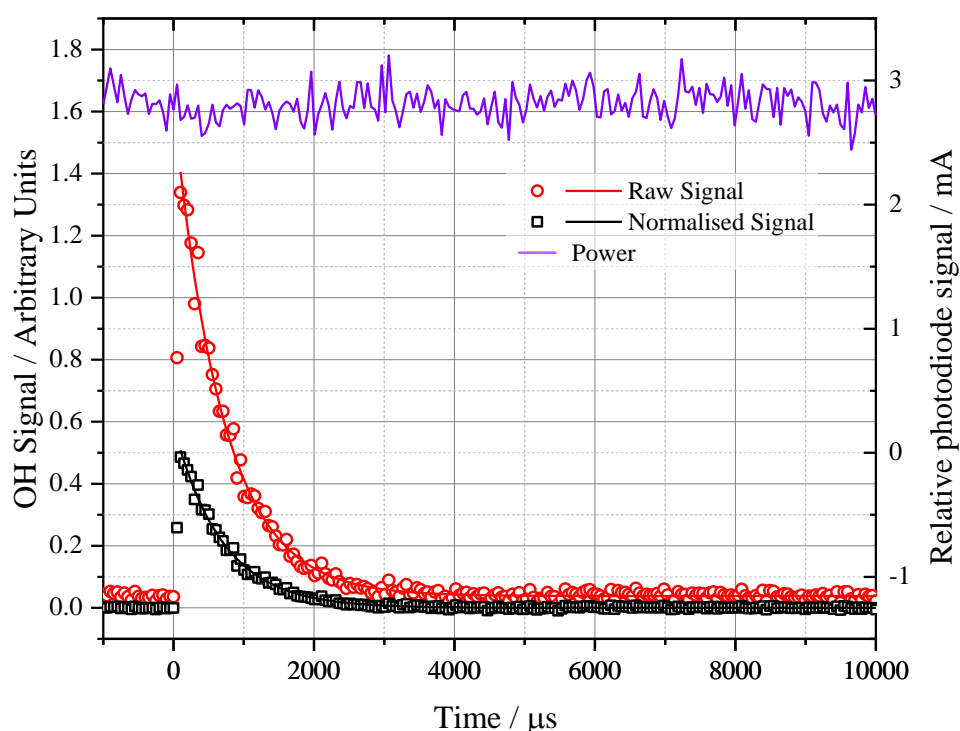


Figure 2-20: Example trace showing laser power fluctuations (purple solid line), raw data signal (red hollow circles and red solid fit line), and normalised data signal (black hollow squares and black fit line). k' obtained from fitting to raw signal = $(1454 \pm 18) \text{ s}^{-1}$ and normalised signal = $(1433 \pm 15) \text{ s}^{-1}$. Uncertainties are statistical at 1σ .

Typically, each concentration measured on the bimolecular plot was measured once, with the experiments conducted in a non-linear fashion, i.e. the concentration was not increased linearly. The error bars for each individual concentration are the reported errors from the OriginPro software when fitting equation E 2-26 to the fluorescence signal, and therefore represent the quality of the equation fit to the signal (referred to throughout this thesis as the statistical error at the 1σ level). Most experiments were analysed using single trace analysis in the OriginPro software, using an instrumental weighting fitting regime. When analysing the bimolecular plot, this fitting regime takes into account the errors in each individual point, and therefore accounts for lesser quality experimental traces obtained by weighting towards those with smaller errors.

For experiments conducted that obtained traces that were not simple single exponential decays, a global fitting regime was introduced. This fitting allows multiple kinetic traces to be fit at once, sharing some of the important parameters (i.e. the bimolecular rate coefficient) and fixing others (i.e. the concentration of the alcohol reagent relevant to each respective trace being fit). This assists in robust parameter retrieval when fitting a set of kinetic traces, and obtains a value for parameters that best describe a series of experimental traces. Typically, smaller errors are often reported from this fitting regime, and therefore the error reported was usually propagated to a more significant error (i.e. in Chapter 4) to provide a more realistic representation of the error in the experiments conducted.

Chapter 3 Temperature Dependent Studies of OH + Butanol Isomers

3.1 Chapter Summary

The reaction of the hydroxyl radical with each of the four butanol isomers has been studied using laser flash photolysis coupled to a laser induced fluorescence detection system for OH radicals. The rate coefficients have been described by modified Arrhenius parameterisations, extending the previous literature temperature highs from around 400 K to approximately 715 K for *n*-butanol, 607 K for *i*-butanol, 690 K for *s*-butanol, and 615 K for *t*-butanol. The reaction of each isomer with OH can be described as a function of temperature by the following modified Arrhenius parameterisations (all in units of $\text{cm}^3 \text{ molecule}^{-1} \text{ s}^{-1}$):

$$k_{n\text{-butanol}+\text{OH}} (298 - 715 \text{ K}) = (1.15 \pm 2.62) \times 10^{-19} \times T^{(2.64 \pm 0.31)} \times \exp\left(\frac{7800 \pm 1100}{R \times T}\right)$$

$$k_{i\text{-butanol}+\text{OH}} (298 - 607 \text{ K}) = (2.05 \pm 6.79) \times 10^{-18} \times T^{(2.20 \pm 0.45)} \times \exp\left(\frac{6800 \pm 1600}{R \times T}\right)$$

$$k_{s\text{-butanol}+\text{OH}} (298 - 690 \text{ K}) = (1.38 \pm 2.58) \times 10^{-21} \times T^{(3.22 \pm 0.25)} \times \exp\left(\frac{10330 \pm 970}{R \times T}\right)$$

$$k_{t\text{-butanol}+\text{OH}} (298 - 614 \text{ K}) = (4.50 \pm 23.7) \times 10^{-21} \times T^{(2.99 \pm 0.71)} \times \exp\left(\frac{5200 \pm 2600}{R \times T}\right)$$

Comparisons with previous literature have also been conducted, including high temperature shock tube data for temperatures above 800 K for each isomer. Concatenate fits to previous literature experimental data and these data have been presented, with discussion of the effect on the high temperature parameterisation beyond the region studied in this work.

3.2 Introduction

The butanol isomers have been suggested as possible biofuels due to their favourable properties compared to other alternative fuels, primarily ethanol, such as higher energy density and being less corrosive to pipelines [95, 96]. Studies into their usefulness as potential fuels have been carried out, looking into emissions from blending with traditional fossil fuels and as standalone fuels, and also ignition delay time tests [45, 53, 97]. Multiple different butanol combustion models have been developed, for example those of Sarathy *et al.* [55], Moss *et al.* [98] and Black *et al.* [99], though when modelling experimental parameters, these models can display wide discrepancies [74]. Consequently, there is a demand for kinetic experimental work to constrain some of the

key reaction rate constants at temperatures relevant to combustion, particularly those highlighted during sensitivity analysis [60].

The initial step in the oxidation of a fuel in the low temperature combustion region is usually reaction with the OH radical, resulting in abstraction of a hydrogen from the fuel. Following this initiation reaction, subsequent reaction with oxygen is key to the chain branching process, as highlighted in Figure 1-5, Section 1.7. For efficient use of these alternate fuels in an engine, the rate at which these reactions occur must be well understood.

Whilst the rate of the initial oxidation step is important for fuel reactivity, the abstraction site it occurs at is also of significance [53]. Depending on the site of the initial abstraction, the subsequent reactive species produced during secondary stages of oxidation are affected. In recent work by Agbro *et al.*, the importance of the branching ratio for the reaction of *n*-butanol with OH was highlighted in a sensitivity analysis examining the effect of each of the reactions involved in low temperature combustion on simulated ignition delay times. At 725 K, 15 bar and an equivalence ratio of 1, it was found in the Agbro *et al.* study that two of the most sensitive reactions are the H-atom abstraction reactions at the alpha- and gamma-site (relative to the OH group). Following this abstraction, reaction with oxygen at these sites can lead to chain terminating reactions at low temperatures, such as those forming HO₂ (shown in the top left panel of Figure 3-1).

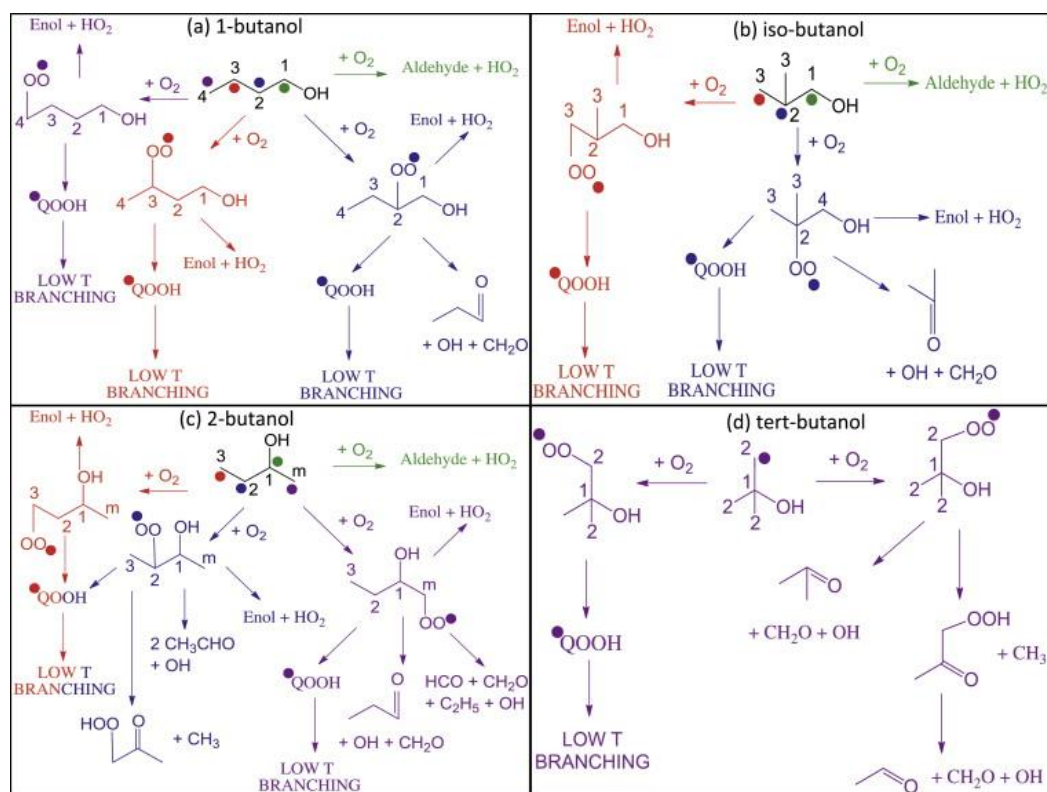


Figure 3-1: Simplified schematic of low temperature reaction pathways resulting from abstraction at different reactive sites for the four isomers of butanol [1].

Unfortunately, site specific reactivity and branching ratios are difficult to measure experimentally, and often require complex experimental procedure and analysis, such as that of Carr *et al.* [100] for the reaction of ethanol with OH. Currently, the branching ratios for fuel oxidation reactions are estimated based on combinations of computational calculations and structure activity parameterisations [55, 78, 101], and require experimental data to confirm accuracy. Experimental measurements of the total rate of reaction of a potential fuel with the hydroxyl radical are of crucial importance for constraining these structure-activity relationships (SAR), and provide confirmation of the validity of the parameters at temperatures outside the range in which they were initially calculated for.

In the combustion models currently in use for the butanol isomers, there exists a large gap in the knowledge of kinetic information for the reaction of OH with each of the butanol isomers, between approximately 400 – 800 K (as highlighted in Figure 3-2 for *n*-butanol). In this chapter, the total rate of reaction for OH with each of the butanol isomers has been measured, reducing the knowledge gap in the literature and providing

modified Arrhenius parameterisations over the temperature regions vital for low temperature combustion.

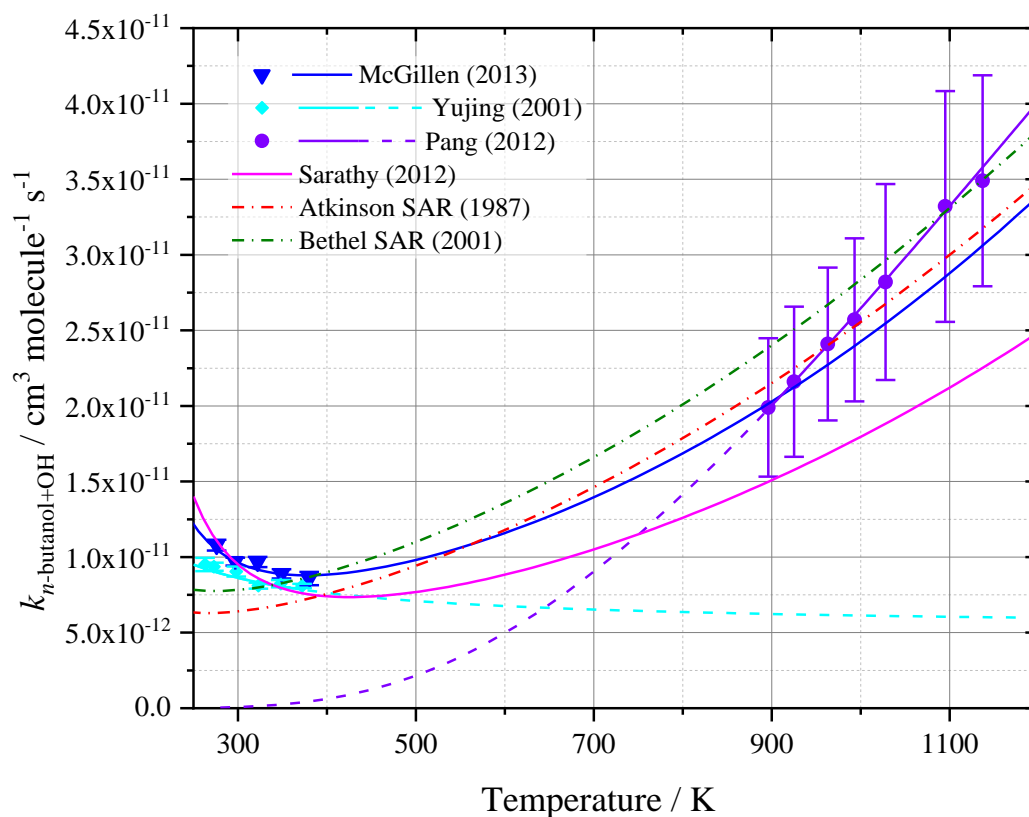
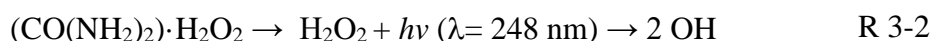


Figure 3-2: Current literature for temperature dependence of the reaction of *n*-butanol with OH, demonstrating gap in the knowledge for experimental data between 400 and 900 K. See Section 3.4.1 for in-depth discussion.

3.3 Experimental

All experiments conducted for this chapter were carried out using the pulsed laser photolysis – laser induced fluorescence set up described in Section 2.7. Alcohol reagents were made up into 10 L glass bulbs, diluted in nitrogen. For temperatures above 480 K, the initial concentration of fuel reagent delivered was increased through utilising the bubbler method of delivery (as described in Section 2.7.1.3). Total pressures were typically maintained at 30 – 130 Torr, with the experimental conditions found in the summary table for each isomer in the subsections of this chapter. OH radicals were generated from pulsed laser photolysis (10 Hz) at 248 nm (KrF Excimer laser) of hydrogen peroxide precursor, with some experiments conducted using urea hydrogen peroxide (UHP) precursor.



OH radicals were either detected using either off-resonant fluorescence or on-resonant fluorescence, depending on the system set up utilised. OH laser induced fluorescence traces were obtained under pseudo first order conditions, such that $[\text{fuel}] \gg [\text{OH}]_0$. For temperatures below approximately 480 K, single exponential decays were obtained, and were analysed as described in Chapter 2. Experiments conducted above 480 K demonstrated biexponential behaviour as a result of OH recycling following the initial abstraction reaction, and these traces were then fit using the biexponential equation (outlined in Chapter 4). For this chapter, only the parameter k_a , for measuring the bimolecular rate coefficient, is of interest. For a further detailed explanation of the other parameters obtained during these experiments, please refer to Chapter 4.

Chemicals used: *n*-butanol (Sigma-Aldrich, $\geq 99.4\%$), *i*-butanol (Sigma-Aldrich, $\geq 99.0\%$), *s*-butanol (Sigma-Aldrich, $\geq 99.5\%$), *t*-butanol (Sigma-Aldrich, $\geq 99.0\%$), hydrogen peroxide/water (H_2O_2 , Sigma-Aldrich, 50 % (w/w) in H_2O), urea hydrogen peroxide ($\text{CO}(\text{NH}_2)_2 \cdot \text{H}_2\text{O}_2$, UHP, Sigma-Aldrich, 97 %). Nitrogen (BOC, 99.99 %) gas was used straight from the cylinder.

3.4 *n*-butanol

The reactions of *n*-butanol are the most studied of the butanol isomers, with numerous studies into the reaction with the hydroxyl radical (OH) at temperatures relevant to atmospheric research, and in combustion condition experimental studies such as rapid compression machines [102, 103] and shock tubes [103]. The production of *n*-butanol *via* the acetone-butanol-ethanol (ABE) fermentation method has been known since the early 1900s, however low yields of alcohol compared to the production of ethanol from yeast fermentation explains why ethanol was selected as the alternative fuel of choice during the early developmental stages of biofuels [12]. Recent developments in bio-butanol synthesis methods [104] [105] and commercial interest [106] has resulted in a rejuvenated interest in these alternate fuels, and an increase in experimental studies.

Room temperature measurements of the reaction of *n*-butanol with OH have been conducted using relative rate methods [80, 107-110], pulse radiolysis-UV spectroscopy [111], and flash photolysis – resonance fluorescence [77]. Two temperature dependent studies at atmospherically relevant temperatures have been conducted previously, by Yujing *et al.* [111] in 2001 across the temperature range 253 – 372 K, and most recently by McGillen *et al.* [78] between 221 – 381 K, both of which utilised pulsed laser photolysis – laser induced fluorescence methods. A high temperature study by Pang *et al.* [73] was conducted using shock tube-combustion modelling, at temperatures of 900 – 1200 K. The temperature dependent parameterisations of these experimental studies and some high-level computational calculations [55, 112, 113] show some disagreement with each other and with previous structure-activity relationship parameterisations, with some parameterisations disagreeing by almost 75 % at 700 K. Consequently, there exists a need for experimental measurement in the intermediate temperatures between the two temperature extremes studied in the region of 400 – 900 K.

n-butanol has 5 different possible hydrogen abstraction sites: 2 secondary alpha sites, 2 secondary beta sites, 2 secondary gamma sites, 3 primary delta sites and the OH site. The full structure of *n*-butanol including all the possible abstraction sites can be seen below in Figure 3-3.

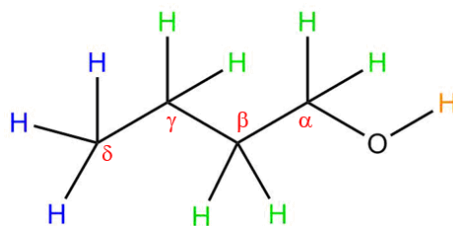


Figure 3-3: Possible abstraction sites from *n*-butanol by OH. Primary abstraction sites in blue, secondary abstraction sites in green, and hydroxyl group abstraction in orange. Carbon positions relative to hydroxyl group labelled in red.

H atom abstraction from *n*-butanol by the OH radical can result in a number of structurally different radicals depending on the position of the abstraction site, each of which can be seen below in Figure 3-4, for reactions R 3-3a – R 3-3e. In this work, the total overall rate coefficient for the reaction between OH and *n*-butanol is measured, which includes all possible H atom abstractions.

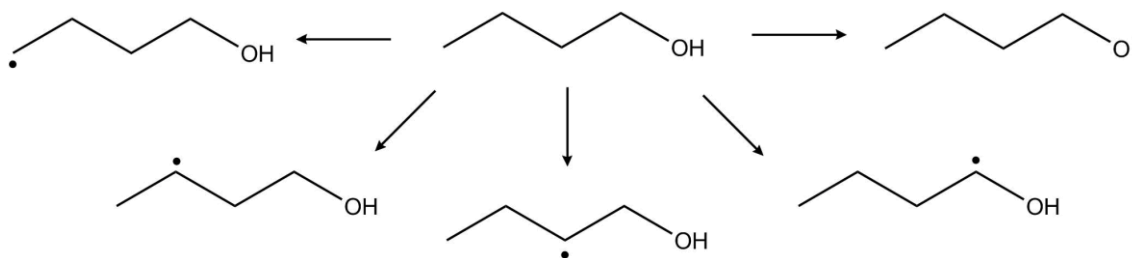
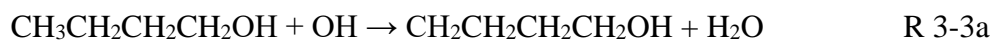


Figure 3-4: Resulting *n*-butyl and *n*-butoxy radicals formed from H atom abstraction by OH at each potential abstraction site.



3.4.1 *n*-butanol + OH: Temperature Dependence

An example kinetic trace obtained in this work at 298 K and 35 Torr for the reaction of OH with *n*-butanol following photolysis of *n*-butanol/N₂/H₂O₂ mixtures can be seen below in Figure 3-5, with an example bimolecular plot obtained in Figure 3-6. The errors reported are as explained previously in Section 2.7.5, where the statistical uncertainty is the error of the goodness of fit of equation E 2-26 to the fluorescence signal obtained in the trace, and is therefore individual to each trace measured. Similarly, the quoted bimolecular error is the statistical uncertainty of the straight line fit to the k' values obtained, to demonstrate precision of experimental measurements.

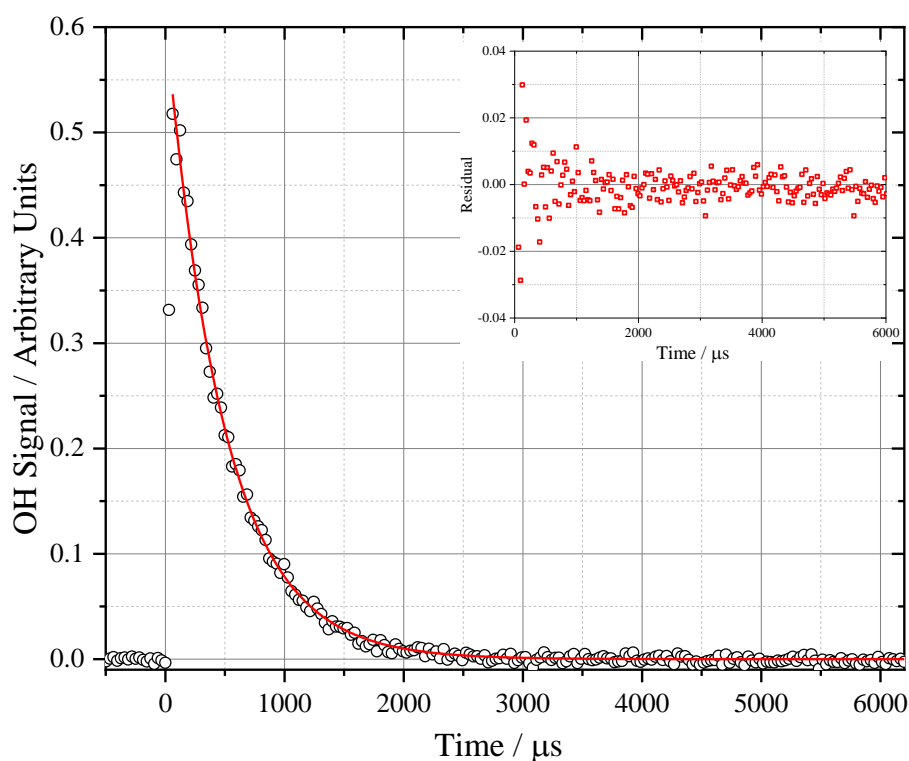


Figure 3-5: Example kinetic trace for *n*-butanol + OH, with single exponential equation (Equation E 2-26) fit, $k' = (2050 \pm 20) \text{ s}^{-1}$, where the error is the statistical uncertainty at a 1σ level. Obtained at 298 K and 35 Torr, $[n\text{-butanol}] = 2.09 \times 10^{14} \text{ molecule cm}^{-3}$.

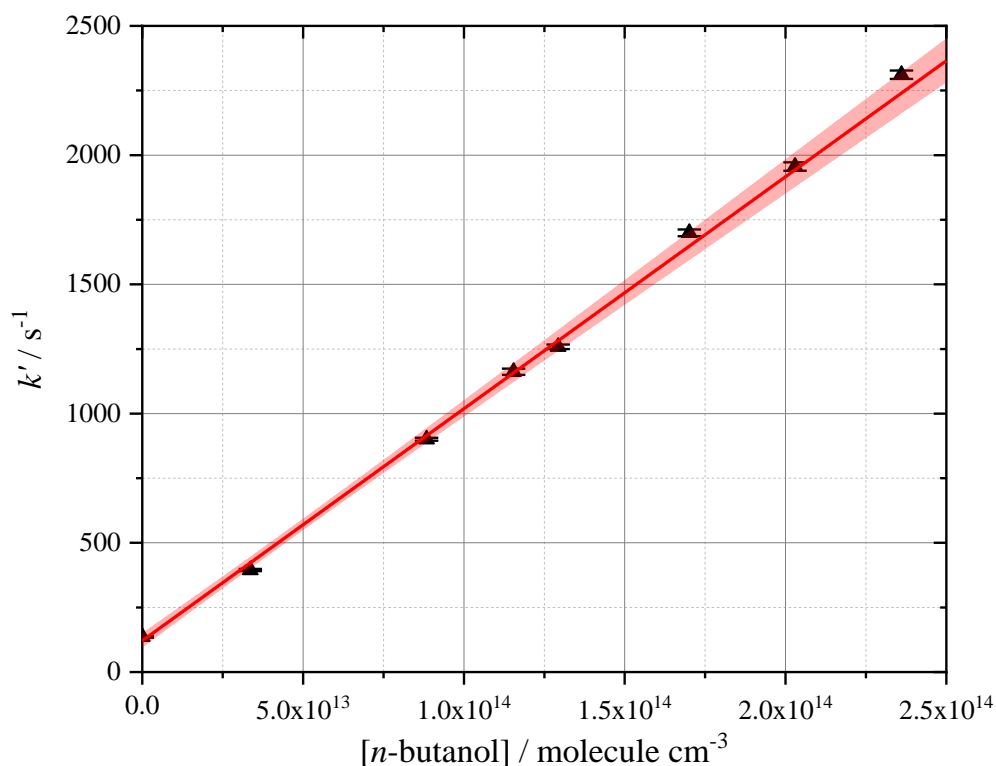


Figure 3-6: Example bimolecular plot for OH + *n*-butanol at 35 Torr and 298 K. Plot of pseudo-first order rate constant k' (s^{-1}) against $[n\text{-butanol}]$ (molecule cm^{-3}). $k_{n\text{-butanol}+\text{OH}} = (8.98 \pm 0.16) \times 10^{-12} \text{ cm}^3 \text{ molecule}^{-1} \text{ s}^{-1}$, where the quoted bimolecular error is the 1σ statistical analysis of the linear fit, with the 95 % confidence limits in red filled area. Experimental points as black filled triangles with 1σ error bars from single trace fitting, with instrumental fit to data points.

Rate coefficients for the reaction of *n*-butanol with OH have been measured across the temperature range 298 – 715 K, at pressures between 23 and 135 Torr. The experimental conditions studied and the bimolecular rate coefficients obtained can be seen in Table 3-1. The majority of experiments conducted utilised the off-resonant fluorescence method and bulb method of delivery for alcohol reagent. Experiments conducted using the bubbler method of delivery (pressures above 40 Torr), utilised on-resonant fluorescence for monitoring of OH radicals.

The relatively low vapour pressure of the *n*-butanol made accurate delivery of the reagent into the bulb difficult, and consequently each time a new bulb of reagent was filled, a bimolecular rate coefficient at 298 K was measured to ensure the accuracy of the bulb concentration. These repeat measurements at 298 K were used to calculate an average room temperature measurement of $k_{n\text{-butanol}+\text{OH}}$, with the standard deviation of

these measurements used to calculate an error percentage to apply to the other temperatures studied using the bulb method of delivery. All measurements recorded using the bulb method of delivery can be seen in Figure 3-7, represented by filled black circles. The bimolecular points represented by filled red triangles in Figure 3-7 utilised the bubbler method for delivery of *n*-butanol into the system. In order to determine the reagent concentration in the cell, the vapour pressure of the *n*-butanol reservoir within the delivery bubbler is estimated based on the temperature of the room (measured via thermocouple prior to each trace being taken), and thus introduces some uncertainty to the delivered concentration. Conducting experiments at 298 K using the bubbler and bulb methods of *n*-butanol delivery successively showed that a correction factor of 26 % was required to correct $k_{n\text{-butanol}+\text{OH}}$ obtained using the bubbler delivery to the value measured experimentally using the bulb of known concentration. Bimolecular rate coefficients obtained using the bubbler delivery method for reagent have a more significant uncertainty, which has been estimated as 10 %. This larger error has been assigned to factor in the errors resulting from uncertainty introduced from calculating the concentration delivered, the accuracy of both the temperature and pressure measurements of the reaction cell, and other experimental factors such as the calibration of the mass flow controllers.

Table 3-1 : Summary of experimental conditions and bimolecular rate coefficients (k) obtained in this work for the n -butanol and OH reaction.

Temperature / K	Pressure / Torr	[n -butanol] / 10^{14} molecule cm^{-3}	k / 10^{-12} cm^3 molecule $^{-1} \text{ s}^{-1}$
298	40	0.7 – 2.1	9.27 ± 0.14^a
298	31	0.8 – 3.0	9.07 ± 0.16^a
298	44	0.8 – 2.0	8.92 ± 0.22^a
298	35	0.4 – 2.4	8.98 ± 0.16^a
298 ‡	70	4.8 – 32.8	$8.85 (7.02) \pm 0.89^c$
298 ‡	130	5.3 – 48.0	$9.22 (7.32) \pm 0.92^c$
367	23	0.3 – 2.2	9.13 ± 0.42^b
370	39	0.1 – 2.4	9.17 ± 0.42^b
409	40	0.1 – 1.7	8.82 ± 0.51^b
410	23	0.1 – 2.5	9.21 ± 0.43^b
449	40	0.3 – 1.7	9.51 ± 0.44^b
450	33	0.3 – 1.5	8.84 ± 0.41^b
490	41	0.2 – 1.4	10.2 ± 0.54^b
494	35	0.8 – 1.5	9.50 ± 0.44^b
535	35	0.5 – 1.5	10.1 ± 0.46^b
535	35	0.2 – 1.5	9.85 ± 0.45^b
547	35	0.7 – 1.3	10.9 ± 0.50^b
555 ‡	134	2.9 – 29.0	$12.0 (9.49) \pm 1.20^c$
564	35	0.6 – 1.2	11.0 ± 0.51^b
576	35	0.8 – 1.4	10.9 ± 0.50^b
580 ‡	130	19.0 – 31.1	$13.5 (10.7) \pm 1.35^c$
599 ‡	132	2.3 – 14.0	$12.6 (10.0) \pm 1.26^c$
600	35	0.96 – 1.40	12.0 ± 0.72^b
650 ‡	131	10.0 – 15.0	$13.2 (10.4) \pm 1.32^c$
670 ‡	134	8.5 – 18.0	$14.8 (11.7) \pm 1.48^c$
693 ‡	135	10.0 – 20.0	$15.0 (11.9) \pm 1.50^c$
715 ‡	135	12.3 – 17.0	$14.4 (11.5) \pm 1.44^c$

‡ Reagent introduced from bubbler. Value obtained before 26 % correction shown in parentheses. ^a Standard 1σ error from origin fitting. ^b ± 6 % error calculated based on standard deviations of room temperature measurements. ^c ± 10 % error assumed for rate coefficients measured using bubbler delivery method.

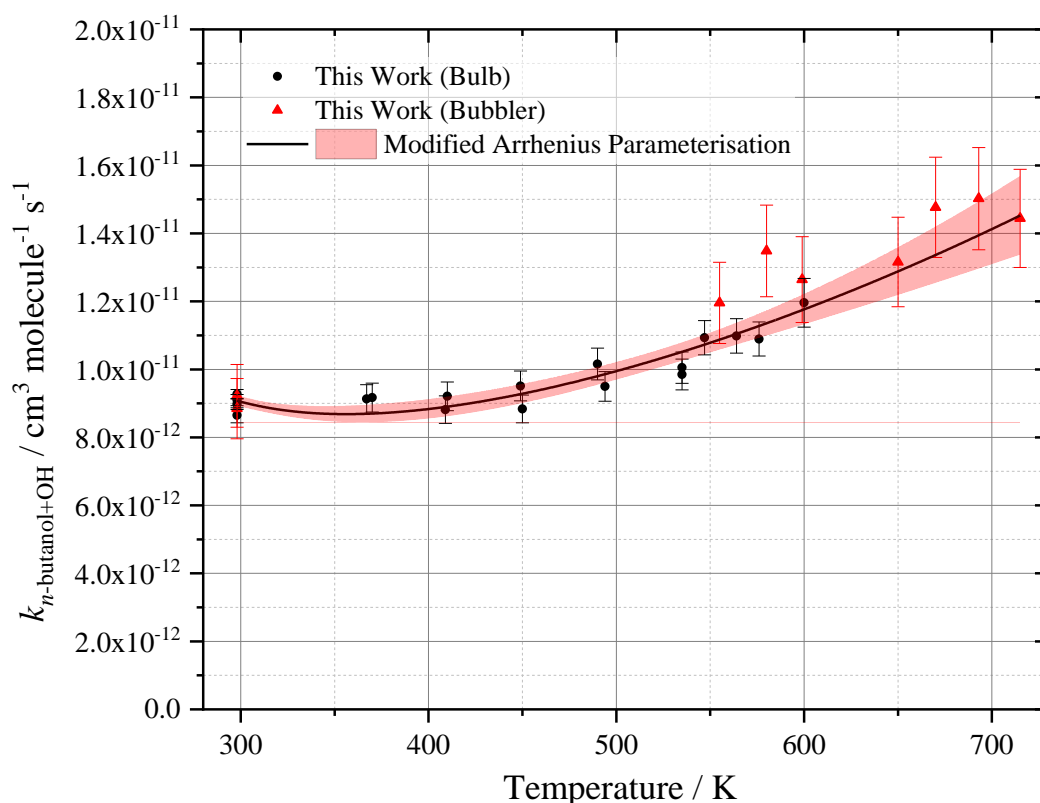


Figure 3-7: All experimentally obtained $k_{n\text{-butanol}+\text{OH}}$ rate coefficients in this work, with Arrhenius parameterisation and 95 % confidence limits (red shaded region). Filled black circles represent experimental measurements conducted using the bulb method for reagent delivery, and filled red triangles are those utilising the bubbler method. See Table 3-1 for error justification.

The total bimolecular rate coefficients measured for the reaction between *n*-butanol and the OH radical, plotted in Figure 3-7, generally display a positive temperature dependence above 350 K, with some slight negative temperature dependence seen between 300 – 350 K. This negative temperature dependence is common amongst the reactions of OH with oxygenated species, and has been observed experimentally by McGillen *et al.* [78] and Yujing and Mellouki [111]. Further discussion of this phenomenon is provided in the isomer comparison section of this chapter, Section 3.8.

The modified Arrhenius fit to the experimentally obtained data can be described as $k_{n\text{-butanol}+\text{OH}}(298 - 715 \text{ K}) = (1.15 \pm 2.62) \times 10^{-19} \times T^{2.64 \pm 0.31} \times \exp\left(\frac{7800 \pm 1100}{R \times T}\right) \text{ cm}^3 \text{ molecule}^{-1} \text{ s}^{-1}$, with an overall error in the parameterisation of 8 % across the temperatures studied in this work. The reported Arrhenius parameterisation error represents the standard 1σ error from the least squares fitting to the data, and the

percentage error represents the widest part of the 95 % confidence limit bands. All previous literature values obtained at 298 K can be seen summarised below in Table 3-2, the values for which are represented graphically in Figure 3-8 alongside temperature dependent parameterisations obtained from the literature.

The average rate coefficient obtained at 298 K was $k_{n\text{-butanol}+\text{OH}} = (9.00 \pm 0.52) \times 10^{-12} \text{ cm}^3 \text{ molecule}^{-1} \text{ s}^{-1}$, with the error reported at the 1σ level, in good agreement within experimental error with previous literature obtained. In the most recent study by McGillen *et al.* [78], the reported 298 K bimolecular rate coefficient measured was around 14% faster than the other previous LFP–LIF study by Yujing *et al.* [111] with no overlap within experimental error, and 16 % higher than the flash photolysis-resonance fluorescence study by Wallington [77], with the reported errors overlapping by $0.01 \times 10^{-12} \text{ cm}^3 \text{ molecule}^{-1} \text{ s}^{-1}$. In the work by McGillen *et al.*, it was noted that pseudo first order rate constants for the reaction of *n*-butanol and OH obtained during isotope experiments conducted with ^{18}OH were faster than that of those measured in the ^{16}OH experiments. This was attributed to a previously unmeasured rapid OH regeneration channel, leading to bimolecular rate coefficients in the literature that are consequently too slow. This work however agrees with the McGillen study within experimental error, suggesting that this bias towards slower bimolecular rate coefficients is not observed in this work.

Table 3-2: Measured $k_{n\text{-butanol}+\text{OH}}$ (298 K) for this work with all previous literature values.

Reference	k^a (298 K) / \times 10^{-12} cm^3 $\text{molecule}^{-1} \text{ s}^{-1}$	Temperature / K	Pressure / Torr	Method
Wallington <i>et al.</i> (1987) [77]	8.31 ± 0.63^b	296	25–50	FP–RF
Nelson <i>et al.</i> (1990) [80]	7.8 ± 1.8	298	760	PR–UV
Nelson <i>et al.</i> (1990) [80]	8.56 ± 2.14 <i>(8.0 \pm 2.6)</i>	298	760	RR
Yujing <i>et al.</i> (2001) [111]	8.47 ± 0.34	253–372	30–300	LFP–LIF
Oh <i>et al.</i> (2001) [109]	9.3 ± 0.4	298	760	RR ^e
Oh <i>et al.</i> (2001) [109]	9.1 ± 0.3 <i>(8.80)</i>	298	760	RR ^f
Cavalli <i>et al.</i> (2002) [110]	8.28 ± 0.85 <i>(7.71 \pm 0.85)</i>	298	740	RR
Wu <i>et al.</i> (2003) [108]	8.66 ± 0.66^c <i>(8.82 \pm 0.66)</i>	295	760	RR
Hurley <i>et al.</i> (2009) [107]	8.86 ± 0.85^b	296	700	RR
Pang <i>et al.</i> (2012) [73]	0.0072 ^{*,d}	900–1200	~760	ST
McGillen <i>et al.</i> (2013)[78]	9.68 ± 0.75	221–381	51–216	LFP–LIF
Sarathy (2012) [55]	9.61	200 – 1800	n/a	ST–CM
Atkinson (1987) [114]	6.39	n/a	n/a	SAR
Bethel (2001) [101]	7.82	n/a	n/a	SAR
This work	9.00 ± 0.52	298 – 715	23 – 135	LFP–LIF

^a Errors quoted to 2σ level, experiments conducted at 298 K unless stated otherwise. ^b measured at 296 K. ^c measured at 295 K. ^d Extrapolated from Arrhenius parameterisation obtained at from high temperature experiments. Methods: LFP–LIF: Laser flash photolysis–laser induced fluorescence. RR: Relative rate. PR–UV: Pulse radiolysis–UV spectroscopy. FP–RF: Flash photolysis–resonance fluorescence. ST: Shock tube. ST–CM: Shock tube-combustion modelling. SAR: Structure-activity relationship. Updated values for relative rates shown in italics. ^e Using p-xylene as a reference compound. ^f Using cyclohexane as a reference compound.

In the study of Nelson *et al.* [80], studies were conducted using both pulse radiolysis–UV spectroscopy (PR-UV) and the relative rate (RR) method. The rate constants and errors reported ($7.8 \pm 0.2 \times 10^{-12} \text{ cm}^3 \text{ molecule}^{-1} \text{ s}^{-1}$ for PR-UV and $8.56 \pm 0.70 \times 10^{-12} \text{ cm}^3 \text{ molecule}^{-1} \text{ s}^{-1}$ for RR) include solely the statistical errors from data fitting. However, for the PR-UV method, a more significant overall error of 20 % was recommended, giving an increased error value of $(7.8 \pm \mathbf{1.8}) \times 10^{-12} \text{ cm}^3 \text{ molecule}^{-1} \text{ s}^{-1}$ which would result in better agreement with this study and all other previous literature. For the relative rate study, the authors suggested an additional error of 25%, when the error for the reference rate coefficient is factored in, giving an updated error of $(8.56 \pm 2.84) \times 10^{-12} \text{ cm}^3 \text{ molecule}^{-1} \text{ s}^{-1}$. Cyclohexane was used as the reference compound for the relative rate study, with a reference rate coefficient of $7.49 \times 10^{-12} \text{ cm}^3 \text{ molecule}^{-1} \text{ s}^{-1}$. Updating this rate coefficient to $6.97 \times 10^{-12} \text{ cm}^3 \text{ molecule}^{-1} \text{ s}^{-1}$, the most recent recommendation by Atkinson in 2003 [87], the rate coefficient for the reaction of *n*-butanol with OH decreases to $(8.0 \pm 2.6) \times 10^{-12} \text{ cm}^3 \text{ molecule}^{-1} \text{ s}^{-1}$. This is overall in better agreement with their PR-UV study rate coefficient, but in worse overall agreement with this work and other previous literature.

Oh *et al.* [109] conducted relative rate studies using two different reference compounds, *p*-xylene (1,4-dimethylbenzene, the rate coefficient for which was measured during the study, $1.29 \times 10^{-11} \text{ cm}^3 \text{ molecule}^{-1} \text{ s}^{-1}$) and cyclohexane ($7.21 \times 10^{-12} \text{ cm}^3 \text{ molecule}^{-1} \text{ s}^{-1}$, from the Atkinson recommended value). The updated recommended rate coefficient by Atkinson (2003, [87]) for the reaction of cyclohexane with OH is $6.97 \times 10^{-12} \text{ cm}^3 \text{ molecule}^{-1} \text{ s}^{-1}$. This results in a decrease in the rate coefficient for the reaction of *n*-butanol with OH ($8.80 \pm 0.3 \times 10^{-12} \text{ cm}^3 \text{ molecule}^{-1} \text{ s}^{-1}$) in equally good agreement with the value obtained in this work. There is no recommended update value for the reaction of OH with *p*-xylene. The original value however is in reasonable agreement with this work.

Cavalli *et al.* [110] also conducted a relative rate study, using the photolysis of methyl nitrite in a chamber with black lamps to generate the OH precursor. A cyclohexane reference compound was used, with a reference rate coefficient of $7.49 \times 10^{-12} \text{ cm}^3 \text{ molecule}^{-1} \text{ s}^{-1}$. As mentioned previously, the recommended rate coefficient for this reaction has been updated by Atkinson in 2003, to $6.97 \times 10^{-12} \text{ cm}^3 \text{ molecule}^{-1} \text{ s}^{-1}$. Updating to the recommended rate coefficient results in an updated value of $k_{n\text{-butanol}+\text{OH}}$ of $(7.71 \pm 0.85) \times 10^{-12} \text{ cm}^3 \text{ molecule}^{-1} \text{ s}^{-1}$, in greater disagreement with this work.

Wu *et al.* [108] utilised 254 nm photolysis of hydrogen peroxide precursor in a chamber relative rate study, using propane as the reference compound, and a reference rate coefficient of $k = 1.08 \times 10^{-12} \text{ cm}^3 \text{ molecule}^{-1} \text{ s}^{-1}$. The updated value for this reference rate coefficient from Atkinson (2003) is $k = 1.10 \times 10^{-12} \text{ cm}^3 \text{ molecule}^{-1} \text{ s}^{-1}$, giving a rate coefficient for the reaction of *n*-butanol with OH of $k = (8.82 \pm 0.66) \times 10^{-12} \text{ cm}^3 \text{ molecule}^{-1} \text{ s}^{-1}$, in better agreement with previous literature and the value obtained in this work.

Hurley *et al.* [107] conducted the most recent relative rate study into the reaction of *n*-butanol with OH at 298 K. Two relative rate experiments were conducted, relative to acetylene (with a reference compound rate coefficient of $8.45 \times 10^{-13} \text{ cm}^3 \text{ molecule}^{-1} \text{ s}^{-1}$) and ethene ($8.52 \times 10^{-12} \text{ cm}^3 \text{ molecule}^{-1} \text{ s}^{-1}$), yielding almost identical values for the reaction of *n*-butanol with OH. There are no updates to the recommended rate coefficients for these reference compounds, however excellent agreement is already obtained between this work and the values obtained by Hurley *et al.*

An extrapolation of the temperature dependent parameterisation of Pang *et al.* [73], although not recommended by the authors, back to 298 K results in a rate coefficient for the reaction of *n*-butanol with OH that is over three orders of magnitude slower than obtained in this work and all previous literature. This demonstrates that the parameterisation obtained in their work does not correctly capture the curvature of the temperature dependence of the reaction, and cannot be reliably extrapolated outside the region of their work.

The original structure activity relationship of Atkinson [114] estimates a room temperature rate coefficient for the reaction of *n*-butanol with OH around 40 % slower than was measured experimentally in this work. The updated SAR of Bethel [101] estimates a total bimolecular rate coefficient of $7.82 \times 10^{-12} \text{ cm}^3 \text{ molecule}^{-1} \text{ s}^{-1}$, which is in better agreement with this work and other literature, but is still outside of the error margins of this work.

In the previous temperature dependent study by McGillen *et al.* [78], modified Arrhenius parameters were determined from experimental results obtained in the temperature range 250–380 K and high temperature data obtained by Pang *et al.* [73], alongside structure activity relationship parameterisations. The study conducted by Sarathy *et al.* [55] also provided a modified Arrhenius parameterisation, determined from experimental shock tube data and combustion modelling validation of output parameters such as ignition delay time. Two theoretical studies have been conducted by Zhou *et al.*

[112], using the G3 and CCSD methods, calculated over the temperature range 500 – 2000 K. These parameterisations can be seen compared to the experimental results obtained in this work in Figure 3-8 and Table 3-3, alongside the temperature dependent study of Yujing *et al.* [111], the structure activity relationships of Atkinson [114] and Bethel *et al.* [101], and the high temperature data and Arrhenius parameterisation obtained by Pang *et al.*

Table 3-3: Arrhenius parameterisation for the OH + *n*-butanol reaction from previous literature and this study.

Ref.	T / K	Site	$k(T) = A T^n \exp(-E/RT) F_x(T)$			
			A / cm ³ molecule ⁻¹ s ⁻¹	<i>n</i>	E/R / K	F _x (T)
McGillen <i>et al.</i> [78]	200 – 2000	α	6.38×10^{-18}	1.93	-792	
		β	3.31×10^{-25}	4.11	-1858	
		γ	2.43×10^{-20}	2.67	-797	
		δ	4.49×10^{-18}	2	258	
		OH	2.10×10^{-18}	2	23	
Pang <i>et al.</i> [73]	896 – 1197	Total	3.24×10^{-10}	–	2505	
Yujing <i>et al.</i> [111]	253–372	Total	$(5.3 \pm 1.62) \times 10^{-12}$	–	$-(146 \pm 92)$	
Sarathy <i>et al.</i> [55]	200 – 1800	α	6.00×10^{-21}	2.89	-1154	
		β	2.56×10^{-24}	3.7	-1881	
		γ	1.89×10^{-21}	2.87	-1473	
		δ	8.77×10^{-15}	0.97	799	
		OH	9.76×10^{-22}	2.82	-295	
Atkinson [114]	SAR	α	4.32×10^{-18}	2	-233	exp(76/T) exp(365/T)
		β	4.32×10^{-18}	2	-233	exp(76/T) exp(76/T)
		γ	4.32×10^{-18}	2	-233	exp(76/T)
		δ	4.47×10^{-18}	2	303	exp(76/T)
		OH	1.89×10^{-18}	2	460	exp(76/T)

Table 3-3 cont.

Ref.	T / K	Site	$k(T) = A T^n \exp(-E/RT) F_x(T)$			
			A / cm ³ molecule ⁻¹ s ⁻¹	n	E/R / K	F _x (T)
Bethel <i>et al.</i> [101]	SAR	α	4.50×10^{-18}	2	- 253	exp(62/T) exp(317/T)
		β	4.50×10^{-18}	2	- 253	exp(62/T) exp(285/T)
		γ	4.50×10^{-18}	2	- 253	exp(62/T)
		δ	4.49×10^{-18}	2	320	exp(62/T)
		OH	2.10×10^{-18}	2	85	exp(62/T)
Zhou <i>et al.</i> [112]	500 – 2000 (G3)	Total	6.69×10^{-23}	3.57	- 2128	
	500 – 2000 (CCSD)	Total	2.89×10^{-23}	3.69	- 1703	
This Work	298 – 715	Total^a	$(1.15 \pm 2.62) \times 10^{-19}$	2.64 ± 0.31	- 940 ± 140	
		Total^b	$(3.49 \pm 4.61) \times 10^{-20}$	2.81 ± 0.18	- 1010 ± 80	

^a Not constrained and ^b Constrained to high temperature data from Pang *et al.*

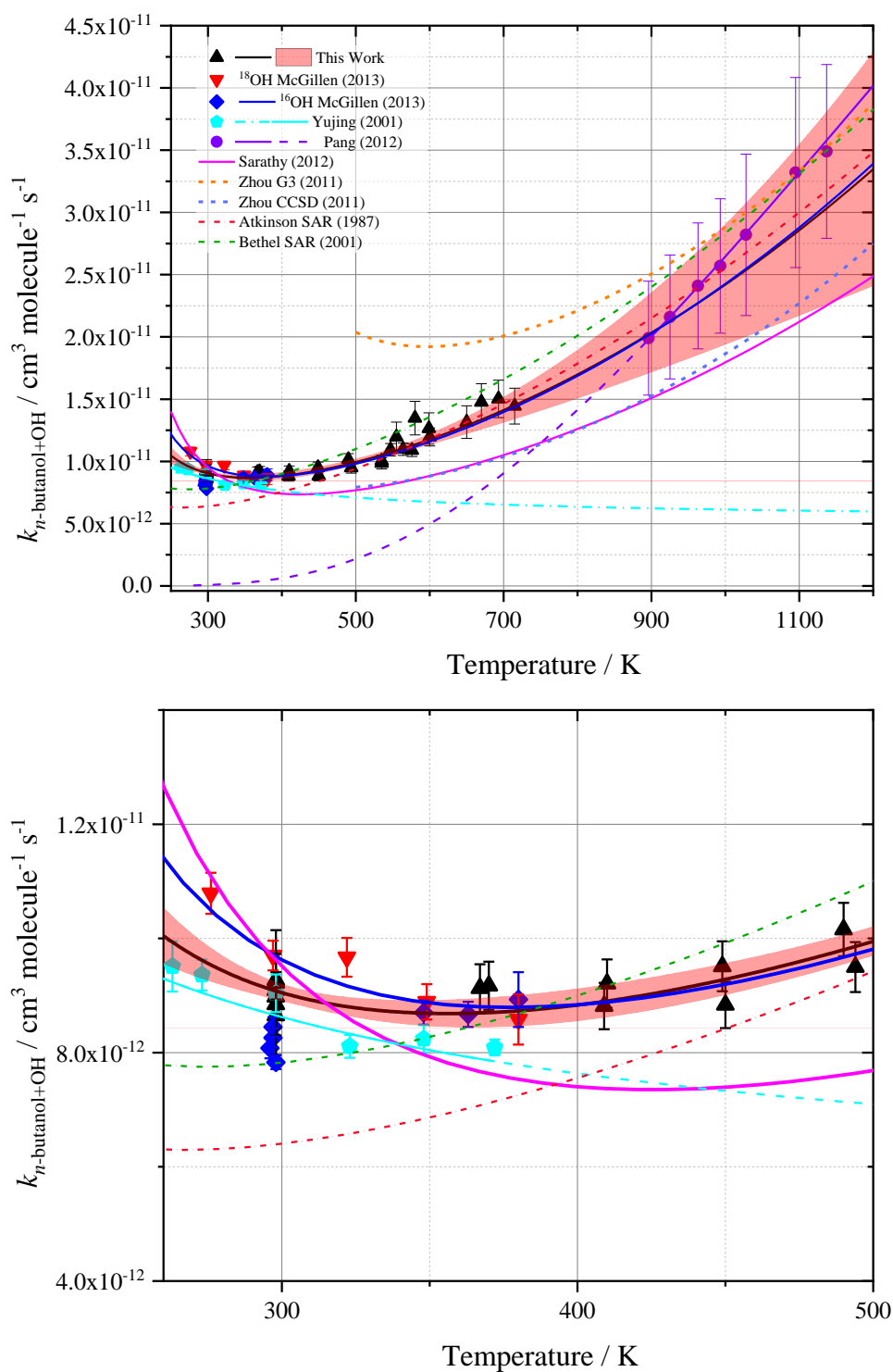


Figure 3-8: Rate coefficient data for the n -butanol + OH reaction: This work (black triangles, black solid line, 95 % confidence limits in red shaded region). Compared with Pang *et al.* (purple circles, purple solid line and dashed line for extrapolated region), McGillen *et al.* (red inverted triangles and blue diamonds, blue solid line), Yujing *et al.* (light blue pentagons, light blue solid line and dashed line for extrapolated region) experimental data; Sarathy *et al.* (solid pink line), Zhou *et al.* G3 (orange dotted line) and CCSD (lilac dashed line) calculations; SAR of Atkinson (Red dot-dash line) and Bethel *et al.* (green dot-dash line). Data replicated from [78], [111], [73], [55], [112], [114], and [101].

As evident in Figure 3-8, the Arrhenius parameterisation in this work agrees excellently with the total calculated bimolecular rate coefficient from the McGillen *et al.* [78] parameterisation, overlapping almost entirely. The total bimolecular rate coefficient parameterisation by McGillen *et al.* was obtained by conducting a smooth interpolation of the experimental data from their study with the high temperature data from Pang *et al.* [73]. Site-specific reactivity was estimated from end product branching ratios from other work, and the SAR of Bethel *et al.* [101] at temperatures above 1200 K. At temperatures above 1000 K, the parameterisation of this work agrees well (within less than 15 %) with the high temperature experimental data of Pang *et al.* When the modified Arrhenius parameterisation obtained in this work is extrapolated to temperatures nearing 1200 K, the overall uncertainty calculated by the 95 % confidence limits is approximately 28 %. The extrapolation of the Pang *et al.* parameterisation to temperatures approaching ambient temperature underestimates the total bimolecular rate coefficient by 3 orders of magnitude, as discussed previously. The Sarathy *et al.* [55] parameterisation underestimates the total bimolecular rate coefficient across all temperatures below 300 K, and over estimates the negative temperature dependence seen below 300 K.

The modified Arrhenius parameterisation for the data obtained in this work has also been fit and constrained to the high temperature data by Pang *et al.* by including their data in the parameterisation, shown in Figure 3-9. A modified Arrhenius parameterisation of $k_{n\text{-butanol}+\text{OH}}$ (298 – 1200 K) = $(3.49 \pm 4.61) \times 10^{-20} \times T^{2.81 \pm 0.18} \times \exp\left(\frac{8370 \pm 670}{R \times T}\right) \text{ cm}^3 \text{ molecule}^{-1} \text{ s}^{-1}$ was obtained for this concatenate fit, with an error of 5 % at the 95 % confidence limit level across the temperature range studied in this work (298 – 715 K) and an overall error of 16 % across the full temperature range. The reported Arrhenius parameterisation error represents the standard 1σ error from the least squares fitting to the data, and the percentage error represents the widest part of the 95 % confidence limit bands. This provides an equally good fit to the experimental measurements of the bimolecular rate coefficient obtained in this study, and reduces the size of the 95 % confidence limits and the overall error at the highest temperatures by 12 %.

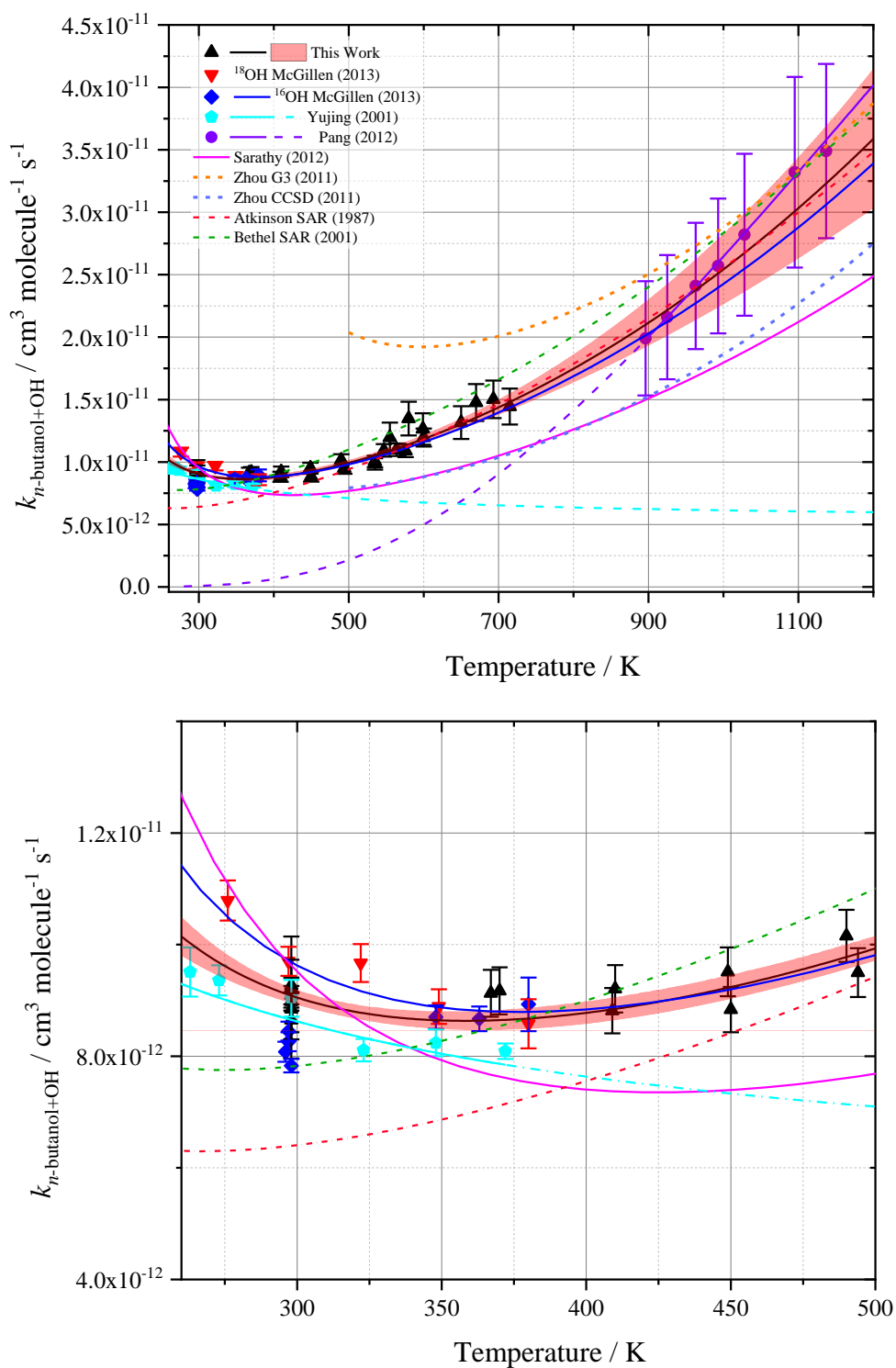


Figure 3-9: Concatenate fit to rate coefficient data for the *n*-butanol + OH reaction: This work (black triangles, black solid line, 95 % confidence limits in red shaded region), with Arrhenius parameterisation constrained to high temperature data of Pang *et al.* (purple circles, purple solid line and dashed line for extrapolated region). Compared to McGillen *et al.* (red inverted triangles and blue diamonds, blue solid line), Yujing *et al.* (light blue pentagons, light blue solid line and dashed line for extrapolated region) experimental data; Sarathy *et al.* (solid pink line), Zhou *et al.* G3 (orange dotted line) and CCSD (lilac dashed line) calculations; SAR of Atkinson (Red dot-dash line) and Bethel *et al.* (green dot-dash line). Data replicated from [78], [111], [73], [55], [112], [114], and [101].

As mentioned previously, the computational calculations conducted demonstrate some disagreement with the temperature dependent parameterisations of the experimental studies, and with the SAR parameterisations. The CCSD calculation by Zhou *et al.* [112] shows a better overall agreement with the low temperature experimental data obtained in this work than that of the G3 calculation, but is consistently lower at all temperatures than the experimental measurements of this work and the study by Pang *et al.* [73]. A better agreement is obtained at high (1000 K) temperatures between the G3 calculation of Zhou *et al.* and the high temperature experimental data of Pang *et al.*, however this could be a result of aspects of the Zhou *et al.* calculation being used in the fitting of the experimental data of Pang *et al.* The temperature dependent branching ratios calculated by Zhou *et al.* were used to obtain site specific rate constants for each site of *n*-butanol with OH.

In the analysis by Pang *et al.*, it was assumed that the net consumption of OH through the beta abstraction channel was near zero, due to the rapid β -scission to reproduce an OH radical. As the calculated branching ratios by Zhou *et al.* estimated the β -channel branching ratio to be 6 % at 925 K, it was assumed that this channel would not significantly contribute to the total measured bimolecular rate coefficient. Significant assumptions were also made as to the rate and pressure dependence of the decomposition of the β -hydroxybutyl radical, based on the reverse of the addition reaction of OH to propene estimated by Curran *et al.* [115]. A sensitivity analysis conducted to examine the effect of changing the initial β -site abstraction branching ratio (by up to 30 %) and the rate of decomposition of the subsequent radical (by a factor of 2), found an overall contribution of 4% to the uncertainty at 925 K, and 6 % at 1197 K. A significant contribution to the uncertainty was also calculated from altering the branching ratio of abstraction at the δ abstraction site, with a 12 % at 927 K and 14 % at 1197 K. These contributions to the overall calculated uncertainty of 20 – 23 % across all temperatures could alter the temperature dependence of the bimolecular rate coefficient, bringing it more in line with the predicted temperature dependence by this work. A comparison of the overall reactivity of *n*-butanol with the hydroxyl radical as a function of temperature can be found in Section 3.8, compared to the other structural isomers of butanol.

3.4.2 Conclusion

The bimolecular rate coefficient for the reaction of *n*-butanol with OH has been measured across the temperature range 298 – 715 K at pressures between 23 and 135 Torr.

The average room temperature rate coefficient, $k_{n\text{-butanol}+\text{OH}} = (9.00 \pm 0.52) \times 10^{-12} \text{ cm}^3 \text{ molecule}^{-1} \text{ s}^{-1}$, with the error reported at the 1σ level, was measured in good agreement within experimental error with most previous literature obtained. This work provided confirmation for the previous temperature dependent experimental measurements of McGillen *et al.* [78] up to 400 K, and extended the temperature range studied to 715 K, reducing the gap in the literature for this reaction. This work has also presented a modified Arrhenius parameterisation for the total reaction of *n*-butanol with the hydroxyl radical, and assists in reducing the uncertainties of the total rate of reaction at temperatures relevant to low temperature combustion.

3.5 *i*-butanol

Existing ethanol production plants can be retrofitted in order to become bio-*iso*-butanol fermentation plants relatively easily, through modification of the separation process and fermentation catalyst, and consequently *i*-butanol is of interest as an alternative biofuel [116]. A significant amount of research into the effects of blending *i*-butanol with gasoline for spark ignition engines [117] or with diesel for compression ignition engines [97] has been conducted to compliment the research into the production methods, as well as rapid compression machine [47] and jet-stirred reactor studies [118].

As mentioned previously, for *i*-butanol to be adopted as an alternative fuel, the combustion kinetics of its reactions must be well understood, in particular the initiation reaction of *i*-butanol with the OH radical. Most research conducted into the reaction of *iso*-butanol with OH has been conducted at ambient temperature, and utilised the relative rate method [84, 108, 119]. Two temperature dependent studies have been conducted over narrow temperature ranges; Mellouki *et al.* between 241 – 373 K, and McGillen *et al.* between 224 – 381 K, both utilising the pulsed laser photolysis-laser induced fluorescence methods. A high temperature shock tube study has also been conducted by Pang *et al.* [75] over the temperature range 907 – 1147 K. As with the other isomers of butanol, this leads to a significant gap in the knowledge for the kinetics of this reaction at temperatures relevant to low temperature combustion between these two temperature extremes. This work has measured a rate constant for the reaction of *i*-butanol with OH at 298 K, and as a function of temperature, extending the temperature range from the previous high of 381 K to 620 K.

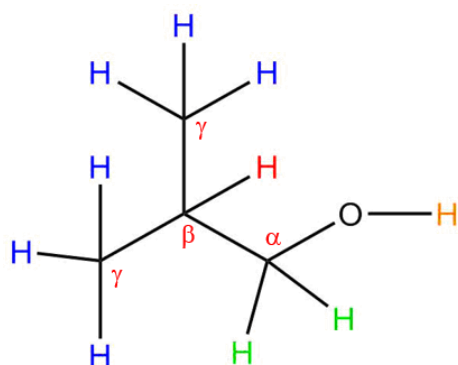


Figure 3-10: Possible abstraction sites from *i*-butanol by OH. Primary abstraction sites in blue, secondary abstraction sites in green, tertiary abstraction sites in red and hydroxyl group abstraction in orange. Carbon positions relative to hydroxyl group labelled in red.

The possible abstraction sites from *i*-butanol can be seen above in Figure 3-10, with the resulting R radicals for each hydrogen abstraction outlined in Figure 3-11. *i*-butanol has 4 distinct reaction sites: 2 secondary alpha sites, 1 tertiary beta site, 6 primary gamma sites on 2 equivalent methyl groups, and the OH site. This work measures the total abstraction rate for all of these potential abstraction sites, R 3-4a – R 3-4d.

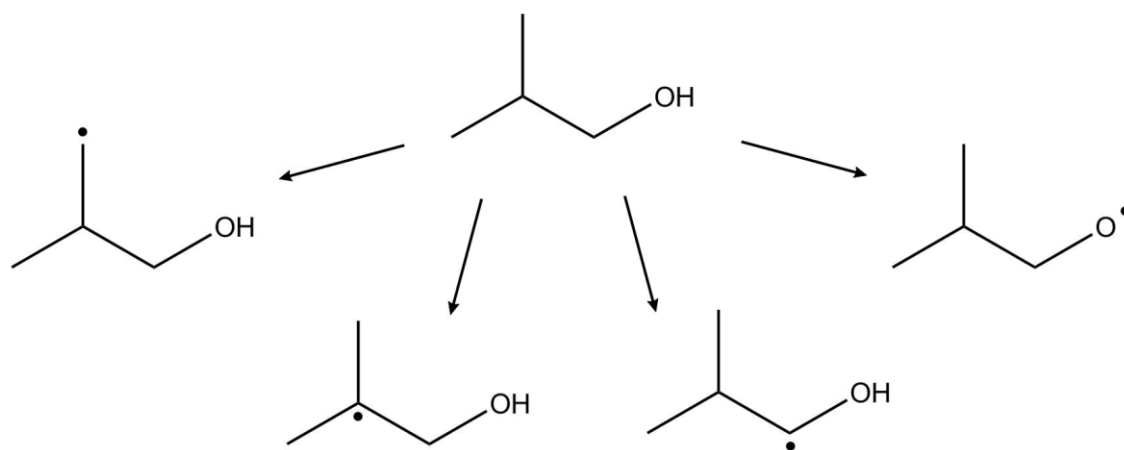


Figure 3-11: Resulting *i*-butyl and *i*-butoxy radicals formed from H atom abstraction by OH at each potential abstraction site.





3.5.1 *i*-butanol + OH: Temperature Dependence

Rate coefficients for the reaction of *i*-butanol (R 3-4) with OH have been measured across the temperature range 298 – 621 K, at pressures between 30 and 82 Torr. The experimental conditions studied and the bimolecular rate coefficients obtained can be seen summarised in Table 3-4, and presented graphically in Figure 3-12. All bimolecular rate coefficients for the reaction of *i*-butanol with the hydroxyl radical were measured utilising the off-resonant fluorescence experimental set up described in Section 2.7, and used hydrogen peroxide as an OH precursor.

A series of repeat measurements conducted at 298 K was used to calculate the standard deviation for the reaction at room temperature in a similar manner to that of *n*-butanol (Section 3.4.1), and this was then applied as a percentage error of 6 % to all other experimental results obtained using the bulb method of delivery. Where the statistical error reported from the linear fit to the bimolecular was bigger, this was chosen, to ensure that the errors for lesser quality data were not underestimated. As explained in Section 2.7.1.3, some bimolecular rate constants were obtained using the bubbler delivery method for the alcohol reagent. For *i*-butanol however, an improvement to the experimental set-up allowed a thermostatted bubbler to be used, in which the temperature was maintained using a Dewar of water surrounding the pressurised glass bubbler. This provided a more accurate and stable temperature reading for calculating the vapour pressure of the reagent from the Antoine parameters. An experimental measurement of the bimolecular rate coefficient for *i*-butanol with OH using the thermostatted bubbler at 509 K was conducted and was found to fit well with previous experimental measurements conducted using the bulb method of delivery. It was therefore assumed that the thermostatted bubbler provided a more accurate method for calculating the amount of reagent delivered to the cell, and these results were consequently not subject to a correction factor. An estimated error of 10 % was applied to all bubbler measurements to account for the increased uncertainty in the amount of reagent delivered, owing to the indirect nature of calculating the concentration and the other errors described previously for *n*-butanol (Section 3.4.1). Measurements conducted using the bubbler method of

delivery are highlighted in Table 3-4, and are represented by hollow red circles on Figure 3-12.

Table 3-4: Summary of experimental conditions and bimolecular rate coefficients (k) obtained for the reaction of *i*-butanol and OH.

Temperature / K	Pressure / Torr	[<i>i</i> -butanol] / 10^{14} molecule cm^{-3}	$k / 10^{-12} \text{ cm}^3$ molecule $^{-1} \text{ s}^{-1}$
298	30	0.4 – 3.0	8.74 ± 0.14^a
298	30	0.3 – 2.0	9.06 ± 0.18^a
298	30	0.8 – 5.4	9.21 ± 0.20^a
298	30	0.4 – 2.9	8.76 ± 0.28^a
298	30	0.6 – 2.8	9.25 ± 0.64^a
364	30	0.7 – 5.1	7.77 ± 0.42^b
368	30	0.3 – 2.2	8.70 ± 0.47^b
368	30	0.3 – 2.3	8.66 ± 0.47^b
410	30	0.3 – 2.0	9.78 ± 0.53^b
420	30	0.6 – 4.6	8.27 ± 0.45^b
450	30	0.3 – 2.0	8.46 ± 0.46^b
450	30	0.3 – 1.7	9.22 ± 0.50^b
490	30	0.2 – 1.8	9.10 ± 0.49^b
509 [#]	81	9.0 – 16.0	9.32 ± 0.93^c
530	30	0.3 – 1.5	9.24 ± 0.50^b
540 [#]	81	9.1 – 21	9.68 ± 0.97^c
551 [#]	82	14 – 24	9.71 ± 0.97^c
564 [#]	81	9.0 – 26.0	10.1 ± 1.01^c
587 [#]	81	8.6 – 19.6	10.5 ± 1.05^c
595 [#]	82	10.2 – 30.0	10.5 ± 1.05^c
607 [#]	82	15.0 – 24.5	11.0 ± 1.10^c

[#] Reagent introduced from thermostatted bubbler.

^a Standard 1σ error from Origin fitting.

^b $\pm 6\%$ error calculated based on standard deviations of room temperature measurements.

^c $\pm 10\%$ error assumed for rate coefficients measured using bubbler delivery method.

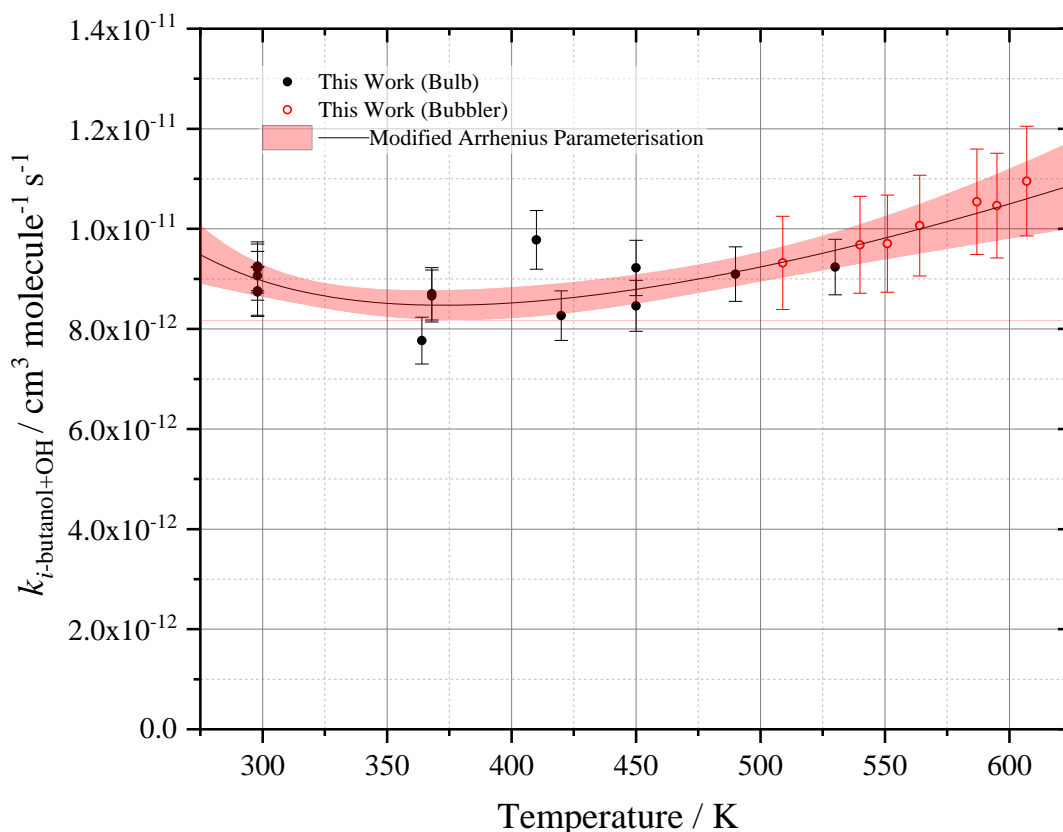


Figure 3-12: All experimentally obtained $k_{i\text{-butanol}+\text{OH}}$ bimolecular rate coefficients in this work, with Arrhenius parameterisation and 95 % confidence limits (red shaded region). See Table 3-4 for error justification.

The bimolecular reaction of *i*-butanol with OH demonstrates a negative temperature dependence below around 380 K, and a positive temperature dependence at temperatures above this. A discussion of the negative temperature dependent region can be found in section 3.8, in the context of all butanol isomers studied in this work. The Arrhenius fit to the experimentally obtained data can be described as $k_{i\text{-butanol}+\text{OH}}(298 - 607 \text{ K}) = (2.05 \pm 6.79) \times 10^{-18} \times T^{2.20 \pm 0.45} \times \exp\left(\frac{6800 \pm 1600}{R \times T}\right) \text{ cm}^3 \text{ molecule}^{-1} \text{ s}^{-1}$, with a fitting total error of 7 % across the temperatures studied in this work. The reported Arrhenius parameterisation error represents the standard 1σ error from the least squares fitting to the data, and the percentage error represents the widest part of the 95 % confidence limit bands. All previous literature values obtained at 298 K can be seen summarised in Table 3-5, and are represented graphically in Figure 3-13 alongside temperature dependent parameterisations obtained from the literature.

Table 3-5: Measured $k_{\text{OH}+i\text{-butanol}}$ (298 K) for this work with all previous literature values.

Reference	k (298 K) ^a / 10^{-12} cm^3 $\text{molecule}^{-1} \text{ s}^{-1}$	Temperature / K	Pressure / Torr	Method
Wu (2003) [108]	9.08 ± 0.35 ^c <i>(9.25 ± 0.36)</i>	295	760	RR ^f
Wu (2003) [108]	9.59 ± 0.45 ^c <i>(9.26 ± 0.43)</i>	295	760	RR ^g
Mellouki (2004) [119]	9.20 ± 1.50	298	760	RR
Mellouki (2004) [119]	10.0 ± 1.0 ^d	241–373	760	LFP–LIF
Andersen (2010) [84]	11.4 ± 1.7 ^d	296	700	RR
Pang (2012) [75]	9.68 ^e	907 – 1147	~760	ST
McGillen (2013) [78]	9.72 ± 0.72	224 – 381	60 – 216	LFP–LIF
Sarathy (2012) [55]	11.27	200 – 1800	N/A	ST–CM
Atkinson (1987) [114]	6.45	N/A	N/A	SAR
Bethel (2001) [101]	8.92	N/A	N/A	SAR
This work	9.01 ± 0.49 ^b	298 – 621	30 – 83	LFP–LIF

^a Errors are 2σ unless otherwise stated. ^b Standard deviation of 5 repeat readings. ^c Conducted at 295 K. ^d Conducted at 296 K. Methods: RR: Relative rate. LFP–LIF: Laser flash photolysis–laser-induced fluorescence. ST–CM: Shock tube combustion modelling. SAR: Structure – activity relationship. ^e Calculated from three-parameter expression provided, obtained by constraining fit to low temperature data of Mellouki *et al.* ^f Measured relative to propane reference. ^g Measured relative to cyclohexane reference. Updated values for relative rates shown in italics.

An average bimolecular rate coefficient for the reaction of *i*-butanol with OH at 298 K in this work was obtained as $k_{i\text{-butanol}+\text{OH}} = (9.01 \pm 0.49) \times 10^{-12} \text{ cm}^3 \text{ molecule}^{-1} \text{ s}^{-1}$, with the error reported at the 1σ level, which agrees within the experimental error with all previous literature obtained. Wu *et al.* [108] conducted two relative rate studies, utilising propane and cyclohexane as the two reference rate compounds. The reference rate coefficient used for propane, $1.08 \times 10^{-12} \text{ cm}^3 \text{ molecule}^{-1} \text{ s}^{-1}$, has been updated by

Atkinson (2003, [87]), to $1.10 \times 10^{-12} \text{ cm}^3 \text{ molecule}^{-1} \text{ s}^{-1}$. Using this updated reference rate coefficient gives an updated value of $k_{i\text{-butanol}+\text{OH}} = (9.25 \pm 0.36) \times 10^{-12} \text{ cm}^3 \text{ molecule}^{-1} \text{ s}^{-1}$. For the experiments conducted using cyclohexane as the reference compound, a reference rate coefficient of $k = 7.22 \times 10^{-12} \text{ cm}^3 \text{ molecule}^{-1} \text{ s}^{-1}$ was used. Updating this reference reaction rate coefficient to the more recent value of $6.97 \times 10^{-12} \text{ cm}^3 \text{ molecule}^{-1} \text{ s}^{-1}$ of Atkinson, gives a bimolecular rate coefficient of $k_{i\text{-butanol}+\text{OH}} = (9.26 \pm 0.43) \times 10^{-12} \text{ cm}^3 \text{ molecule}^{-1} \text{ s}^{-1}$. Both values are now in excellent agreement with each other following updates to the reference rate coefficients, and are overall in good agreement with the value obtained in this work.

In the Mellouki *et al.* [119] study of 2004, both the indirect relative rate method and the absolute LFP-LIF method were used. The relative rate study utilised two reference compounds; *n*-butanol ($k = (8.47 \pm 0.34) \times 10^{-12} \text{ cm}^3 \text{ molecule}^{-1} \text{ s}^{-1}$) and 1,3-dioxolane ($k = (11.1 \pm 0.9) \times 10^{-12} \text{ cm}^3 \text{ molecule}^{-1} \text{ s}^{-1}$). There is currently no updated bimolecular rate coefficient for the reaction of 1,3-dioxolane with OH, and therefore this bimolecular rate coefficient for *i*-butanol with OH remains unchanged. The recommended reference rate coefficient for the reaction of OH and *n*-butanol however has been updated by IUPAC (2007), to $k = 8.50 \times 10^{-12} \text{ cm}^3 \text{ molecule}^{-1} \text{ s}^{-1}$. This yields an updated bimolecular rate coefficient for the reaction of *i*-butanol with OH of $k = (8.53 \pm 0.10) \times 10^{-12} \text{ cm}^3 \text{ molecule}^{-1} \text{ s}^{-1}$. To the same degree of accuracy as was quoted in the original study, the average combined value reported for the two relative rate studies remains as $k_{i\text{-butanol}+\text{OH}} = 9.20 \pm 0.15 \times 10^{-12} \text{ cm}^3 \text{ molecule}^{-1} \text{ s}^{-1}$. The absolute study of Mellouki using the LFP-LIF method measured a rate constant over 10 % greater than was measured in this work, however the two values agree within experimental error. McGillen *et al.* [78] also utilised the LFP-LIF method, obtaining a 298 K bimolecular rate coefficient in excellent agreement with this work.

The most recent relative rate study conducted by Andersen *et al.* [84] used two relative rate reference compounds; propene (where the reference rate coefficient $k_{\text{propene}+\text{OH}} = 2.63 \times 10^{-11} \text{ cm}^3 \text{ molecule}^{-1} \text{ s}^{-1}$) and ethene (reference rate coefficient $k_{\text{ethene}+\text{OH}} = 1.2 \times 10^{-11} \text{ cm}^3 \text{ molecule}^{-1} \text{ s}^{-1}$). There are currently no updated values for either of the two reference rate coefficients, and therefore the calculated bimolecular rate coefficients for the reaction of *i*-butanol with OH remain unchanged. The average rate coefficient for this reaction reported is in reasonable agreement with some previous literature, and is approximately 15 % faster than was measured in this study.

The room temperature bimolecular rate coefficient from Pang *et al.* [75] in the summary table has been calculated from an extrapolation of the temperature dependent parameterisation, giving a value of $k = 9.68 \times 10^{-12} \text{ cm}^3 \text{ molecule}^{-1} \text{ s}^{-1}$, approximately 7 % faster than was obtained in this work. The parameterisation obtained in their work was constrained at lower temperatures using the low temperature experimental data of Mellouki *et al.* [119].

As with *n*-butanol, McGillen *et al.* [78] provided site specific modified Arrhenius parameterisation calculated from experimental observations, end-product yields and Structure-Activity Relationships (SAR) for the reaction of *i*-butanol with OH, constrained by high temperature data from Pang *et al.* [75]. Shock tube high temperature data by Pang *et al.* also obtained an Arrhenius parameterisation for the total bimolecular rate coefficient at combustion relevant temperatures, which as mentioned earlier, was constrained to the low temperature data of Mellouki *et al.* [119]. Site specific reactivity has been parameterised by Sarathy *et al.* [55] using shock tubes, combustion modelling and computational calculations for the reaction of *i*-butanol with OH. The total bimolecular rate coefficient obtained from the structure activity relationship of Atkinson [114] has also been included, alongside the updated SAR of Bethel and Atkinson of 2001 [101]. These parameterisations are summarised below in Table 3-6, and are compared to this experimental study in Figure 3-13.

Table 3-6: Arrhenius parameterisation for the OH + *i*-butanol reaction from previous literature and this study.

Reference	T / K	Site	$k(T) = A T^n \exp(-E/RT) F_x(T)$			
			$A / \text{cm}^3 \text{ molecule}^{-1} \text{ s}^{-1}$	n	$E/R / \text{K}$	$F_x(T)$
McGillen <i>et al.</i> [78]	224 – 1800	α	9.91×10^{-19}	2.18	-924	
		β	1.63×10^{-20}	2.64	-1289	
		γ	8.98×10^{-18}	2	258	
		OH	2.10×10^{-18}	2	23	
Pang <i>et al.</i> [75]	907 – 1147	Total	1.65×10^{-21}	3.18	-1304	
Sarathy <i>et al.</i> [55]	200 – 1800	α	6.00×10^{-21}	2.89	-1174	
		β	1.28×10^{-24}	3.7	-2488	
		γ	1.27×10^{-17}	1.84	-75	
		OH	9.76×10^{-22}	2.82	-295	
Atkinson [114]	SAR	α	4.32×10^{-18}	2	-233	$\exp(76/T)$ $\exp(365/T)$
		β	1.89×10^{-18}	2	-711	$\exp(76/T)$
		γ	$8.94 \times 10^{-18*}$	2	303	$\exp(76/T)$
		OH	1.89×10^{-18}	2	460	$\exp(76/T)$
Bethel <i>et al.</i> [101]	SAR	α	4.50×10^{-18}	2	-253	$\exp(62/T)$ $\exp(317/T)$
		β	2.12×10^{-18}	2	-696	$\exp(285/T)$
		γ	$8.98 \times 10^{-18\ddagger}$	2	303	$\exp(62/T)$
		OH	2.10×10^{-18}	2	85	$\exp(62/T)$
This Work	298 – 607	Total^a	$(2.05 \pm 6.79) \times 10^{-18}$	2.20 ± 0.45	-820 ± 190	
		Total^b	$(1.16 \pm 1.15) \times 10^{-19}$	2.61 ± 0.13	-980 ± 70	

* $2 \times 4.47 \times 10^{-18} \text{ cm}^3 \text{ molecule}^{-1} \text{ s}^{-1}$. ‡ $2 \times 4.49 \times 10^{-18} \text{ cm}^3 \text{ molecule}^{-1} \text{ s}^{-1}$. ^a Not constrained and ^b Constrained to high temperature data from Pang *et al.*

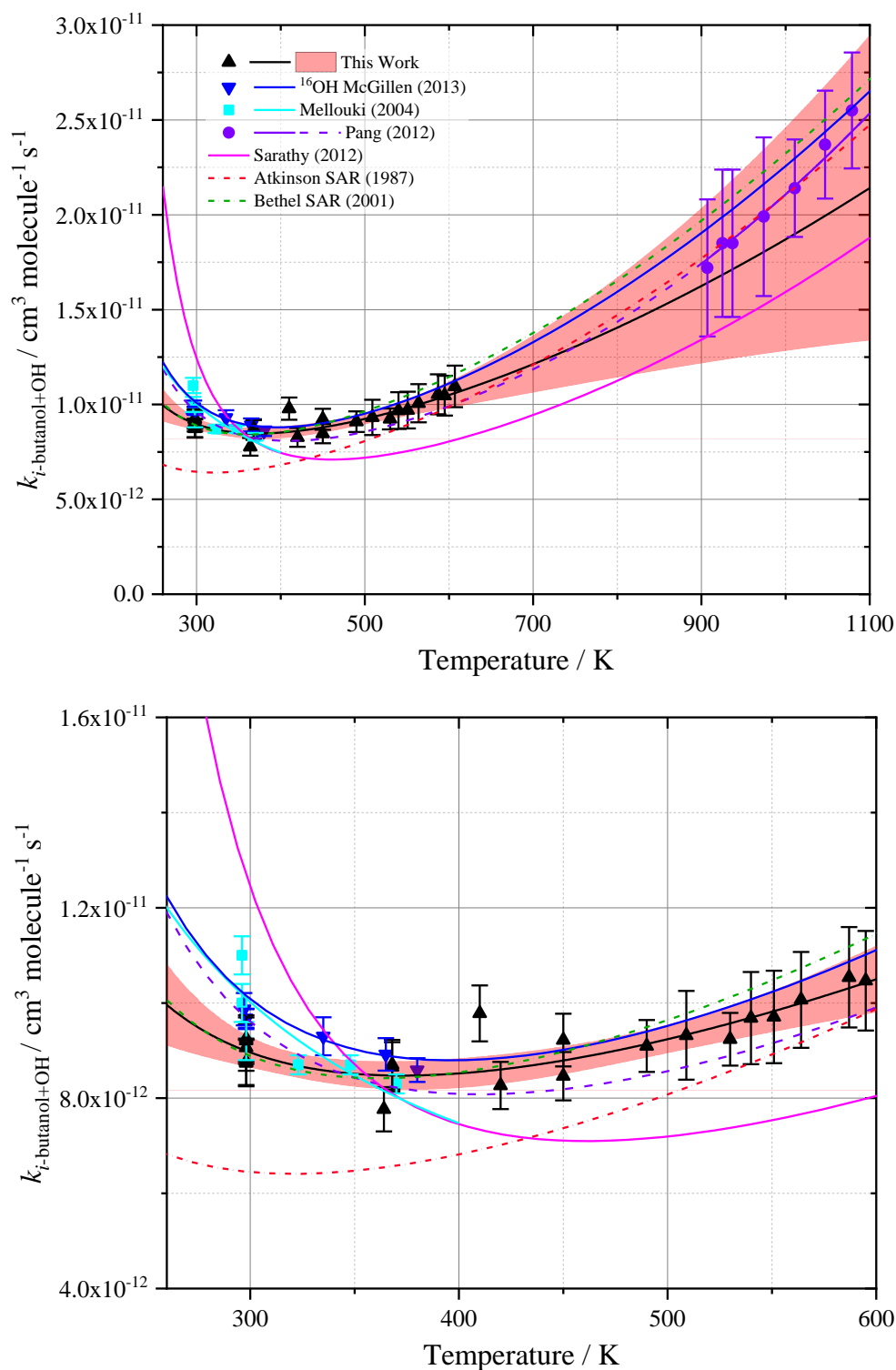


Figure 3-13: Rate coefficient data for *i*-butanol + OH reaction: This work (black triangles, black solid line, 95 % confidence limits in red shaded region). Compared with Pang *et al.* (purple circles, purple solid line and dashed line for extrapolated region), McGillen *et al.* (blue inverted triangles, blue solid line), Mellouki *et al.* (light blue squares, light blue solid line) experimental data; Sarathy *et al.* (solid pink line) calculation; SAR of Atkinson (Red dot-dash line) and Bethel *et al.* (green dot-dash line). Data replicated from [78], [119], [75], [55], [114], and [101].

Figure 3-13 shows reasonable agreement between the modified Arrhenius parameterisation of McGillen *et al.* [78], Pang *et al.* [75], and the experimental data and parameterisation obtained in this work. When the modified Arrhenius parameterisation obtained in this work is extrapolated to temperatures nearing 1100 K, the overall uncertainty calculated by the 95 % confidence limits is approximately 37.6 %.

The modified Arrhenius parameterisation of this work was repeated to provide a concatenate fit that includes the high temperature shock tube data obtained by Pang *et al.* [75], shown in Figure 3-14, giving a total parameterisation of $k_{i\text{-butanol}+\text{OH}}$ (298 – 605 K) = $(1.16 \pm 1.15) \times 10^{-19} \times T^{(2.61 \pm 0.13)} \times \exp\left(\frac{8150 \pm 550}{R \times T}\right) \text{ cm}^3 \text{ molecule}^{-1} \text{ s}^{-1}$. The concatenate fit provides a stronger curvature to the parameterisation, reflected in the increase in the T^n factor, with the high temperature parameterisation brought more in line with the literature data by Pang *et al.* This concatenate parameterisation gives a maximum overall error of 3.1 % at the 95 % confidence limit level across the temperature range studied in this work (298 – 607 K). The reported Arrhenius parameterisation error represents the standard 1σ error from the least squares fitting to the data, and the percentage error represents the widest part of the 95 % confidence limit bands. This concatenate fit provides an equally good fit to the experimental data obtained in this study, and reduces the size of the 95 % confidence limits and the overall error at the highest temperatures from 37.6 % to 8.9 %.

In the same manner as for *n*-butanol, a smooth interpolation was conducted by McGillen *et al.* [78] between the low temperature data obtained experimentally in their work and the high temperature data of Pang *et al.* [75]. At the lowest temperatures, the experimental data from McGillen *et al.* is consistently higher than the experimental measurements obtained in this work. This likely resulted in the parameterisation giving values that are higher across all temperatures than this work. However, excellent agreement can be seen in the curvature of the total parameterisations, with the overall total reactivity in good to excellent agreement. The total parameterisation for the reaction of the OH radical with *i*-butanol was not available in the literature and thus a more analytical comparison beyond this is non-trivial.

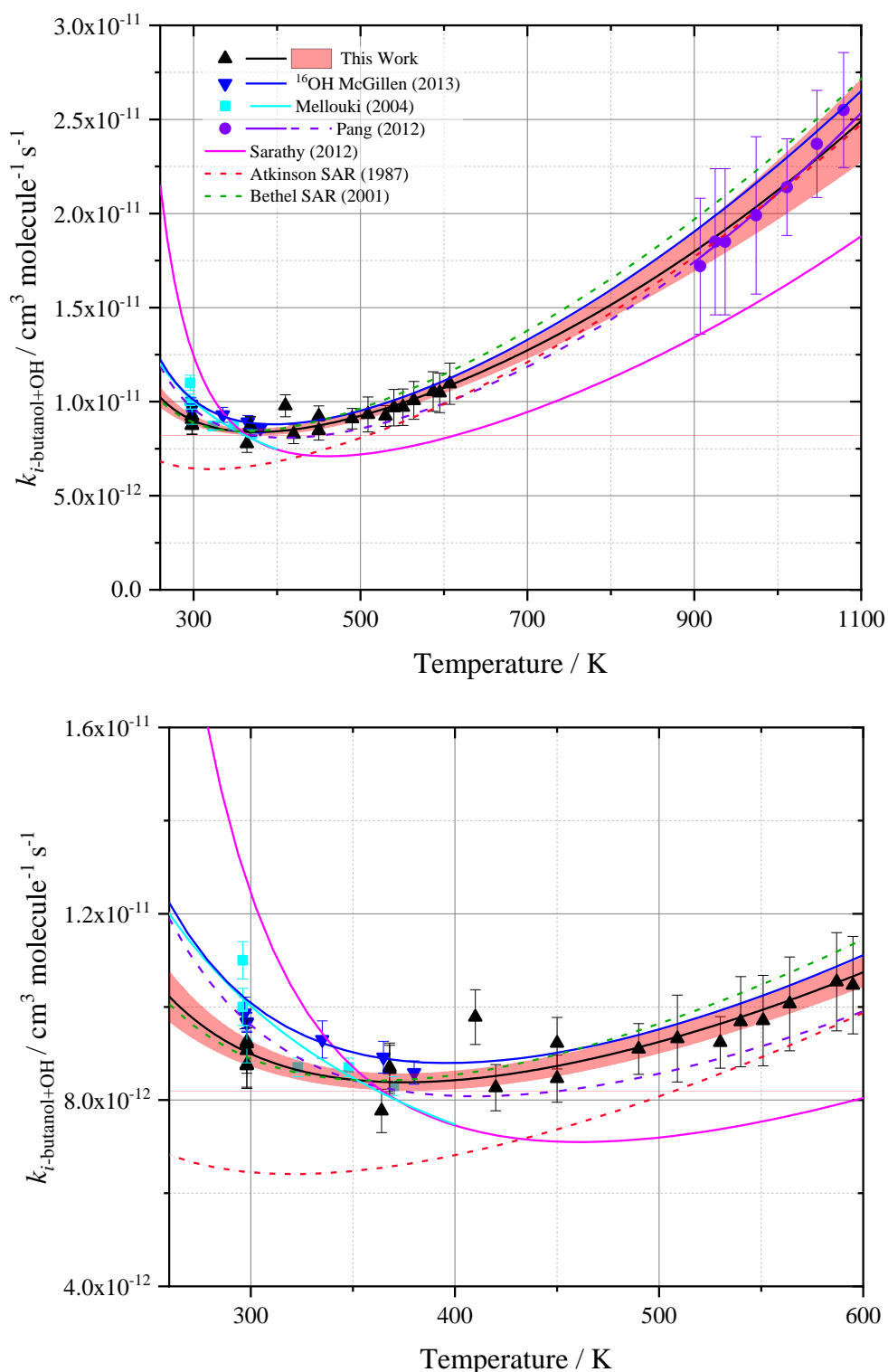


Figure 3-14: Concatenate fit to rate coefficient data for *i*-butanol + OH reaction: This work (black triangles, black solid line, 95 % confidence limits in red shaded region), with the modified Arrhenius parameterisations constrained to the high temperature data from Pang *et al.* (purple circles, purple solid line and dashed line for extrapolated region). Compared with McGillen *et al.* (blue inverted triangles, blue solid line), Mellouki *et al.* (light blue squares, light blue solid line) experimental data; Sarathy *et al.* (solid pink line) calculation; SAR of Atkinson (Red dot-dash line) and Bethel *et al.* (green dot-dash line). Data replicated from [78], [119], [75], [55], [114], and [101].

The parameterisation of Sarathy *et al.* [55] overpredicts the rate constant at temperatures in the range 280 – 340 K, and under predicts the experimental data by almost 30 % at around 600 K, with even greater deviation from the high temperature experimental data from Pang *et al.* In the Sarathy *et al.* review summary of alcohols as biofuels [1], they acknowledge that widely discrepant rate constants for multiple reactions within combustion models are able to accurately simulate historical experimental data for *i*-butanol. As rate coefficients were calculated from a combination of theoretical studies, experimental data and Evans-Polanyi type correlations, and validated against experimental measurements for parameters such as ignition delay times, a range of parameterisations for multiple reactions could provide equally good modelled output parameters.

The high temperature data of Pang *et al.* [75] was reported as both $k_{non-\beta}$, the total abstraction rate coefficient minus the beta site abstraction, and k_{total} , the total rate of reaction of OH with *i*-butanol. In their work, Pang *et al.* stated that they were not sensitive to the β -abstraction channel due to the rapid recycling of OH following abstraction at this site, and therefore the value measured experimentally is representative of $k_{non-\beta}$. Consequently, the OH abstraction rate coefficient for the beta site calculated by Merchant and Green [120] was added to the Pang *et al.* parameterisation of the total abstraction rate coefficient of *i*-butanol with OH. This beta site parameterisation was selected as a result of the total measured rate coefficient for the other abstraction sites, $k_{non-\beta}$, by Merchant and Green showing the best agreement with the experimental results of the Pang *et al.* study. Values of $k_{non-\beta}$ obtained from the Sarathy *et al.* [55] mechanism and the Grana *et al.* [121] mechanism were 15 – 25 % and 25 – 40 % slower respectively than the Pang *et al.* measured values. When fitting to both the total abstraction rate coefficient of Pang *et al.* and this work, excellent agreement is obtained between both sets of data. The concatenate fit to both sets of data also shows excellent agreement with the total parameterisation of McGillen *et al.*, which was also obtained from fitting to the high temperature parameterisation of Pang *et al.*

3.5.2 Conclusion

The bimolecular rate coefficient for the reaction of *i*-butanol with OH has been measured across the temperature range 298 – 621 K, at pressures between 30 and 82 Torr. The average room temperature rate coefficient, $k_{i\text{-butanol}+\text{OH}} =$

$(9.01 \pm 0.49) \times 10^{-12} \text{ cm}^3 \text{ molecule}^{-1} \text{ s}^{-1}$, with the error reported at the 1σ level, was measured in good agreement within experimental error with most previous literature obtained. This work provided confirmation for the previous temperature dependent experimental measurements of McGillen *et al.* [78] up to 380 K, and extended the temperature range studied to 621 K, significantly reducing the gap in the literature for the temperature dependence of this reaction. This work has also presented a modified Arrhenius parameterisation for the total reaction of *i*-butanol with OH, in excellent agreement with the previous parameterisations by McGillen *et al.* and in good agreement with Pang *et al.* [75], assisting in reducing the uncertainties of the total rate of reaction as a function of temperature.

3.6 *s*-butanol

sec-butanol, also known as 2-butanol, can be produced from biomass sources in a two-step process [14]. First, a bacterial fermentation converts a starting material such as starch or glucose into an intermediate product. Following further conversion and separation, this intermediate is converted to *s*-butanol with a conversion efficiency of approximately 90 – 95%. Despite this potentially efficient production route from biomass sources, the reaction between *sec*-butanol and the OH radical is the least studied of the four butanol isomers, both in terms of atmospherically relevant measurements and engine studies. Similar to the other isomers studied in this work, the previous temperature range over which the reaction has been studied is minimal, with two studies at room temperature (Baxley and Wells [122], and Chew and Atkinson [86]), and two separate studies by Jimenez *et al.* [123] and McGillen *et al.* [78] over relatively narrow temperature ranges (298 – 354 K and 298 – 381 K respectively). A high temperature shock tube study has also been conducted by Pang *et al.* [74] at temperatures between 888 – 1178 K. This work extends the temperature range for measurements for the bimolecular rate constant from 381 K up to 690 K.

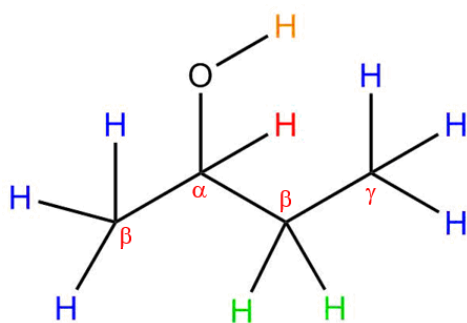


Figure 3-15: Possible abstraction sites from *s*-butanol by OH. Primary abstraction sites in blue, secondary abstraction sites in green, tertiary abstraction sites in red and hydroxyl group abstraction in orange. Carbon positions relative to hydroxyl group labelled in red.

The possible H abstraction sites for *s*-butanol and the resulting R radicals can be seen in Figure 3-15 and Figure 3-16 respectively. *s*-butanol possesses 4 distinct potential abstraction sites: one tertiary alpha hydrogen, three primary beta hydrogens, two secondary beta hydrogens and three primary gamma hydrogens. This work measures the total bimolecular rate coefficient, encompassing all potential abstraction sites, R 3-5a – R 3-5e.

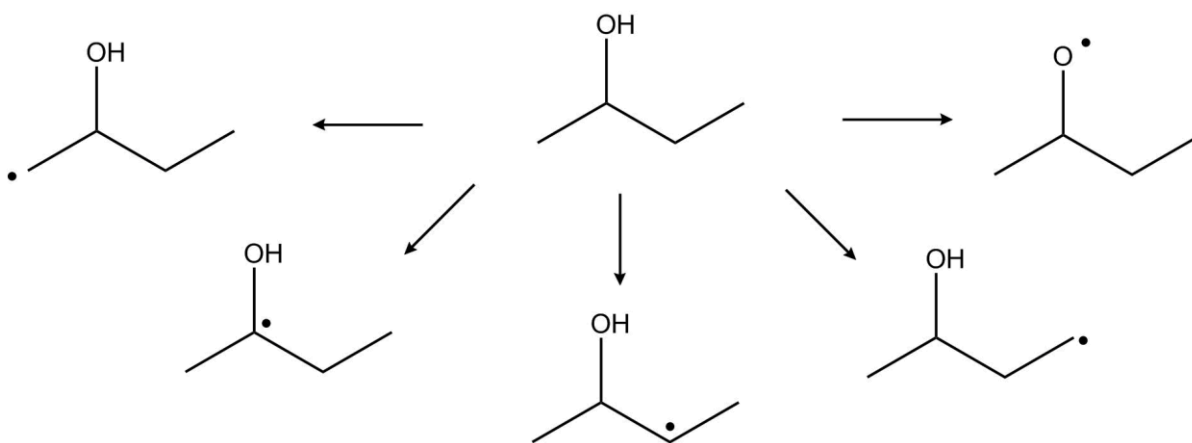
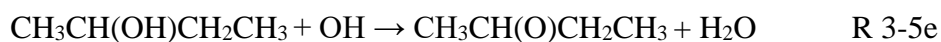
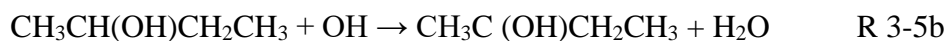


Figure 3-16: Resulting *s*-butyl and *s*-butoxy radicals formed from H atom abstraction by OH at each potential abstraction site.



3.6.1 *s*-butanol + OH: Temperature Dependence

Bimolecular rate coefficients for the reaction of *s*-butanol with the hydroxyl radical have been obtained from 298 – 690 K, at pressures of 30 – 110 Torr. All experimentally obtained values can be seen below in Table 3-7 and represented graphically in Figure 3-17. Experiments were conducted using either hydrogen peroxide/water or urea hydrogen peroxide as an OH precursor, as highlighted in Table 3-7. The majority of experiments conducted also utilised on-resonant fluorescence monitoring of the OH radical, however some were conducted using off-resonant fluorescence depending on the availability of the experimental equipment. Those that used off-resonant fluorescence have been stated in the summary table of results.

The errors reported for the 298 K values represent the standard 1σ error from Origin linear least squares fitting, and are used solely to represent the quality of data fitting obtained in this work. The obtained errors from the individual fits were then propagated to give an overall percentage error of 7 %, which was subsequently applied to all measurements made using the bulb method of delivery. Where the standard origin error was bigger, this was chosen, to ensure that the errors for lesser quality data were not underestimated. A bimolecular rate coefficient was obtained at 298 K using the bubbler method of reagent delivery, followed by a measurement of the rate coefficient using the bulb method of delivery under the same temperature and pressure conditions. From this it was found that the values differed by approximately 12 %. The same test was conducted at 372 K, and the same 12 % increase correction factor to the bubbler measurement was obtained. Consequently, all bimolecular rate coefficients measured using the bubbler delivery method were increased by a factor of 12 %, and an overall error of 10 % was applied to these values to factor in the larger uncertainty in the delivered reagent concentration.

Table 3-7: Summary of experimental conditions and bimolecular rate coefficients (k) obtained in this work for the *s*-butanol and OH reaction.

T / K	Pressure / Torr	Precursor	[<i>s</i>-butanol] / 10¹⁴ molecule cm⁻³	k / 10⁻¹² cm³ molecule⁻¹ s⁻¹
298	30	H ₂ O ₂	0.5 – 3.6	8.66 ± 0.33 ^a
298	30	H ₂ O ₂	0.95 – 4.0	8.46 ± 0.48 ^a
298	30	H ₂ O ₂	0.5 – 4.8	8.56 ± 0.97 ^a
298	50	UHP	8.2 – 44	8.53 ± 0.16 ^a
298 ‡	50	UHP	8.2 – 44	8.84 (7.89) ± 0.89 ^c
298 ‡	50	UHP	4.6 – 19.0	8.48 (7.57) ± 0.85 ^c
298 ‡	50	UHP	7.0 – 38.0	8.37 (7.48) ± 0.84 ^c
369	30	H ₂ O ₂	0.3 – 3.1	8.00 ± 0.56 ^b
372	50	UHP	3.2 – 13.6	7.27 ± 0.51 ^b
372 ‡	50	UHP	4.0 – 23.1	7.25 (6.47) ± 0.73 ^c
410	30	H ₂ O ₂	0.3 – 2.6	8.08 ± 0.57 ^b
420 ‡	50	UHP	1.9 – 17.5	6.94 (6.20) ± 0.70 ^c
450	30	H ₂ O ₂	0.3 – 2.6	7.94 ± 0.56 ^b
450	30	H ₂ O ₂	0.3 – 2.8	8.04 ± 0.56 ^b
473 ‡	110	H ₂ O ₂	0.3 – 2.5	8.05 (7.12) ± 0.81 ^c
550 ‡	50	UHP	0.9 – 22.5	8.90 (7.95) ± 0.89 ^c
562 ‡	110	H ₂ O ₂	3.9 – 26.1	9.75 (8.63) ± 0.98 ^c
612 #	110	UHP	3.0 – 13.8	10.8 ± 1.08 ^b
615 ‡	50	UHP	8.4 – 27.1	10.4 (9.29) ± 1.04 ^c
660 ‡	50	UHP	8.5 – 22.4	12.1 (10.8) ± 1.21 ^c
660 #	110	UHP	4.1 – 18.5	10.4 ± 1.04 ^c
690 ‡	50	UHP	6.8 – 28.2	11.6 (10.4) ± 1.16 ^c

‡ Reagent introduced from bubbler. Value obtained before 12 % correction shown in parentheses. # Reagent introduced from thermostatted bubbler, and therefore not subject to correction factor. UHP: Urea Hydrogen Peroxide.

^a Standard 1 σ error from Origin fitting.

^b ± 7 % error calculated based on propagation of room temperature repeat measurement errors.

^c ± 10 % error assumed for rate coefficients measured using bubbler delivery method.

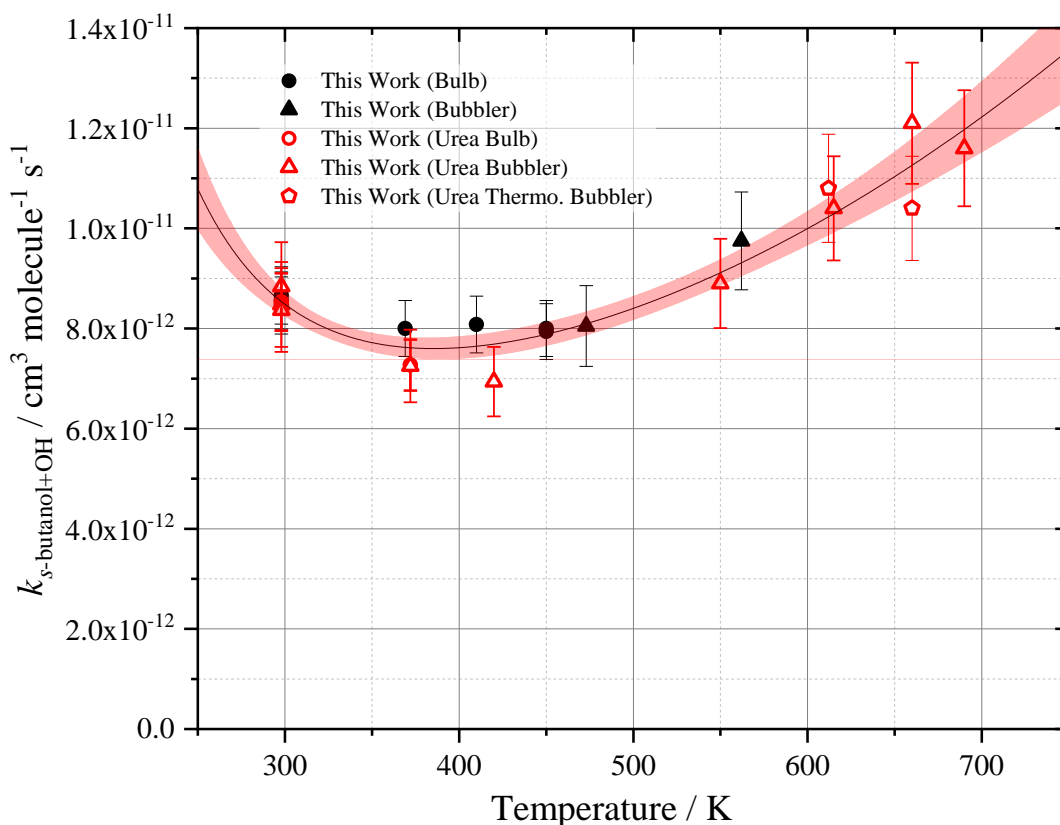


Figure 3-17: Experimentally obtained bimolecular rate coefficients with Arrhenius parameterisation (solid black line) and 95 % confidence limits (red shaded region). Experiments conducted using Hydrogen peroxide/water precursor are filled black shapes (circle for bulb delivery, triangle for bubbler delivery), and experiments conducted using urea hydrogen peroxide are hollow red shapes (circles for bulb delivery, triangles for bubbler delivery and pentagons for thermostatted bubbler).

Figure 3-17 shows all experimentally obtained total rate constants for the reaction of *s*-butanol with the OH radical. The temperature dependent parameterisation is described by the expression $k_{s\text{-butanol}+\text{OH}}(298 - 690 \text{ K}) = (1.38 \pm 2.58) \times 10^{-21} \times T^{3.22 \pm 0.25} \times \exp\left(\frac{10330 \pm 970}{R \times T}\right) \text{ cm}^3 \text{ molecule}^{-1} \text{ s}^{-1}$, with an overall error of 5.9 % across the temperatures studied in this work. The reported Arrhenius parameterisation error represents the standard 1σ error from the least squares fitting to the data, and the percentage error represents the widest part of the 95 % confidence limit bands

Above 400 K, a positive temperature dependence is observed. Between 298 – 400 K, a negative temperature dependence can be seen, which has also been observed for *n*- and *i*-butanol in this study. This is likely as a result of a pre-reaction complex forming between the hydroxyl group of the *sec*-butanol and the OH radical, a

phenomena that has been observed previously in literature [77, 78, 124]. Further explanation is found in Section 3.8, where comparisons are drawn for each isomer.

Excellent agreement is also observed between the different precursors and reagent delivery methods. In particular, the empty red pentagon shapes represent measurements taken using the thermostatted bubbler method for reagent delivery, which have not been subject to a correction factor. These show that good agreement with the bulb method of delivery can be obtained when the temperature within the bubbler is maintained at a constant temperature. This however is not always practical within the constraints of the laboratory, and in these situations, a correction factor with a more significant error is suitable. All previous literature values obtained at 298 K can be seen summarised in Table 3-8, and are represented graphically in Figure 3-18 alongside temperature dependent parameterisations obtained from the literature.

Table 3-8: Measured $k_{s\text{-butanol}+\text{OH}}$ (298 K) for this work with all previous literature values

Reference	k (298 K) ^a / $\times 10^{-12}$ $\text{cm}^3 \text{ molecule}^{-1} \text{ s}^{-1}$	Temperature / K	Pressure / Torr	Method
Chew (1996) [86]	$9.2^b \pm 2.4$ <i>(8.6 ± 2.2)</i>	296	760	RR
Baxley (1998) [122]	$9.26^c \pm 2.32$ <i>(8.81 ± 2.21)</i>	297	760	RR
	$8.14^c \pm 2.04$ <i>(7.57 ± 1.89)</i>	297	760	RR
Jimenez (2005) [123]	8.77 ± 1.46	263 – 354	41 – 193	LFP–LIF
Pang (2012) [74]	8.18^d	888 – 1178	722 – 942	ST
McGillen (2013) [78]	8.88 ± 0.69	226 – 381	61 – 218	LFP–LIF
Sarathy (2012) [55]	6.59	200 – 1800	N/A	ST–CM
Atkinson (1987) [114]	9.51	N/A	N/A	SAR
Bethel (2001) [101]	10.1	N/A	N/A	SAR
This work	8.55 ± 0.57^e	298 – 692	30 – 110	LFP–LIF

^a Errors are 2σ , measured at 298 K unless otherwise specified. ^b Recorded at 296 K. ^c Recorded at 297 K. ^e Error is standard deviation of 4 measurements. Methods: LFP–LIF: Laser flash photolysis–laser-induced fluorescence. RR: Relative rate. ST–LIF: Shock tube–laser induced fluorescence. ST–CM: Shock tube combustion modelling. SAR: Structure – activity relationship. ^d From modified Arrhenius parameterisation based on a fit that also includes the data from Jimenez *et al.* Updated values using IUPAC reference rate coefficients for relative rates shown in italics.

A rate constant for the reaction of *s*-butanol with OH at 298 K was obtained as $k_{\text{OH}+s\text{-butanol}} = (8.55 \pm 0.57) \times 10^{-12} \text{ cm}^3 \text{ molecule}^{-1} \text{ s}^{-1}$, with the error reported at the 1σ level. As seen in Table 3-8, this is in excellent agreement with the previous literature. Chew *et al.* [86] conducted the first relative rate study for the reaction of *s*-butanol with OH, utilising cyclohexane as a reference rate compound, with a reference rate of $k_{\text{OH}+\text{cyclohexane}} = 7.45 \times 10^{-12} \text{ cm}^3 \text{ molecule}^{-1} \text{ s}^{-1}$. Updating this to the most recent recommended reference rate of Atkinson [87], $k_{\text{OH}+\text{cyclohexane}} = 6.97 \times 10^{-12} \text{ cm}^3 \text{ molecule}^{-1} \text{ s}^{-1}$, gives an updated value of $k_{\text{OH}+s\text{-butanol}} = (8.6 \pm 2.2) \times 10^{-12} \text{ cm}^3 \text{ molecule}^{-1} \text{ s}^{-1}$, in excellent agreement with the value obtained experimentally in this work.

Baxley *et al.* [122] also conducted two relative rate studies at room temperature, utilising *n*-nonane as a reference compound, with $k_{\text{OH}+n\text{-nonane}} = 10.2 \times 10^{-12} \text{ cm}^3 \text{ molecule}^{-1} \text{ s}^{-1}$ and dodecane, with $k_{\text{OH}+\text{dodecane}} = 14.2 \times 10^{-12} \text{ cm}^3 \text{ molecule}^{-1} \text{ s}^{-1}$. The current recommended values from the Atkinson review of 2003 [87] are $k_{\text{OH}+n\text{-nonane}} = 9.7 \times 10^{-12} \text{ cm}^3 \text{ molecule}^{-1} \text{ s}^{-1}$ and $k_{\text{OH}+\text{dodecane}} = 13.2 \times 10^{-12} \text{ cm}^3 \text{ molecule}^{-1} \text{ s}^{-1}$. This gives updated rate constants of $k_{\text{OH}+s\text{-butanol}} = (8.81 \pm 2.21) \times 10^{-12} \text{ cm}^3 \text{ molecule}^{-1} \text{ s}^{-1}$ for the experiment conducted using *n*-nonane, in excellent agreement with this work. For dodecane, an updated value of $k_{\text{OH}+s\text{-butanol}} = (7.57 \pm 1.89) \times 10^{-12} \text{ cm}^3 \text{ molecule}^{-1} \text{ s}^{-1}$ is obtained, in worse overall agreement with this work and all previous literature.

Jimenez *et al.* [123] conducted a laser photolysis-laser induced fluorescence temperature dependent study utilising hydrogen peroxide as an OH precursor, obtaining results in excellent agreement with the work studied here at 298 K. The results obtained in the work of Jimenez were used to constrain the low temperature modified Arrhenius parameterisation by Pang *et al.* [74], and the extrapolation of this parameterisation to 298 K is in reasonable agreement with the value obtained in this work within experimental error. McGillen *et al.* [78] conducted the most recent experimental study, also utilising the LFP-LIF method used in this work, and obtained a room temperature rate coefficient for the reaction of *s*-butanol with the hydroxyl radical in excellent agreement with this study.

The structure activity relationship of Atkinson [114] calculates a 298 K bimolecular rate coefficient of $9.51 \times 10^{-12} \text{ cm}^3 \text{ molecule}^{-1} \text{ s}^{-1}$, approximately 10 % faster than was measured experimentally in this work. The updated SAR of Bethel *et al.* [101] calculates a faster bimolecular rate coefficient, in relatively poor agreement with this work and all previous literature. Both structure activity relationships however obtain rate

coefficients in much better agreement with this work and all other literature than that of the extrapolation of the Sarathy *et al.* mechanism [55], although not recommended by the authors, which calculates a 298 K value of $6.59 \times 10^{-12} \text{ cm}^3 \text{ molecule}^{-1} \text{ s}^{-1}$, approximately 22 % slower than this work.

McGillen *et al.* provided site specific modified Arrhenius parameterisation calculated from experimental observations, end-product yields and structure-activity relationships for the reaction of *s*-butanol with OH. Shock tube high temperature data by Pang *et al.* [74] also obtained an Arrhenius parameterisation for the total bimolecular rate coefficient at combustion relevant temperatures, which was constrained at lower temperatures by the experimental study of Jimenez *et al.* [123]. Site specific reactivity has also been parameterised by Sarathy *et al.* [55] using shock tubes and combustion modelling for the reaction of *s*-butanol with OH. These parameterisations have been compared to the SAR of Atkinson [114], and the updated SAR of Bethel *et al.* [101], summarised below in Table 3-9 and are compared to this experimental study graphically in Figure 3-18.

Table 3-9: Arrhenius parameterisation for the OH + *s*-butanol reaction from previous literature and this study.

Reference	T/ K	Site	$k(T) = A T^n \exp(-E/RT) F_x(T)$			
			A / cm ³ molecule ⁻¹ s ⁻¹	n	E/R / K	F _x (T)
McGillen <i>et al.</i> [78]	221 – 1800	α	4.91×10^{-19}	2.20	-1107	
		β_{sec}	9.71×10^{-20}	2.52	-656	
		$\beta_{\text{prim}} +$ γ_{prim}	2.75×10^{-19}	2.41	-595	
		OH	2.10×10^{-18}	2	23	
Pang <i>et al.</i> [74]	888 – 1178	Total	4.95×10^{-20}	2.66	1123	
Sarathy <i>et al.</i> [55]	200 – 1800	α	3.00×10^{-21}	2.89	-1315	
		β_{prim}	3.84×10^{-24}	3.7	-1483	
		β_{sec}	2.56×10^{-24}	3.7	-1881	
		γ	8.58×10^{-18}	1.81	6	
		OH	9.76×10^{-22}	2.82	-295	
Atkinson [114]	SAR	α	1.89×10^{-18}	2	-711	exp(76/T) exp(365/T)
		β_{prim}	4.47×10^{-18}	2	303	exp(76/T)
		β_{sec}	4.32×10^{-18}	2	-233	exp(76/T)
		γ	4.47×10^{-18}	2	303	exp(76/T)
		OH	1.89×10^{-18}	2	460	exp(76/T)
Bethel <i>et al.</i> [101]	SAR	α	2.12×10^{-18}	2	-696	exp(317/T) exp(62/T)
		β_{prim}	4.49×10^{-18}	2	320	exp(285/T)
		β_{sec}	4.49×10^{-18}	2	-253	exp(285/T)
		γ	4.49×10^{-18}	2	320	exp(62/T)
		OH	2.10×10^{-18}	2	85	exp(62/T)
This Work	298 – 690	Total^a	(1.38 ± 2.58) × 10⁻²¹	3.22 ± 0.25	-1243 ± 116	
		Total^b	(3.00 ± 3.86) × 10⁻²¹	2.13 ± 0.17	- 808 ± 84	

^a Not constrained and ^b Constrained to high temperature data from Pang *et al.*

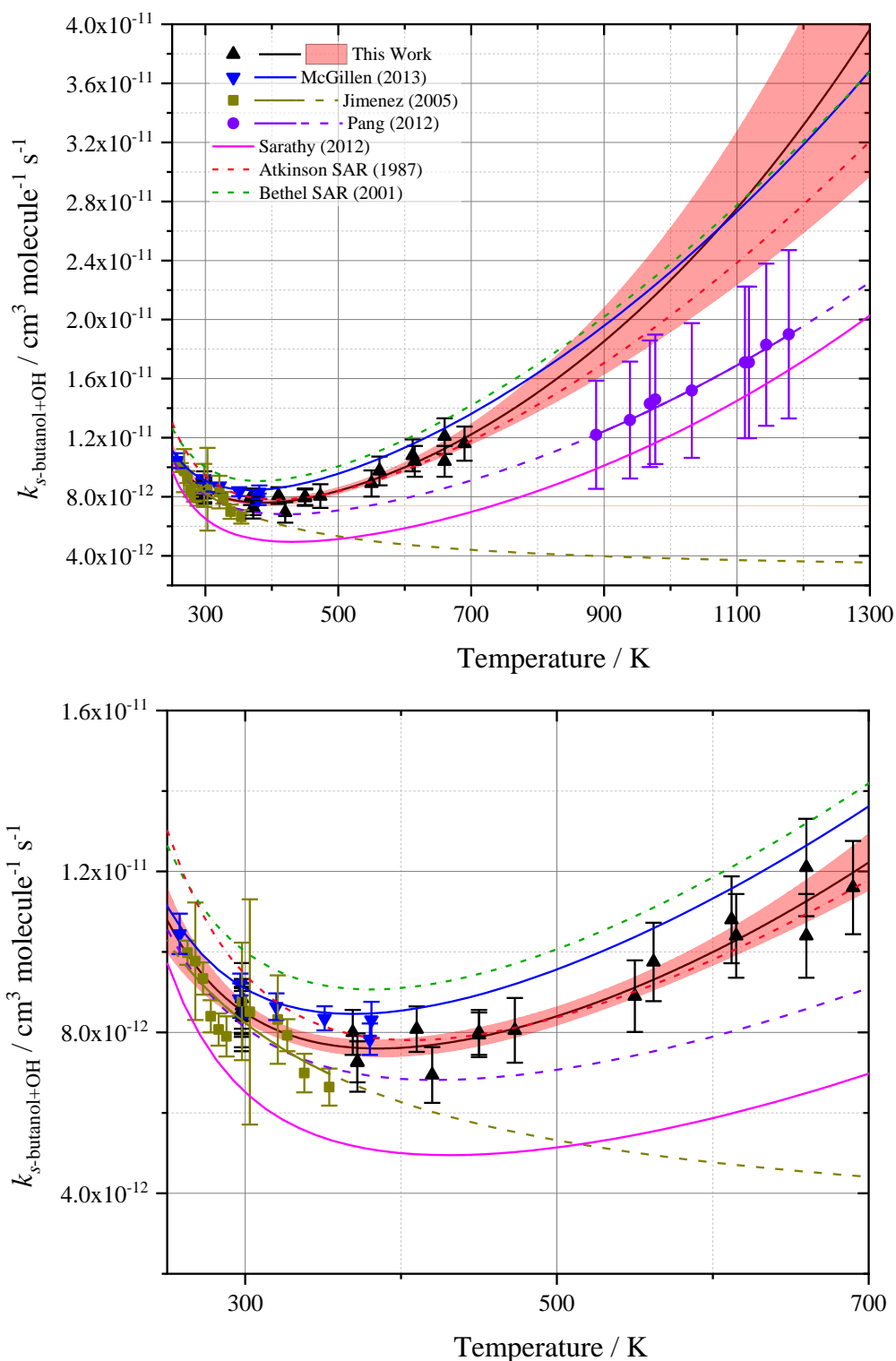


Figure 3-18: Rate coefficient data for *s*-butanol + OH reaction: This work (black triangles, black solid line, 95 % confidence limits in red shaded region). Compared with Pang *et al.* (purple circles, purple solid line and dashed line for extrapolated region), McGillen *et al.* (blue inverted triangles, blue solid line), Jimenez *et al.* (olive squares, olive solid line with dashed line for extrapolated region) experimental data; Sarathy *et al.* (solid pink line) calculation; SAR of Atkinson (Red dot-dash line) and Bethel *et al.* (green dot-dash line). Data replicated from [78], [123], [74], [55], [114] and [101].

When the modified Arrhenius parameterisation obtained in this work is extrapolated to temperatures nearing 1200 K, the overall uncertainty calculated by the 95 % confidence limits is approximately 25.3 %. This work agrees well overall with the total temperature dependent parameterisation by McGillen *et al.* [78], with the largest disagreement in the region of 600 – 900 K, at approximately 30 %. Despite the availability of the high temperature shock tube data from Pang *et al.* [74], the McGillen *et al.* study did not conduct a smooth interpolation between the two temperature ranges, as they did for *n*- and *i*-butanol. It is not clear from their work why they chose not to do so. The total parameterisation of this work shows a good overall agreement with the SAR of Bethel *et al.* [101], which was also used to constrain the McGillen *et al.* total parameterisation at temperatures above 1200 K. As suggested in the study of McGillen *et al.*, at these high temperatures, the total reactivity is expected to display reactivity resembling that of the alkane analogues. In the study of Jimenez *et al.* [123], a negative temperature dependence was observed over all temperatures studied. A simple Arrhenius parameterisation was fit through the data, and this parameterisation is therefore unable to capture the curvature of the experimental data observed here.

A concatenate fit to the experimental data obtained in this work and the high temperature data of Pang *et al.* was also conducted, giving a modified Arrhenius parameterisation of $k_{s\text{-butanol+OH}}$ (298 – 1200 K) = $(3.00 \pm 3.86) \times 10^{-21} \times T^{(2.13 \pm 0.17)} \times \exp\left(\frac{6700 \pm 700}{R \times T}\right) \text{ cm}^3 \text{ molecule}^{-1} \text{ s}^{-1}$. This concatenate parameterisation gives an overall error of 4.3 % at the 95 % confidence limit level across the temperature range studied in this work (298 – 690 K) and an overall error of 15.0 % across the full temperature range. The reported Arrhenius parameterisation error represents the standard 1σ error from the least squares fitting to the data, and the percentage error represents the widest part of the 95 % confidence limit bands.

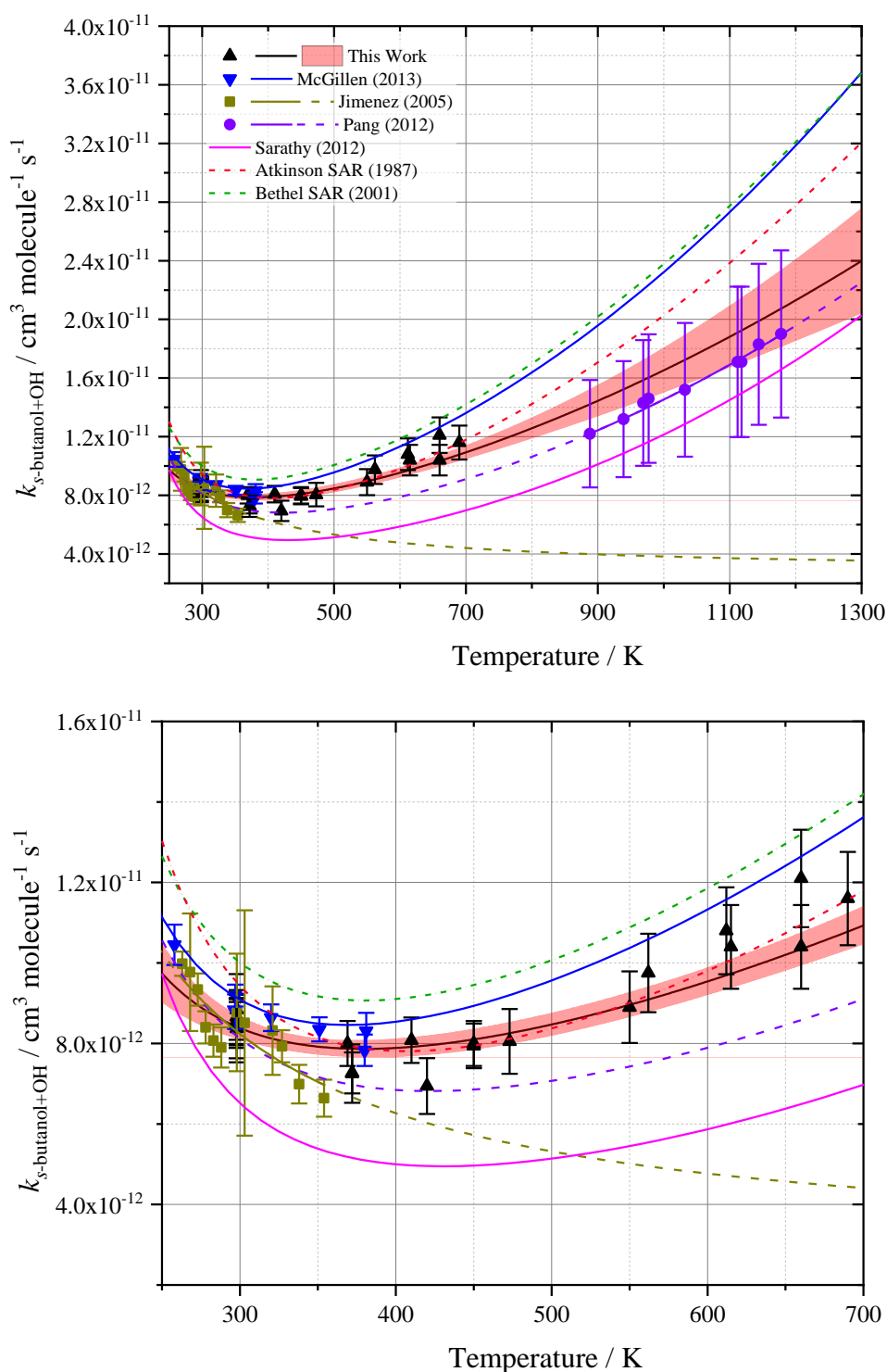


Figure 3-19: Concatenate fit to rate coefficient data for *s*-butanol + OH reaction: This work (black triangles, black solid line, 95 % confidence limits in red shaded region) with the Arrhenius parameterisations constrained to the high temperature data from Pang *et al.* (purple circles, purple solid line and dashed line for extrapolated region). Compared with McGillen *et al.* (blue inverted triangles, blue solid line), Jimenez *et al.* (olive squares, olive solid line with dashed line for extrapolated region) experimental data; Sarathy *et al.* (solid pink line) calculation; SAR of Atkinson (Red dot-dash line) and Bethel *et al.* (green dot-dash line). Data replicated from [78], [123], [74], [55], [114] and [101].

The concatenate fit to the experimental measurements made in this work and the high temperature data of Pang *et al.* [74] provides a worse fit to the data points obtained in this work. The discrepancy obtained between the experimental work obtained here up to 700 K and the experimental work of Pang *et al.* [74] above 888 K particularly highlights the need for future experiments in this intermediate temperature range, to bridge the uncertainty between the two sets of experimental data.

In order to obtain a total bimolecular rate coefficient in the Pang *et al.* shock tube study, the experimental OH traces were fit to modified versions of three combustion models found in the literature; the mechanisms of Frassoldati *et al.* [125], Hansen *et al.* [126] and Sarathy *et al.* [55]. The average total bimolecular rate coefficient for the reaction of *s*-butanol with OH was then reported, with the significant error bars reported encompassing the upper and lower limit of the rate coefficients calculated from fitting to the mechanism. The rate constant determined in their work was therefore dependent on the mechanism used for fitting to the data, as well as being reliant upon the reaction rates of significant amounts of secondary chemistry and multiple branching ratios.

In the Hansen *et al.* model used to fit the OH traces, the branching ratios tend towards significant amounts of OH recycling (82 % from the primary β -radical and 77 % from the secondary β -radical), and thus this model provided the fastest bimolecular rate coefficient for the reaction of OH with *s*-butanol to accurately simulate the OH time profile obtained from experiment. This is in contrast to the Frassoldati *et al.* and Sarathy *et al.* mechanisms, where the branching ratios for the secondary chemistry result in decomposition and isomerisation to non-OH products dominating (e.g., only 6 % OH formation from the primary β -radical in the Frassoldati *et al.* mechanism), and consequently these models calculate slower bimolecular rate coefficients for OH with *s*-butanol. Pang *et al.* concluded that the best agreement obtained between the model fitting and their data came from the modified Sarathy *et al.* mechanism, but acknowledged this may be a consequence of errors in various rate constants cancelling out to give the best simulated OH profile. When compared to this work and other previous experimental data, the total bimolecular rate coefficient calculated from the mechanism of Sarathy *et al.* performs the worst of all the temperature dependent parameterisations. The use of this model and the branching ratios involved may explain the slower total bimolecular rate coefficient calculated by Pang *et al.* in their shock tube study through the use of the Sarathy *et al.* model.

3.6.2 Conclusion

The bimolecular reaction between OH and *s*-butanol has been measured across the temperature range 298 – 692 K, across pressures of 30 – 110 Torr. The average room temperature rate coefficient, $k_{s\text{-butanol}+\text{OH}} = (8.55 \pm 0.57) \times 10^{-12} \text{ cm}^3 \text{ molecule}^{-1} \text{ s}^{-1}$, with the error reported at the 1σ level, was measured in good agreement within experimental error with previous experimental literature. The experimental data at temperatures between 298 K and 400 K was in excellent overall agreement with the previous temperature dependent study by McGillen *et al.* [78], and excellent agreement was also obtained between the two modified Arrhenius parameterisations.

Agreement with the high temperature shock tube data of Pang *et al.* [74] was relatively poor in comparison with the agreement observed for the other butanol isomers. This is likely a consequence of the different method of analysis utilised by Pang *et al.* compared to the other butanol isomers studied by the group. Three different fitting sub-mechanisms formed from combustion models in the literature were used to fit the OH profiles obtained in their work, and the value reported for the bimolecular rate coefficient was the average value obtained from each mechanism. For Pang *et al.*, the best agreement was observed with the mechanism of Sarathy *et al.* [55] for other reactions measured, but it was acknowledged this may be a consequence of errors cancelling out within the mechanism. The total bimolecular rate coefficient of Sarathy *et al.* showed the worst agreement with the rate coefficients obtained in this work, and therefore this could explain the bias towards a slower total bimolecular rate coefficient obtained by Pang *et al.*

3.7 *t*-butanol

Whilst *t*-butanol cannot be produced currently from biological sources and is solely a petrochemical product, it is already currently used as an octane enhancer in engines [47, 55, 76, 127], and thus its rate of reaction with the OH radical is of interest. There have been a few temperature dependent studies of the reaction of *t*-butanol with OH by Teton *et al.* (1996) [128], McGillen *et al.* (2013) [78] and Wallington *et al.* (1988) [127], which extend to upper temperature limits of 372 K, 381 K and 440 K respectively. Most recently, Stranic *et al.* [76] studied the reaction between 900 – 1200 K using shock tube apparatus and kinetic modelling of isotopically labelled *t*-butan¹⁸ol, allowing the absolute total OH abstraction rate to be measured without the interference of the β -abstraction site radical recycling channel. Between these two temperature extremes,

there exists a significant gap in the literature. This work extends the temperature range studied to 614 K.

t-butanol represents the simplest of the four butanol isomers, possessing only two different possible abstraction sites for the reaction with the hydroxyl radical. These two distinct sites and the resulting radicals following abstraction reactions can be seen below in Figure 3-20 and Figure 3-21. The three equivalent primary methyl groups result in one unique C–H abstraction environment for *t*-butanol, compared with four possible different C–H abstraction environments found in *n*- and *s*-butanol, and three found in *i*-butanol.

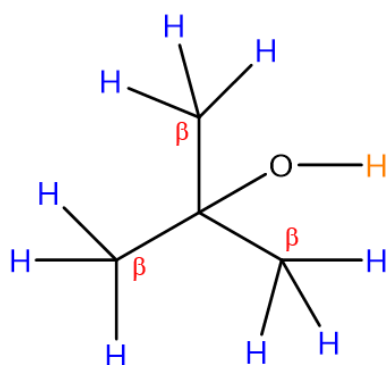


Figure 3-20: Possible abstraction sites from *t*-butanol by OH. Primary abstraction sites in blue and hydroxyl group abstraction in orange. Carbon positions relative to hydroxyl group labelled in red.

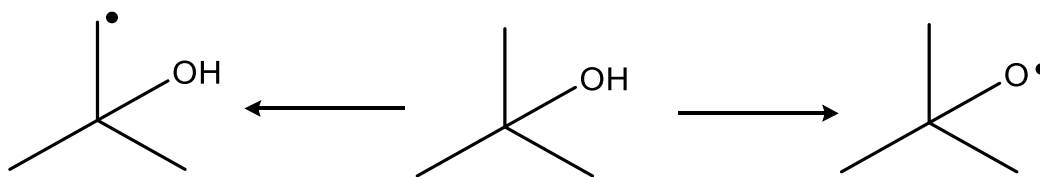
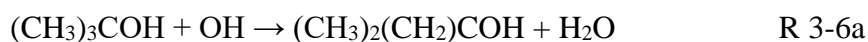


Figure 3-21: Resulting *t*-butyl and *t*-butoxy radicals formed by H atom abstraction by OH at each potential abstraction site.



3.7.1 *t*-butanol + OH: Temperature Dependence

The bimolecular rate coefficient for the reaction of *t*-butanol with the hydroxyl radical has been measured at temperatures from 298 – 614 K, at pressures of 30 – 90 Torr total pressure. All experiments were conducted using hydrogen peroxide as an OH precursor, and utilised the off-resonant fluorescence experimental set up. All the experimentally obtained bimolecular rate constants are summarised in Table 3-10 and Figure 3-22, with footnotes to explain quoted errors and any key experimental details that differ from the usual setup.

For experiments conducted at temperatures above 535 K and pressures above 80 Torr, the bubbler method of reagent delivery was utilised. Experiments conducted consecutively found that a correction of 36 % was required to correct the bimolecular rate constant value obtained by the bubbler to that of the known concentration bulb. In order to assign an error to all measurements obtained via the bulb method of delivery, the standard deviation of five repeat measurements at 298 K was calculated. These measurements were carried out using different filled bulbs of reagent and across different days of experiments, to measure the true variation between repeat measurements. This was converted to a percentage error of 9 %, which has then been applied to all other bulb measurements. Measurements conducted using the bubbler method of delivery are likely to possess a more significant uncertainty in the quantity of reagent delivered to the cell, and these experimental results therefore have a larger associated uncertainty of 15 %. These differences are highlighted in Figure 3-22, in which experiments conducted using the bulb and bubbler method of reagent delivery are represented by filled black circles and red triangles, respectively.

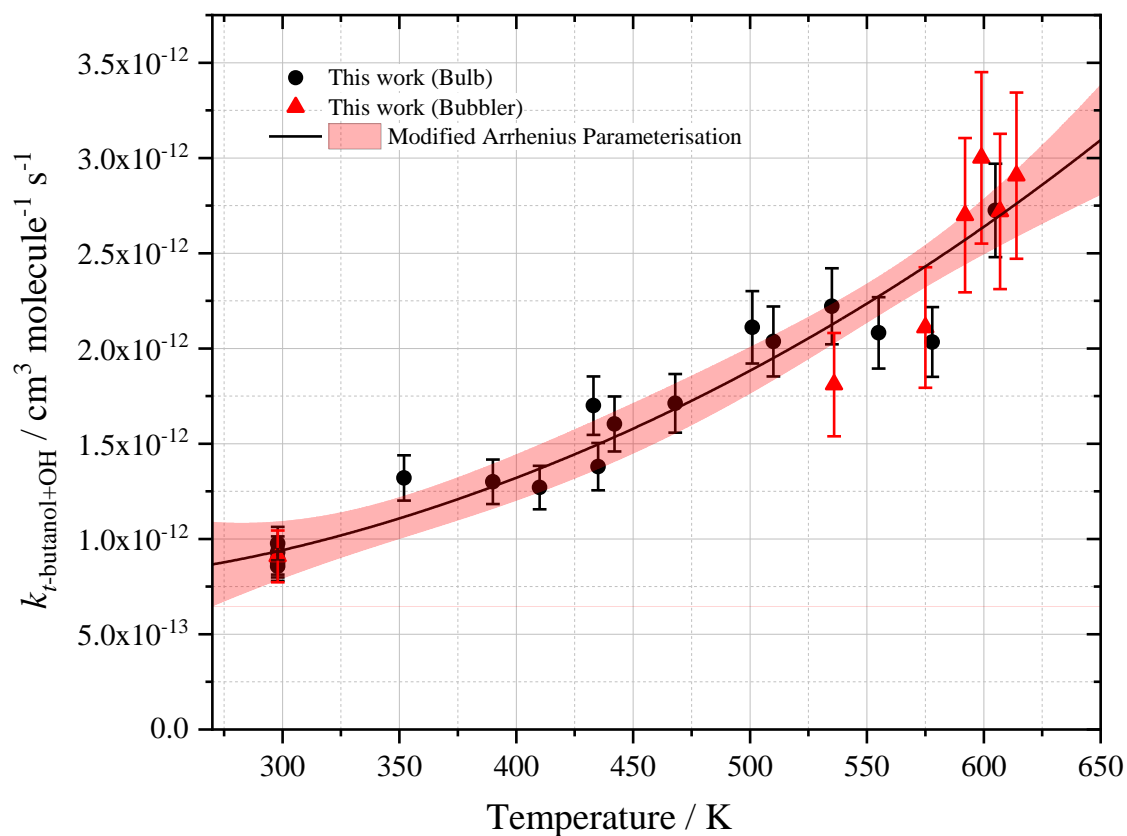


Figure 3-22: All experimentally obtained rate coefficient data for the reaction of *t*-butanol with OH, obtained between 30 – 88 Torr. Experimental data measured using bulb method (filled black circles) and bubbler method (filled red triangles) of reagent delivery.

Table 3-10: Summary of experimental conditions and bimolecular rate coefficients (k) obtained for the *t*-butanol and OH reaction.

Temperature / K	Pressure / Torr	[<i>t</i> -butanol] / 10 ¹⁴ molecule cm ⁻³	k / 10 ⁻¹² cm ³ molecule ⁻¹ s ⁻¹
298	31	1.40 – 12.3	0.88 ± 0.02 ^a
298	31	1.02 – 7.60	0.98 ± 0.03 ^a
298	33	1.65 – 12.2	0.86 ± 0.02 ^a
298	33	1.29 – 9.25	0.89 ± 0.02 ^a
298	33	1.35 – 9.18	0.93 ± 0.03 ^a
298 [‡]	90	32 – 310	0.91 (0.67) ± 0.09 ^c
352	32	1.12 – 8.86	1.32 ± 0.12 ^b
390	34	1.11 – 7.31	1.30 ± 0.12 ^b
410	31	1.18 – 10.12	1.27 ± 0.11 ^b
433	33	0.95 – 7.45	1.70 ± 0.15 ^b
435	31	2.65 – 9.65	1.38 ± 0.12 ^b
442	34	0.99 – 6.57	1.60 ± 0.14 ^b
468	34	1.12 – 8.51	1.71 ± 0.15 ^b
501	34	1.01 – 8.00	2.11 ± 0.19 ^b
510	34	0.69 – 4.42	2.04 ± 0.18 ^b
535	34	0.68 – 6.75	2.22 ± 0.20 ^b
536 [‡]	83	29 – 115	1.81 (1.33) ± 0.27 ^c
555	35	0.64 – 4.27	2.08 ± 0.19 ^b
575 [‡]	48	45 – 86	2.11 (1.55) ± 0.32 ^c
578	35	0.53 – 3.67	2.03 ± 0.18 ^b
587	42	56 – 130	2.01 ± 0.16 ^b
592 [‡]	88	65 – 210	2.69 (1.98) ± 0.41 ^c
599 [‡]	86	67 – 197	3.01 (2.21) ± 0.45 ^c
605	38	3.8 – 7.1	2.73 ± 0.25 ^b
607 [‡]	87	60 – 197	2.72 (2.00) ± 0.41 ^c
614 [‡]	88	63 – 203	2.91 (2.14) ± 0.44 ^c

[‡] Reagent introduced from bubbler. Value obtained before 36 % correction shown in parentheses. ^a 2σ error from standard origin fitting. ^b ± 9 % error, calculated from standard deviation of repeat measurements at 298 K. ^c ± 15 % error, resulting from uncertainty in bubbler method of delivery.

All experimental bimolecular rate coefficient data for the *t*-butanol + OH reaction is summarised in Figure 3-22, and can be described by the expression $k_{t\text{-butanol}+\text{OH}}(298 - 614 \text{ K}) = (4.50 \pm 23.7) \times 10^{-21} \times T^{(2.99 \pm 0.71)} \times \exp\left(\frac{5200 \pm 2600}{R \times T}\right) \text{ cm}^3 \text{ molecule}^{-1} \text{ s}^{-1}$, with an overall error of 9 % across the temperatures studied in this work. The reported Arrhenius parameterisation error represents the standard 1σ error from the least squares fitting to the data, and the percentage error represents the widest part of the 95 % confidence limit bands.

For *t*-butanol, a positive temperature dependence was observed across all temperatures studied in this work, in contrast to the other three isomers which all displayed a degree of negative temperature dependence at the lowest temperatures, potentially from formation of a hydrogen bonded complex (see Section 3.8). For this isomer, after complex formation, the energy barrier to abstraction is likely higher than the entrance channel, and thus at lower temperatures, the formation of a complex does not enhance the reactivity in contrast to the other isomers.

Table 3-11: Summary of previous studies on $k_{t\text{-butanol}+\text{OH}}$ conducted in literature compared with this work.

Reference	$k^{\text{a}}(298\text{ K}) / 10^{-12}$ $\text{cm}^3 \text{molecule}^{-1}$ s^{-1}	Temperature / K	Pressure / Torr	Method ^b
Wallington (1988) [127]	1.07 ± 0.08	240 – 440	25 – 50	FP–RF
Saunders (1994) [129]	0.81 ± 0.17	298	1	DF–LIF
Teton (1996) [128]	1.08 ± 0.10	230 – 372	100	LFP–LIF
Wu (2003) [108]	1.11 ± 0.07 (1.13 ± 0.07)	295	760	RR
Sarathy (2012) [55]	1.00	200 – 1800	N/A	ST–CM
McGillen (2013) [78]	1.04 ± 0.08	221 – 381	55 – 205	LFP–LIF
Stranic (2013) [76]	0.03^{c}	900 – 1200	760^{d}	ST
Atkinson (1987) [114]	0.60	N/A	N/A	SAR
Kwok (1995) [130]	0.68	N/A	N/A	SAR
Bethel (2001) [101]	1.24	N/A	N/A	SAR
This work	$0.91 \pm 0.09^{\text{b}}$	298 – 614	36 – 89	LFP–LIF

^a Errors reported are 2σ , conducted at 298 K unless otherwise specified. ^b Error is standard deviation of 6 measurements. LFP–LIF: Laser flash photolysis–laser-induced fluorescence, FP–RF: flash photolysis–resonance fluorescence, DF–LIF: discharge flow–laser induced fluorescence. ST–CM: Shock tube combustion modelling. SAR: Structure-activity relationship. ^c Extrapolated from high temperature experiment Arrhenius parameterisation. ^d Experiments conducted at ‘near atmospheric pressure’. Updated values using IUPAC reference rate coefficients for relative rates shown in italics.

The room temperature rate coefficient obtained for the reaction of *t*-butanol with OH in this study, $(9.1 \pm 0.9) \times 10^{-13} \text{ cm}^3 \text{ molecule}^{-1} \text{ s}^{-1}$ (with the error reported at the 1σ

level), is in good overall agreement with previous literature. Wallington *et al.* [127] utilised flash photolysis-resonance fluorescence at $\lambda \geq 165$ nm of H₂O precursor, obtaining a value of $k_{t\text{-butanol}+\text{OH}} = 1.07 \pm 0.08 \times 10^{-12} \text{ cm}^3 \text{ molecule}^{-1} \text{ s}^{-1}$, in reasonable agreement with the value obtained in this work. The study conducted by Saunders *et al.* [129] using the discharge flow-laser induced fluorescence method is the slowest experimentally measured rate coefficient for the reaction of *t*-butanol with the hydroxyl radical, and also agrees reasonably well with this work.

Wu *et al.* [108] conducted the only relative rate study into this reaction, using a reference compound of propane, with a reference rate of $k_{\text{propane}+\text{OH}} = 1.08 \times 10^{-12} \text{ cm}^3 \text{ molecule}^{-1} \text{ s}^{-1}$. An updated value for this reference rate according to the IUPAC recommended values is $k_{\text{propane}+\text{OH}} = 1.10 \times 10^{-12} \text{ cm}^3 \text{ molecule}^{-1} \text{ s}^{-1}$. This provides an updated value of $k_{t\text{-butanol}+\text{OH}} = 1.13 \times 10^{-12} \text{ cm}^3 \text{ molecule}^{-1} \text{ s}^{-1}$, in poor overall agreement with the bimolecular rate coefficient obtained in this work. The most recent room temperature experimental study by McGillen *et al.* [78] is in good overall agreement with the value obtained in this work across all precursors studied.

The earlier structure activity relationships (SAR) of Atkinson [114] and Kwok and Atkinson [130] do not reproduce the room temperature rate coefficients well, calculating total bimolecular rate coefficients that are approximately 35 % slower than the experimentally measured value from this work. Conversely, the updated structure-activity relationship calculated value by Bethel *et al.* [101] is approximately 30 % faster than the experimental value obtained in this work. The predicted value of Sarathy *et al.* [55] is in good agreement with this work, however the extrapolation of the study by Stranic *et al.* [76] is slow by over an order of magnitude at 298 K, and is therefore not likely a reliable extrapolation past the experimentally studied region.

For comparison of the temperature dependent parameterisation of this work with previous literature, both total and site specific temperature dependent parameterisations for the reaction of *t*-butanol with the hydroxyl radical can be seen summarised in Table 3-12, and represented graphically in Figure 3-23.

Table 3-12: Arrhenius parameterisation for the OH + *t*-butanol reaction from previous literature and this study.

Reference	T/ K	Site	$k(T) = A T^n \exp(-E/RT) F_x(T)$			
			A / cm ³ molecule ⁻¹ s ⁻¹	n	E/R / K	F _x (T)
McGillen <i>et al.</i> [78]	220 – 1800	β_{prim}	1.34×10^{-17}	2	227	
		β_{complex}	6.83×10^{-14}		-548	
		OH [‡]	1.89×10^{-18}	2	460	
Stranic <i>et al.</i> [76]	900 – 1200	Total	1.24×10^{-10}	-	2501	
Sarathy <i>et al.</i> [55]	200 – 1800	β	1.15×10^{-23}	3.7	-1217	
		OH	9.76×10^{-22}	2.82	-295	
Atkinson [114]	SAR	β	$1.35 \times 10^{-17*}$	2	303	exp(76/T)
		OH	1.89×10^{-18}	2	460	exp(76/T)
Kwok and Atkinson [130]	SAR	β	$1.35 \times 10^{-17*}$	2	320	exp(62/T)
		OH	2.10×10^{-18}	2	85	exp(62/T)
Bethel <i>et al.</i> [101]	SAR	β	$1.35 \times 10^{-17*}$	2	320	exp(285/T)
		OH	2.10×10^{-18}	2	85	exp(62/T)
This Work	298 – 614	Total^a	$(4.50 \pm 23.7) \times 10^{-21}$	2.99 ± 0.71	-630 ± 320	
		Total^b	$(3.90 \pm 4.10) \times 10^{-23}$	3.67 ± 0.13	-886 ± 80	

‡ Value from personal communication, not value reported in paper [131]
* $3 \times 4.49 \times 10^{-18}$ cm³ molecule⁻¹ s⁻¹. ^a Not constrained and ^bConstrained to high temperature data from Stranic *et al.*

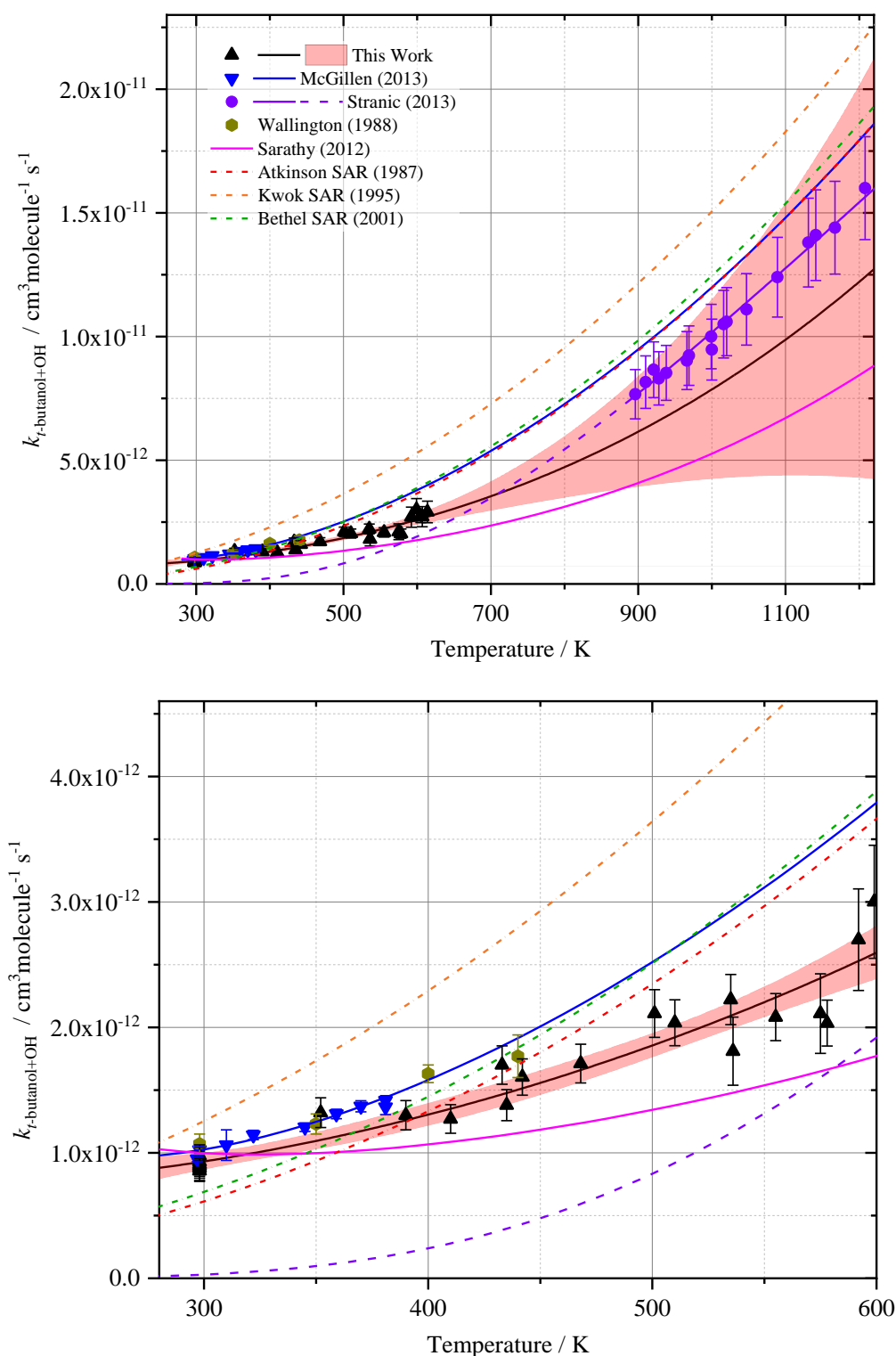


Figure 3-23: Rate coefficient data for *t*-butanol + OH reaction: This work (black triangles, black solid line, 95 % confidence limits in red shaded region). Compared with Stranic *et al.* (purple circles, purple solid line and dashed line for extrapolated region), McGillen *et al.* (blue inverted triangles, blue solid line), Wallington *et al.* (olive hexagons) experimental data; Sarathy *et al.* (solid pink line) calculation; SAR of Atkinson (red dot-dash line), Kwok and Atkinson (orange dot-dash line) and Bethel *et al.* (green dot-dash line). Data replicated from [78], [76], [127], [55], [114], [130] and [101].

When the modified Arrhenius parameterisation obtained in this work is extrapolated to temperatures nearing 1200 K, the overall uncertainty calculated by the 95 % confidence limits is approximately 65 %. This work is in good agreement with the temperature dependent experimental work above 298 K by McGillen *et al.* [78] to 382 K and Wallington *et al.* [127] up to 440 K, displaying a slight positive temperature dependence. The corrected structure activity relationship (SAR) parameterisation of McGillen *et al.* [131] for the β site abstraction through direct and complex channels was used in conjunction with the OH abstraction from the SAR of Atkinson [114], $k_{\text{OH}} = 1.89 \times 10^{-18} \times T^2 \times \exp\left(\frac{-460}{T}\right) \text{ cm}^3 \text{ molecule}^{-1} \text{ s}^{-1}$, to fit the corresponding data. Above 440 K, the experimentally obtained bimolecular rate coefficients in this work display a temperature dependence in reasonable agreement with the McGillen *et al.* modified Arrhenius parameters. All experimental measurements obtained here are faster than the predicted temperature dependence from Sarathy *et al.* [55], with an almost 50 % discrepancy by 600 K. Due to the width of the 95 % confidence limits, the work of Stranic *et al.* is within the experimental error of this work, however the modified Arrhenius parameterisation of this work is consistently slower than was measured in the high temperature study.

The modified Arrhenius parameterisation for the data obtained here has also been fit and constrained to the high temperature data measured by Stranic *et al.* by including their data in the parameterisation, shown in Figure 3-24. A modified Arrhenius parameterisation of $k_{t\text{-butanol}+\text{OH}}$ (298 – 614 K) = $(3.93 \pm 4.07) \times 10^{-23} \times T^{(3.67 \pm 0.13)} \times \exp\left(\frac{7370 \pm 660}{R \times T}\right) \text{ cm}^3 \text{ molecule}^{-1} \text{ s}^{-1}$ was obtained for this concatenate fit. This concatenate parameterisation gives an overall error of 6 % at the 95 % confidence limit level across the temperature range studied in this work (298 – 614 K) and a maximum overall error of 7 % across the full temperature range. The reported Arrhenius parameterisation error represents the standard 1σ error from the least squares fitting to the data, and the percentage error represents the widest part of the 95 % confidence limit bands. This provides an equally good fit to the experimental data obtained in this study, and also significantly reduces the size of the 95 % confidence limits at the highest temperatures, as it provides a constraint for the curvature of the temperature dependence.

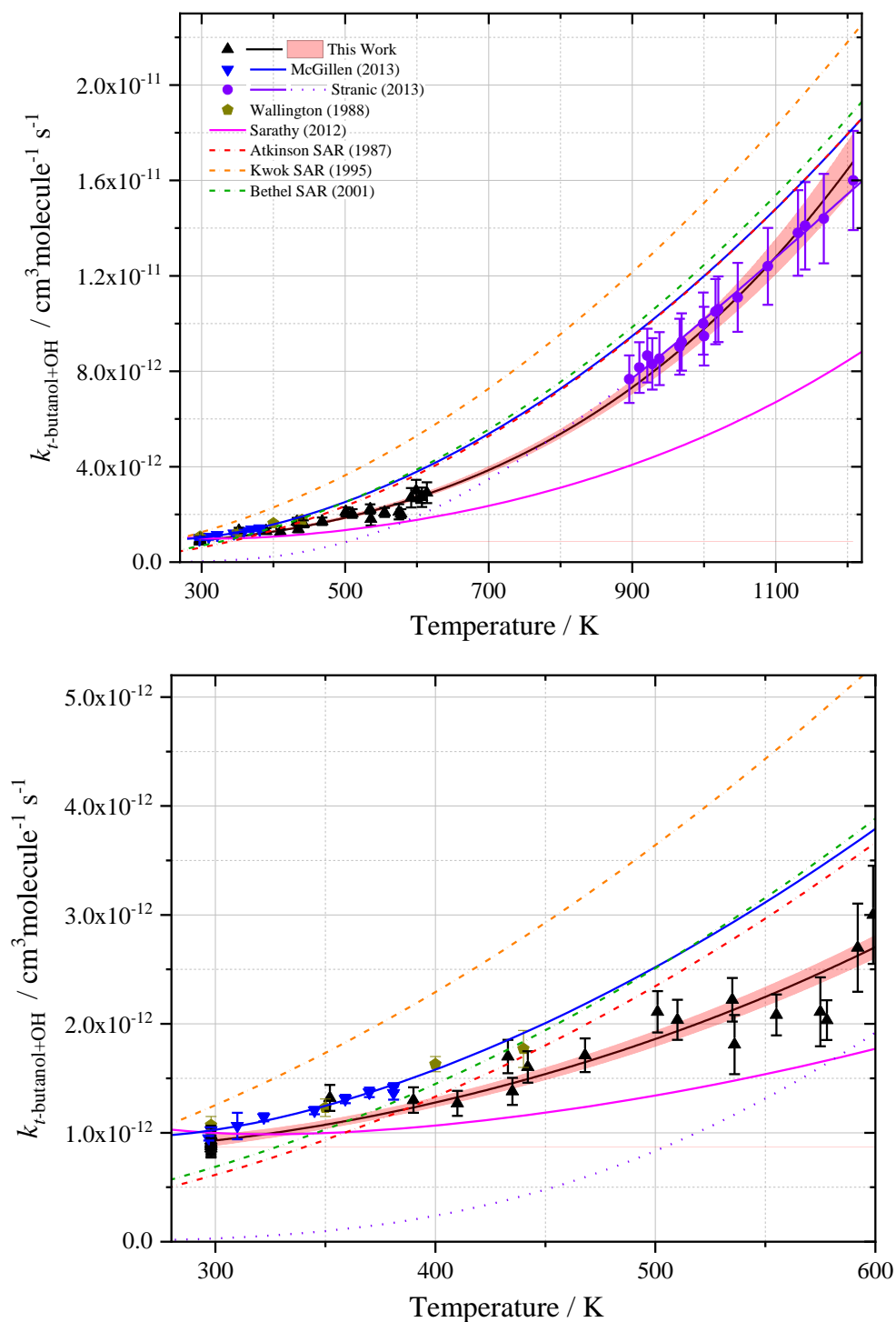


Figure 3-24: Concatenate fit to rate coefficient data for t -butanol + OH reaction: This work (black triangles, black solid line, 95 % confidence limits in red shaded region), with the modified Arrhenius parameterisation constrained to the high temperature data of Stranic *et al.* (purple circles, purple solid line and dashed line for extrapolated region). Compared with McGillen *et al.* (blue inverted triangles, blue solid line), Wallington *et al.* (olive hexagons) experimental data; Sarathy *et al.* (solid pink line) calculation; SAR of Atkinson (red dot-dash line), Kwok and Atkinson (orange dot-dash line) and Bethel *et al.* (green dot-dash line). Data replicated from [78], [76], [127], [55], [114], [130] and [101].

As the Stranic *et al.* experimental data were measured using isotopically labelled *t*-butan-¹⁸ol, there is no interference from the unimolecular decomposition β -recycling channel, and therefore this can be assumed to be an accurate measurement of the total OH abstraction rate at these high temperatures.

Each of the Structure-activity relationship total abstraction ratios overestimate the rate of reaction of OH with *t*-butanol, with the update of Kwok and Atkinson overestimating the total abstraction rate at 500 K by almost a factor of two. Whilst the curvature of the temperature dependence for the total rate of abstraction is well captured, the SAR parameterisations are consistently faster than the experimentally measured values over all temperatures above 400 K.

The updated total bimolecular rate coefficient obtained in this work for the reaction of *t*-butanol with the hydroxyl radical has been used in combustion modelling in Section 5.4.3 of this thesis, to investigate the effect of updating this rate constant on the modelled ignition delay time.

3.7.2 Conclusion

The bimolecular reaction between OH and *t*-butanol has been measured across the temperature range 298 – 615 K, across pressures of 30 – 89 Torr. The average room temperature rate coefficient, $k_{t\text{-butanol}+\text{OH}} = (0.91 \pm 0.09) \times 10^{-12} \text{ cm}^3 \text{ molecule}^{-1} \text{ s}^{-1}$, with the error reported at the 1σ level, was measured in excellent agreement within experimental error with previous experimental literature.

The experimental data at temperatures between 298 K and 400 K was in good overall agreement with the previous temperature dependent studies by McGillen *et al.* [78] and Wallington *et al.* [127]. The modified Arrhenius temperature parameterisation of McGillen *et al.* is faster than the parameterisation of this work across all temperatures studied, and the structure-activity relationships of Atkinson [114], Kwok [130] and Bethel *et al.* [101] also show relatively poor agreement with this work, particularly that of Kwok. Excellent agreement is obtained from a concatenate fit to this work and the high temperature experimental data obtained by Stranic *et al.* [76], significantly reducing the uncertainties in the total bimolecular rate coefficient for *t*-butanol with OH at temperatures between 400 K and 900 K.

3.8 Isomer Comparison

For each of the isomers studied, good agreement was obtained with all previous literature studies, particularly with the temperature dependent parameterisations by McGillen *et al.* The previous literature experimental studies for each isomer agreed with the values obtained in this work at 298 K within the uncertainties provided, with the most significant disagreement occurring between the measurement for *i*-butanol in this work and that of Andersen *et al.* [84], which disagree by approximately 27 %.

The order of reactivity observed at 298 K was *n*-butanol = *i*-butanol > *s*-butanol >> *t*-butanol, ranging from $(0.9 - 9) \times 10^{-12} \text{ cm}^3 \text{ molecule}^{-1} \text{ s}^{-1}$ in magnitude. *t*-butanol measured the slowest rate coefficient across all temperatures studied, and did not display a negative temperature dependent region in this work. Temperature dependent reactivity was similar for all other isomers, with all displaying a slight negative temperature dependent region at or below 350 K, and a positive dependence above this. *n*-butanol demonstrates the strongest temperature dependence at the highest temperatures, and the fastest total rate of reaction with the hydroxyl radical at temperatures relevant to low temperature combustion.

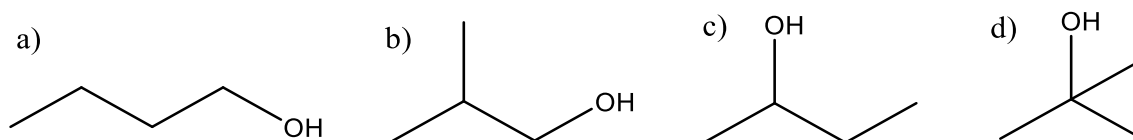


Figure 3-25: Four structures of the butanol isomers: a) *n*-butanol, b) *i*-butanol, c) *s*-butanol and d) *t*-butanol.

Given the structures of the four isomers of butanol, highlighted in Figure 3-25, the reactivity towards the OH radical can be linked to several structural features. *t*-butanol is the only of the four isomers without a potential hydrogen abstraction site alpha to the hydroxyl group. The low reactivity shown by this isomer toward the hydroxyl radical, particularly at room temperature, suggests that the alpha site contributes significantly to reactivity at low temperatures.

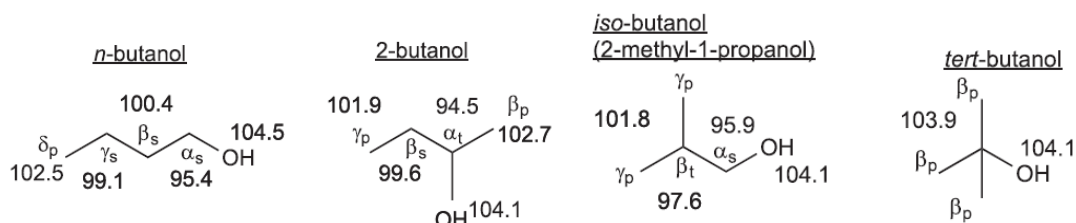


Figure 3-26: C–H Bond dissociation energies (kcal mol^{-1}) calculated at CBS-QB3 level of theory, replicated from Sarathy *et al.* [1].

The presence of an OH group weakens the C–H bond neighbouring to this in the alpha position, as seen in Figure 3-26, and thus the alpha hydrogen is the easiest to abstract. The type of C–H bond also influences the strength of the bond, for example the β -site secondary C–H bond of *n*-butanol is a stronger bond than that of the β -site tertiary C–H bond in *s*-butanol. The bond strengths demonstrated by the β C–H bonds increase in the order of tertiary C–H < secondary C–H < primary C–H, as would be expected owing to the inductive effects of the neighbouring alkyl groups. The β -primary sites in tertiary butanol have the strongest bond energies of any calculated for the butanol isomers, and thus you would expect them to have the slowest rate of reactivity towards reaction with the OH radical, as reflected in the experimental measurements made in this work.

When going to C–H environments further than the β position from the OH group, the effect of the hydroxyl group on reactivity is expected to diminish, according to Mellouki *et al.* [132]. A slight reduction in reactivity is expected when going from the β - to the γ -carbon site, and beyond these positions, the potential C–H abstraction sites are expected to behave like their unsubstituted alkane equivalents.

The bimolecular rate coefficients obtained at 298 K and the temperature dependent parameterisations can to some extent be rationalised by the C–H bond strengths. However, calculation of bimolecular rate constants and the branching ratios from calculated energies is complicated and often in poor agreement with experimentally measured values, due to the existence of multiple conformers and low energy barriers to abstraction [78] [55].

Each of the four isomers of butanol, apart from *t*-butanol, showed some degree of negative temperature dependence at the lowest temperatures studied in this work. This has been observed in the literature previously by McGillen *et al.* [78], who also observed this behaviour for *t*-butanol at temperatures below 298 K. This low (< 350 K) temperature

negative temperature dependent region is often attributed to the formation of a hydrogen-bonded pre-reactive complex. This was first suggested by Smith and Ravishankara [133], through consideration of the reaction of OH with other oxygenated species such as carboxylic acids and ketones. In their work, it was suggested that the formation of a hydrogen-bonded complex results in a lower activation energy for reaction compared to a direct H-abstraction reaction for some abstraction sites. The formation of a hydrogen bond between the O atom of the alcohol species and the H atom of the hydroxyl radical, and a second hydrogen bond between an H atom of the alcohol alkyl chain and the O atom of the hydroxyl radical, results in formation of a ring-system in which H-atom migration can occur. Some possible structures of this ring-system are shown in Figure 3-27. The extent of the influence of complex formation on the low temperature reactivity of the butanol isomers depends on the energetic barrier to abstraction and the stability of the complex formed in each case. In this work, the strongest negative temperature dependence was observed for *s*-butanol, suggesting this isomer forms the most stable complex, and results in the lowest energetic barriers for H-atom abstraction.

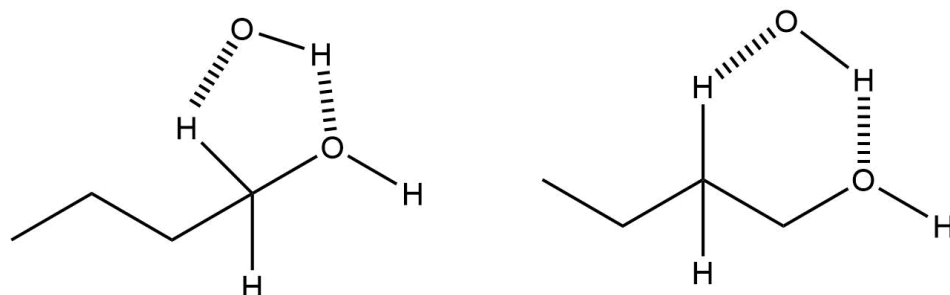


Figure 3-27: Potential pre-reactive complex structures formed during the reaction of *n*-butanol with OH. a) Five-membered ring system and b) Six-membered-ring system.

The total measured bimolecular rate coefficients are of crucial importance to developing and improving structure-activity relationships, which ultimately lead to calculations of the branching ratios for the reaction with OH. The most recent measurements of McGillen *et al.* [78] provided a good estimate of the temperature dependence for the reaction of OH with each of the butanol isomers, which has been built on in this work. Most parameterisations were in excellent agreement with this work, however the calculated parameters for *t*-butanol and *s*-butanol demonstrate some degree of disagreement.

Future work should look to calculate site specific parameterisations from this work combined with the study of McGillen *et al.* and the high temperature work of Pang *et al.* and Stranic *et al.* for each of the butanol isomers, as the total bimolecular rate coefficient for each isomer with OH is now well defined. Future work could also look into further isotope experiments, similar to those carried out by Pang *et al.* for *n*-butanol and Stranic *et al.* for *t*-butanol, to constrain the branching ratios of the different channels.

3.9 Summary

This work provides new kinetic data for reaction of OH with the butanol isomers at temperatures relevant to low temperature combustion conditions. This work has provided total reaction data for each isomer, which can be used in future in combustion modelling to constrain OH + butanol isomer reactivity. The uncertainty of the bimolecular rate coefficients for each of the isomers of butanol has been significantly reduced, by reducing the gap in the literature of experimental measurements.

A good overall agreement was observed for all isomers with the total temperature dependent parameters of the McGillen *et al.* study. Good to excellent agreement was also obtained with high temperature shock tube experimental data of Pang *et al.* and Stranic *et al.*, at temperatures above around 800 K. A concatenate fit to this work and the high temperature shock tube data was provided in each case, and can be used in future work to constrain the total reactivity of the butanol isomers in combustion modelling and structure-activity parameterisations.

Chapter 4 Unimolecular Decomposition of the β -hydroxy-butyl Isomers Following β -site Abstraction by OH

4.1 Chapter Summary

An experimental and theoretical investigation into the unimolecular decomposition of β -hydroxy-butyl radicals has been conducted. This chapter reports first order decomposition rate constants for *n*-, *i*-, *s*- and *t*-butanol over temperatures ranging from 490 – 715 K, pressures between 30 – 130 Torr in nitrogen bath gas using the laser flash photolysis-laser induced fluorescence method for detection of OH.

Ab initio calculations at the CCSD(T)/aug-cc-pVTZ//M06-2X/aug-cc-pVTZ level have been carried out using the Gaussian 09 software in conjunction with master equation analysis using the widely available Master Equation Solver for Multi-Energy well Reactions (MESMER) programme, to obtain optimised energies for the energetic barrier to this decomposition. An optimised barrier of (103.4 ± 4.0) kJ mol⁻¹ for decomposition of the *t*-hydroxybutyl radical was obtained from master equation analysis, in good agreement with the *ab initio* calculated barrier of 107.8 kJ mol⁻¹. A barrier to the decomposition of the *i*-hydroxybutyl beta radical was calculated theoretically as 99.9 kJ mol⁻¹, in reasonable agreement with the MESMER optimised barrier, (93 ± 4.0) kJ mol⁻¹. For the *n*-hydroxybutyl radical, an optimised barrier of (100.0 ± 4.0) kJ mol⁻¹ for decomposition was obtained from master equation analysis, in good agreement with the *ab initio* calculated barrier of 98.8 kJ mol⁻¹. For *s*-butanol, master equation analysis of the recycling first order rate constants was not possible, and in this case, a literature comparison of the three calculated barriers was carried out.

4.2 Introduction

R radicals formed from abstraction reactions between OH and fuel (Chapter 3) are important species in low temperature combustion. These radicals formed can decompose by unimolecular decomposition channels, or react with O₂ to form RO₂ radicals. Ultimately, the formation of RO₂ radicals leads to the chain-branching reactions integral to autoignition.

One potential mechanism of decomposition for alcohol fuel radicals is unimolecular decomposition by β -scission, resulting in formation of an OH radical and an alkene species. This mechanism of decomposition was first observed by Hess and

Tully (1988) [134], when measuring the kinetics of the reaction of OH with alcohols such as ethanol, 2-propanol and *t*-butanol. In their work, biexponential OH fluorescence decays were observed between 500 and 620 K, which they attributed to the formation of an OH radical from an OH-alkene intermediate formed from abstraction at the beta hydrogen site. Hess and Tully also conducted experiments utilising both ^{16}OH and ^{18}OH reacting with 2-propanol, with LIF monitoring of the OH radical. An example of a kinetic trace obtained in each case is shown in Figure 4-1. For the ^{16}OH fluorescence experiments, biexponential fluorescence traces were observed, compared with a linear fluorescence signal log plot obtained in the ^{18}OH experiments. This confirms the recycling of OH observed occurs from the abstraction radicals, consistent with the suggested hypothesis of decomposition of the 2-propanol radical formed at the β -site.

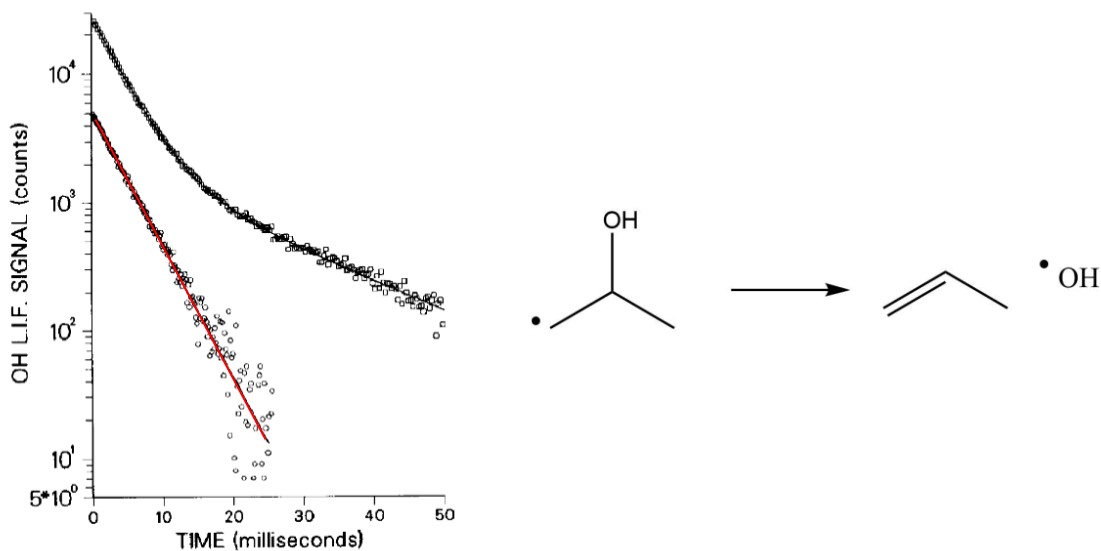


Figure 4-1: Experimental OH fluorescence traces obtained by Hess and Tully [134] for the reaction of 2-propanol ($(\text{CH}_3)_2\text{CHOH}$) with ^{16}OH (hollow squares, black solid line) and ^{18}OH (hollow circles, with red fit line added), obtained at 535 K and 544 K respectively, with radical decomposition mechanism shown for the resulting 2-propanol radical.

Further work investigating this unimolecular decomposition channel was carried out by Dunlop and Tully (1993) [135], who carried out a more extensive temperature dependent study of the reaction of 2-propanol with OH across the temperature range 293 – 745 K at 750 Torr total pressure of helium bath gas. In their work, ^{16}OH and ^{18}OH radicals were formed from the 193 nm photolysis of N_2^{16}O or N_2^{18}O in the presence of H_2O , which was monitored by LIF. For experiments conducted using ^{16}OH , biexponential traces were observed between 504 and 600 K. Above this temperature, single exponential

traces were obtained for ^{16}OH , however the pseudo-first order rate coefficients for the reaction of OH with 2-propanol were significantly smaller than those measured below 504 K.

At temperatures above 600 K, the rate of OH recycling occurring from the β -radical exceeded the initial abstraction reaction, such that OH reformed almost as fast as it reacted with the 2-propanol reagent. In order to measure the OH recycling parameter at temperatures higher than 600 K, it was noted that the concentration of 2-propanol would have to be increased by 15 times to obtain a rate for the initial abstraction reaction faster than the rate of OH regeneration. At these high concentrations, the interference from 193 nm photolysis of alcohol reagent would make the fluorescence traces obtained too complicated for analysis.

From the measured rates of the unimolecular decomposition of the 2-propanol β -radical obtained between 504 and 600 K by Dunlop and Tully [135], a barrier to unimolecular decomposition to give propene and OH was calculated as $112.5 \pm 6.3 \text{ kJ mol}^{-1}$. More recently, the kinetics of the reaction between propene and hydroxyl were studied theoretically by Zádor *et al.* [136], in which quantum chemical calculations were combined with RRKM-based master equation solving. The addition of OH to the double bond of propene was considered for addition to both the central and terminal carbons, resulting in β -radicals for 2-propanol and 1-propanol respectively. In their work, the calculated barrier to decomposition of the 1-propanol β -radical was $106.3 \text{ kJ mol}^{-1}$, compared to $110.0 \text{ kJ mol}^{-1}$ for decomposition of the equivalent 2-propanol radical. The potential energy surface (PES) calculated by Zádor *et al.* for 2-propanol is shown in Figure 4-2, with energies reported in kcal mol^{-1} , relative to the OH + propene entrance channel. This calculated barrier for 2-propanol is in excellent agreement with the value obtained by Dunlop and Tully previously.

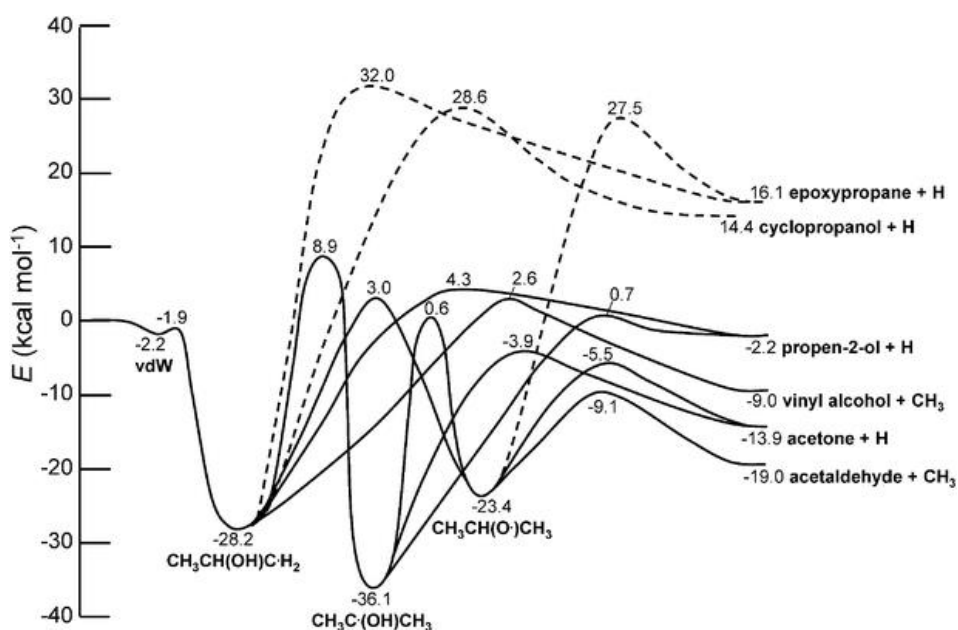


Figure 4-2: Potential energy surface calculated for the 2-propanol β -radical by Zádor *et al.*, replicated from [136]. All energies reported in kcal mol⁻¹, relative to the entrance channel of propene + OH.

The decomposition of the β -radical has been explored to some degree for *t*-butanol in high temperature pyrolysis [137] and flow reactor studies [138], with complementary modelling based on the combustion model of Grana *et al.* [121]. Qualitative experimental observations have been made by Welz *et al.* [139] for *n*-butanol radical decomposition at temperatures relevant to low temperature combustion oxidation, through the monitoring of butene end-product yield (following reaction of *n*-butanol with chlorine radicals) at 650 K and 700 K. Welz *et al.* also observed iso-butene formation for *t*-butanol and *i*-butanol radical decomposition in a separate study at 700 K utilising the same method [140]. *Ab initio* barriers for the decomposition of *n*-butanol hydroxybutyl and butoxy radicals have also been calculated by Zhang, Klippenstein and Law [141], and for *s*-butanol radical decomposition by Antonov, Kwok, Zádor and Sheps [142]. Further discussion of the methods and barriers obtained through these calculations is provided in the relevant results sections in this chapter.

Decomposition rate constants for the different β -hydroxybutyl radicals are often present in combustion models for the isomers of butanol, reported as a reversible reaction for the addition of OH to the relevant butene isomer. In the model of Grana *et al.* [121], the decomposition rate constant for the β -radical of each isomer possesses the same A factor ($3 \times 10^{13} \text{ s}^{-1}$) and an activation energy of between 138 – 146 kJ mol⁻¹. The

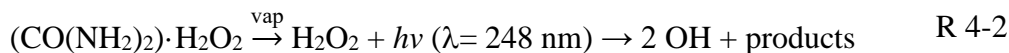
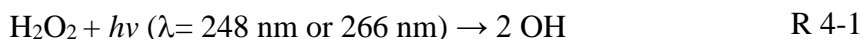
combustion model of Black *et al.* [99] for *n*-butanol reports an estimated value of the hydroxyl radical addition to *n*-butene of $9.93 \times 10^{11} \exp(483/T) \text{ cm}^3 \text{ mol}^{-1} \text{ s}^{-1}$, with the reverse calculated by microscopic reversibility. The method of Black *et al.* was also adopted in the widely used combustion model of Sarathy *et al.* [55], who used the same OH addition to butene rate for each of the four isomers reported by Black *et al.*, despite the different butene isomers involved in the decomposition reactions for the different butanol starting reagents. In the Sarathy *et al.* study however, they do state that using these rate estimates for other systems, e.g. the addition of OH to the central carbon of isobutene, warrants further investigation, as the rate of OH addition is likely to differ for addition to a tertiary carbon. From the study of Zádor *et al.* for the two isomers of propanol [136], it is unlikely that the barriers to decomposition for the four isomers of butanol are all equivalent. Consequently, kinetic investigations into the decomposition barriers for β -hydroxybutyl radicals to OH and butene is of interest to combustion modellers for improving this aspect of butanol combustion modelling.

Above approximately 480 K for each of the four butanol isomers studied in this work, biexponential OH fluorescence signal traces were observed, which has been attributed to the β abstraction site unimolecular decomposition to an alkene and an OH radical. *Ab initio* energies for the species involved have also been calculated, with the energetic barrier to decomposition optimised using master equation solving for *n*-, *i*-, and *t*-butanol. As multiple β -site radicals are formed from the reaction of OH with *s*-butanol, it was beyond the scope of this work to optimise the multiple energetic barriers to this decomposition, and therefore an extensive literature comparison has been conducted for this isomer. The *ab initio* computational calculations for *t*-butanol decomposition to OH and iso-butene were carried out by Dr. Diogo J. Medeiros.

4.3 Experimental

All experiments were conducted using laser flash photolysis-laser induced fluorescence and the flow system described in Chapter 2.7. OH radicals were generated from pulsed laser photolysis (10 Hz) at 248 nm (KrF Excimer laser) or 266 nm (3rd harmonic of a pulsed Nd:YAG laser) of hydrogen peroxide precursor, with some experiments conducted using urea hydrogen peroxide (UHP) precursor. Experiments were also conducted using oxalyl chloride ((COCl)₂) precursor as a chlorine radical

source for *t*-butanol and *i*-butanol. The specific experimental details relating to these experiments can be found in their respective results sections.



Hydrogen peroxide was delivered via a flow of nitrogen over a reservoir of liquid hydrogen peroxide in a pressurised bubbler, positioned upstream of the mass flow controller (MFC). Urea hydrogen peroxide was introduced by flowing a steady stream of nitrogen over the top of a small amount of solid urea hydrogen peroxide, placed in the bottom of a pressurised bubbler. This bubbler was then placed in a water bath maintained at 298 K to ensure a stable amount of hydrogen peroxide was released from the solid precursor. For experiments using oxalyl chloride, a bulb of known concentration was made of the precursor in nitrogen bath gas.

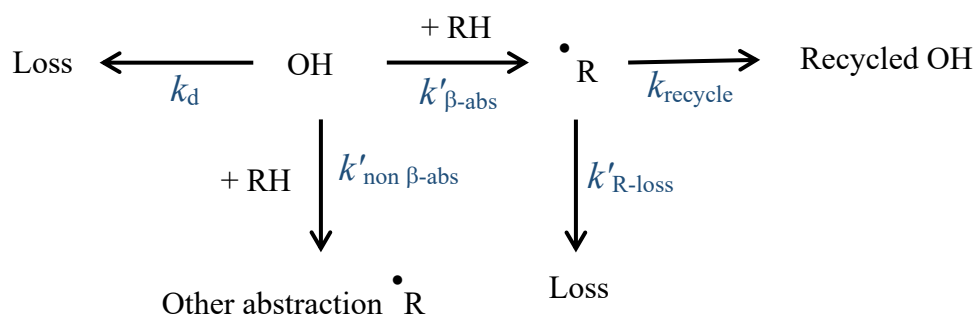
OH radicals were detected using laser induced fluorescence with detection at approximately 308 nm. All experiments, with the exception of *t*-butanol, were conducted utilising on-resonant fluorescence, with 308 nm probe laser light generated from the doubling of a Nd:YAG-pumped dye laser (utilising DCM special dye). For off-resonant fluorescence for *t*-butanol, 282 nm probe laser light was generated from the frequency doubling of a Nd:YAG-pumped dye laser operating on Rhodamine 6G dye.

Total pressures were typically maintained at 30 – 130 Torr, with the experimental conditions found in the summary table for each isomer in the subsections of this chapter. Alcohol reagent diluted in nitrogen was delivered using the bubbler method outlined in Section 2.7.1.3.

Chemicals used: *n*-butanol (Sigma-Aldrich, ≥ 99.4 %), *i*-butanol (Sigma-Aldrich, ≥ 99.0 %), *s*-butanol (Sigma-Aldrich, ≥ 99.5 %), *t*-butanol (Sigma-Aldrich, ≥ 99.0 %), hydrogen peroxide/water (H_2O_2 , Sigma-Aldrich, 50 % (w/w) in H_2O), urea hydrogen peroxide ($(\text{CO}(\text{NH}_2)_2) \cdot \text{H}_2\text{O}_2$, UHP, Sigma-Aldrich, 97 %), oxalyl chloride ($(\text{COCl})_2$, Sigma Aldrich ≥ 99 %). Nitrogen (BOC, 99.99 %) gas was used straight from the cylinder.

4.3.1 Kinetics and Analysis

Kinetic traces obtained in this temperature range exhibited biexponential behaviour, and therefore required fitting with a more complex fitting equation. The biexponential equation was previously derived by Dr L. Onel at the University of Leeds, and further explanation of the derivation can be found in previous publications [143], [88]. The parameters obtained from the biexponential fit are outlined in Scheme 4-1: $k'_{\beta\text{-abs}}$, the pseudo-first order rate coefficient for the abstraction reaction at the β site of the alcohol, $k'_{\text{non } \beta\text{-abs}}$, the pseudo-first order rate coefficient total for abstraction at the other possible abstraction sites, k_{recycle} , the rate coefficient for the reforming of OH from the R radical generated by $k'_{\beta\text{-abs}}$, $k'_{\text{R-loss}}$, the other loss processes for this R radical, and k_d , other removal processes for OH (as before in the single exponential equation). The full fitting equations are outlined E 4-1 – E 4-6.



Scheme 4-1: Obtained kinetic parameters from biexponential fit to experimental traces.

$$S = -(k'_d + k'_{\beta\text{-abs}} + k'_{\text{non } \beta\text{-abs}}) \quad \text{E 4-1}$$

$$M1 = k'_d + k'_{\beta\text{-abs}} + k'_{\text{non } \beta\text{-abs}} + k_{\text{recycle}} + k'_{\text{R-loss}} \quad \text{E 4-2}$$

$$M2 = (k'_d + k'_{\beta\text{-abs}} + k'_{\text{non } \beta\text{-abs}}) \times (k_{\text{recycle}} + k'_{\text{R-loss}}) - k'_{\beta\text{-abs}} \times k_{\text{recycle}} \quad \text{E 4-3}$$

$$L1 = \frac{(-M1 + \sqrt{M1^2 - 4 \times M2})}{2} \quad \text{E 4-4}$$

$$L2 = \frac{(-M1 - \sqrt{M1^2 - 4 \times M2})}{2} \quad \text{E 4-5}$$

$$y = \text{OH} \times \left(\frac{(S-L2)}{(L1-L2)} \right) \times \exp^{(L1 \times t)} - \exp^{(L2 \times t)} + \exp^{(L2 \times t)} \quad \text{E 4-6}$$

A yield parameter has also been defined as:

$$\text{OH Yield \%} = \frac{k_{\text{recycle}}}{k_{\text{recycle}} + k_{\text{non-OH}}} \times 100 \quad \text{E 4-7}$$

where $k_{\text{non-OH}} = k'_{\text{R-loss}} + k'_{\text{non } \beta\text{-abs}}$. The pseudo first order rate coefficients are defined relative to each isomer in the subsequent discussion sections, respective to the relevant isomer.

4.3.2 Master Equation Analysis

Using vibrational frequencies, rotational constants, zero point energies and absolute energies calculated using *ab initio* methods, master equation solving can be conducted. In this work, energy grained master equation (EGME) solving was conducted using the widely available Master Equation Solver for Multi-Energy well Reactions (MESMER) programme [144].

For master equation solving, all reactants, products and transition states must be defined, and the energy levels within each species are then partitioned into “grains” of a set energy width. Reactive loss and gain across the grains in the system is modelled using unimolecular rate coefficients calculated from RRKM theory as described previously, and the collisional energy transfer between grains is then modelled using the exponential down term, $\langle \Delta E \rangle_{\text{down}}$, which describes the average energy transferred on collision with the bath gas. A representation of a model formed for EGME solving for a typical association reaction is shown in Figure 4-3.

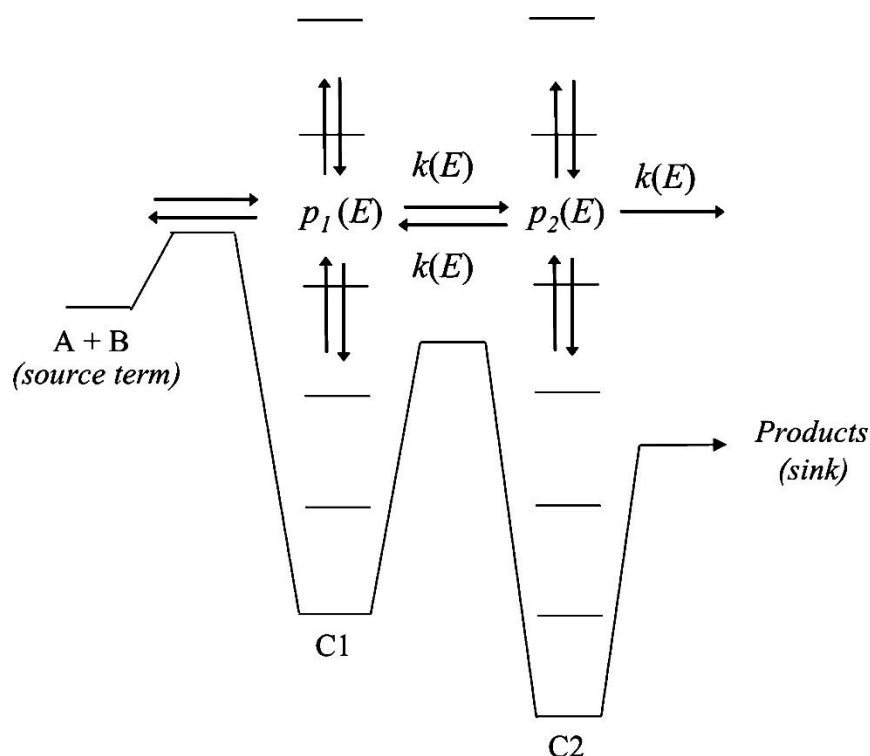


Figure 4-3: Representation of a model for Energy Grained Master Equation (EGME) solving for a typical association reaction, replicated from Glowacki *et al.* [144]

By providing MESMER with experimental measurements of rate coefficient data, a potential energy surface calculated by *ab initio* methods can be optimised through fitting using the Marquardt algorithm. The optimisation process acts to reduce the value of the statistical measure of goodness of fit, χ^2 , for a set of experimental parameters, described by equation E 4-8:

$$\chi^2 = \sum_{i=1}^N \left(\frac{(k_{i,\text{ob}}(p_i, T_i) - k_{i,\text{mod}}(p_i, T_i))^2}{\sigma_i^2} \right) \quad \text{E 4-8}$$

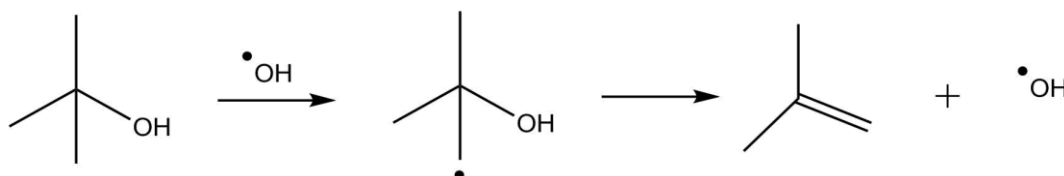
where $k_{i,\text{ob}}(p_i, T_i)$ is the experimentally measured rate, $k_{i,\text{mod}}(p_i, T_i)$ is the modelled value at the same conditions, and σ_i^2 is an estimate of the error in the experimentally observed value.

In this work, MESMER models were constructed for the decomposition of the β -hydroxybutyl radicals formed for each butanol isomer to an OH radical and the relevant butene isomer *via* a transition state structure. The energetic barrier to decomposition of

each abstraction radical to OH and butene was entered as a variable parameter, and allowed to optimise to minimise the total value of χ^2 for the experimental data points obtained for each radical. Following this optimisation, MESMER calculated values for the decomposition rate coefficient k_{recycle} were compared to the experimentally obtained values for given temperatures and pressures, and also simulated values at the high pressure limit have been calculated.

4.4 *t*-Butanol

The first isomer that will be considered in this chapter is *t*-butanol, as it represents the structurally simplest butanol isomer due to only possessing one unique C–H abstraction site. Following the abstraction of H from any of the nine equivalent β_{prim} sites by OH, a β -hydroxybutyl radical is formed, which can eliminate the hydroxyl moiety and form isobutene via β -scission, the possible pathway for which can be seen in Scheme 4-2.

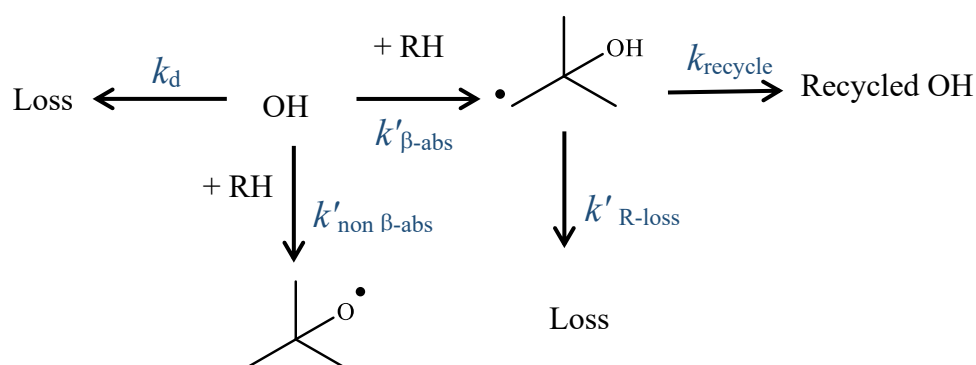


Scheme 4-2: Decomposition mechanism following β -site abstraction from *t*-butanol.

Decomposition of the *t*-butanol β -hydroxybutyl radical has been observed previously in high temperature shock tube studies by Stranic *et al.* [76], who conducted experiments using both *t*-butan¹⁸ol and *t*-butan¹⁶ol with OH. In their work, noticeably smaller bimolecular rate coefficients were obtained when fitting the OH decay profiles for the reaction of *t*-butan¹⁶ol with OH, as a consequence of the unimolecular recycling. When fitting the ¹⁶OH decay profiles for the reaction of *t*-butan¹⁸ol with OH, the ¹⁸OH recycling from the *t*-butanol radical formed would not be observed, and therefore the measured rate coefficients in this case accurately reflect the measurement of OH with *t*-butanol. A low pressure, high temperature pyrolysis study by Cai *et al.*[137] also measured significant production of iso-butene, which was attributed to two channels: decomposition of the *t*-butanol precursor by H₂O elimination, and 99 % of the decomposition of the *t*-hydroxybutyl radical.

Whilst the production of OH and the co-product isobutene have been observed in the literature before, a direct measurement of the rate at which this unimolecular decomposition occurs has not been measured previously. This thesis aims to measure the rate of this β -scission reaction across a range of temperatures and pressures, and calculate the energy barrier to decomposition.

4.4.1 Experimental results



Scheme 4-3: Obtained kinetic parameters for *t*-hydroxybutyl radical decomposition biexponential fit to experimental traces.

The parameters that are obtained from the biexponential fit are outlined in Scheme 4-3: $k'_{\beta\text{-abs}}$, the pseudo-first order rate coefficient for the abstraction reaction at any of the equivalent CH_3 groups; $k'_{\text{non } \beta\text{-abs}}$, the pseudo-first order rate coefficient for abstraction at the OH group; k_{recycle} , the rate coefficient for the reforming of OH from the R radical generated by $k'_{\beta\text{-abs}}$; $k'_{\text{R-loss}}$, the other loss processes for this R radical, such as the reaction with the small amount of oxygen present; and k_d , other removal processes for OH (as before in the single exponential equation).

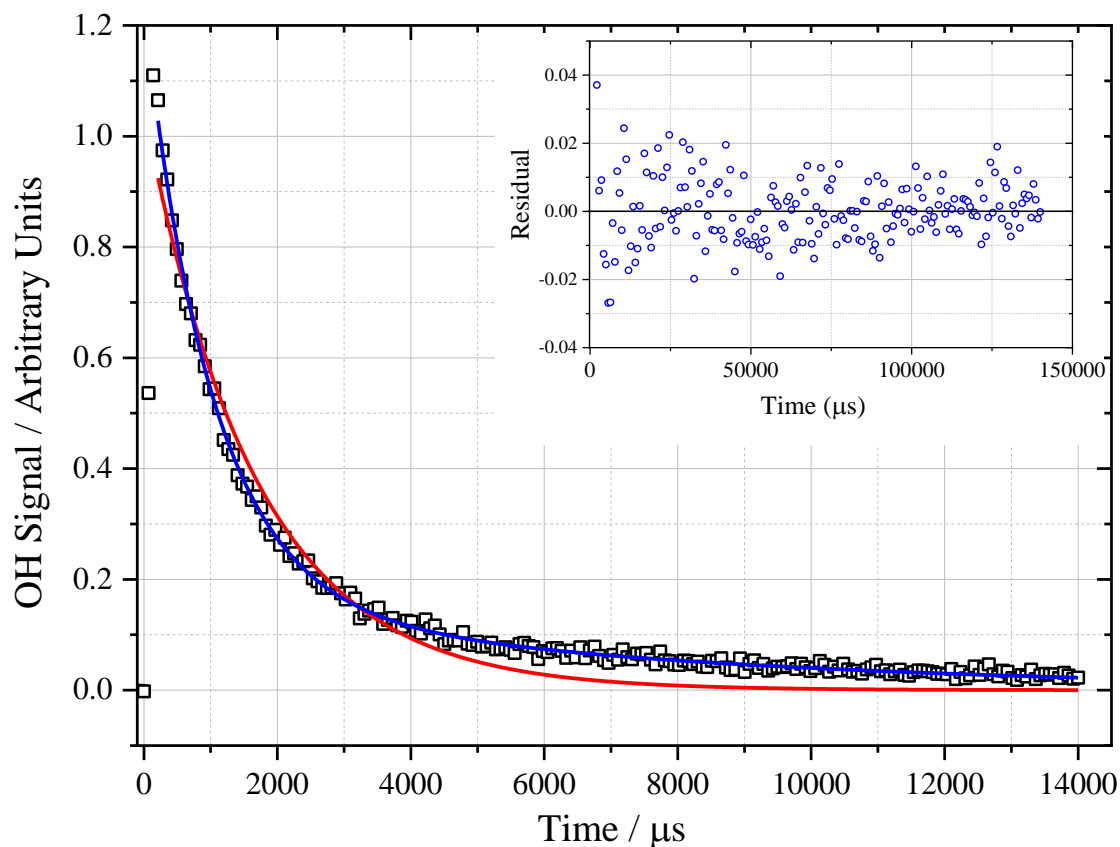


Figure 4-4: A typical kinetic trace obtained above 480 K, where the red line is the single exponential fit from Section 2.7.4, equation E 2-26, ($k' = (6040 \pm 270) \text{ s}^{-1}$) and the blue line is the biexponential function (E 4-6) ($k'_{\beta\text{-abs}} + k_{\text{non}'\beta\text{-abs}} = (9240 \pm 180) \text{ s}^{-1}$, $k_{\text{recycle}} = (870 \pm 50) \text{ s}^{-1}$). The errors obtained are statistical uncertainty at 2σ . The trace was obtained at 535 K, 50 Torr, $[t\text{-butanol}] = 8 \times 10^{15} \text{ molecule cm}^{-3}$. The inset to the figure shows the residual plot of the biexponential equation fitting to trace.

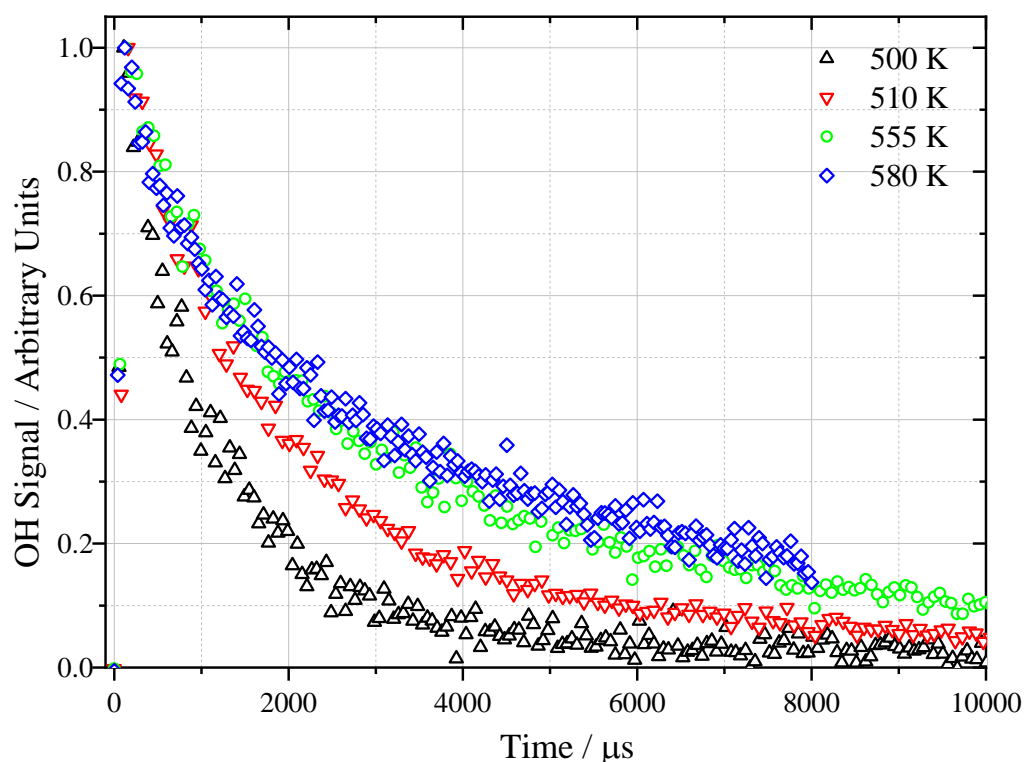


Figure 4-5: Increasing biexponential behaviour observed for increasing temperature. All experiments conducted around 30 Torr with $[t\text{-butanol}] \approx (2\text{-}2.5) \times 10^{14}$ molecule cm^{-3} .

With increasing temperature, the rate of unimolecular decomposition of β -hydroxybutyl radicals to produce OH and iso-butene increases, which is demonstrated by the more prevalent biexponential behaviour observed in the highest temperature traces shown in Figure 4-5. The kinetic parameters obtained when fitting biexponential traces can be seen in Scheme 4-3. The k_d parameter was fixed at a value, typically around $100 - 200 \text{ s}^{-1}$, obtained from a kinetic trace measured in the absence of any alcohol reagent at each given temperature, and the total removal ($k'_{\beta\text{-abs}} + k'_{\text{non } \beta\text{-abs}}$) was obtained by globally sharing the parameter k_{bim} .

In order to ensure meaningful rate coefficients were obtained from the biexponential analysis of kinetic traces, $[t\text{-butanol}]$ was kept sufficiently high, such that $k'_{\beta\text{-abs}} + k'_{\text{non } \beta\text{-abs}} > k_{\text{recycle}}$, maintaining good separation of the initial fast decay and the recycling in the long tail [135]. As the parameter k_{recycle} represents a unimolecular reaction, it is independent of concentration, and therefore was obtained by sharing the parameter globally across a series of traces for a given temperature and pressure. Similarly, the loss parameter $k_{\text{non-OH}}$ was shared across traces. The globally obtained k_{recycle} parameters can be seen summarised in Figure 4-6 as a function of both temperature

and pressure. The error values reported are the 1σ errors obtained from the biexponential global fit to the experimental traces multiplied by a factor of 4. As mentioned previously, the global fit regime produces errors that are unrealistically small when considering the errors involved in the experimental procedure, and thus this scaling factor was used to account for systematic uncertainties whilst retaining the relative uncertainties resulting from the least squares fit to the data, to allow for appropriate weighting in the master equation analysis.

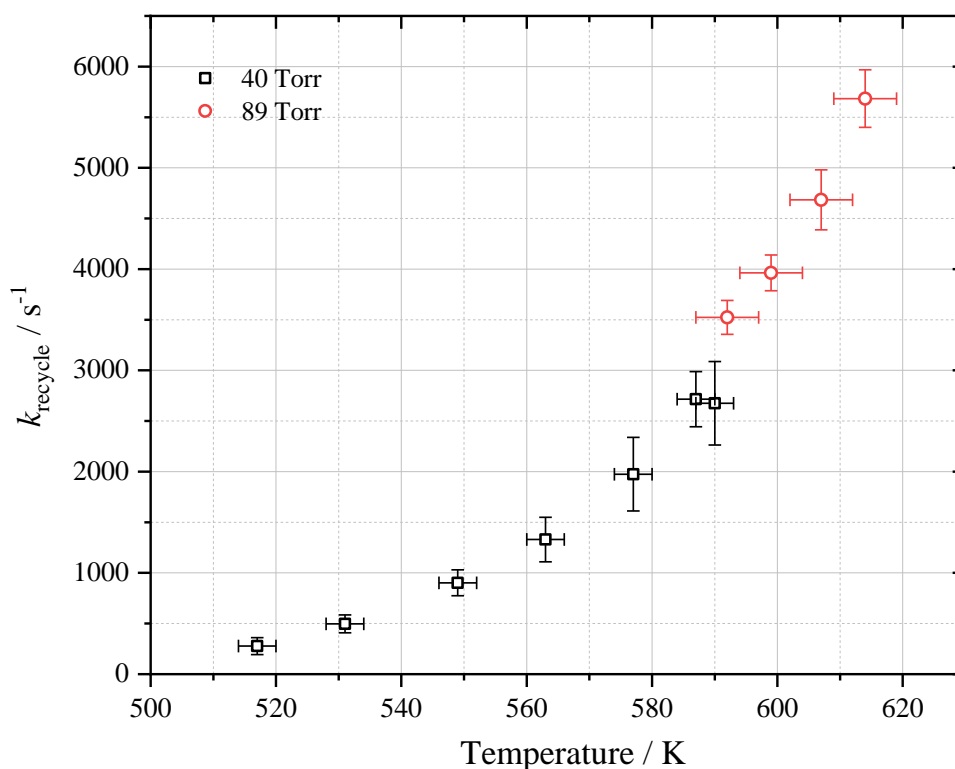


Figure 4-6: Globally obtained k_{recycle} for *t*-butanol β -hydroxybutyl radical. Parameters shown as a function of temperature and pressure. The errors reported in temperatures are ± 3 K for pressures around 40 Torr and ± 5 K for pressures around 89 Torr, and the errors reported for the experimental k_{recycle} values are the 1σ errors obtained from the biexponential global fit to the experimental traces multiplied by a factor of 4.

Table 4-1: Summary of experimental conditions and obtained OH recycling parameter k_{recycle} for *t*-butanol.

T / K	Pressure / Torr	Precursor	Globally obtained $k_{\text{recycle}} / \text{s}^{-1}$	Globally obtained $k_{\text{non-OH}} / \text{s}^{-1}$	Yield / %
517	39	H ₂ O ₂	277 ± 21	8 ± 58	97 ± 22
531	39	H ₂ O ₂	497 ± 22	40 ± 34	92 ± 8
549	39	H ₂ O ₂	902 ± 32	34 ± 24	96 ± 5
563	40	H ₂ O ₂	1330 ± 55	54 ± 27	96 ± 6
577	40	H ₂ O ₂	1975 ± 91	124 ± 34	94 ± 6
587	42	H ₂ O ₂	2716 ± 68	651 ± 22	81 ± 3
590	38	H ₂ O ₂	2675 ± 103	161 ± 32	94 ± 5
592	88	H ₂ O ₂	3523 ± 42	878 ± 15	80 ± 1
599	88	H ₂ O ₂	3963 ± 44	1183 ± 24	77 ± 1
607	87	H ₂ O ₂	4684 ± 74	1313 ± 39	78 ± 2
614	89	H ₂ O ₂	5136 ± 71	1322 ± 21	79 ± 1

The OH formation rate k_{recycle} can be expressed as a percentage of the total removal of the R radicals formed, k_{recycle} and $k_{\text{non-OH}}$, where $k_{\text{non-OH}} = k'_{\text{R-loss}} + k'_{\text{non } \beta\text{-abs}}$, defining the OH yield as equation E 4-7, as defined previously:

$$\text{OH Yield \%} = \frac{k_{\text{recycle}}}{k_{\text{recycle}} + k_{\text{non-OH}}} \times 100 \quad \text{E 4-7}$$

This yield represents the percentage of abstraction reactions that reform OH via the suggested route in Scheme 4-3 following abstraction at the methyl groups, as there is no known route to reform OH from the oxygen centred radical formed from abstraction at the hydroxyl group. The calculated OH yields with the propagated errors from global fitting for the individual parameters obtained can be seen in Table 4-1.

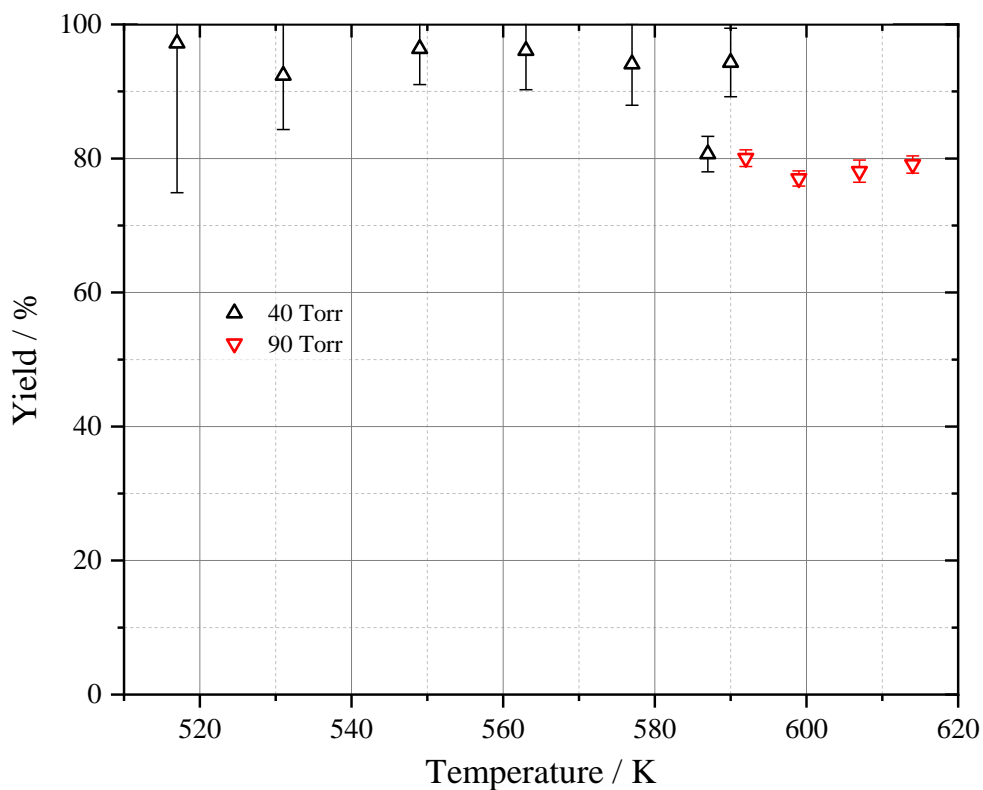
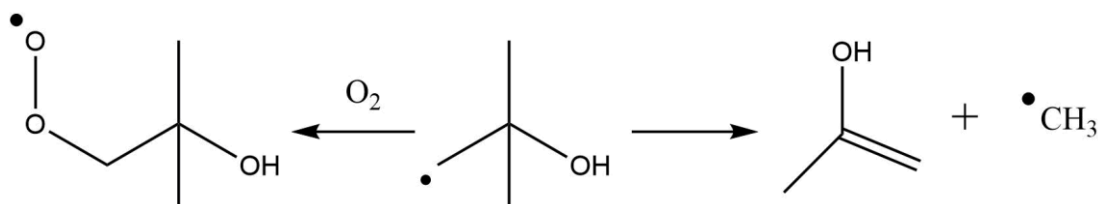


Figure 4-7: Graph of OH yield (% , percentage of abstraction reactions that reform OH via the suggested route in Scheme 4-3) against temperature (K), conducted at 40 – 90 Torr. Error bars represent propagated errors of k'_{R-loss} and k_{non-OH} obtained from single trace analysis.

The measured k_{non-OH} parameter represents other loss processes for the R radicals generated during the initial abstraction that do not result in the reformation of OH. Some of this loss could stem from the reaction of the C_4H_8OH radical with the small amount of residual oxygen present in the system to form a stable RO_2 radical, or loss through other decomposition channels, such as that to propenol and CH_3 , as highlighted in Scheme 4-4.



Scheme 4-4: Other potential fates of C_4H_8OH radical not resulting in recycled OH.

As discussed in the experimental methods, delivery of hydrogen peroxide precursor into the reaction cell results in a residual amount of oxygen also being delivered. Using the method described by Potter *et al.* [88], the amount of oxygen estimated to be in the system has been calculated as 2.0×10^{14} molecule cm^{-3} for experiments at total cell pressures around 40 Torr at 298 K, and 2.4×10^{14} molecule cm^{-3} for experimental pressures around 90 Torr at 298 K. The reaction of $\text{C}_4\text{H}_8\text{OH}$ with oxygen could contribute to $k_{\text{non-OH}}$. However, $\text{R} + \text{O}_2$ reactions have a weak temperature dependence, unlike the β -hydroxybutyl radical decomposition; the weak dependence of the yield on temperature suggests that this contribution to $k_{\text{non-OH}}$ is not major.

4.4.2 *Ab initio* calculations and Master Equation analysis

The optimized geometries of the β -hydroxy species, the resulting OH and iso-butene species, and the transition state were all obtained at the DFT level M06-2X/aug-cc-pVTZ [145] using the Gaussian 09 program [146]. The M06-2X suite of functionals were used for optimisations of all structures, as these calculations are widely thought of as being the optimum set for calculating main group kinetics. The optimized structures were then used to calculate the single point energies at the CCSD(T)/CBS level [147, 148]. Further information regarding the convergence criteria and the calculations carried out can be found in Appendix C. The harmonic oscillator approximation was used for the majority of the vibrational frequency density of state calculations, however for the β -hydroxy radical species reactant, two bonds were treated with the hindered rotor approximation (highlighted in Figure 4-8). These bonds were treated with the hindered rotor approximation as this has been found to better describe the density of states found within the species of interest when carrying out master equation analysis [149]. The descriptions of these hindered rotors were obtained through a relaxed scan of each dihedral angle at 15° steps, with optimisations carried out at the M06-2X/aug-cc-pVTZ at each step, and were used during the master equation solving. For the alternative decomposition channel to methyl and propenol, the optimised structures were also obtained at the M06-2X/aug-cc-pVTZ level, and the single point energies were calculated at the less computationally expensive CCSD(T)/aug-cc-pVTZ level (the energetic barrier to OH and iso-butene formation was also carried out at this level of theory for comparison).

Using these calculated energies and vibrational frequencies, master equation modelling was also conducted using the Master Equation Solver for Multi Energy well Reactions (MESMER) package [144]. The values of k_{recycle} calculated by MESMER were compared with experiment with the barrier for $\text{C}_4\text{H}_8\text{OH}$ decomposition to OH and iso-butene as a variable parameter. The use of master equation calculations also allows for investigation into the pressure dependence of the unimolecular decomposition process, and for this dependence to be parameterised. The potential energy surface obtained can be seen in Figure 4-9, with energies (in kJ mol^{-1}) relative to OH + iso-butene, the energies of which were calculated separately and added together, and have been defined as zero.

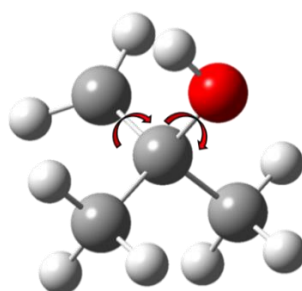


Figure 4-8: Rotations described by hindered rotor approximation (highlighted by red arrows)

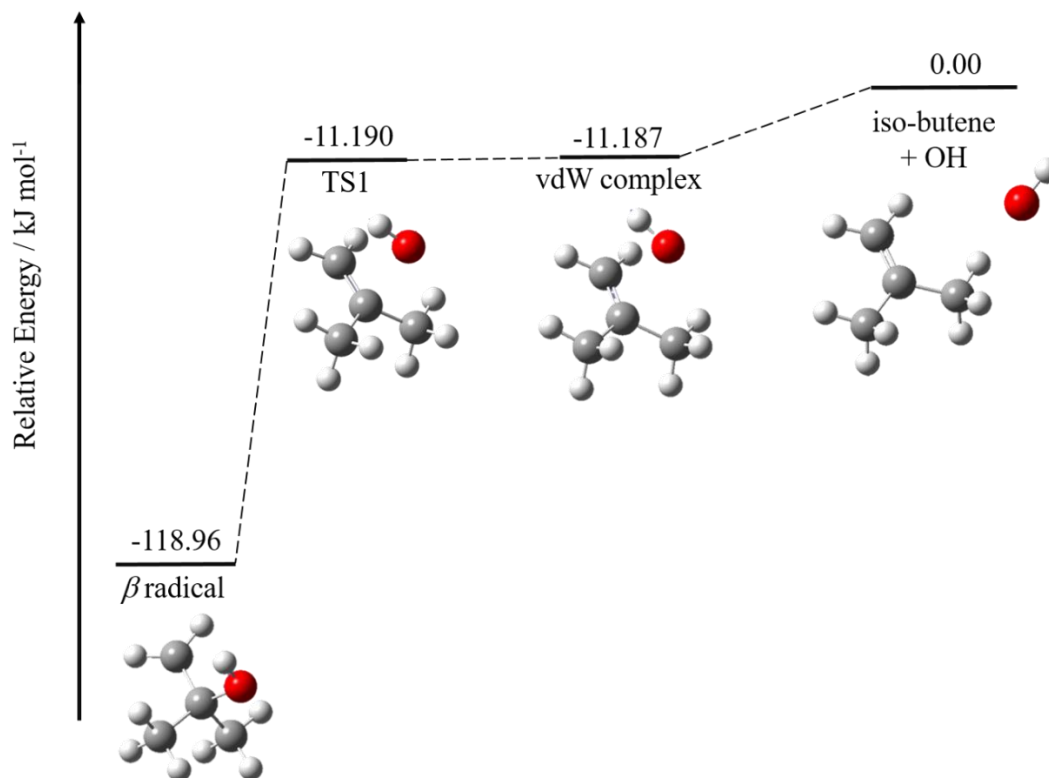
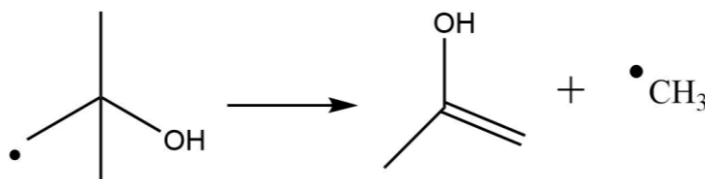


Figure 4-9: Potential energy surface for the decomposition of β *t*-hydroxybutyl radical, calculated at CCSD(T)/CBS//M06-2X/aug-cc-pVTZ level.

An *ab initio* calculated barrier for the decomposition of the hydroxybutyl radical to produce a methyl radical and a propenol co-product (shown in Scheme 4-5) was calculated as $128.8 \text{ kJ mol}^{-1}$ at the M06-2X/aug-cc-pVTZ level. This is approximately 21.1 kJ mol^{-1} higher than the barrier to decomposition to give OH and isobutene at the equivalent calculation level ($107.1 \text{ kJ mol}^{-1}$).



Scheme 4-5: Decomposition of the *t*-hydroxybutyl radical to give 2-propenol and a methyl radical.

The MESMER fit to the experimental rate coefficients obtained predicts a barrier of $(103.4 \pm 4.0) \text{ kJ mol}^{-1}$ for β -scission, with the error quoted encompassing the error calculated by MESMER (1.3 kJ mol^{-1}) and an estimate of the systematic errors, in good agreement with the *ab initio* calculated barrier for the transition state, $107.8 \text{ kJ mol}^{-1}$. Figure 4-10 shows that the experimentally obtained k_{recycle} values are in reasonably good agreement with MESMER predicted rate coefficients across all of the pressures and temperatures studied, with the largest discrepancy observed at the highest temperatures studied. Figure 4-10 also includes an error in the temperature reported for the experimentally obtained k_{recycle} values. The experiments conducted at temperatures below 590 K (40 and 50 Torr, typically around 1 L min^{-1} flow) have an estimated error in the temperature of $\pm 3 \text{ K}$, and those at the highest temperatures (89 Torr total pressure, typical flow 2 L min^{-1}) have an estimated associated error of $\pm 5 \text{ K}$. This larger error at the highest temperatures studied could aid in explaining the discrepancy between the MESMER predicted rate coefficients and the experimentally obtained values of k_{recycle} . Figure 4-10 also shows the MESMER predicted values for the unimolecular decomposition at a pressure of 8000 Torr, demonstrating that the majority of experiments conducted here were not carried out at the high pressure limit of the reaction.

The decomposition barrier obtained by Dunlop and Tully for the 2-propanol hydroxyl radical was calculated as $(112.6 \pm 6.3) \text{ kJ mol}^{-1}$, obtained from an Arrhenius fit to the experimental data obtained over a relatively narrow temperature range

(approximately 60 K) [135]. This is a comparable energy to the barrier estimated by master equation fitting in this work, (103.4 ± 4.0) kJ mol⁻¹, for unimolecular decomposition of the β -hydroxy *t*-butanol radical. The lower energy for β -scission of the *t*-butanol radical can be rationalised by the presence of two methyl groups, compared to the methyl and hydrogen R groups of the 2-propanol radical. The presence of two inducting methyl groups in *t*-butanol would weaken the C-OH bond compared to that of 2-propanol, resulting in a lower barrier to the breaking of this bond to form the alkene-OH complex.

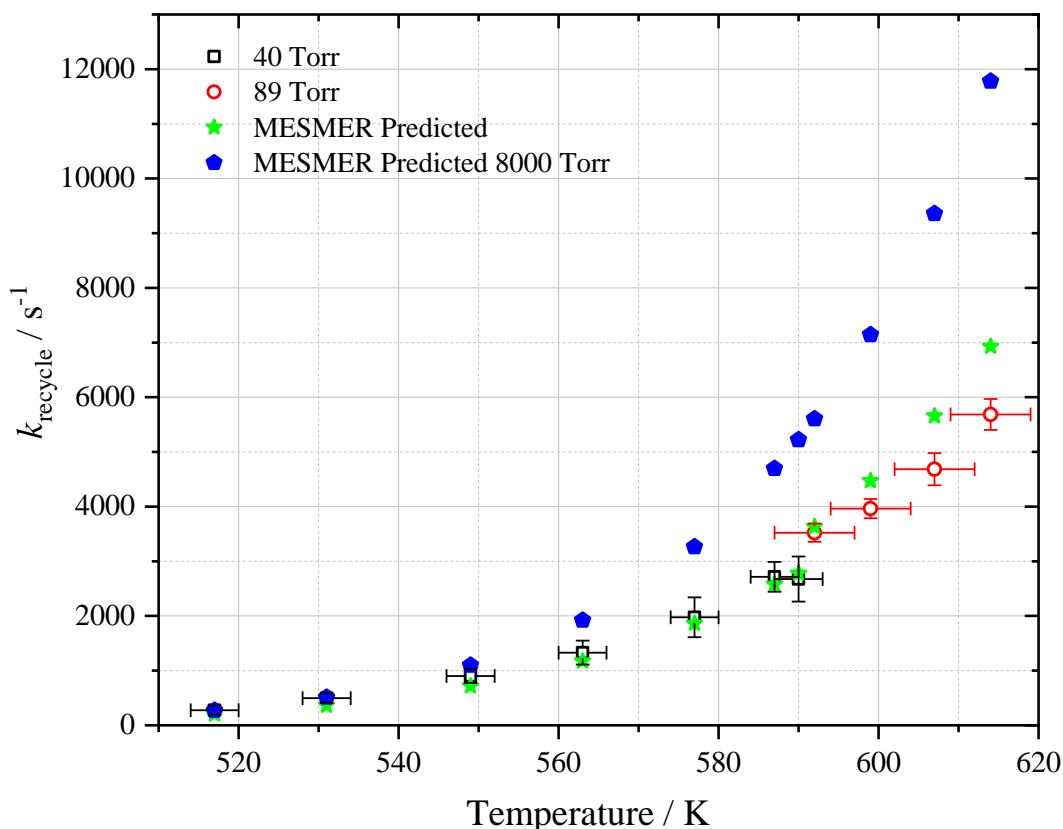


Figure 4-10: Globally obtained k_{recycle} for *t*-butanol β -hydroxybutyl radical decomposition as a function of temperature and pressure, compared with corresponding MESMER fitted values and MESMER high pressure limit predicted values for decomposition. Decomposition barrier estimated by MESMER = (103.4 ± 1.3) kJ mol⁻¹. The errors reported in temperatures are ± 3 K for pressures around 40 Torr and ± 5 K for pressures around 89 Torr, and the errors reported for the experimental k_{recycle} values are the 1σ errors obtained from the biexponential global fit to the experimental traces multiplied by a factor of 4.

4.4.3 Discussion of Branching Ratios

Both this work and that of Stranic *et al.* [76] measure an overall OH regeneration yield which is a combination of the branching ratio of the initial abstraction ($BR1 = k'_{\beta\text{-abs}} / (k'_{\beta\text{-abs}} + k'_{\text{non-}\beta\text{-abs}})$) and of hydroxybutyl decomposition ($BR2 = (k_{\text{recycle}} / (k_{\text{recycle}} + k_{\text{non-OH}}))$) with other minor loss processes such as diffusional loss and reaction of hydroxybutyl with oxygen.

In the study of Stranic *et al.* [76], the following method for analysing the OH yield was adopted. The parameter ‘BR1BR2’ was defined as the branching ratio of the initial abstraction channel (BR1) multiplied by the branching ratio of the resulting β -radical (BR2). Across the entire temperature range studied (900 – 1200 K), the value of BR1BR2 was approximately equal to 0.8. The initial abstraction branching ratio, BR1, was estimated as 96 ± 6 % in the Stranic *et al.* study, based on a calculation for the reaction rate coefficient of $k'_{\text{non-}\beta\text{-abs}}$ assuming a similar bond dissociation energy for the O–H bond to that of *n*-butanol, obtained from the Zhou, Simmie and Curran calculations [112]. This implies that BR2 is 0.83 ± 0.05 in order to obtain an overall branching ratio for OH regeneration of 0.80.

In this work, an *ab initio* calculated barrier for the decomposition of the hydroxybutyl radical to produce a methyl radical and a propenol co-product was calculated as $128.8 \text{ kJ mol}^{-1}$ (see *ab initio* section), 21.7 kJ mol^{-1} higher than that calculated for the iso-butene and OH route, suggesting that this non-OH producing route is a minor channel. Assuming a similar pre-exponential factor for both decomposition channels for entropic reasons, the decomposition to form a methyl radical and propenol is likely less than 2 % of the potential decompositions at the temperatures studied in this work, and it is unlikely that this channel would have a significant effect on the yield observed. The two decomposition channels may however exhibit different pressure dependent falloff behaviour, potentially resulting in a change in BR2 at different pressures.

The *ab initio* calculations and an assessment of oxygen side reactions suggest that virtually all the hydroxybutyl formed decomposed under these conditions to OH and iso-butene. Therefore branching at the abstraction stage of the process primarily determines the OH yield. The overall yield determined in this study is (86 ± 5) % where 5 % is the widest part of the 95 % confidence limits. Other previous literature for the initial

branching ratio is displayed in Table 4-2. With ~98 % of hydroxybutyl regenerating OH, this means that BR1 is ~ 88 %. Our estimate of BR1 is in good agreement with the predictions of the literature values in Table 4-2, with the exception of Kwok and Atkinson [130]. Both the studies from McGillen *et al.* [78] and Sarathy *et al.* [55] show some decrease in the abstraction from the β -sites with temperature.

The bond strength of the O–H bond in *t*-butanol is greater than that of C–H and therefore one would expect BR1 to decrease with temperature consistent with several, but not all, of the SAR/predictions of BR1 shown in Table 4-2. Our yield results are slightly scattered (± 11 % from the mean yield obtained), but the data shown in Figure 4-11 does suggest a slight decrease in yield with temperature and this would be consistent with the lower yield of ~0.80 under the higher temperatures of the Stranic *et al.* data. Further work either on the pressure dependence of the decomposition channels, end product analyses or isotopically labelled *t*-butanol experiments [100] would be required to provide more precise determinations of the branching ratios.

Table 4-2: Fraction of OH abstractions occurring at beta site of *t*-butanol, according to branching ratios from literature.

T / K	Sarathy [55] (2012)	McGillen [78] (2013)	Moss [98] (2008)	Atkinson [114] (1985)	Kwok [130] (1995)	Bethel [101] (2001)
298	0.98	0.96	0.90	0.92	0.75	0.86
460	0.95	0.93	0.90	0.91	0.79	0.89
480	0.95	0.93	0.90	0.91	0.80	0.89
500	0.95	0.93	0.90	0.91	0.80	0.89
520	0.94	0.92	0.90	0.91	0.80	0.90
540	0.94	0.92	0.90	0.91	0.81	0.90
560	0.94	0.92	0.90	0.90	0.81	0.90
580	0.94	0.92	0.90	0.90	0.81	0.90
600	0.94	0.92	0.90	0.90	0.81	0.90
620	0.94	0.92	0.90	0.90	0.81	0.90

The high experimental OH yield and the higher calculated barrier for CH₃ vs OH elimination from the β *t*-hydroxybutyl radical is in contrast to earlier flow reactor studies

[138] and modelling studies [121] but in good agreement with the shock tube work of Stranic *et al.* and more recent modelling studies.[137] Lefkowitz *et al.* [138] rationalised significant acetone yields as arising from methyl elimination from C_4H_8OH , but Welz *et al.* [140] showed that acetone could be formed following $O_2C_4H_8OH$ formation and an RO_2 to QOOH isomerization. Decomposition of the $HOOCH_2C(CH_3)(CH_2)OH$, QOOH species generates OH, acetone and formaldehyde.

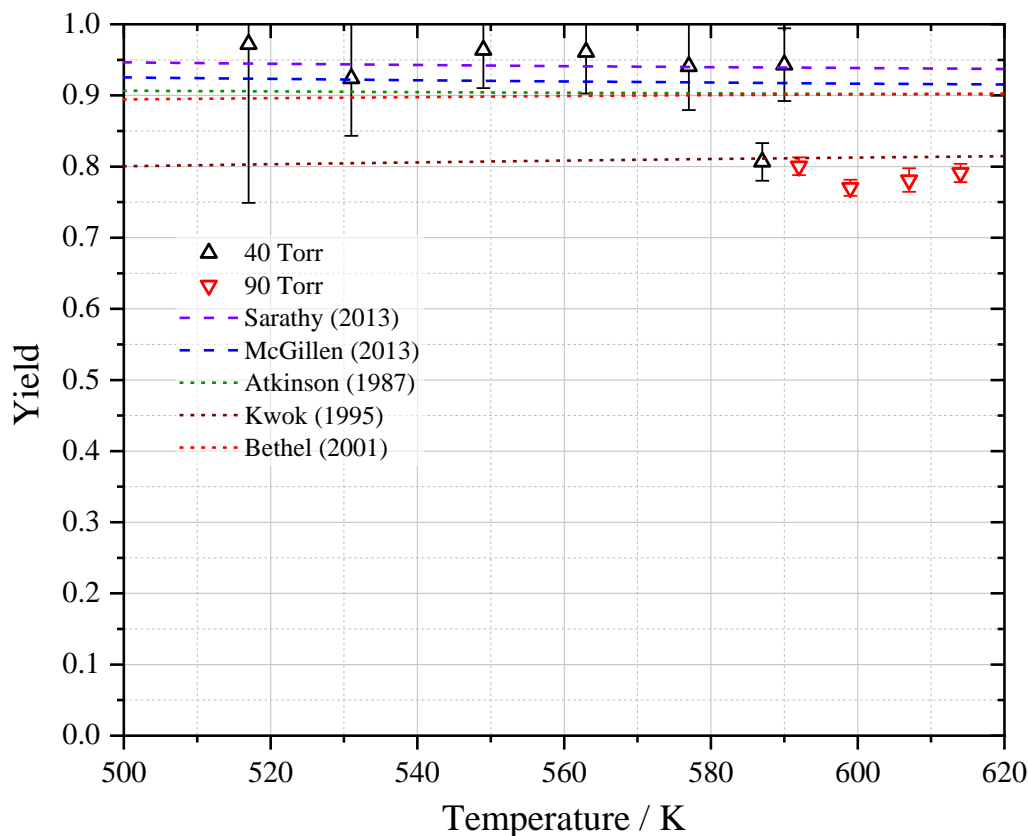
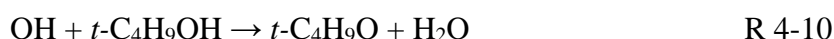
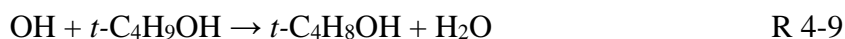


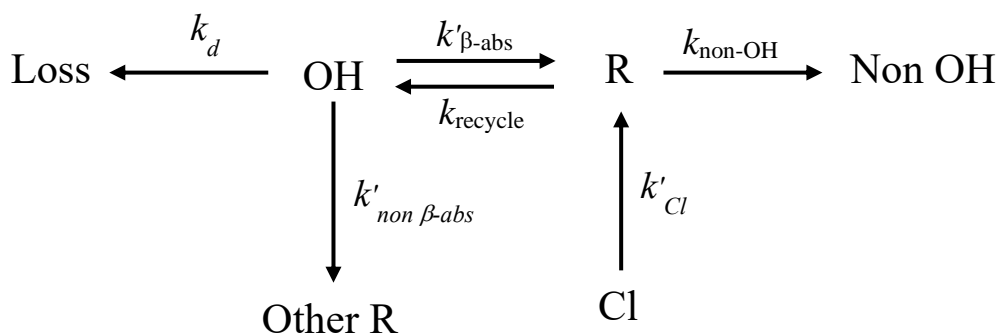
Figure 4-11: A graph of yield of OH for *t*-butanol radical decomposition as a function of temperature and pressure, where the error bars represent propagated errors of k_{recycle} and $k_{\text{non-OH}}$ obtained from global analysis. The literature lines represent the branching ratio of *t*-butanol abstraction reactions occurring at the beta site from literature: Sarathy *et al.* (purple dashed line), McGillen *et al.* (blue dashed line) and the SAR of Atkinson (orange short dashed line), the updated SAR of Kwok and Atkinson (Brown dashed line) and the SAR of Bethel *et al.* (red dashed line). Data replicated from: [55], [78], [114], [130], and [101].

4.4.4 *t*-butanol + Chlorine

When the hydrogen peroxide/water precursor is introduced to the reaction cell through the bubbling of nitrogen over a liquid reservoir of precursor in a pressurised bubbler, a small amount of oxygen is also delivered. This is as a result of contact of the hydrogen peroxide with the inside of the mass flow controllers used for delivery, and results in a residual unavoidable amount of oxygen being present in the system, typically of the order of around 2×10^{14} molecule cm^{-3} (see Section 2.7.1.1).

As the decomposition mechanism suggested for regenerating OH in Section 4.4.2 does not depend on the presence of oxygen, the use of a different initiating precursor that does not result in the introduction of oxygen should still result in the observation of this recycled OH signal. A series of experiments were therefore conducted using oxalyl chloride ($(\text{COCl})_2$) as a chlorine radical precursor source, as this should not result in the introduction of oxygen to the system on contact with the mass flow controller. While the rate and site of reaction of chlorine radicals with *t*-butanol is likely different to that of OH radicals, these experiments can provide qualitative confirmation that recycled OH observed is a result of the decomposition mechanism suggested, and not the result of the presence of small amounts of oxygen in the system. The reactions involved are as described in reactions R 4-3 – R 4-10, and the rate parameters obtained from fitting to the traces are described in Scheme 4-6.

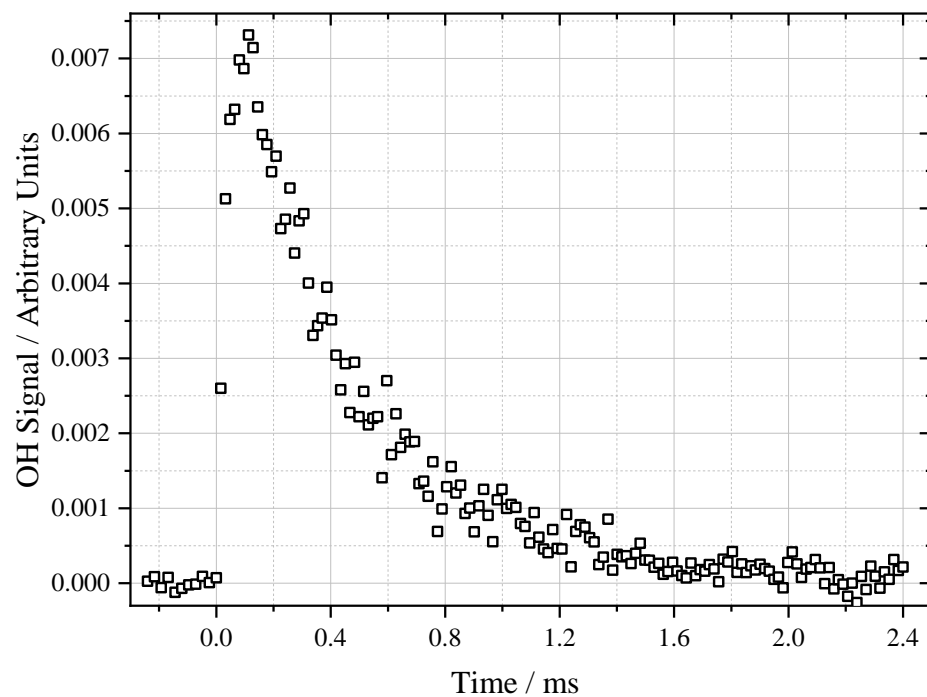




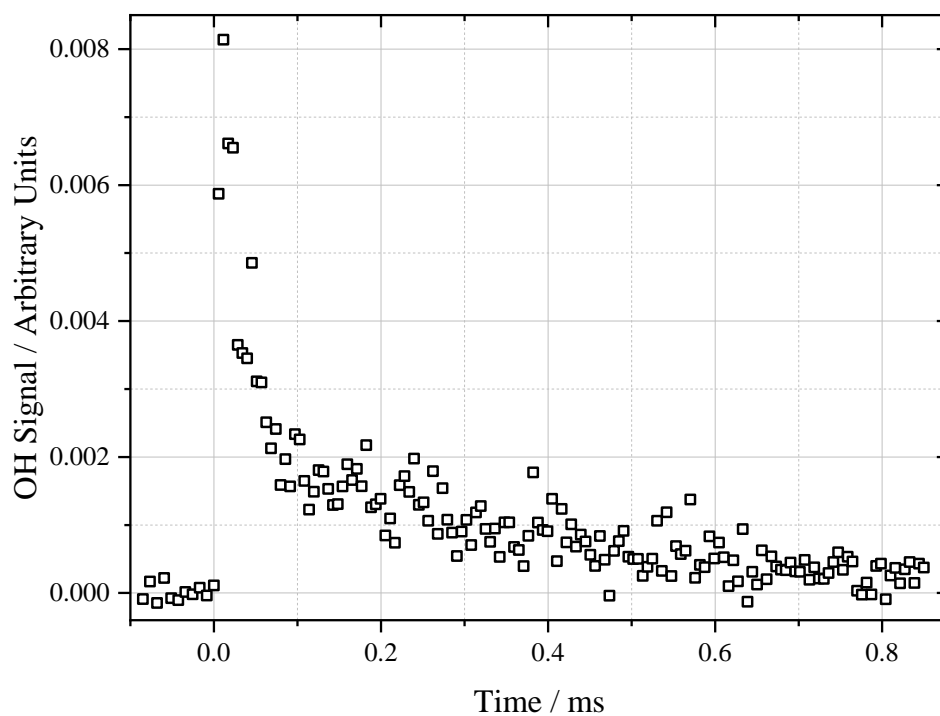
Scheme 4-6: Reaction scheme describing the kinetic parameters that can be obtained from kinetic trace fitting to experiments conducted using oxalyl chloride precursor.

The full expanded fitting equation described by Scheme 4-6 can be found in Appendix A. In these experiments utilising a chlorine precursor, a growth of OH signal was observed after the photolysis pulse generated the chlorine radical, initiating the chlorine abstraction reaction of *t*-butanol to produce the appropriate *t*-hydroxybutyl radical for unimolecular decomposition. An example trace obtained under these conditions can be seen in Figure 4-12 compared to a trace obtained under the same conditions which utilised hydrogen peroxide as an OH precursor.

As these experiments were conducted in an oxygen free environment, it can be stated with confidence that the OH signal observed is a result of the β -radical decomposition. However, due to the complex nature of the reaction mechanism occurring, analysis of these experimental traces was complicated, and prevented a thorough and robust analysis for obtaining the required kinetic parameters. If some of the parameters in the global fitting regime were fixed to known values, then reasonably agreeable rate constants could be obtained. In order to do this, experiments were carried out utilising hydrogen peroxide precursor in place of the oxalyl chloride, to obtain pseudo first order rate constants for the reaction of OH with *t*-butanol under the same conditions, allowing this parameter to be fixed in the oxalyl chloride trace fitting. A summary of the OH recycling parameter, k_{recycle} , is provided in Table 4-3 for experiments conducted using hydrogen peroxide and oxalyl chloride precursors, and the experimental conditions under which they were obtained.



a)



b)

Figure 4-12: Example kinetic traces obtained a) Utilising oxalyl chloride as the radical precursor with *t*-butanol, 640 K, 130 Torr, [*t*-butanol] = 4×10^{15} molecule cm^{-3} and an estimated starting Cl radical concentration of 1×10^{13} molecule cm^{-3} . b) Utilising hydrogen peroxide radical precursor with *t*-butanol, 640 K, 130 Torr, [*t*-butanol] = 4×10^{15} molecule cm^{-3} and an estimated starting OH concentration of 2×10^{12} molecule cm^{-3} .

Table 4-3: Summary of experimental conditions for comparable experiments conducted using hydrogen peroxide and oxalyl chloride at high temperatures with *t*-butanol.

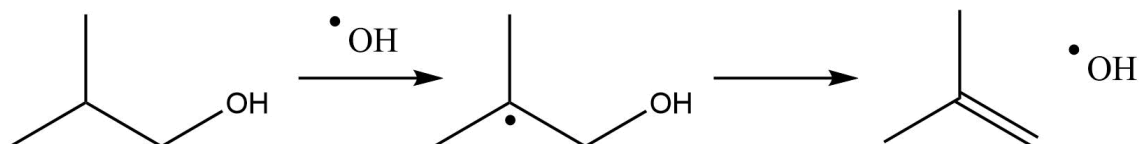
Temperature / K	Pressure / Torr	H ₂ O ₂ k_{recycle} value / s ⁻¹	(COCl) ₂ k_{recycle} value / s ⁻¹
579	125	3290 ± 450	570 ± 1480
637	131	9400 ± 500	8360 ± 2090
644	128	10300 ± 490	13830 ± 6140

Table 4-3 highlights the reasonable agreement for the OH recycling parameter k_{recycle} obtained between the two different radical precursors used. The values obtained for the oxalyl chloride precursor have significantly larger errors, as a result of the larger number of parameters obtained during the fitting of traces. The measurements obtained at the lowest temperature show the worst agreement between the two initiating radical precursors, as this is likely where the reaction of OH with *t*-butanol was comparable to the rate of unimolecular decomposition of the β -hydroxybutyl radical, and there was not good separation of the two rate constants.

While the chlorine radical experiments did not allow for robust parameter retrieval of the OH recycling parameter, it did provide qualitative confirmation that the recycled OH is produced via the proposed oxygen free mechanism. At the highest temperatures studied, whilst the retrieved parameters had significant errors, they were in agreement with the values obtained from the hydrogen peroxide experiments within the calculated error bounds.

4.5 *i*-Butanol

i-butanol possesses one potential abstraction site that would result in the appropriate β -hydroxyalkyl radical for decomposition to an alkene and an OH radical, which is a tertiary C–H site. Similar to the decomposition of the *t*-butanol β -radical scission, the decomposition of *i*-hydroxybutyl radical results in formation of iso-butene and OH, as outlined in Scheme 4-7.



Scheme 4-7: β -scission decomposition mechanism following β -site abstraction from *i*-butanol.

The decomposition of the *i*-butanol β -hydroxybutyl radical has been observed qualitatively previously by Welz *et al.* in a study examining the low temperature oxidation chemistry of *i*-butanol at 550 K and 700 K [140]. A significant increase in the iso-butene signal at 700 K was attributed to this unimolecular decomposition channel. The observation of iso-butene despite the presence of approximately 1×10^{16} molecule cm^{-3} of oxygen in the system suggests this unimolecular decomposition channel is competitive with the addition of oxygen at temperatures relevant to low temperature combustion, and therefore of interest to combustion chemistry modelling.

4.5.1 Experimental results

All experimentally obtained k_{recycle} parameters are summarised in Table 4-4, and represented graphically in Figure 4-13. The different symbols represent different approximate groupings of pressure, with experiments conducted at 37 – 39 Torr represented by black hollow squares, and results obtained at 81 – 82 Torr represented by hollow red circles. Experiments conducted at 82 Torr of total pressure utilised a total flow of gas around 2 L min^{-1} , and consequently the temperature correction has a larger uncertainty associated of $\pm 5 \text{ K}$, whereas experiments at 38 Torr used 1 L min^{-1} total flow, and are subject to a smaller uncertainty of $\pm 3 \text{ K}$.

Table 4-4: Summary of experimental conditions and obtained OH recycling parameter k_{recycle} for *i*-butanol

T / K	Pressure / Torr	Reagent Range^a	Precursor	Globally obtained $k_{\text{recycle}} / \text{s}^{-1}$	Globally obtained $k_{\text{non-OH}} / \text{s}^{-1}$	Yield / %
493	36	0.45 – 3.85	H ₂ O ₂	38 ± 3	248 ± 27	13 ± 2
510	81	9.7 – 16.1	H ₂ O ₂	113 ± 27	1396 ± 550	7 ± 5
518	37	0.93 – 3.77	H ₂ O ₂	88 ± 5	468 ± 32	16 ± 2
527	37	0.43 – 3.77	H ₂ O ₂	107 ± 6	545 ± 31	16 ± 2
540	81	9.1 – 26.6	H ₂ O ₂	241 ± 19	1515 ± 227	14 ± 3
550	37	0.89 – 3.46	H ₂ O ₂	245 ± 13	907 ± 40	21 ± 2
551	81	9.0 – 25.6	H ₂ O ₂	343 ± 22	1849 ± 171	16 ± 2
564	81	8.7 – 19.6	H ₂ O ₂	507 ± 20	1882 ± 106	21 ± 2
580	38	1.24 – 3.50	H ₂ O ₂	369 ± 25	1379 ± 63	21 ± 2
587	82	10.5 – 24.0	H ₂ O ₂	908 ± 35	2269 ± 105	29 ± 2
587	81	10.2 – 23.0	H ₂ O ₂	874 ± 37	2345 ± 133	27 ± 2
595	82	16.4 – 22.7	H ₂ O ₂	1006 ± 28	2180 ± 77	32 ± 2
600	39	2.66 – 3.38	H ₂ O ₂	383 ± 19	1313 ± 50	23 ± 2
607	82	8.9 – 20.1	H ₂ O ₂	1732 ± 46	2381 ± 78	42 ± 2
614	82	13.2 – 19.6	H ₂ O ₂	1746 ± 55	2181 ± 94	44 ± 3
621	82	18.2 – 20.2	H ₂ O ₂	2656 ± 111	2532 ± 137	51 ± 4

^a / 10¹⁴ molecule cm⁻³

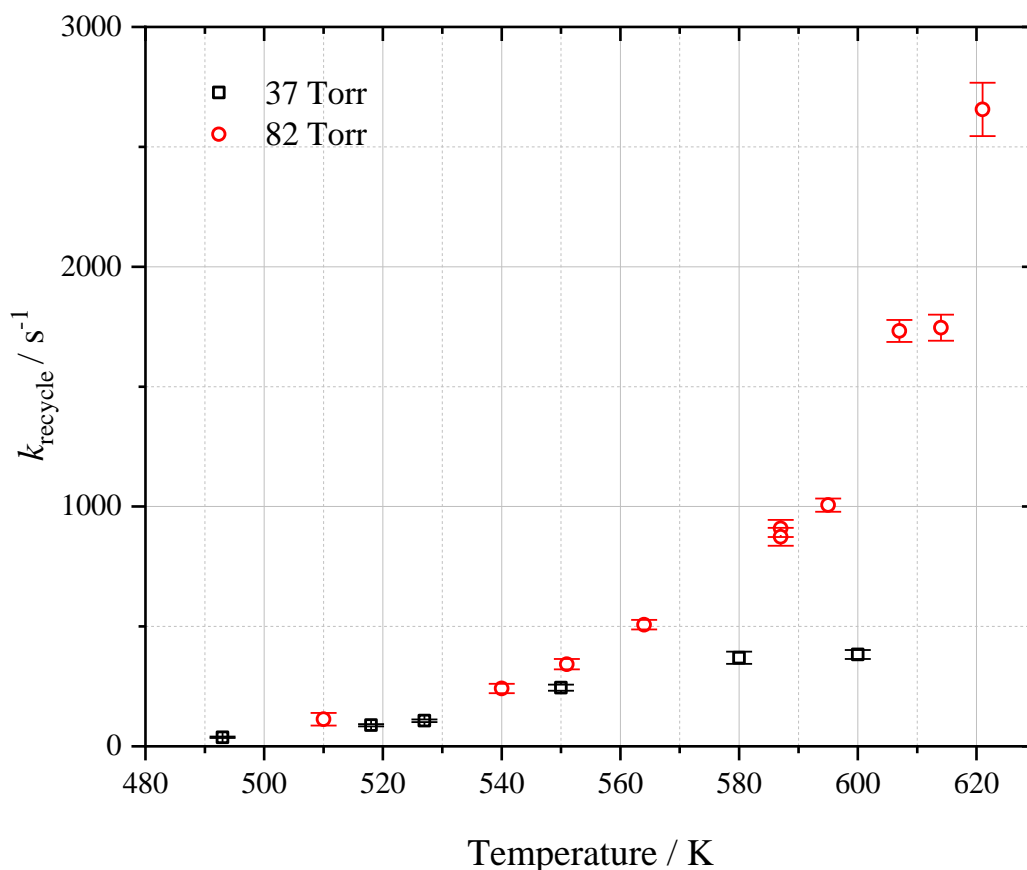


Figure 4-13: Globally obtained k_{recycle} for *i*-hydroxybutyl β -radical decomposition as a function of temperature and pressure, with hollow black squares representing experiments at 37 Torr and hollow red circles for experiments at 82 Torr. The reported error bars represent the 1σ errors obtained from the biexponential global fit to the experimental traces multiplied by a factor of 4.

4.5.2 *Ab initio* Calculations and Master Equation Analysis

As before, the optimized geometries of the β -hydroxybutyl species, the resulting OH and iso-butene species, and the transition state were all obtained at the DFT level M06-2X/aug-cc-pVTZ [145, 150] using the Gaussian 09 program [146]. The energy of the Van der Waals complex was not calculated in this work for the *i*-butanol system, but by analogy with the *t*-butanol system, has been included in Figure 4-15 for completion.

The optimized structures were used to calculate the single point energies at the CCSD(T)/aug-cc-pVTZ level [147]. The harmonic oscillator approximation was used for the majority of the vibrational frequency density of state calculations. The *i*-butanol β -hydroxybutyl radical species and the iso-butene product were treated with hindered rotor approximations, with the bonds involved shown in Figure 4-14. The descriptions of

these hindered rotors were obtained through a relaxed scan of each dihedral angle at 15° steps, with optimisations carried out at the M06-2X/aug-cc-pVTZ at each step. The potential energy surface calculated is represented in Figure 4-15, with energies (in kJ mol^{-1}) relative to OH + iso-butene, which has been defined as zero.

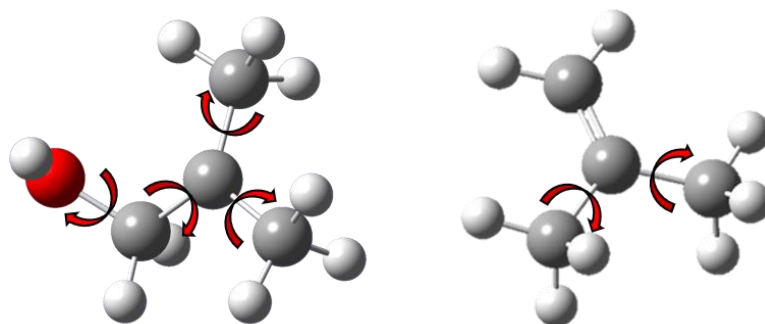


Figure 4-14: Rotations described by hindered rotors, calculated for *i*-butanol β -hydroxybutyl radical and iso-butene. Bonds described are highlighted by red arrows.

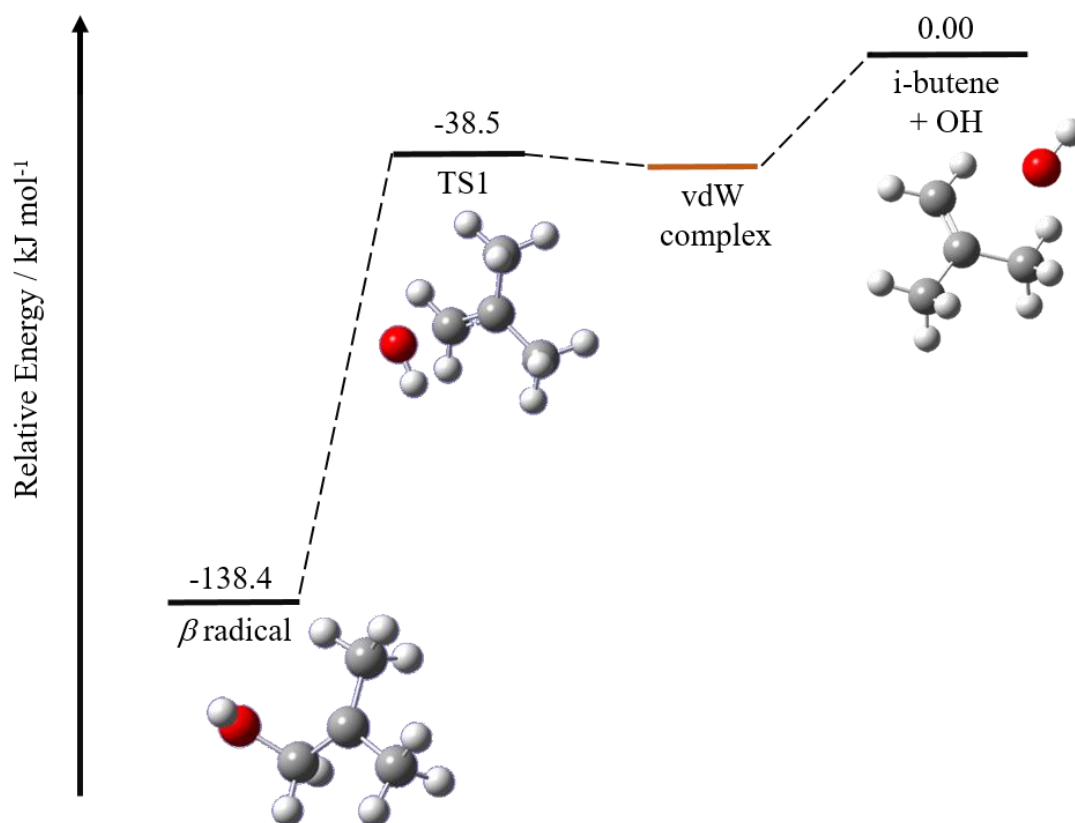


Figure 4-15: Potential energy surface for the decomposition of β *i*-hydroxybutyl radical, calculated at CCSD(T)/aug-cc-pVTZ//M06-2x/aug-cc-pVTZ level. Van der Waals complex not calculated but included based on analogy with *t*-butanol system (shown in orange).

Using these calculated energies and vibrational frequencies, master equation modelling was again conducted using the MESMER package [144]. The values of k_{recycle} calculated by MESMER were compared with experimentally obtained values with the barrier for *i*-C₄H₈OH decomposition to OH and iso-butene as a variable parameter. The MESMER fit to the experimental rate coefficients obtained predicts a barrier of (93 ± 4) kJ mol⁻¹ for β -scission, with the error quoted encompassing the error calculated by MESMER (1.0 kJ mol⁻¹) and an estimate of the systematic errors, in reasonable agreement with the *ab initio* calculated barrier for the transition state, 99.9 kJ mol⁻¹. From Figure 4-16, the experimentally obtained k_{recycle} values are in good agreement with MESMER predicted rate coefficients across all of the pressures and temperatures studied, with the largest discrepancy observed at the highest temperatures studied.

Figure 4-16 also shows the MESMER predicted recycling parameters at an assumed high pressure limit of 8000 Torr. Despite the reasonable agreement between the experimental values and the MESMER predicted k_{recycle} values, the pressure dependence of the unimolecular decomposition is not well defined. This is highlighted by the MESMER predicted $\langle \Delta E \rangle_{\text{down}}$ parameter possessing a significant error of over 100 %, ($\langle \Delta E \rangle_{\text{down}} = 180 \pm 279$ cm⁻¹). Whilst good agreement is observed between the experimental and MESMER predicted k_{recycle} values obtained at low pressures and temperatures less than 560 K, at higher pressures, the experimental values are consistently faster than the MESMER predicted values. At 580 K, the MESMER predicted value for the low pressure reading is almost a factor of two faster than the experimentally measured value. This is likely a consequence of a lack of low pressure experimental measurements at the highest temperatures studied. However, the value obtained for the $\langle \Delta E \rangle_{\text{down}}$ parameter is reasonable for a species in nitrogen bath gas.

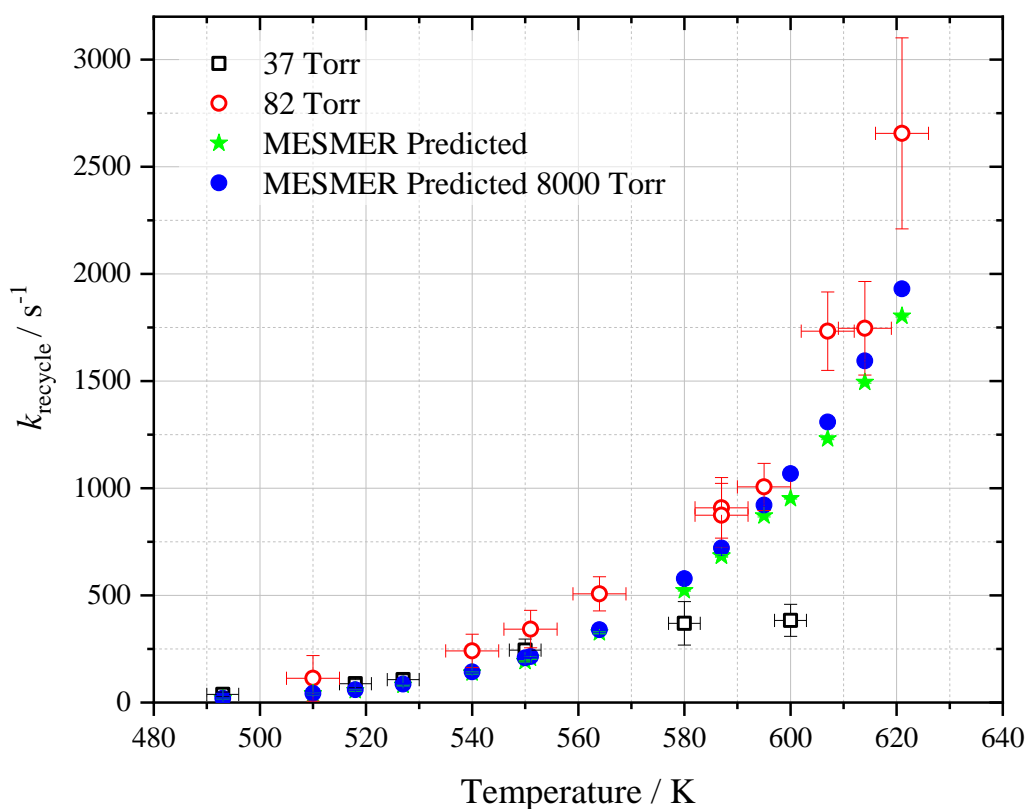


Figure 4-16: Globally obtained k_{recycle} for *i*-butanol β -hydroxybutyl radical decomposition as a function of temperature and pressure, compared with corresponding MESMER fitted values and MESMER high pressure limit predicted values for decomposition. Decomposition barrier estimated by MESMER = $(93 \pm 1) \text{ kJ mol}^{-1}$. The errors reported in temperatures are $\pm 3 \text{ K}$ for pressures around 37 Torr and $\pm 5 \text{ K}$ for pressures around 82 Torr, and the errors reported for the experimental k_{recycle} values are the 1σ errors obtained from the biexponential global fit to the experimental traces multiplied by a factor of 4.

Figure 4-17 shows a graph of the MESMER predicted values for the unimolecular recycling parameter against the experimentally measured values with their associated errors. A line of best fit with a fixed origin at zero has been fit to the data, alongside a perfect ratio of 1:1 linear fit, which would be obtained if the MESMER predicted values matched perfectly with the experimentally obtained values. This also demonstrates the reasonable agreement obtained between the MESMER predicted values and the experimentally measured values, with the experimentally measured values being slightly slower than the MESMER calculated.

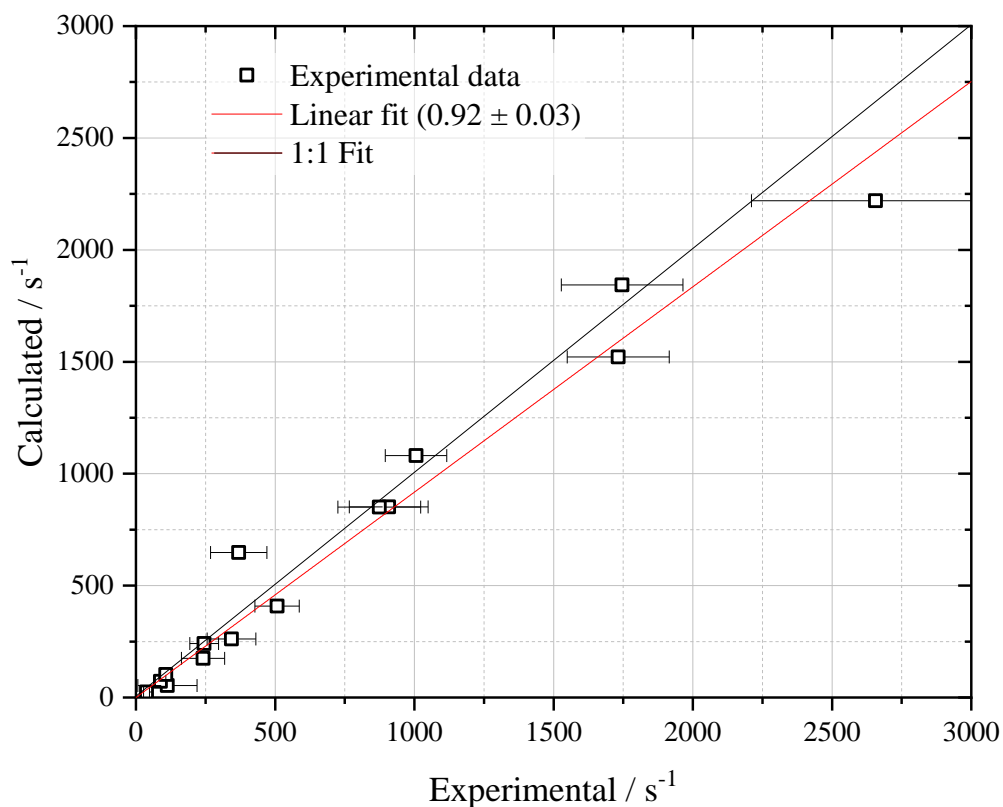


Figure 4-17: A graph of the MESMER predicted values for *i*-butanol radical decomposition compared to the experimentally obtained recycling parameters, with a linear fit (red solid line). A perfect 1:1 fit (black solid line) has also been fit.

4.5.3 Discussion of Branching Ratios

Assuming that all abstractions that occur at the β -site of *i*-butanol result in the recycling of OH, the yield parameter calculated can be assumed to be a proxy for the percentage of abstractions occurring at this site, as described previously for *t*-butanol. In this work, the calculated yield parameter displays a slight positive temperature dependence across the temperatures and pressures studied. The values obtained in this work can be seen summarised previously in Table 4-4, and are represented graphically in Figure 4-18, compared to branching ratios for abstraction by OH at the β -site obtained from the literature.

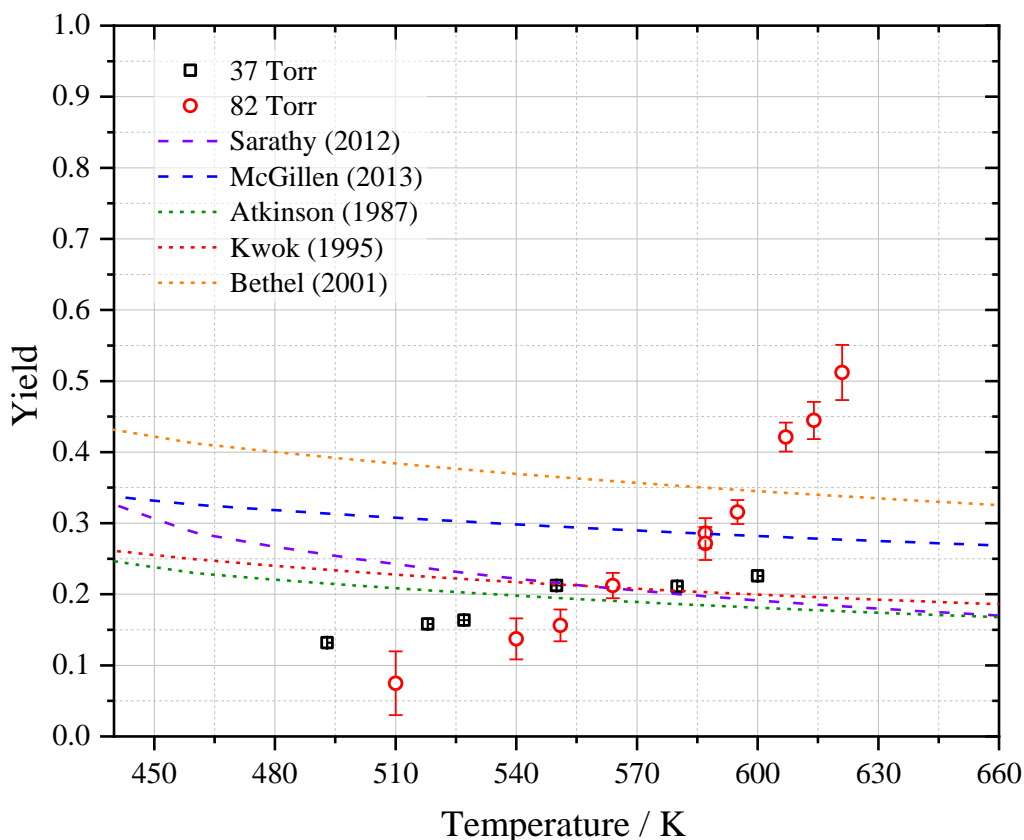


Figure 4-18: A graph of yield of OH for *i*-butanol radical decomposition as a function of temperature and pressure, where the error bars represent propagated errors of k_{recycle} and $k_{\text{non-OH}}$ obtained from global analysis. The literature lines represent the branching ratio of *i*-butanol abstraction reactions occurring at the beta site from literature: Sarathy *et al.* (purple dashed line), McGillen *et al.* (blue dashed line) and the SAR of Atkinson (green dashed line), the updated SAR of Kwok and Atkinson (red dashed line) and SAR of Bethel *et al.* (orange dashed line). Data replicated from: [55], [78], [114], [130], and [101].

In this work, the yield parameter calculated demonstrates a slight positive temperature dependence, with reasonable agreement between the two pressure sets within the experimental errors. At temperatures above 600 K, the yield parameter increases at a steeper rate than at temperatures and pressures below this, with the experimentally obtained k_{recycle} values at these temperatures also possessing the most significant uncertainty measured for *i*-butanol radical unimolecular decomposition.

As reflected in the branching ratios obtained from the literature, with increasing temperature, one would expect a slight decrease in the percentage of abstractions occurring at the beta site of *i*-butanol, as the relative contributions from the methyl groups

(γ -sites) would be expected to increase with elevated temperatures. This however is not reflected in the yield parameter calculated here. As described for *t*-butanol in Section 4.4.3, the yield parameter represents an overall OH regeneration yield, which factors in both the initial abstraction branching ratio and the branching ratio of the decomposition of the resulting β -hydroxybutyl radical to give OH and butene or other removal reactions. Whilst for *t*-butanol the non-OH producing channels were assumed to be minor, this may not be the case for *i*-butanol, and some other loss process may be competing with decomposition to give OH and butene.

At the highest temperatures above 600 K, it is possible that there has been some small amount of interference from the residual amount of oxygen present in the system (see Section 2.7.1.1). Additional OH recycling may occur *via* O₂ addition to the other hydroxybutyl radicals formed during OH abstraction reactions, followed by isomerisation to QOOH and decomposition to regenerate OH, as highlighted in Section 1.7. The recycled OH from QOOH decomposition would be indistinguishable from the OH produced by unimolecular decomposition of the β -hydroxybutyl radical, and would manifest as an increased k_{recycle} parameter and an increased yield parameter. As this occurs from the other *i*-butanol radicals generated by the initial OH abstraction reactions, it would not affect the yield of recycling occurring through the β -abstraction channel, but may appear as an increase in the total yield obtained.

Table 4-5: Fraction of OH abstractions occurring at beta site of *i*-butanol, according to branching ratios from literature.

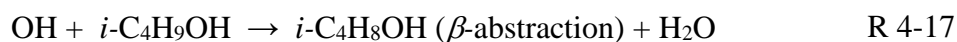
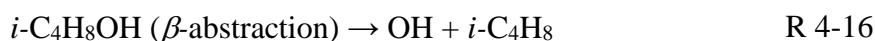
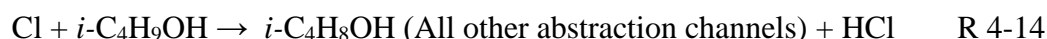
T / K	Sarathy <i>et al.</i> [55] (2012)	McGillen <i>et al.</i> [78] (2013)	Atkinson [114] (1987)	Kwok <i>et al.</i> [130] (1995)	Bethel <i>et al.</i> [101] (2001)
298	0.61	0.42	0.36	0.34	0.57
460	0.29	0.33	0.23	0.25	0.41
480	0.27	0.32	0.22	0.24	0.40
500	0.25	0.31	0.21	0.23	0.39
520	0.23	0.30	0.20	0.22	0.38
540	0.22	0.30	0.20	0.22	0.37
560	0.21	0.29	0.19	0.21	0.36
580	0.20	0.29	0.19	0.20	0.35
600	0.19	0.28	0.18	0.20	0.35
620	0.18	0.28	0.18	0.19	0.34
640	0.18	0.27	0.17	0.19	0.33
660	0.17	0.27	0.17	0.19	0.33

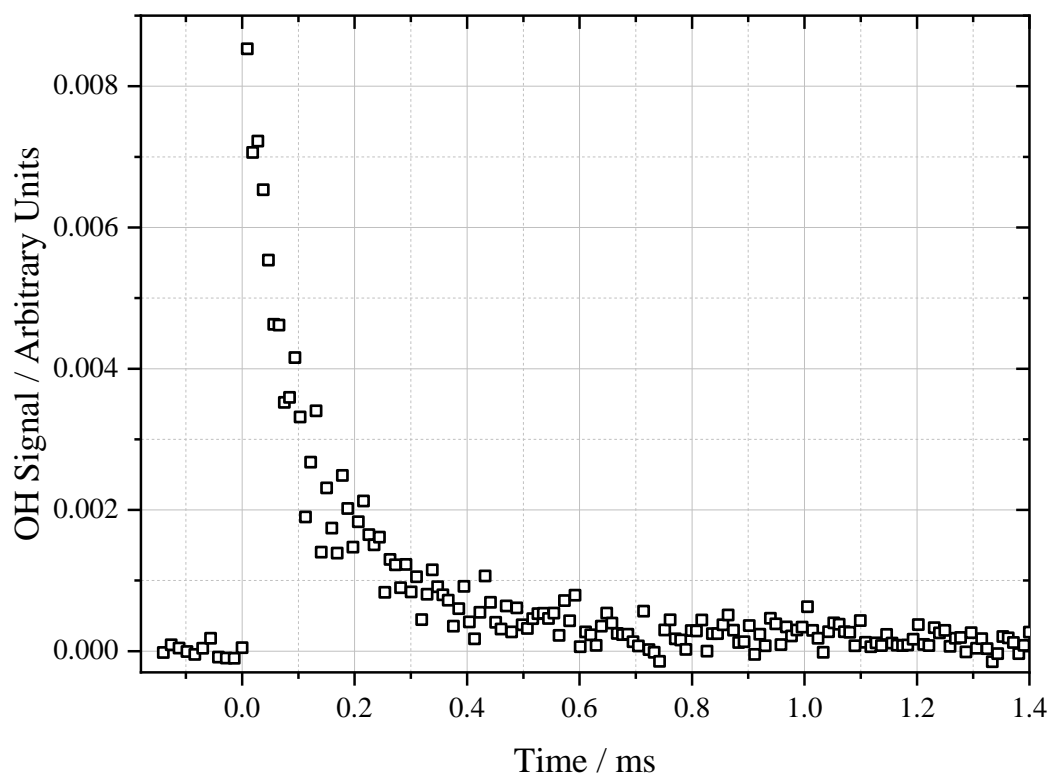
The calculated yield parameter in this work displays a slight positive temperature dependence, whereas all literature sources demonstrate slight negative temperature dependences (see Table 4-5). Despite the total bimolecular rate coefficient calculated by Sarathy *et al.*[55] for *i*-butanol with OH demonstrating slower overall reactivity at the temperatures relevant to this results section (see section 3.5.1), the calculated beta channel branching ratio is in reasonable agreement. The structure activity relationship of Atkinson (1987) [114] demonstrates similar agreement with the experimental yield values obtained in this work to that of Sarathy, with excellent agreement at the intermediate temperatures. The updated SAR of Bethel *et al.* [101] however calculates a beta site abstraction ratio that is consistently higher than the experimental yields of this work below 600 K, with the calculated branching ratio at 540 K more than double what was

measured here. The parameterisation of McGillen *et al.* [78] was constrained using the SAR of Bethel *et al.*, and a single measurement at room temperature of an end-product yield of acetone by Andersen *et al.* [84]. While this end-product yield will assist in constraining the room temperature branching ratio, it does not provide information about the temperature dependence of the different abstraction sites, and instead relies on the temperature dependent branching ratios of Bethel *et al.*, which shows the greatest discrepancy with the experimental results obtained in this work.

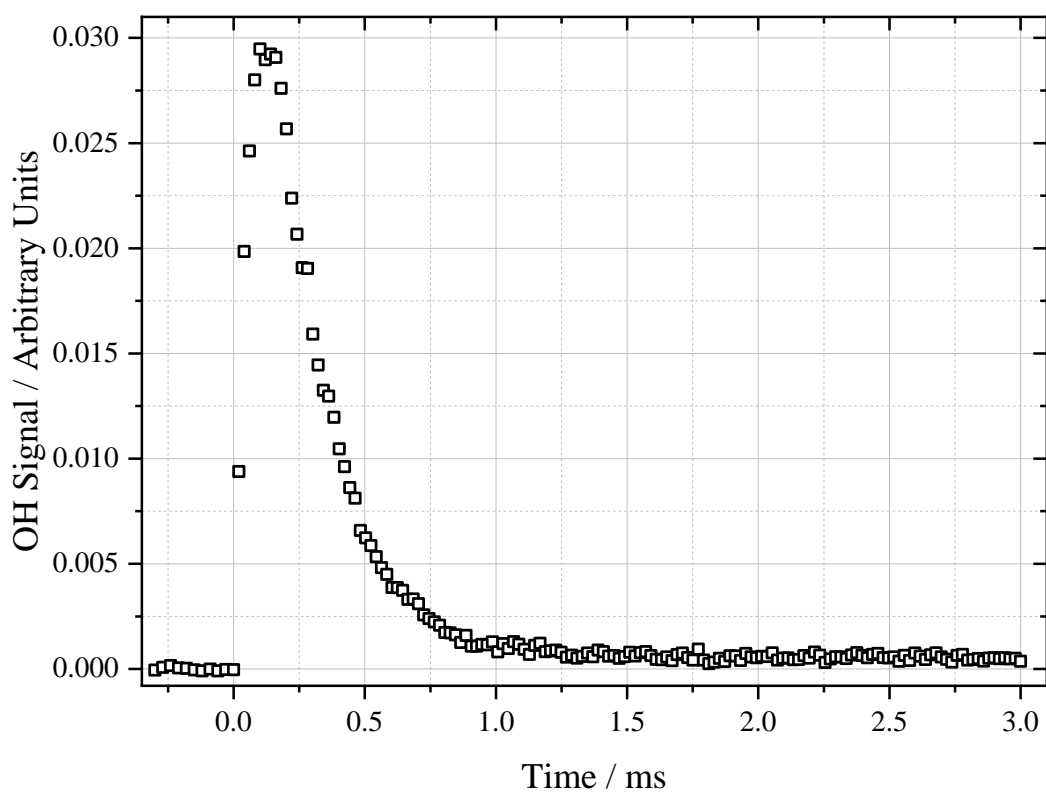
4.5.4 *i*-butanol + Chlorine

As the OH recycling mechanism suggested in Scheme 4-7 does not depend on the presence of oxygen in the system, experiments conducted at temperatures where unimolecular recycling is observed that use a guaranteed oxygen-free precursor should still demonstrate OH recycling. As before for *t*-butanol, experiments were conducted utilising oxalyl chloride as a chlorine radical precursor, to initiate the chain of reactions described in equations R 4-11 – R 4-18.





a)



b)

Figure 4-19: Example kinetic traces obtained a) Utilising oxalyl chloride as the radical precursor with *i*-butanol, 640 K, 130 Torr, [*i*-butanol] = 9.8×10^{14} molecule cm^{-3} and an estimated starting Cl concentration of 1×10^{13} molecule cm^{-3} . b) Utilising hydrogen peroxide radical precursor with *i*-butanol, 640 K, 130 Torr, [*i*-butanol] = 9.8×10^{14} molecule cm^{-3} and an estimated starting OH concentration of 2×10^{12} molecule cm^{-3} .

An example trace utilising oxalyl chloride precursor and *i*-butanol is shown in Figure 4-19, showing a growth of OH fluorescence signal after the initial photolysis pulse to generate the chlorine radicals. As there is no introduction of hydrogen peroxide to the system, it can be stated with confidence that these experiments are oxygen free, and thus the OH recycling mechanism is not dependent on oxygen, and is likely a result of the unimolecular decomposition mechanism outlined previously. As the photolysis pulse in these experiments does not photolyse an OH radical precursor, the signal appears and decays over time, as a result of the formation and removal reactions outlined in reactions R 4-11 – R 4-18. The same fitting equation outlined in Section 4.4.4 was used to fit the kinetic traces obtained. Experiments were also conducted using hydrogen peroxide at the same conditions (Figure 4-19 b), in order to obtain values for pseudo-first order rate constants, such as that of OH + *i*-butanol, which could be fixed in the chlorine trace fitting to assist in obtaining reasonable parameters.

As was the case with *t*-butanol, due to the complex nature of the reaction mechanism, analysis of these experimental traces was complicated, and accurate fitting to the kinetic traces could not be carried out. Despite the fixing of the pseudo first order rate constant for the reaction of *i*-butanol with OH, a solution to the fitting equation that resulted in reasonable rate constants for the other reactions and a good fit to the experimental trace was not possible. The best example comparison of the fitting parameters obtained from fitting to two traces that share experimental conditions is shown in Table 4-6 below.

Table 4-6: Kinetic parameters (all in s⁻¹) obtained from fitting to traces obtained at 640 K and 130 Torr, utilising either hydrogen peroxide or oxalyl chloride as an initiating radical source.

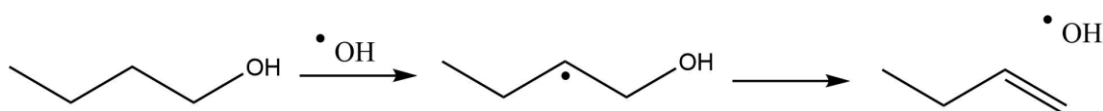
Precursor	$k'_{\beta\text{-abs}} + k'_{\text{non } \beta\text{-abs}}$	k_{recycle}	$k_{\text{non-OH}}$	k_{d}	k'_{Cl}
H ₂ O ₂	11530 ± 680	1690 ± 370	2770 ± 490	150*	-
(COCl) ₂	11500*	3710 ± 610	6930 ± 260	50*	135200 ± 23900

* Fixed value

While the chlorine experiments did not allow any parameter retrieval, they did provide qualitative confirmation that the OH recycling observed occurs via the proposed oxygen free mechanism.

4.6 *n*-Butanol

In order to generate the *n*-butanol β -hydroxybutyl radical, abstraction by OH must occur from either of the secondary C–H bonds in the beta position of the four carbon chain. The beta scission decomposition of this radical then generates *n*-butene (1-butene) and the hydroxyl radical, as outlined in Scheme 4-8.



Scheme 4-8: Decomposition mechanism following β -site abstraction from *n*-butanol.

No quantitative experimental measurements for the decomposition of the *n*-butyl β -hydroxybutyl radical have been conducted to the best of our knowledge, however it has been observed qualitatively by Welz *et al.* at 650 K and 700 K [139]. The β -scission decomposition has also been studied theoretically previously by Zhang, Klippenstein and Law [141]. In their work, the resulting *n*-butene and OH was described as the entrance channel, and a submerged van der Waals complex was identified as an inner transition state to the addition of OH to *n*-butene. The well depth between the transition state to addition and the resulting β -radical was calculated as 106.7 kJ mol⁻¹ at the [QCISD(T)/CBS]1//B3LYP/6-311++G(d,p) level, and 105.0 kJ mol⁻¹ at the [QCISD(T)/CBS]1//CASPT2/aug-cc-pVDZ level.

4.6.1 Experimental results

The results obtained are summarised in Table 4-7 and represented graphically in Figure 4-20. Experiments conducted at 135 Torr of total pressure utilised a total flow of gas around 2 L min⁻¹, and consequently the temperature correction has a larger uncertainty associated of ± 5 K, whereas experiments at 35 Torr used 1 L min⁻¹ total flow, and are subject to a smaller uncertainty of ± 3 K.

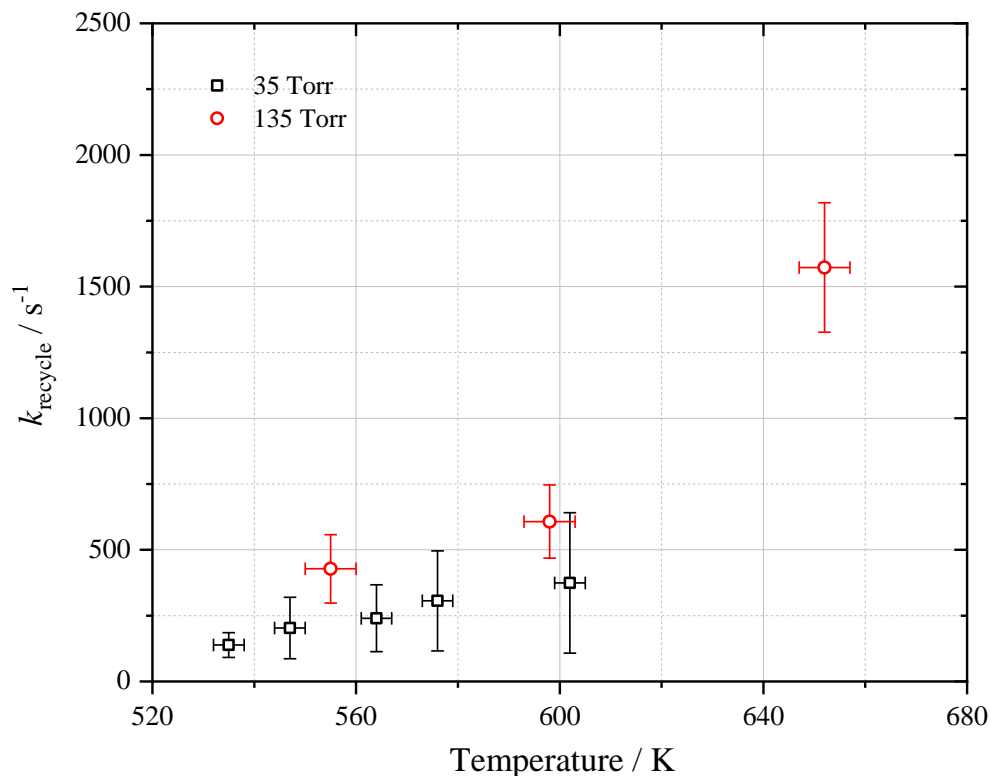


Figure 4-20: Globally obtained k_{recycle} for *n*-butanol β -hydroxybutyl radical decomposition, as a function of temperature and pressure. The reported error bars represent the 1σ errors obtained from the biexponential global fit to the experimental traces multiplied by a factor of 4.

As evident in Figure 4-20, reasonable agreement was obtained between the two pressure ranges studied. However, the steep exponential temperature dependence expected for a unimolecular decomposition with a positive energy barrier is not observed, as it was for the other isomers studied. At the highest temperatures and pressures, the recycling parameter may not have been well separated from the other kinetic parameters, and resulted in an unreliable measurement of k_{recycle} . Consequently, the parameters obtained above 652 K were excluded from the master equation analysis carried out.

Table 4-7: Summary of experimental conditions and obtained OH recycling parameter k_{recycle} for *n*-butanol

T / K	Pressure / Torr	Precursor	Range of <i>n</i>-butanol ^a	Globally obtained $k_{\text{recycle}} / \text{s}^{-1}$	Globally obtained $k_{\text{non-OH}} / \text{s}^{-1}$	Yield / %
535	34	H ₂ O ₂	0.26 - 1.51	138 ± 12	489 ± 29	22 ± 2
547	35	H ₂ O ₂	0.71 - 1.34	203 ± 29	659 ± 65	24 ± 4
555	134	H ₂ O ₂	0.28 - 2.84	428 ± 32	1068 ± 81	29 ± 3
564	35	H ₂ O ₂	0.68 - 1.31	240 ± 32	766 ± 63	24 ± 4
576	35	H ₂ O ₂	0.83 - 1.41	306 ± 48	943 ± 81	25 ± 4
598	132	H ₂ O ₂	9.36 - 14.0	607 ± 35	962 ± 74	39 ± 3
602	35	H ₂ O ₂	0.61 - 1.36	374 ± 67	1025 ± 97	27 ± 5
652	128	H ₂ O ₂	8.67 - 17.3	1573 ± 61	1389 ± 69	53 ± 3
670	133	H ₂ O ₂	8.47 - 16.8	1082 ± 53	1195 ± 86	48 ± 3
693	135	H ₂ O ₂	15.1 - 18.4	1264 ± 53	1503 ± 87	46 ± 3
718	136	H ₂ O ₂	12.3 - 16.3	2167 ± 94	2037 ± 92	52 ± 3

^a / 10¹⁴ molecule cm⁻³

4.6.2 *Ab initio* Calculations and Master Equation Analysis

The potential energy surface for the decomposition of the *n*-butanol β -hydroxybutyl radical was calculated at the DFT level M06-2X/aug-cc-pVTZ, obtaining optimised geometries for the radical species, the transition state and the *n*-butene and OH products. As for the *i*-butanol system, the energy of the Van der Waals complex was not calculated in this work for the *n*-butanol hydroxybutyl radical decomposition, but by analogy with the *t*-butanol system, has been included in Figure 4-22 for completion.

The optimised structures were then used to calculate the single point energy of each species at the CCSD(T)/aug-cc-pVTZ level. The harmonic oscillator approximation was used for the majority of the vibrational frequency density of state calculations, however hindered rotor approximations were used for some bond vibrations in the initial

radical species and *n*-butene products. The descriptions of these hindered rotors were obtained through a relaxed scan of each dihedral angle at 15° steps, with optimisations carried out at the M06-2X/aug-cc-pVTZ at each step. The bonds treated with the hindered rotor approximation are highlighted in Figure 4-21 by red arrows.

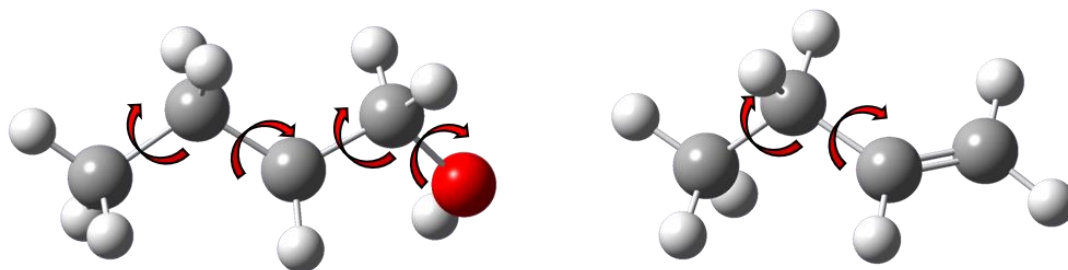


Figure 4-21: Rotations described by hindered rotors, calculated for the *n*-butanol β -hydroxybutyl radical and *n*-butene. Bonds described are highlighted by red arrows.

The potential energy surface calculated is outlined in Figure 4-22, relative to the *n*-butene and hydroxyl radical products of the unimolecular decomposition reaction, which has been set at 0 kJ mol⁻¹.

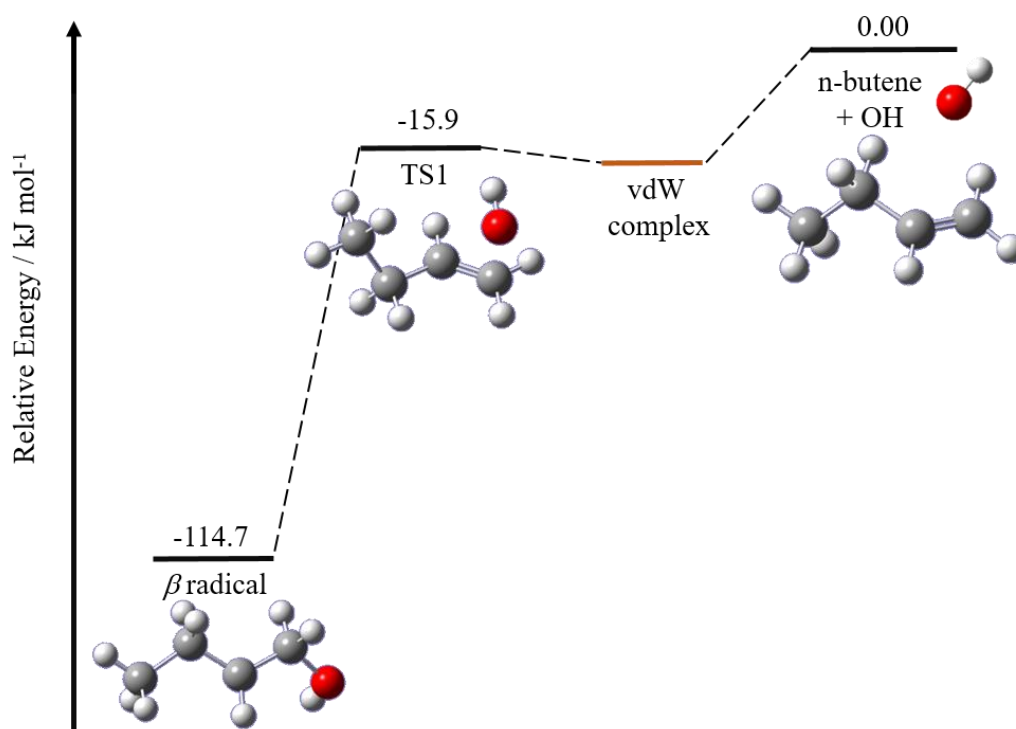


Figure 4-22: Potential energy surface for the decomposition of β *n*-hydroxybutyl radical, calculated at CCSD(T)/aug-cc-pVTZ//M06-2X/aug-cc-pVTZ level. Van der Waals complex not calculated but included based on analogy with *t*-butanol system (shown in orange).

The *ab initio* calculated structures and vibrational frequencies were used in master equation analysis in combination with the k_{recycle} values obtained from experiments, in order to calculate a barrier to the decomposition of the $n\text{-C}_4\text{H}_8\text{OH}$ radical to produce $n\text{-butene}$ and OH . The MESMER fit to the experimental rate coefficients obtained predicts a barrier of $(100.0 \pm 2.6) \text{ kJ mol}^{-1}$ for β -scission, with the error quoted encompassing the error calculated by MESMER (2.6 kJ mol^{-1}) and an estimate of the systematic errors, in good agreement with the *ab initio* calculated barrier for the transition state, 98.8 kJ mol^{-1} . From Figure 4-23, the experimentally obtained k_{recycle} values are in reasonable agreement with MESMER calculated rate coefficients across all of the pressures and temperatures studied, with the largest discrepancy observed at the lowest temperatures studied.

As the errors associated with *ab initio* calculated barriers are usually around 4 kJ mol^{-1} , a reasonable agreement is observed between this work and the work of Zhang *et al.* [141] despite the different levels of theory. The MESMER optimised barrier ($100 \pm 4.0 \text{ kJ mol}^{-1}$) to decomposition obtained in this work is in better overall agreement with both of the *ab initio* calculated barriers of Zhang *et al.*, calculated using the two different geometry optimisations (106.7 and 105 kJ mol^{-1}), when compared to the *ab initio* calculated barrier of this work.

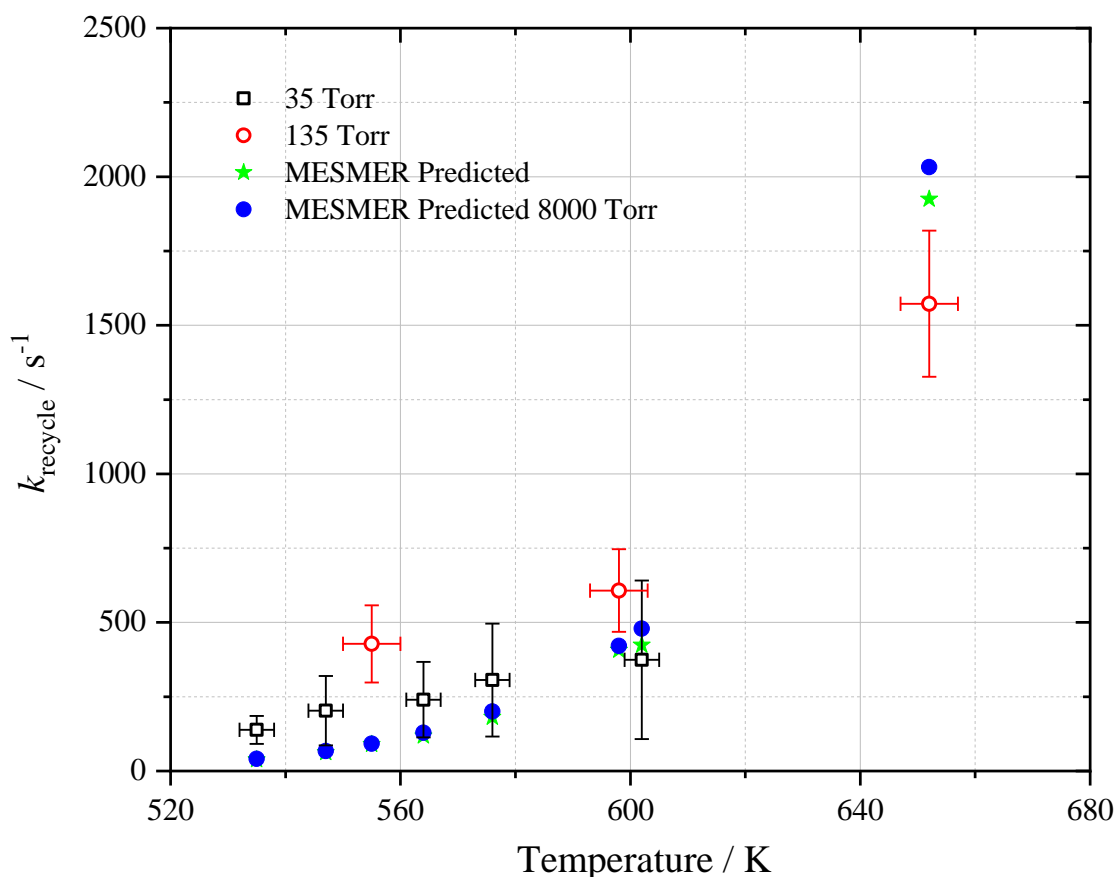


Figure 4-23: Globally obtained k_{recycle} for *n*-butanol β -hydroxybutyl radical decomposition as a function of temperature and pressure, compared with corresponding MESMER fitted values and MESMER high pressure limit predicted values for decomposition. Decomposition barrier estimated by MESMER = (100 ± 2.6) kJ mol⁻¹. The errors reported in temperatures are ± 3 K for pressures around 37 Torr and ± 5 K for pressures around 82 Torr, and the errors reported for the experimental k_{recycle} values are the 1σ errors obtained from the biexponential global fit to the experimental traces multiplied by a factor of 4.

The master equation analysis carried out by the MESMER programme acts to reduce the χ^2 value, i.e. reducing the total error between the MESMER calculated values for the rate constant and the experimentally measured values, within the bounds of the errors provided (see Section 4.3.2). Therefore, despite the reasonably poor agreement between the experimentally measured k_{recycle} values and the MESMER predicted values, the calculated barrier of (100 ± 2.6) kJ mol⁻¹ provides the best overall fitting to the experimental data. Figure 4-24 shows a graph of the MESMER predicted values for the unimolecular recycling parameter against the experimentally measured values with their

associated errors. A line of best fit with a fixed origin of zero has been fit to the data. A perfect ratio of 1:1 linear fit has also been fit to the data, which shows what would be obtained if the MESMER predicted values matched perfectly with the experimentally obtained values. This demonstrates the moderate agreement obtained between the MESMER predicted values and the experimentally measured values, with the experimentally measured values being on the whole slightly slower than the MESMER predicted. The calculated $\langle\Delta E\rangle_{\text{down}}$ parameter, $\langle\Delta E\rangle_{\text{down}} = 180 \pm 808 \text{ cm}^{-1}$, possesses a significant error. This suggests that the pressure dependence of the decomposition has not been well captured in the master equation solving, likely a result of the lack of high pressure experimental data at the intermediate temperatures between 600 and 650 K. A comparison of the calculated and optimised energetic barriers obtained for each isomer is provided at the end of this chapter in Section 4.8.

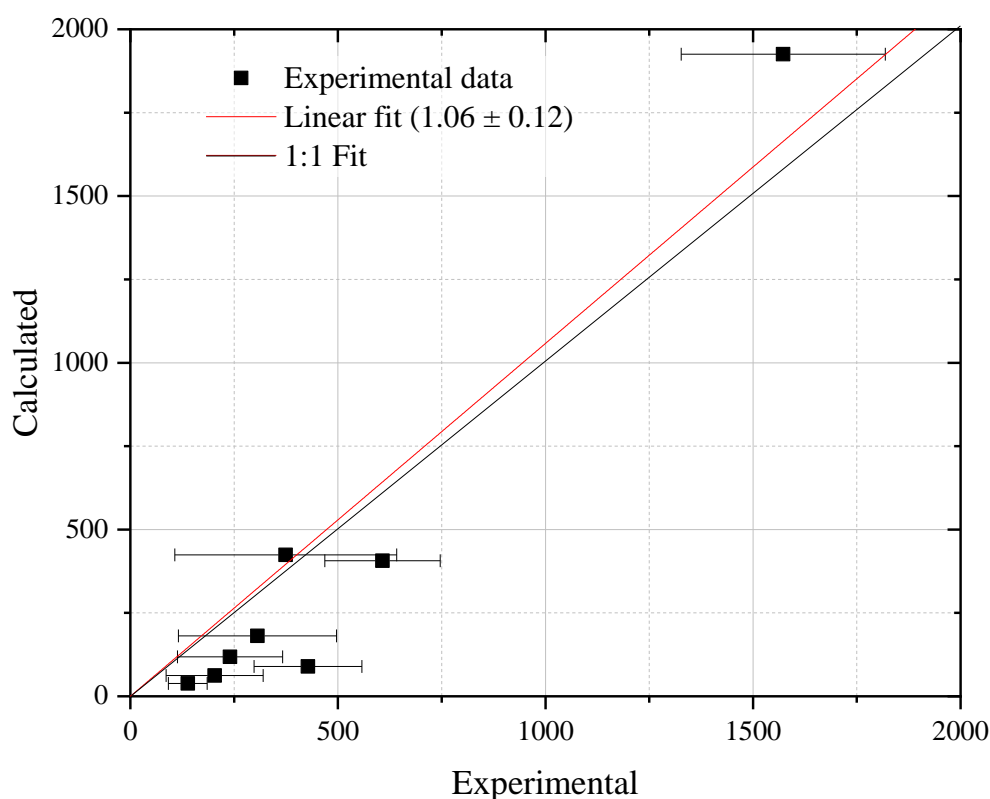


Figure 4-24: A graph of the MESMER predicted values for *n*-butanol radical decomposition compared to the experimentally obtained recycling parameters, with a linear fit (red solid line). A perfect 1:1 fit (black solid line) has also been fit.

4.6.3 Discussion of Branching Ratios

As discussed for the other isomers of butanol, assuming that all abstraction reactions that occur at the beta site result in the recycling of OH, the calculated yield parameter can act as a proxy for the branching ratio of the initial abstractions occurring at this site. A summary of the fraction of abstractions occurring at the beta site of *n*-butanol as a function of temperature calculated from the literature is summarised in Table 4-8, and compared graphically to the yield parameters obtained in this work in Figure 4-25.

Table 4-8: Fraction of OH abstractions occurring at beta site of *n*-butanol, according to branching ratios from literature.

T / K	Sarathy <i>et al.</i> [55] (2012)	McGillen <i>et al.</i> [78] (2013)	Atkinson [114] (1987)	Kwok <i>et al.</i> [130] (1995)	Bethel <i>et al.</i> [101] (2001)
298	0.21	0.26	0.22	0.20	0.38
460	0.15	0.18	0.21	0.20	0.37
480	0.14	0.18	0.21	0.20	0.37
500	0.14	0.18	0.21	0.20	0.37
520	0.14	0.18	0.21	0.20	0.37
540	0.13	0.17	0.21	0.19	0.37
560	0.13	0.17	0.21	0.19	0.37
580	0.13	0.17	0.21	0.19	0.36
600	0.13	0.17	0.21	0.19	0.36
620	0.12	0.17	0.21	0.19	0.36
640	0.12	0.17	0.21	0.19	0.36
660	0.12	0.17	0.20	0.19	0.36
680	0.12	0.17	0.20	0.19	0.36
700	0.12	0.17	0.20	0.19	0.36
720	0.12	0.17	0.20	0.19	0.36
740	0.12	0.17	0.20	0.19	0.36

If the high temperature (> 650 K) and pressure data is discounted from further analysis, as it was in the MESMER parameter fitting to the experimental data, a very

slight positive temperature dependence of the yield is observed. This disagrees with all the literature branching ratios, which show varying degrees of negative temperature dependence for the β -abstraction site reaction with OH.

Between 500 – 700 K, the branching ratios calculated by Sarathy *et al.* [55], McGillen *et al.* [78] and the SAR of Atkinson [114] are in reasonable agreement with each other, varying between 14 – 21 % at 500 K and 12 – 20 % at 700 K. The updated SAR of Bethel *et al.*[101] shows the worst agreement with the other literature, and is almost a factor of two higher than the calculated branching ratio of McGillen *et al.* This work shows the best agreement with the SAR calculated branching ratios of Atkinson and Kwok across the temperature range studied, however there is some scatter obtained in this work between the two pressure sets. For the total overall bimolecular reaction of *n*-butanol with OH, the bimolecular rate coefficient calculated from the parameterisation of Sarathy *et al.* underestimates the experimentally measured values of this work by approximately 25 % (see Section 3.4.1). The poor agreement between the suggested beta abstraction branching ratio obtained in this work and the branching ratio from Sarathy *et al.* may stem from an underestimation of the reactivity of this channel by Sarathy *et al.* It can be assumed that an increase in the estimated rate coefficient for H atom abstraction at this channel would increase the overall reactivity of *n*-butanol with OH to more in line with what was measured experimentally in this work, and would also increase the branching ratio to more in line with this work, the SAR estimates of Atkinson and Kwok, and the estimate of McGillen *et al.*

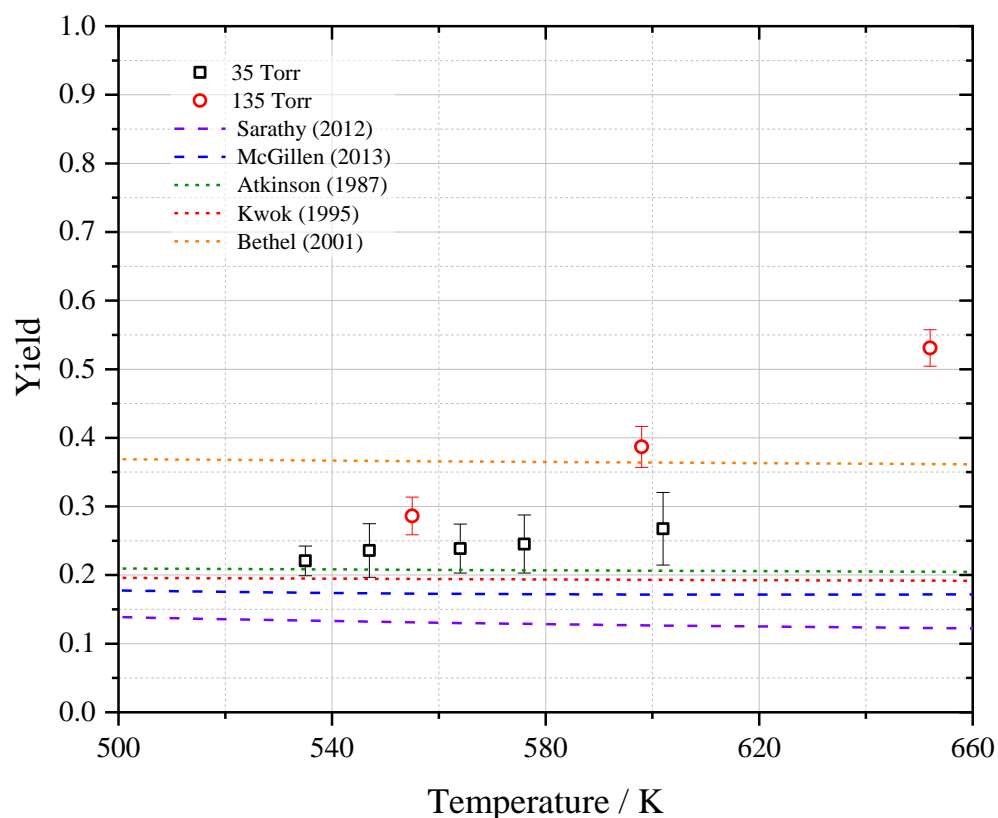
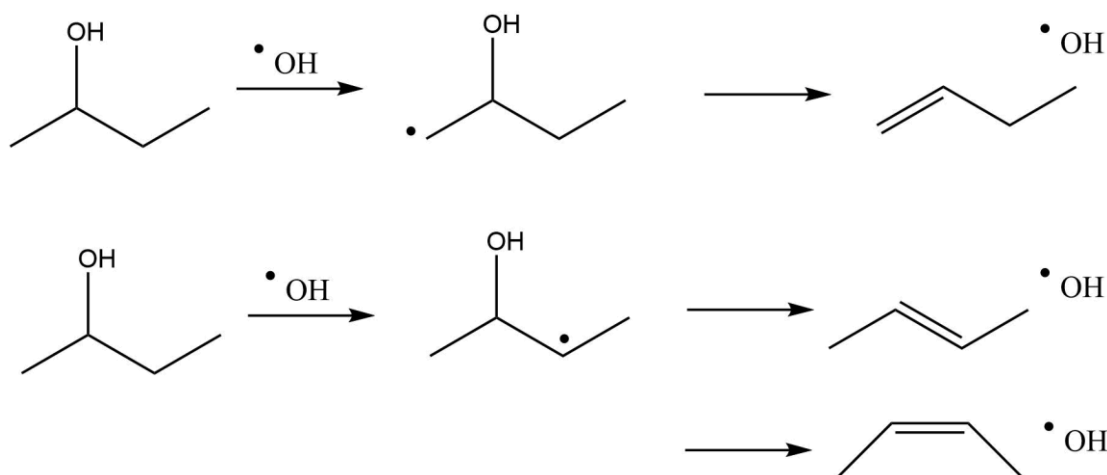


Figure 4-25: A graph of yield of OH for *n*-butanol radical decomposition as a function of temperature and pressure, where the error bars represent propagated errors of k_{recycle} and $k_{\text{non-OH}}$ obtained from global analysis. The literature lines represent the branching ratio of *n*-butanol abstraction reactions occurring at the beta site from literature: Sarathy *et al.* (purple dashed line), McGillen *et al.* (blue dashed line) and the SAR of Atkinson (green dashed line), the updated SAR of Kwok and Atkinson (red dashed line) and the SAR of Bethel *et al.* (orange dashed line). Data replicated from: [55], [78], [114], [130], and [101].

4.7 *s*-Butanol

s-butanol possesses two distinct beta abstraction sites, and therefore is capable of generating two β -hydroxybutyl elimination products, in contrast to the other isomers of butanol. These two possible mechanisms for unimolecular decomposition are shown in Scheme 4-9: abstraction from the primary beta carbon (referred to as C1) results in *n*-butene, and abstraction from the secondary beta carbon (C3) results in 2-butene, which can exist in either *cis* or *trans* conformers.



Scheme 4-9: Decomposition mechanisms following β -site abstraction from *s*-butanol. Upper panel: Abstraction from C1 carbon, resulting in *n*-butene following decomposition. Lower panel: Abstraction from C3 carbon, resulting in *trans*-2-butene or *cis*-2-butene.

Unimolecular decomposition of the C3 β -radical has been reported previously by Antonov and Zador [142], who conducted a theoretical and experimental study of OH + *cis*- and *trans*-butene at temperatures between 400 – 800 K. In their work, *ab initio* calculated energies for the radical species, transition states, submerged van der Waals complexes and the products were obtained at the CCSD(T)-F12a/cc-pVTZ-F12//M06-2X/6-311++G(d,p) level. When combined with master equation solving alongside the experimental rate constants obtained for the association and dissociation reactions in their work, the calculated barrier to the *cis*-2-butene transition state was increased from 112.8 to 114.1 kJ mol⁻¹, and the *trans*-2-butene transition state was increased from 108.5 to 111.0 kJ mol⁻¹. In their work, they also make note of corrections of a similar magnitude being applied to calculations of the analogous barriers for the OH + ethene and OH + isoprene system, despite different levels of theory for the *ab initio* calculations.

4.7.1 Experimental results

For *s*-butanol, experiments have been conducted at pressures between 34 – 113 Torr total pressure N₂, and at temperatures of 497 – 692 K. Two different OH radical precursors have been used to study the unimolecular decomposition of the *s*-butanol β -hydroxybutyl radical, and example kinetic traces obtained using both OH precursors are shown in Figure 4-26. All experimentally obtained global fitting k_{recycle} recycling parameters are summarised in Table 4-9, and represented graphically in Figure 4-27.

Table 4-9: Summary of experimental conditions and obtained OH recycling parameter k_{recycle} for *s*-butanol

T / K	Pressure / Torr	Reagent Range ^a	Precursor	Globally obtained $k_{\text{recycle}} / \text{s}^{-1}$	Globally obtained $k_{\text{non-OH}} / \text{s}^{-1}$	Yield / %
496	35	1.20 - 2.66	H ₂ O ₂	75 ± 7	370 ± 33	17 ± 3
497	35	0.82 - 2.89	H ₂ O ₂	50 ± 6	280 ± 36	15 ± 3
516	35	0.45 - 2.79	H ₂ O ₂	93 ± 7	334 ± 21	22 ± 3
537	35	0.78 - 2.17	H ₂ O ₂	177 ± 11	463 ± 20	28 ± 3
539	99	0.84 - 2.89	H ₂ O ₂	156 ± 8	472 ± 19	25 ± 2
540	35	0.78 - 2.18	H ₂ O ₂	125 ± 8	406 ± 20	24 ± 2
549	38	10.4 - 22.6	UHP	115 ± 14	303 ± 178	28 ± 15
557	35	1.53 - 2.77	H ₂ O ₂	296 ± 16	727 ± 26	29 ± 2
565	112	3.9 - 19.5	H ₂ O ₂	259 ± 15	611 ± 94	30 ± 5
578	36	1.72 - 2.72	H ₂ O ₂	347 ± 40	863 ± 59	29 ± 5
584	35	1.39 - 2.46	H ₂ O ₂	547 ± 45	1010 ± 43	35 ± 4
614	54	9.0 - 27	UHP	666 ± 31	1223 ± 118	35 ± 4
617	98	8.4 - 31.1	UHP	522 ± 36	1035 ± 145	34 ± 6
661	51	9.9 - 21.1	UHP	1230 ± 37	1728 ± 140	42 ± 3
663	108	10.5 - 22.4	UHP	1989 ± 93	2673 ± 164	43 ± 4
692	36	7.1 - 18.0	UHP	2288 ± 118	3615 ± 175	39 ± 3
692	55	7.1 - 18.0	UHP	2963 ± 164	4318 ± 189	41 ± 4
692	96	11.3 - 25.7	UHP	4144 ± 241	6713 ± 390	38 ± 4

^a / 10¹⁴ molecule cm⁻³. UHP: Urea Hydrogen Peroxide.

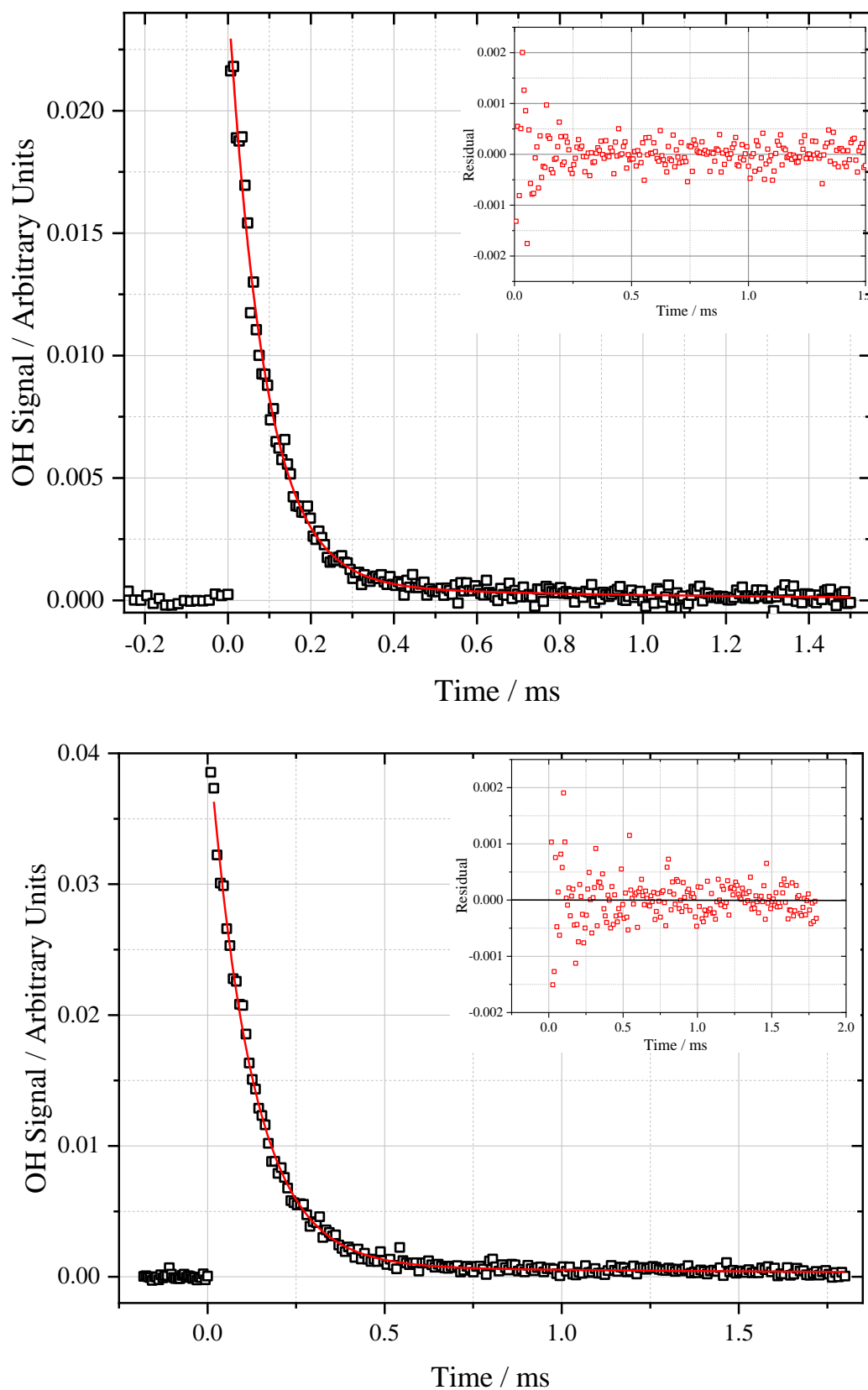


Figure 4-26: Example kinetic traces obtained for *s*-butanol above 490 K using different OH radical precursors. a) Hydrogen peroxide/water precursor, 112 Torr, 560 K, 1.4×10^{15} molecule cm^{-3} . b) Urea hydrogen peroxide precursor, 37 Torr, 550 K, 1.05×10^{15} molecule cm^{-3} . Insets to each trace show residual from fit of biexponential equation to data.

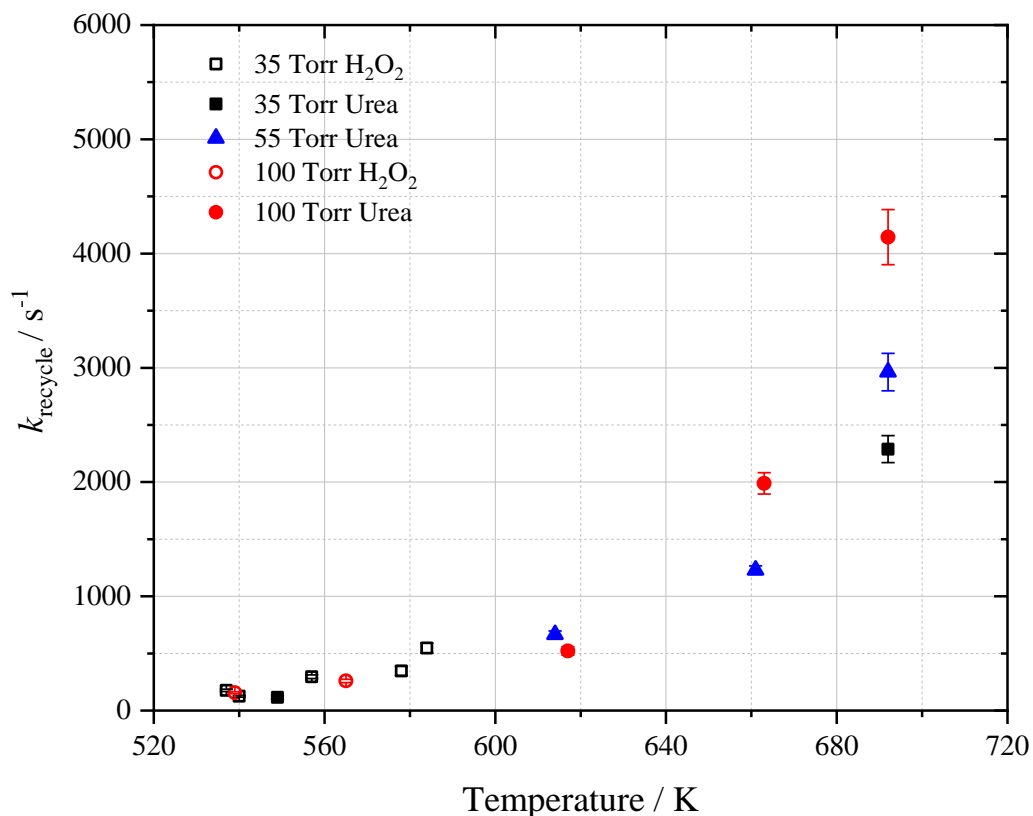


Figure 4-27: Globally obtained k_{recycle} for *s*-butanol β -hydroxybutyl radical decomposition, as a function of temperature and pressure. Open shapes represent parameters obtained using hydrogen peroxide precursor and filled shapes represent those obtained using the urea hydrogen peroxide (UHP) precursor.

Filled data points in Figure 4-27 are experimental results obtained using hydrogen peroxide as an OH precursor, and those with hollow data points utilised urea hydrogen peroxide precursor, with different shapes representing different approximate pressure groupings for both precursors. As shown in Figure 4-27, the recycling parameter k_{recycle} increases in an exponential fashion, as would be expected for a unimolecular decomposition as a function of temperature and pressure. Good agreement is also observed between the different precursors, with increasing pressure resulting in increasing k_{recycle} , as expected. Excellent agreement is also observed between the different OH radical precursors for the calculated yield parameter, as demonstrated in Figure 4-28. Note that the significantly larger error bar for the low pressure UHP measurement is a consequence of the 59 % error in the measured $k_{\text{non-OH}}$, resulting from a poorer quality experimental trace, which was then propagated through the yield calculation. Further discussion of the observed apparent yield can be found in Section 4.7.3.

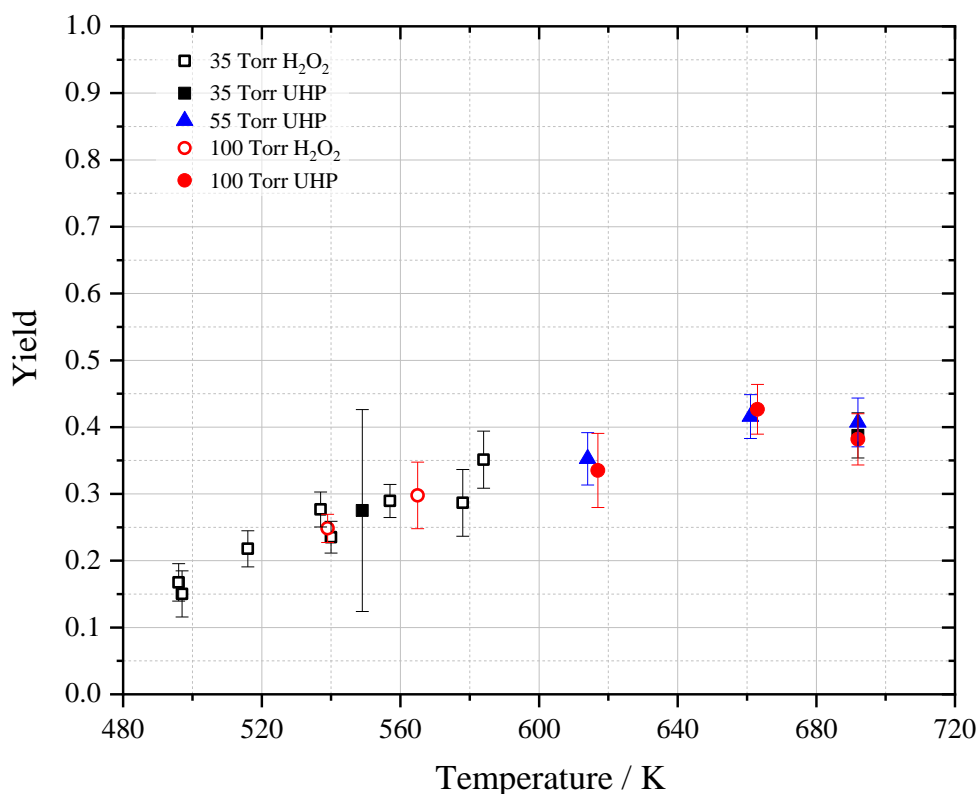


Figure 4-28: A graph of yield of OH as a function of temperature and pressure for *s*-butanol, where the error bars represent propagated errors of k_{recycle} and $k_{\text{non-OH}}$ obtained from global analysis.

4.7.2 *Ab initio* Calculations

The potential energy surface for the decomposition of the *s*-butanol β -hydroxybutyl radicals was calculated at the DFT level M06-2X/aug-cc-pVTZ, obtaining optimised geometries which were then used to calculate the single point energy of each species at the CCSD(T)/aug-cc-pVTZ level. As *s*-butanol possesses two different β -abstraction sites to the hydroxyl group, two different radicals are generated in this initial abstraction. Further to this, abstraction at the secondary carbon results in a radical that can exist in either a *cis* or *trans* conformation. Therefore, energies of both conformers, their respective transition states and 2-butene products have also been calculated. The full potential energy surface can be seen in Figure 4-29, relative to the energy of the *s*-butanol alcohol and OH starting species, prior to the initial abstraction reactions. The energy of the Van der Waals complexes in each case have not been calculated in this work for the *s*-butanol hydroxybutyl radical decompositions, but by analogy with the *t*-butanol system, have been included in Figure 4-29 for completion.

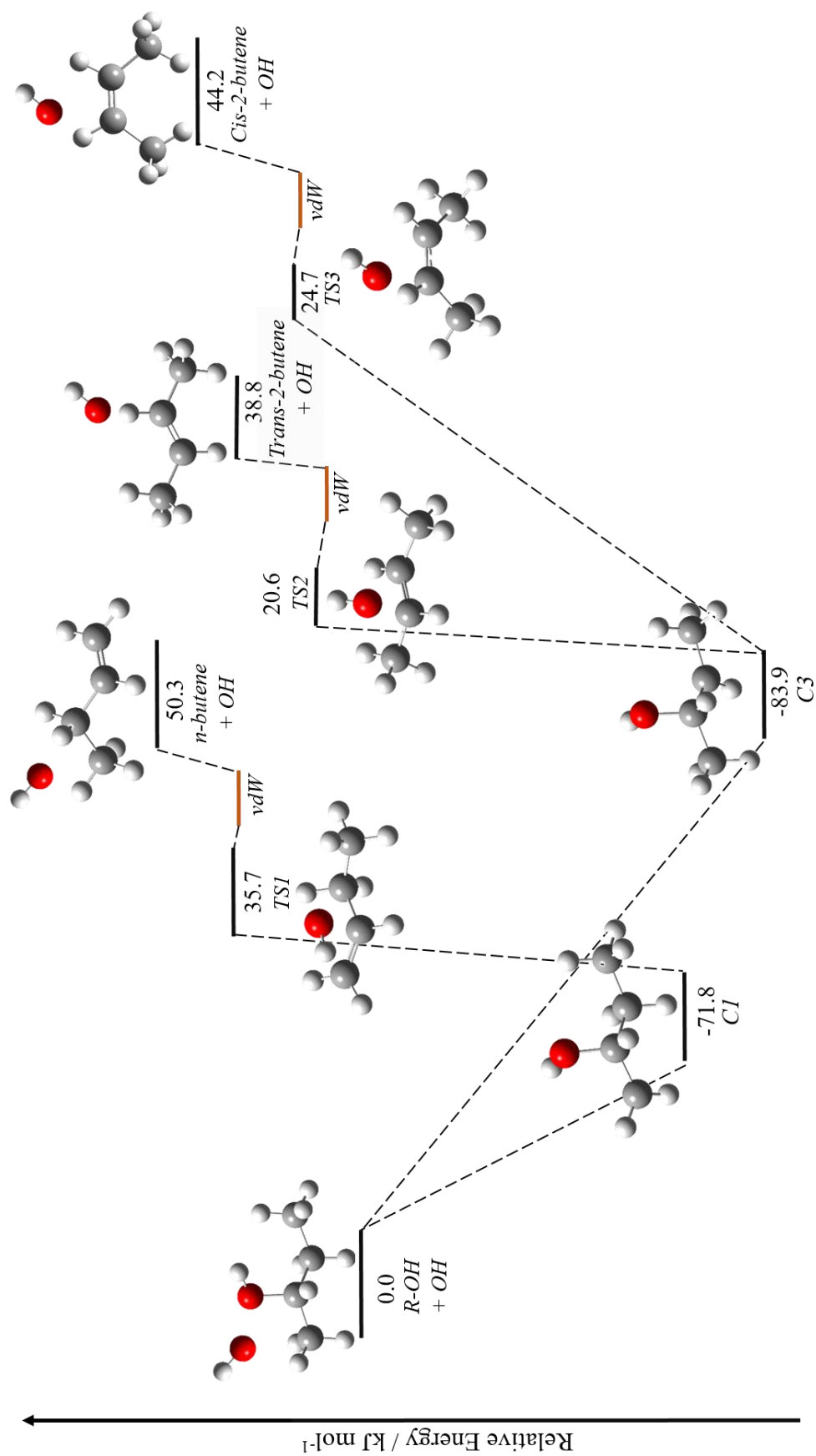


Figure 4-29: Potential energy surface for the decomposition of the two β s-hydroxybutyl radicals, calculated at CCSD(T)/aug-cc-pVTZ//M06-2X/aug-cc-pVTZ level. Water has been omitted as a product from the initial abstraction reaction. Van der Waals complexes not calculated but included based on analogy with *t*-butanol system (shown in orange).

From stationary point energy calculations at the CCSD(T)/aug-cc-pVTZ level, the *s*-butanol C3 abstraction radical is 12.1 kJ mol⁻¹ lower in energy than the C1 abstraction radical, as expected due to the radical stabilisation possible in the secondary C3 radical when compared to the primary C1 radical. The C1 β -hydroxybutyl radical decomposition has a calculated barrier of 107.5 kJ mol⁻¹. The C3 β -hydroxybutyl radical can decompose to two possible stereoisomers of 2-butene. Decomposition to the trans-2-butene isomer has a calculated barrier height of 104.4 kJ mol⁻¹, compared to a calculated barrier height of 108.6 kJ mol⁻¹ for the cis-2-butene products. These calculated barriers are comparable to the β -hydroxybutyl decomposition barriers obtained for the other isomers of butanol, and further comparisons are made in section 4.8.

Antonov *et al.* carried out a combined theoretical and experimental study for the reactions of OH with cis-2-butene and trans-2-butene at low temperature combustion relevant temperatures (400 – 800 K) [142], equivalent to the C3 radical and the related transition states and products. The potential energy surface for both addition and abstraction channels was examined, and compared with master-equation calculations, with adjustments made to *ab initio* calculated barriers to obtain agreement with experimentally measured data. A potential energy surface with the relevant stationary point energies from their work has been constructed and compared to the corresponding energies calculated by this work in Figure 4-30. The *ab initio* calculated barriers from Antonov *et al.* are shown in plain black font, and the master-equation adjusted values are shown in bold black font. The *ab initio* calculated barriers from this work are shown in red italics. All barriers are reported in kcal mol⁻¹, as they are in the study of Antonov *et al.*

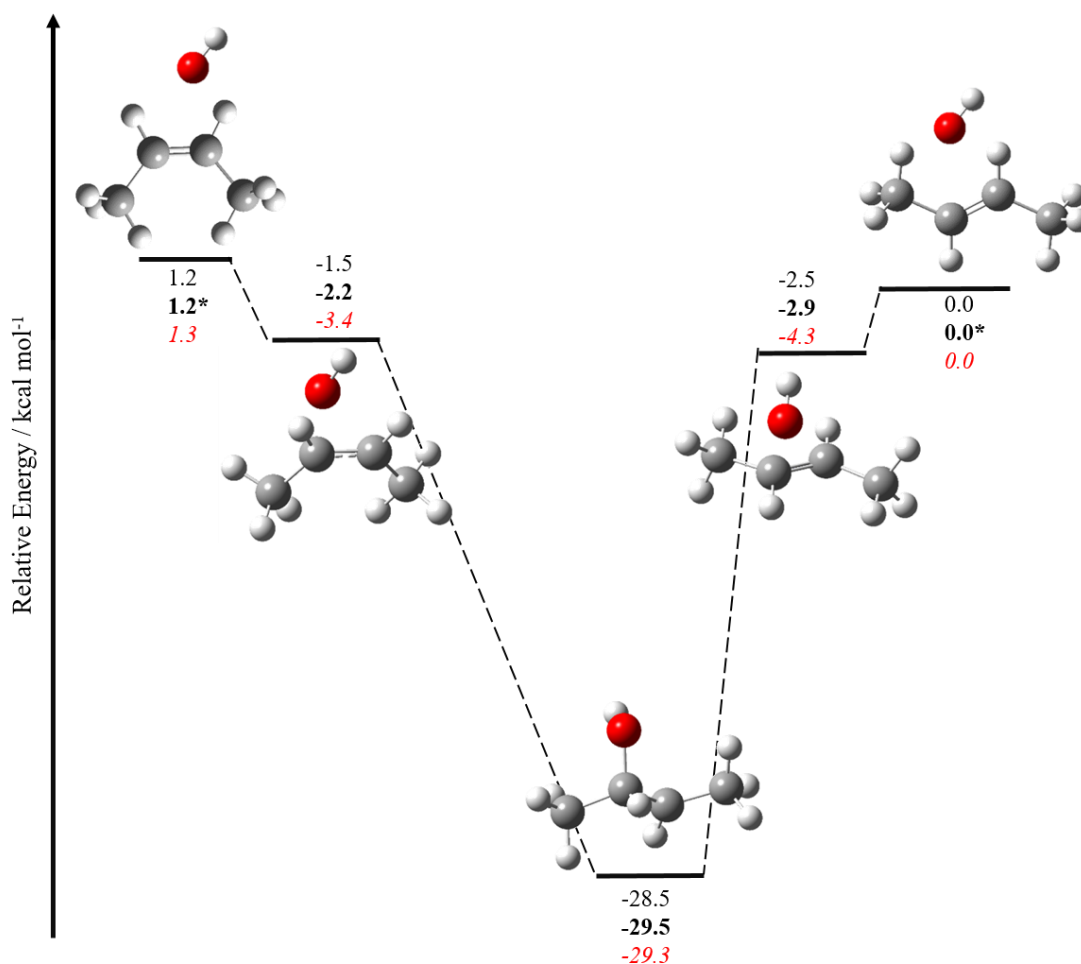


Figure 4-30: C3 radical, transition states, and both cis and trans-2-butene products energies in kcal mol⁻¹, defined relative to trans-2-butene + OH. Plain black font represents *ab initio* calculated barriers (CCSD(T)-F12a/cc-pVTZ-F12//M06-2X/6-311++G(d,p)) and bold black font represents master equation adjusted values, both from Antonov [142], compared with *ab initio* calculated energies from this work in red italics (CCSD/aug-cc-pVTZ//M06-2X/aug-cc-pVTZ). *Value not adjusted in master-equation calculation.

The values obtained in this work are in overall excellent agreement with the master equation corrected stationary point energies of Antonov *et al.* [142], despite the different levels of theory used for the *ab initio* calculations and the energies from this work not being optimised by master equation solving with experimental measurements. Future work for calculating the barriers to decomposition for the *s*-butanol β -hydroxybutyl radicals could use master equation solving of the experimentally obtained k_{recycle} values from this work in conjunction with the reverse rate constants of Antonov *et al.* for the addition of OH at the two potential sites in 2-butene. By constraining the reactivity of the C3 radical, the barrier to decomposition of the C1 radical could be

optimised. A comparison of the calculated energetic barriers for each isomer is provided at the end of this chapter in Section 4.8.

4.7.3 Discussion of Branching Ratios

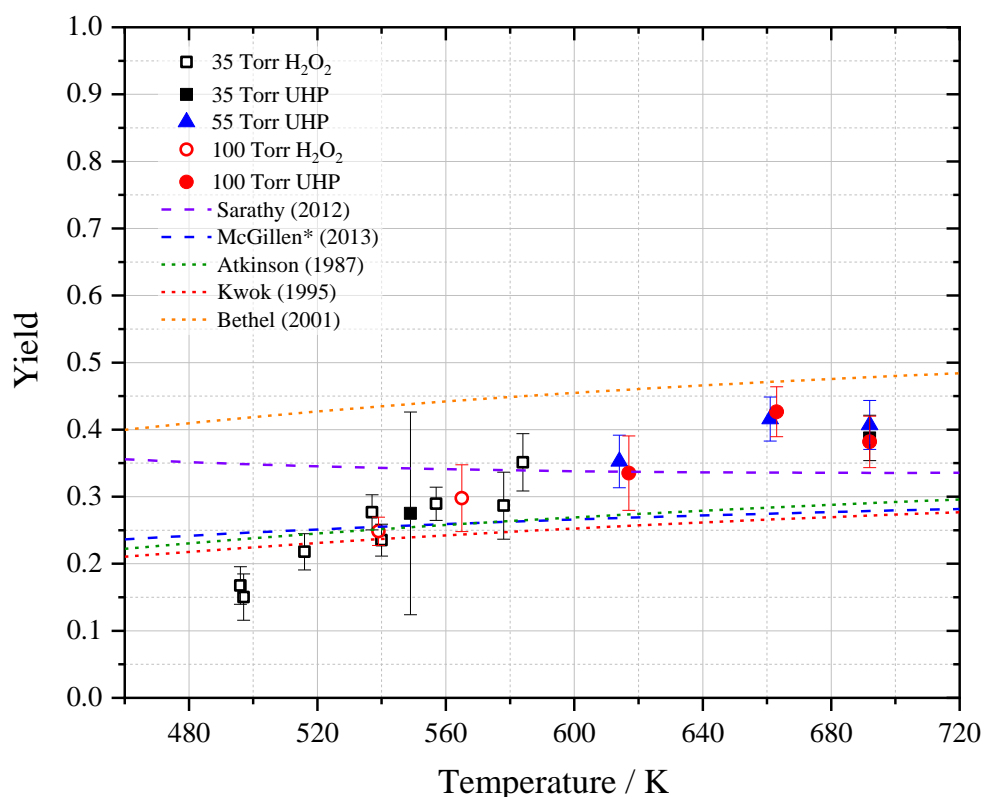


Figure 4-31: A graph of yield of OH for *s*-butanol radical decomposition as a function of temperature and pressure, where the error bars represent propagated errors of k_{recycle} and $k_{\text{non-OH}}$ obtained from global analysis. The literature lines represent the branching ratio of *s*-butanol abstraction reactions occurring at the beta site from literature: Sarathy *et al.* (purple dashed line), McGillen *et al.* (blue dashed line) and the SAR of Atkinson (green dashed line), the updated SAR of Kwok and Atkinson (red dashed line) and the SAR of Bethel *et al.* (orange dashed line). * McGillen *et al.* parameterisation only represents the secondary beta site, as the primary beta site was reported as a total of the primary beta and primary delta sites, and cannot be added. Data replicated from: [55], [78], [114], [130], and [101].

A positive temperature dependence is observed for the calculated yield parameter, with good agreement between the different precursors utilised, as well as the three different pressure ranges. Reasonable agreement is also obtained between the experimental yield calculated in this work, and the total branching ratios for the two beta sites calculated from the literature. The slight curvature in the temperature dependence is

best captured by the SAR of Atkinson [114], which agrees well with this experimental work across all temperatures studied. The parameterisation of McGillen *et al.* only represents the branching ratio for abstraction at the primary beta site of *s*-butanol, as the parameterisation for the secondary beta site was reported as a combination of this site and the neighbouring gamma site, which does not result in the recycling of OH through unimolecular dissociation. Therefore the parameterisation of McGillen *et al.* should be considered a lower limit to the total beta site abstraction fraction. As with *n*- and *i*-butanol, the updated SAR of Bethel *et al.* [101] overestimates the total branching fraction of initial abstractions occurring at the beta sites of *s*-butanol, and is outside the error margins of all the experimental measurements made in this work.

Table 4-10: Fraction of OH abstractions occurring at beta sites of *s*-butanol, according to branching ratios from literature.

T / K	Sarathy <i>et al.</i> [55] (2012)	McGillen <i>et al.</i> * [78] (2013)	Atkinson [114] (1987)	Kwok <i>et al.</i> [130] (1995)	Bethel <i>et al.</i> [101] (2001)
298	0.43	0.17	0.13	0.13	0.28
460	0.36	0.24	0.22	0.21	0.40
480	0.35	0.24	0.23	0.22	0.41
500	0.35	0.25	0.24	0.22	0.42
520	0.35	0.25	0.25	0.23	0.43
540	0.34	0.26	0.25	0.24	0.43
560	0.34	0.26	0.26	0.24	0.44
580	0.34	0.26	0.26	0.25	0.45
600	0.34	0.27	0.27	0.25	0.45
620	0.34	0.27	0.27	0.26	0.46
640	0.34	0.27	0.28	0.26	0.47
660	0.34	0.27	0.28	0.27	0.47
680	0.34	0.28	0.29	0.27	0.48
700	0.34	0.28	0.29	0.27	0.48
720	0.34	0.28	0.30	0.28	0.48

* Only the secondary beta site, as the primary beta site was reported as a total of the primary beta and primary delta sites, and cannot be added.

4.8 Isomer Comparison

The unimolecular decomposition kinetics of the β -hydroxybutyl radicals formed for each isomer following hydrogen abstraction at the β -site have been measured in this chapter as a function of both temperature and pressure.

Using master equation solving in the MESMER package in conjunction with *ab initio* computational calculations, barriers to decomposition have been calculated for *t*-, *i*-, *s*- and *n*-butanol, and optimised for all but *s*-butanol. Whilst this is not the first time this phenomenon has been observed, it is the first time it has been measured and quantified in this way for the three isomers that have been optimised using master equation analysis (*t*-, *i*- and *n*-butanol). The barriers obtained from these calculations and optimisations can be seen summarised in Table 4-11, compared with the structure of the relevant radical for each case.

In order to rationalise the barriers to decomposition obtained for the different β -hydroxybutyl radicals, comparisons should be drawn between the groups neighbouring to the radical site. The lowest optimised barrier obtained is that of decomposition of the *i*-butanol β -hydroxybutyl radical. This is likely a consequence of the three inductive R alkyl groups neighbouring to the radical site, acting to stabilise this radical centre. The relative energies of these decomposition barriers then increase with decreasing alkyl substituents, and increasing C–H bond substituents, with the exception of the C3-radical decomposition to *cis* products, however this is likely due to the steric hindrance of the decomposition to *cis*-2-butene. The decomposition barriers calculated for the C1 *s*-butanol β -hydroxybutyl radical and the *t*-butanol radical are the closest energetically of the barriers calculated. Both possess two C–H bonds neighbouring to the radical centre, confirming that the neighbouring groups have a significant effect on the energy barrier to decomposition.

As the barrier to decomposition has been measured experimentally, calculated *via ab initio* methods and optimised for both *t*-butanol and *i*-butanol β -hydroxybutyl radicals, this could be used in future to calculate the equilibrium constant for the addition of OH to *iso*-butene, and could assist in constraining the branching ratio for this forward addition reaction. The same can also be said for the k_{recycle} parameters obtained for decomposition of *n*-butanol and *s*-butanol, if further work is conducted to optimise the barrier to decomposition of the beta-primary site (C1) of *s*-butanol.

Table 4-11: *Ab initio* calculated barriers at the CCSD/aug-cc-pVTZ//M06-2X/aug-cc-pVTZ level, compared with optimised barriers obtained from MESMER fitting, and radical structure diagrams. *Errors reported only represent the error calculated by MESMER. An error for each barrier including the systematic errors of the system is assumed to be 4 kJ mol⁻¹.

Isomer	Calculated Barrier / kJ mol ⁻¹	Optimised Barrier/ kJ mol ⁻¹ *	Radical structure
<i>t</i> -butanol	107.2	103.4 ± 1.3	
<i>i</i> -butanol	99.9	93.0 ± 1.0	
<i>n</i> -butanol	98.8	100 ± 2.6	
<i>s</i> -butanol (C1)	107.5	-	
<i>s</i> -butanol (C3 – trans products)	104.4	-	
<i>s</i> -butanol (C3 – cis products)	108.6	-	

4.9 Summary

Measurements have been made for the unimolecular decomposition of the β -hydroxybutyl radical decomposition to form OH and the relevant butane isomer for each of the four isomers of butanol at temperatures above 480 K, extending to 614 K for *t*-butanol, 621 K for *i*-butanol, 652 K for *n*-butanol and 692 K for *s*-butanol. *Ab initio* barriers have also been calculated for each isomer at the CCSD/aug-cc-pVTZ//M06-2X/aug-cc-pVTZ level, with *t*-butanol calculated at the CCSD/CBS//M06-2X/aug-cc-pVTZ level. These barriers have then been used in conjunction with master equation solving to obtain optimised barriers to decomposition for *t*-, *i*- and *n*-butanol. By making the assumption that the β -radical formed following abstraction at this site only decomposes to OH and butene, the yield of OH observed can be used as a proxy for the branching ratio of abstraction at the β site. Comparisons have therefore been drawn between the measured OH yields for each isomer in this work and the equivalent branching ratios calculated from combustion models, experimental measurements and SAR estimates from the literature. Overall, good agreement was obtained between the estimated branching ratios from the literature and the yields obtained in this work.

This chapter has confirmed that the barriers to beta-scission decomposition are different for each isomer, and can be rationalised by the inductive effects of the neighbouring groups. Most combustion models currently in use make a series of assumptions for these decomposition reactions. For example, the model of Sarathy *et al.* [55] assumes the same A factor and barrier to decomposition for each isomer, and does not account for a pressure dependence. In the Sarathy *et al.* model, the reaction is also entered as a forward OH + alkene addition reaction, and thus the reverse reaction to OH and alkene products is calculated based on microscopic reversibility, and is sensitive to the thermochemistry entered. This work has proven that each isomer has a different energetic barrier to decomposition of the β -hydroxybutyl radical, and that the decomposition is also pressure dependent. Future work should seek to accurately map out this pressure dependence of the decompositions by conducting experiments across a wider pressure range, in order to obtain better defined $\langle \Delta E \rangle_{\text{down}}$ values when conducting master equation fitting. This could then be used in conjunction with a Troe parameter fitting to obtain pressure dependent parameters for use in combustion models.

In order to test the importance of these reactions when modelling low temperature combustion conditions, modelling simulations should be carried out in conjunction with sensitivity analysis across a range of temperatures and pressures for each of the isomers.

Whilst the β -scission decomposition reaction channel itself does not result in chain branching activity, accounting for the regeneration of OH occurring is still likely to be important to the modelling of the overall reactivity of the system at low to intermediate temperatures where the reactivity is governed by kinetics.

Chapter 5 Potential QOOH Decomposition Observation and a Kinetic Study of O (³P) with *n*-butanol

5.1 Chapter Summary

This chapter presents some unusual OH regeneration behaviour observed following addition of significant amounts of oxygen to the reaction system of butanol with OH investigated in the previous chapters. A growth in OH signal was observed for *t*-butanol at temperatures and pressures above 590 K and 45 Torr, and for *n*-butanol at temperatures and pressures above 650 K and 130 Torr. All experiments reported in Chapters 3 and 4 have been measured in the absence of added oxygen, and therefore the effects observed here should not influence the measurements made in the previous chapters.

One hypothesis suggested that this was a direct observation of the chain branching process described in Section 1.7. In order to test this theory, chemical kinetic simulations of the OH radical profile under the corresponding experimental conditions were carried out, using a submechanism constructed from the Sarathy *et al.* combustion mechanism. Further investigation of the Sarathy mechanism found that simplifying the reactions of the β -hydroxybutyl peroxy radical (β -RO₂) through to products via one concerted reaction step was an oversimplification that requires further investigation.

Following a series of experimental tests, the likely mechanism for the growth in signal obtained for both *n*-butanol and *t*-butanol is the reaction of O (³P) atoms with the alcohol reagent. However, at the highest temperatures studied (> 720 K), an increase in the OH fluorescence signal baseline suggests that some ketohydroperoxide formation and decomposition is also occurring at these temperatures, and could also confirm the decomposition of some small amount of the fuel at these temperatures.

The first experimental measurements of the reaction of O (³P) with *n*-butanol at temperatures above 600 K have been made, and the reaction was studied across the temperature range 490 – 730 K, at pressures of 40 – 55 Torr. The temperature dependent Arrhenius parameterisation obtained across this temperature range is $k_{\text{O}(3\text{P})+n\text{-butanol}}(490 - 730 \text{ K}) = (1.64 \pm 0.55) \times 10^{-10} \times \exp^{(-18700 \pm 1700/RT)} \text{ cm}^3 \text{ molecule}^{-1} \text{ s}^{-1}$.

Some aspects of the work presented in this chapter are speculative in nature, but highlight the need for more robust testing of experimental measurements at high temperatures (> 600 K) in the presence of significant amounts of added oxygen where side reactions can occur and interfere with the desired measurements of reaction kinetics.

5.2 Introduction

Following the initial abstraction reaction of a fuel molecule by a small radical such as OH, the R fuel radical formed can undergo unimolecular decomposition reactions (such as those highlighted in Chapter 4), or the addition of an oxygen. After the formation of the RO₂ species, internal isomerisations can occur, forming a QOOH hydroperoxide species. This species can decompose to OH and other products in a radical propagation reaction, or can undergo the addition of a second oxygen species to form O₂QOOH, another peroxy radical. The O₂QOOH peroxy species can then decompose to give an OH radical and a ketoyhydroperoxide, which in turn decomposes to give a second OH radical and other products. This second decomposition results in the chain branching phenomena needed for low temperature ignition of a fuel.



For the butanol isomers, the reactions described above in reactions R 5-1 to R 5-9 describe the generic mechanism of chain branching observed. However, due to the multiple abstraction sites of each butanol isomer, the actual mechanism for butanol combustion is far more complex. A schematic diagram of some of the potential oxidation pathways for the combustion of *n*-butanol are shown in Figure 5-1, replicated from Sarathy *et al.* [55]. The percentages next to each arrow represent the percentage of reactions going through each reaction channel, according to a reaction path analysis of a simulation conducted using the model of Sarathy *et al.* at 800 K, 1 atmosphere of total pressure and a fuel equivalence ratio of 1, for 20 % of the fuel consumption.

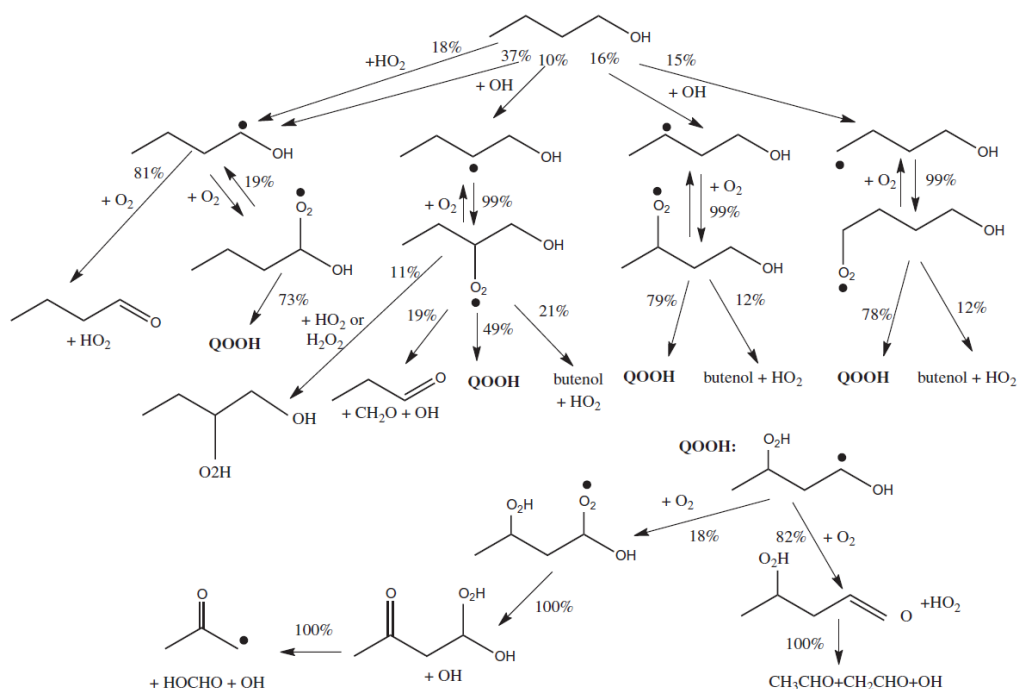


Figure 5-1: Sarathy *et al.* combustion model reaction path analysis for *n*-butanol combustion at 800 K, 1 atm and $\phi = 1.0$, replicated from [55]. The reaction fluxes are given for 20 % fuel consumption.

Figure 5-1 demonstrates that for each abstraction site in *n*-butanol, isomerisations and decompositions of the RO₂ species are in competition, and the dominant reaction varies for each potential abstraction site. The percentages from the reaction path analysis provide a useful insight into estimating how the reaction will proceed for each site at a given set of conditions, however these numbers are entirely dependent on the reaction rates found in the combustion model.

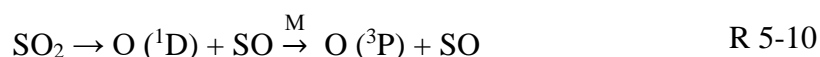
Many of the reactions for the butanol isomers found in combustion models, such as those in the model of Sarathy *et al.* [55], are estimates based on analogous reactions for the butane isomers, with energies lowered to account for some of the activation of C–H bonds resulting from the presence of the OH group in butanol [55]. The reactions further down the chain branching process, i.e. decomposition of the carbonyl alkylhydroxy-hydroperoxides (reaction R 5-8), are estimates based on combustion models for linear and branched hydrocarbons, and thus by the author's admission, should be treated as rough estimates. As highlighted by Sarathy *et al.* [1], experimental and

theoretical studies are required to further constrain the kinetic model parameters, particularly those for reactions specific to alcohols.

5.3 Experimental

The majority of the experiments conducted in this chapter were carried out using the method and set-up described in both Chapter 3 and Chapter 4. Experiments were conducted using both on-resonant and off-resonant fluorescence of OH radicals, for experiments using *n*-butanol and *t*-butanol reagent respectively. OH radicals were generated from the photolysis of H₂O₂ precursor at 248 nm using an excimer laser (KrF).

For the experiments described in Section 5.5.4, photolysis of SO₂ precursor at 248 nm was used to generate O (³P) radicals, for measuring the reaction of O (³P) + *n*-butanol described by the reaction below.



Reacting O (³P) atoms with butanol results in the formation of OH radicals, which were then monitored by on-resonant OH laser-induced fluorescence. Initial experimental tests were conducted at pressures between 20 and 70 Torr of nitrogen to ensure that all O (¹D) had been collisionally deactivated to O (³P) sufficiently at 45 Torr, and no prompt OH formation occurred from reaction of O (¹D) with *n*-butanol. The full reaction scheme and the parameters obtained from fitting these traces is described further in Section 5.5.4. SO₂ reagent was flowed from a glass bulb, in which the reagent had been diluted with nitrogen at around 5 % SO₂ concentration, before being flowed through a mass flow controller into the mixing manifold.

Chemicals used: *n*-butanol (Sigma-Aldrich, ≥ 99.4 %), *t*-butanol (Sigma-Aldrich, ≥ 99.0 %), hydrogen peroxide/water (H₂O₂, Sigma-Aldrich, 50% (w/w) in H₂O), sulphur dioxide (SO₂, BOC, 99.9 %). Nitrogen (BOC, 99.99 %) and oxygen (BOC, 99.999 %) were used straight from the cylinder as supplied.

5.4 *t*-butanol OH Growth Observation and Modelling

5.4.1 Observation of OH Signal Growth

For each of the butanol isomers, biexponential behaviour was observed in the absence of oxygen at temperatures above 480 K. This behaviour was seen to increase with temperature and pressure, and was attributed to the unimolecular decomposition of the β -hydroxybutyl radical, as explained in Chapter 4. A typical trace observed under these conditions is shown in Figure 5-2.

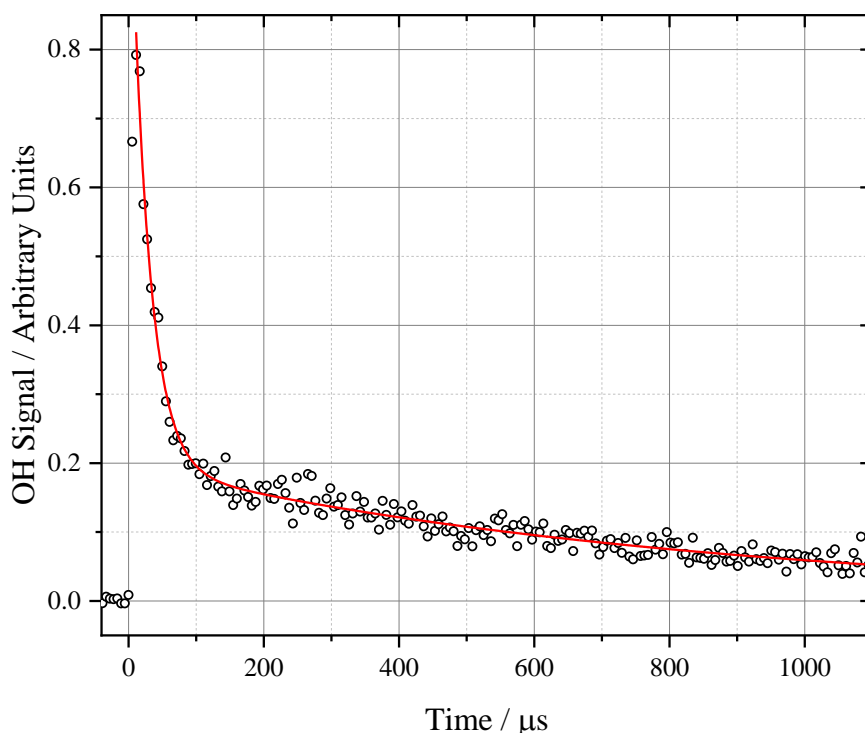


Figure 5-2: An example kinetic trace obtained under biexponential conditions in the absence of added oxygen. Trace obtained at 613 K, 36 Torr N₂, [*t*-butanol] = 1.6×10^{16} molecule cm⁻³. The red line represents a biexponential fit (Equation E 4-6) $k_a = (31400 \pm 1100)$ s⁻¹, $k_{\text{recycle}} = (5980 \pm 210)$ s⁻¹, $k_{\text{non-OH}} = (1420 \pm 50)$ s⁻¹. The quoted errors are statistical at the 1 σ level.

At the lowest temperatures at which this biexponential behaviour occurs, the addition of oxygen to the system did not affect the rate of recycling observed, and the experimental traces observed under these conditions did not show any differences. However, at temperatures above this, the addition of oxygen did appear to increase the rate of the recycling, and an increase in the recycling parameter k_{recycle} was observed. This was expected to be a result of the addition of oxygen to the other abstraction radicals

present in the system, resulting in the scheme of reactions outlined below in reactions R 5-3 – R 5-5 for the general combustion reaction mechanism, and the recycling of OH through chain propagation.

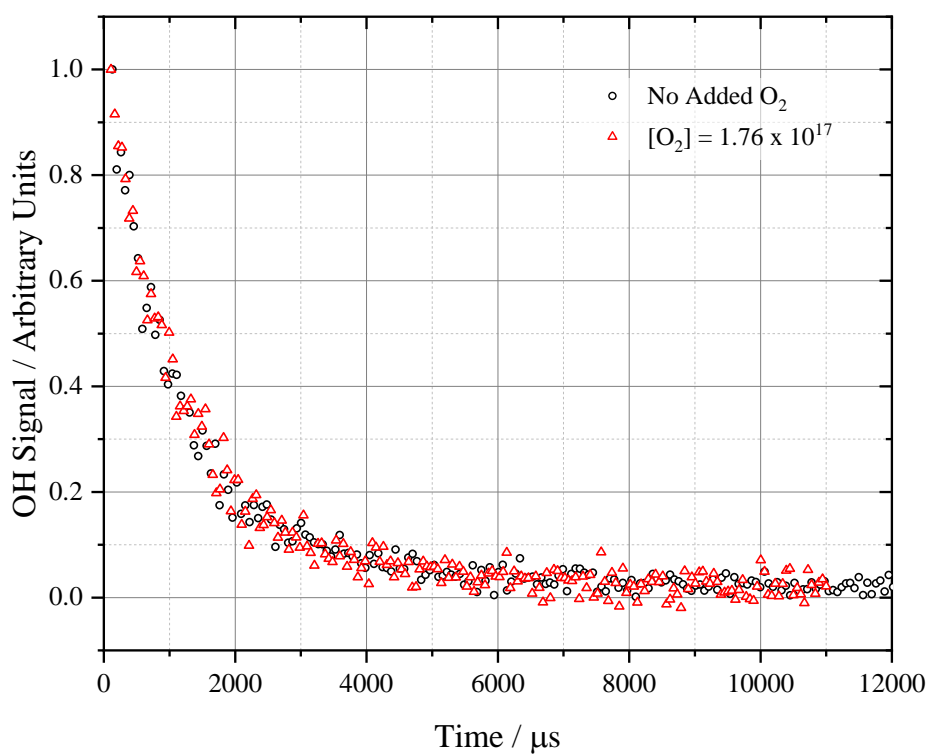
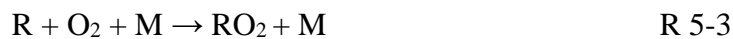


Figure 5-3: Example traces obtained at 500 K, 34 Torr, both with (hollow red triangles) and without (hollow black circles) the addition of significant amounts of oxygen, where added $[O_2] = 1.76 \times 10^{17}$ molecule cm^{-3} .

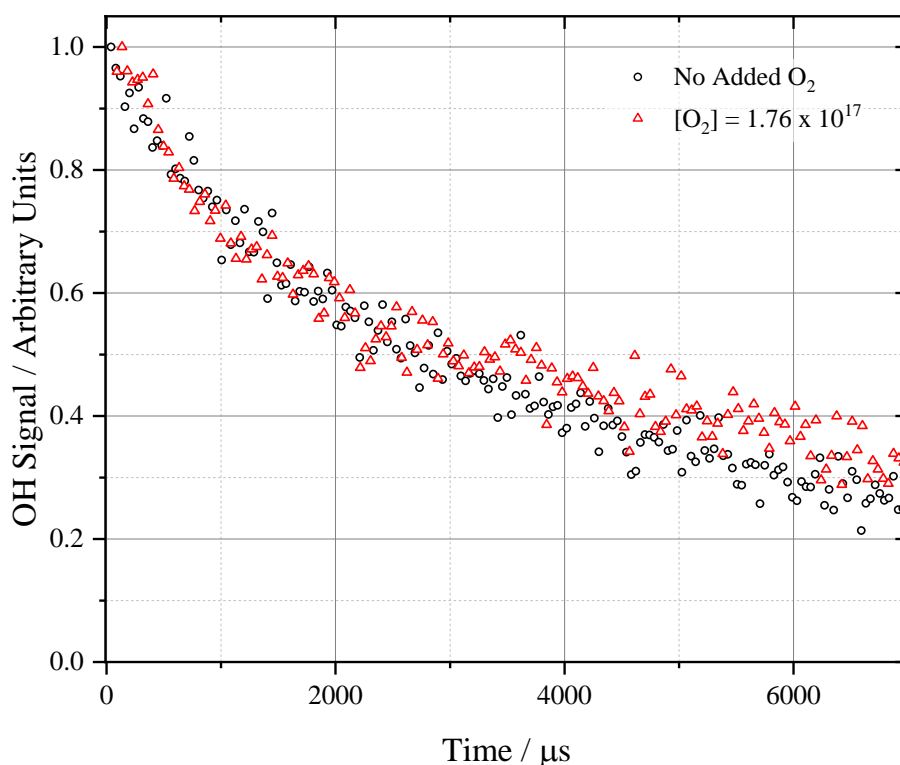


Figure 5-4: Example trace obtained at 580 K, 34 Torr, both with (hollow red triangles) and without (hollow black circles) the addition of significant amounts of oxygen, where added $[\text{O}_2] = 1.76 \times 10^{17}$ molecule cm^{-3} .

At temperatures where addition of oxygen caused a change in the observed kinetic trace, increasing the amount of oxygen in the system resulted in observation of enhanced OH radical recycling. For the observation of increased recycling at 580 K, it is worth noting that significant amounts of oxygen are required; over two orders of magnitude greater than the estimated residual oxygen present in the system from decomposition of hydrogen peroxide precursor (described in Section 2.7.1.1). It is therefore unlikely that any of the observations in this chapter have influenced the kinetics measured in Chapters 3 and 4.

With addition of greater amounts of oxygen, the recycling parameter k_{recycle} and the OH recycling yield (as defined in previously in equation E 4-7) increased, dependent on the oxygen added to the system. Figure 5-5 shows the increasing biexponential behaviour observed as a function of oxygen for a constant amount of *t*-butanol, at a constant temperature and pressure.

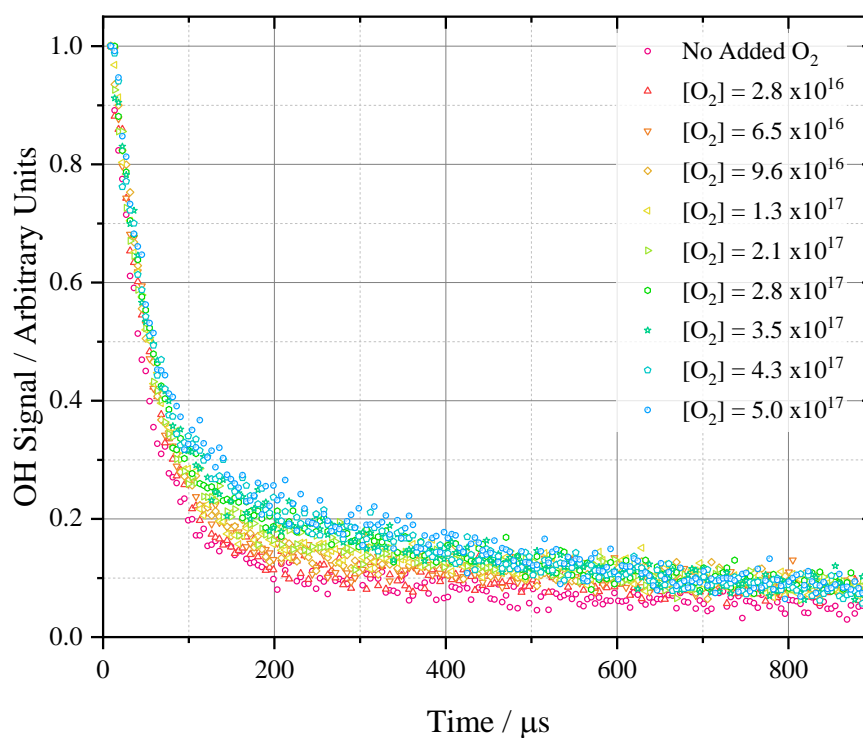


Figure 5-5: A graph of increasing biexponential behaviour as a function of varying oxygen (molecule cm^{-3}). All traces were obtained at 587 K, approximately 82 Torr, with $[t\text{-butanol}] = 1.1 \times 10^{16}$ molecule cm^{-3} . All experimental traces have been rescaled to 1 at point of photolysis for ease of comparison.

At temperatures above 590 K, OH fluorescence traces were obtained that did not show the expected biexponential behaviour, but instead displayed ‘shoulders’ in the OH signal. These traces appeared to show experimental conditions in which OH was being produced at a rate faster than it was being removed, manifesting as a ‘growth’ in the signal. Figure 5-6 shows an example set of conditions under which this occurred for *t*-butanol.

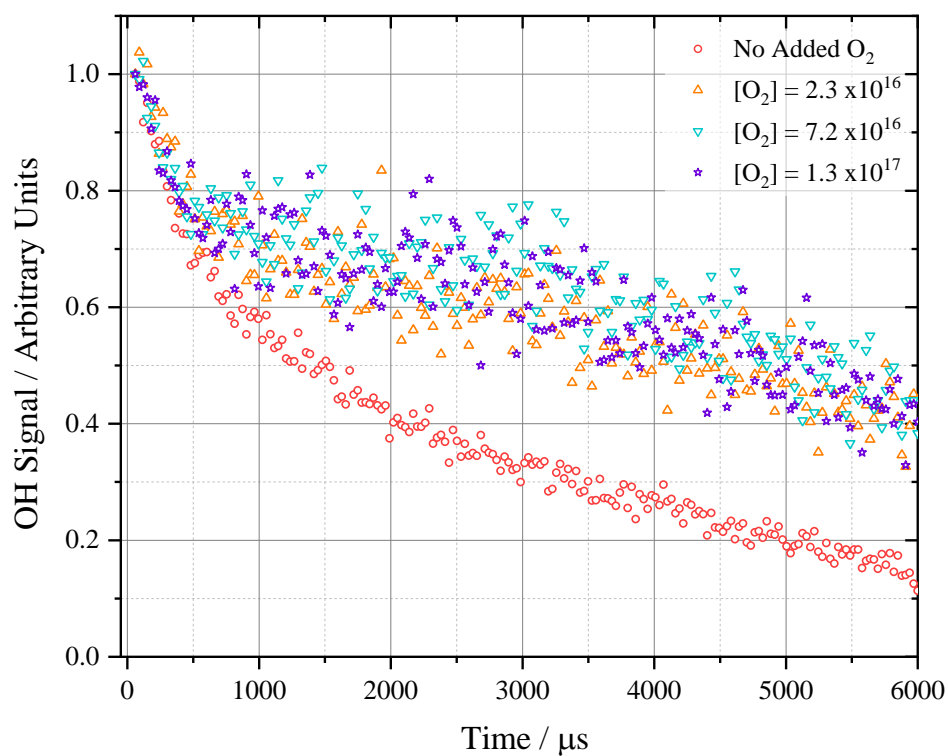


Figure 5-6: Experimental traces showing slight growth of OH signal on addition of varying amounts of oxygen to the system. All traces obtained at approximately 590 K, 45 Torr, $[t\text{-butanol}] = 5.7 \times 10^{14} \text{ molecule cm}^{-3}$.

With increasing temperature beyond those of Figure 5-6, the growth of OH signal appeared to occur at shorter and shorter timescales, such that the growth appeared to occur instantly following the photolysis laser pulse. An example set of traces in which the instant growth is observed are shown in Figure 5-7.

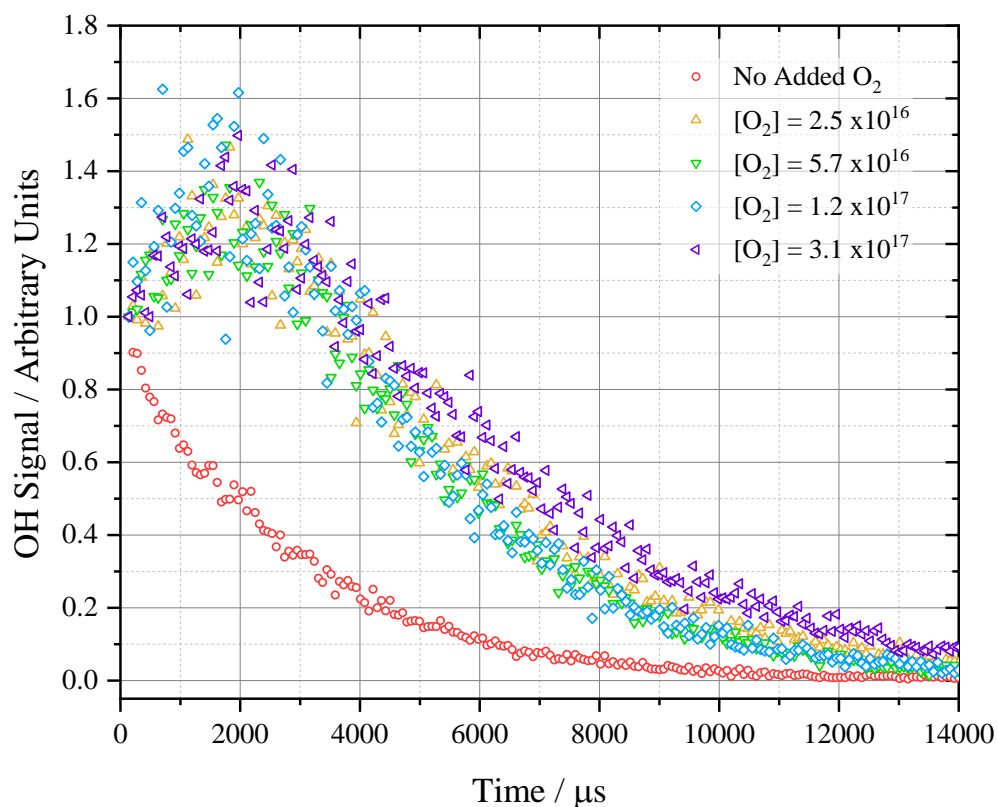
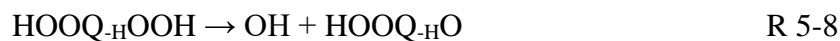
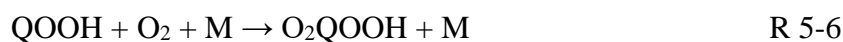


Figure 5-7: An example set of experimental traces obtained with and without the addition of oxygen at 620 K, where addition of oxygen resulted in instantaneous growth of signal following photolysis pulse. Experiments conducted at 45 Torr, [*t*-butanol] = $5.3 - 6.0 \times 10^{14}$ molecule cm^{-3} , added $[\text{O}_2] = 0 - 3.1 \times 10^{17}$ molecule cm^{-3} .

One possible explanation for the observation of this growth in signal is observation of the chain branching phenomenon, described in reactions R 5-5 – R 5-9 for a generic fuel radical R.



5.4.2 Signal Growth Modelling

In order to deduce the source of the rapid OH signal growth occurring almost instantaneously following the photolysis pulse when oxygen was present, kinetic modelling was carried out using the numerical integrator package Kintecus [151]. To construct this model, a sub-model using the reactions and rate parameters from the Sarathy *et al.* butanol combustion mechanism were used [55]. The reactions and the parameterisation for each reaction is outlined in Table 5-1 below.

For the conditions where unusual growth behaviour was observed, an experimental trace was recorded in the absence of any added oxygen. From this, a value for the unimolecular recycling parameter (see Chapter 4) for the β -abstraction radical was measured for the exact experimental conditions (i.e. temperature and pressure) under which the OH growth in signal was observed, and this pseudo first order rate constant was then entered into the Kintecus model as a fixed parameter.

An experimental trace was also recorded in the absence of any alcohol reagent, to allow for an estimate of the loss of OH radical (reaction 1 in Table 5-1), which was also entered in as a constant value for the model simulation. Using the model outlined in Table 5-1, it was not possible to replicate the OH profiles observed in the experimental work in a kinetic simulation. The model simulation was run for varying amounts of oxygen between $1 \times 10^{14} - 1 \times 10^{18}$ molecule cm^{-3} , to examine the effect of varying oxygen on the OH profile. The results from this series of simulations can be seen in Figure 5-8, which show concentration profiles for the OH radical and acetone, which was chosen as a visual marker for increased amount of OH recycling through this reaction channel.

Table 5-1: Reduced model used for kinetic simulations of OH species profiles, constructed from experimental measurements in this work and the butanol combustion model of Sarathy *et al.* [55].

Reaction and number		A	n	Ea	Ref.
1	OH \rightarrow loss				*
2a	$t\text{-C}_4\text{H}_9\text{OH} + \text{OH} \rightarrow t\text{-C}_4\text{H}_9\text{O} + \text{H}_2\text{O}$	9.76E-22	2.82	-585	[55]
2b	$t\text{-C}_4\text{H}_9\text{OH} + \text{OH} \rightarrow t\text{-C}_4\text{H}_8\text{OH} + \text{H}_2\text{O}$	1.15E-23	3.7	-2416	[55]
3	$t\text{-C}_4\text{H}_8\text{OH} \rightarrow i\text{-C}_4\text{H}_8 + \text{OH}$				*
3R	$i\text{-C}_4\text{H}_8 + \text{OH} \rightarrow t\text{-C}_4\text{H}_8\text{OH}$	1.65E-12	0	-960	[55]
4	$t\text{-C}_4\text{H}_8\text{OH} + \text{O}_2 \rightarrow \text{C}_4\text{H}_8\text{OH-O}_2$	7.47E-12	0	0	[55]
4R	$\text{C}_4\text{H}_8\text{OH-O}_2 \rightarrow t\text{-C}_4\text{H}_8\text{OH} + \text{O}_2$	2.85E+20	-1.64	34430	[55]
5	$\text{C}_4\text{H}_8\text{OH-O}_2 \rightarrow$ OH+HCHO+CH ₃ COCH ₃	2.3E+10	0	21886	[55]
6	$\text{C}_4\text{H}_8\text{OH-O}_2 \rightarrow \text{C}_4\text{H}_7\text{OH-OOH}$	7.5E+10	0	27000	[55]
7	$\text{C}_4\text{H}_8\text{OH-O}_2 \rightarrow \text{C}_3\text{KET12} + \text{CH}_3$	2E+09	0	21886	[55]
8	$\text{C}_4\text{H}_7\text{OH-OOH} \rightarrow$ HCHO+OH+C ₃ H ₅ OH	1E+13	0	30000	[55]
9	$\text{C}_4\text{H}_7\text{OH-OOH} \rightarrow \text{OH} + \text{C}_4\text{H}_7\text{OH-O}$	7.5E+10	0	15300	[55]
10	$\text{C}_4\text{H}_7\text{OH-OOH} + \text{O}_2 \rightarrow \text{C}_4\text{H}_7\text{OH-OOH-}$ O ₂	7.5E-12	0		[55]
10R	$\text{C}_4\text{H}_7\text{OH-OOH-O}_2 \rightarrow \text{C}_4\text{H}_7\text{OH-OOH} +$ O ₂	2.9E+20	-1.64	34430	[55]
11	$\text{C}_4\text{H}_7\text{OH-OOH-O}_2 \rightarrow$ OH+HCHO+C ₃ H ₆ O ₃	2.5E+10	0	21886	[55]
12	$\text{C}_4\text{H}_7\text{OH-OOH-O}_2 \rightarrow$ OH+C ₃ H ₅ OHOHCHO	2.5E+10	0	24000	[55]
13	$\text{C}_3\text{H}_5\text{OHOHCHO} \rightarrow \text{PROD} + \text{OH}$	1E+16	0	39000	[55]

R: Reverse of reaction with same number. [55] Sarathy model. *: Value measured experimentally in this work for each set of experimental conditions. Units A: cm³ molecule⁻¹ s⁻¹, Ea: cal mol⁻¹.

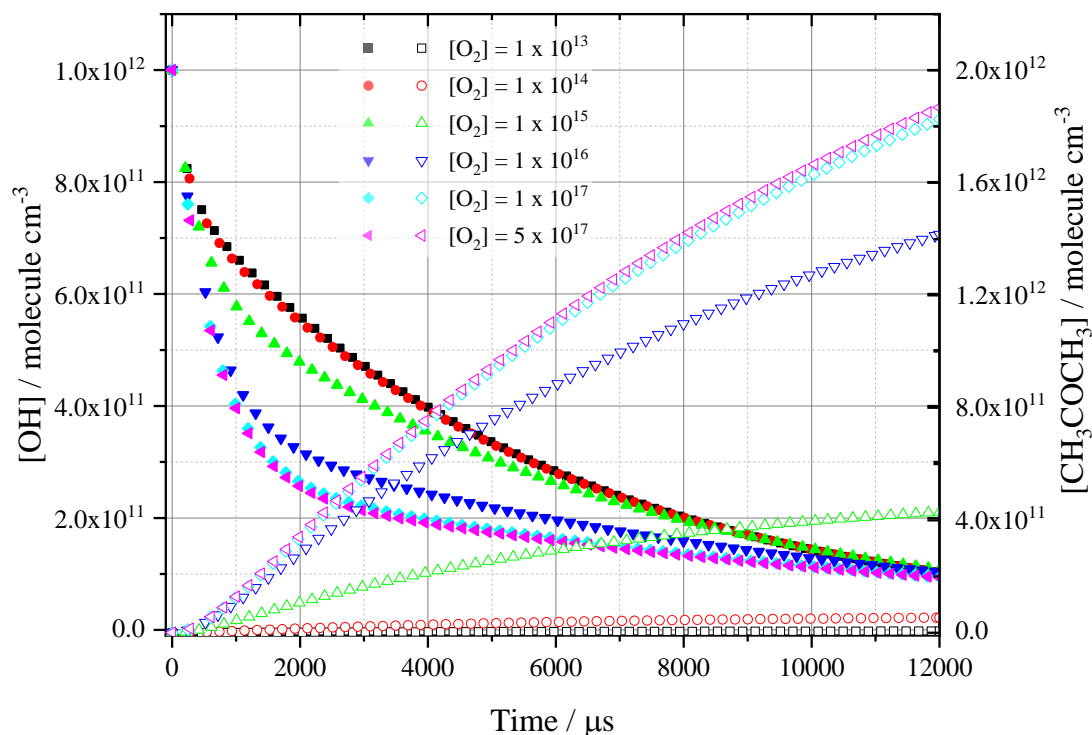


Figure 5-8: Simulations obtained from running *t*-butanol submechanism in kinetic modelling, as a function of oxygen. All simulations run at 620 K, with starting concentration of *t*-butanol = 5.5×10^{14} molecule cm^{-3} . Filled symbols represent OH simulation data and open symbols represent CH_3COCH_3 simulation data (chosen as a marker of $\text{RO}_2 \rightarrow \text{Products}$).

Simulations using the model described in Table 5-1 were also conducted across a range of temperatures, spanning the same conditions as were used in this work where OH signal growth was observed. Through these simulations and those conducted as a function of oxygen, it was established that using the submechanism generated from the Sarathy *et al.* model, it is not possible to recreate the experimental traces observed in this work. It was also established that it is not possible to intercept a QOOH species formed following isomerisation of the RO_2 species, as the isomerisation and decomposition of the RO_2 species is entered as an irreversible product formation step, making it impossible for the QOOH to reverse to RO_2 or form an interceptable QOOH. Without this interception to form the O_2QOOH species, it is not possible to get branching of OH radicals, i.e. formation of two OH radicals, a possible explanation of the signal growth observed in this experimental work.

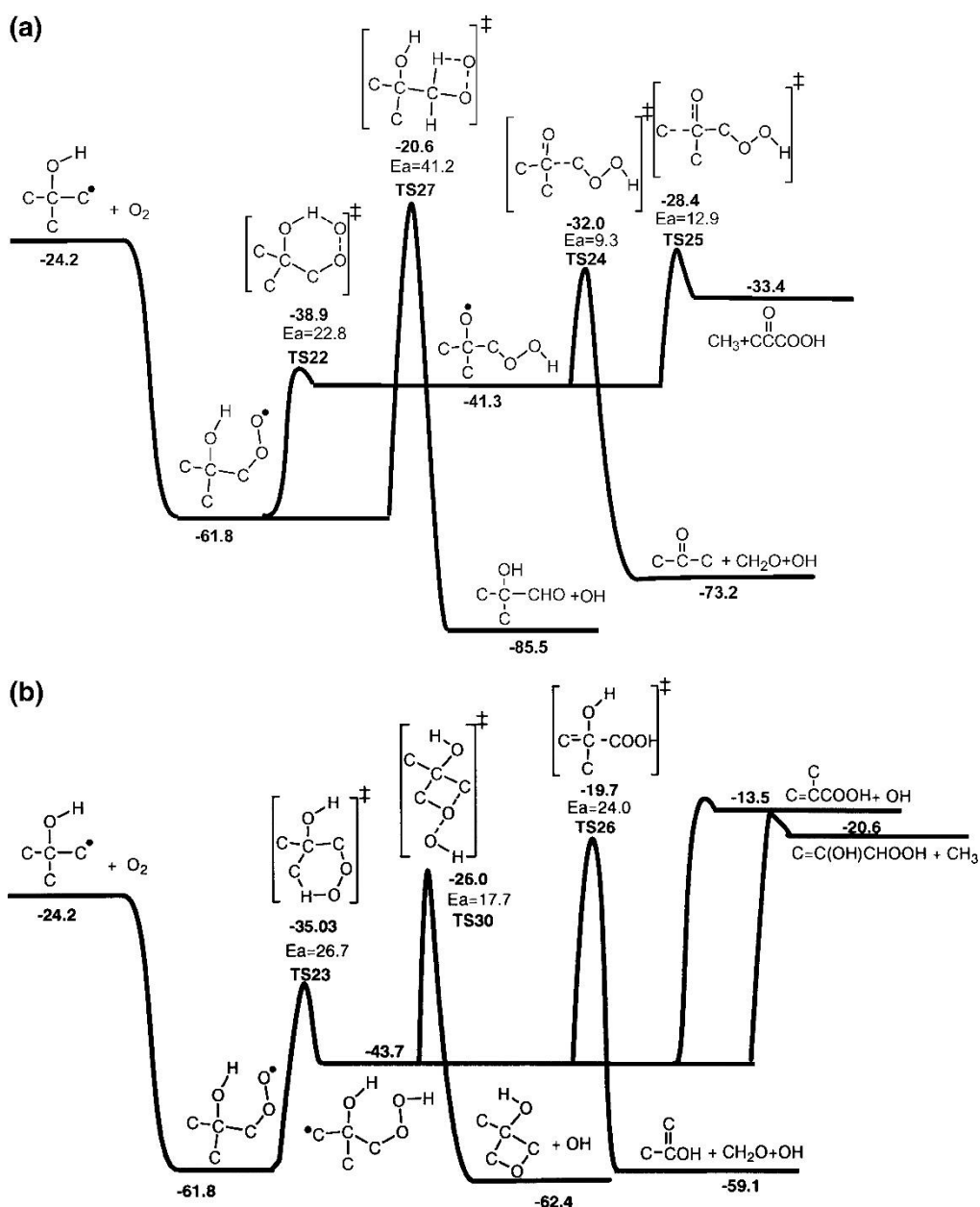


Figure 5-9: Potential energy surface for rearrangement and decompositions of the $C_4H_8OH-O_2$ (RO_2) species formed following β -site abstraction of *t*-butanol calculated by Sun *et al.*, replicated from reference [152]. Energies calculated at the CBS-Q/B3LYP level, reported in kcal mol^{-1} .

The modified Arrhenius parameterisation for the decomposition of the $C_4H_8OH-O_2$ (RO_2) species in the Sarathy *et al.* model [55] was based on the work of Sun, Bozzelli and Law [152], who conducted a theoretical investigation into the reactions and products of oxygen addition to 2-hydroxy-2-methylpropyl radicals (*t*- C_4H_8OH). In their work, it was concluded that the most important product channels are the β -scissions of the QOOH

species that is formed from the isomerisation reaction in which the hydroxyl H migrates to the oxygen centred radical. The QOOH radical is able to undergo decomposition to form acetone, formaldehyde and an OH radical (reaction 5 in Table 5-1) via a Waddington type mechanism (a six-membered ring isomerisation in which the RO₂ species abstracts the H atom from the hydroxyl group), or decomposition to a methyl radical and a ketone species (reaction 7 in Table 5-1). The potential energy surface for these reactions as calculated by Sun *et al.* is shown in Figure 5-9, calculated at CBS-Q/B3LYP level, with energies reported in kcal mol⁻¹. Panel (a) of Figure 5-9 shows the isomerisation of the RO₂ species to QOOH, where the H atom migration occurs from the hydroxyl group, and the energetic barriers to the QOOH formation and decomposition to products. Panel (b) shows the isomerisation migration of H from a methyl group attached to the central carbon, and the energy barriers to this process and the subsequent decomposition reactions.

Using the energy barriers calculated in the study, rate constants were calculated as a function of temperature and pressure for these reactions by Sun *et al.* [152]. In the Sarathy *et al.* combustion model [55], the reactions for the β -RO₂ radical have been written as a single step irreversible process in which the Waddington mechanism products are formed directly without the formation of the intermediate QOOH species. The rate constant assigned to this reaction (shown in Table 5-1, reaction 5) is stated to be in agreement with the high pressure rate constant calculated by Sun *et al.* for the *t*-butanol system, and does not provide any pressure parameterisation for the reaction. This simplification of these two reaction steps will be investigated in the next section, which examines combustion model simulations using the base mechanism of Sarathy *et al.*, and simulations using updated versions of the simplified isomerisation and decomposition steps.

5.4.3 Sarathy Model Modification

In this section, the original combustion model generated by Sarathy *et al.* [55] was altered in a series of updates, and the ignition delay time simulations run for each updated model version, and compared with the experimental ignition delay time data from Weber and Sung [47]. The combustion model was run using an ideal, zero-dimensional constant volume reactor using the widely available Cantera package [153]. Experimental ignition delay times were measured by Weber and Sung at pressures of 15 and 30 bar, at equivalence ratios (E.R, ϕ) of 0.5, 1 and 2. In this section, comparisons are presented for

the experimental data obtained at 15 bar and E.R = 1. Comparisons for the other experimental conditions examined can be seen in Appendix D.

The first update applied to the Sarathy model involved updating the total reactivity of OH + *t*-butanol to match the measured total bimolecular rate coefficient measured experimentally in this work (see Chapter 3). This was carried out by calculating the total bimolecular rate coefficient measured in this work using the modified Arrhenius parameterisation, subtracting the rate coefficient for reaction at the OH site calculated by Sarathy *et al.*, and fitting a modified Arrhenius parameterisation through the resulting rate coefficient data.

Updating this total bimolecular reactivity for the reaction of *t*-butanol with OH resulted in simulated ignition delay times that were reduced by 37 % at 700 K, where the most significant reduction in IDT was observed. This results in a worse agreement with the experimental data measured, from simply updating the measured total OH + *t*-butanol reactivity to that which was measured in this work.

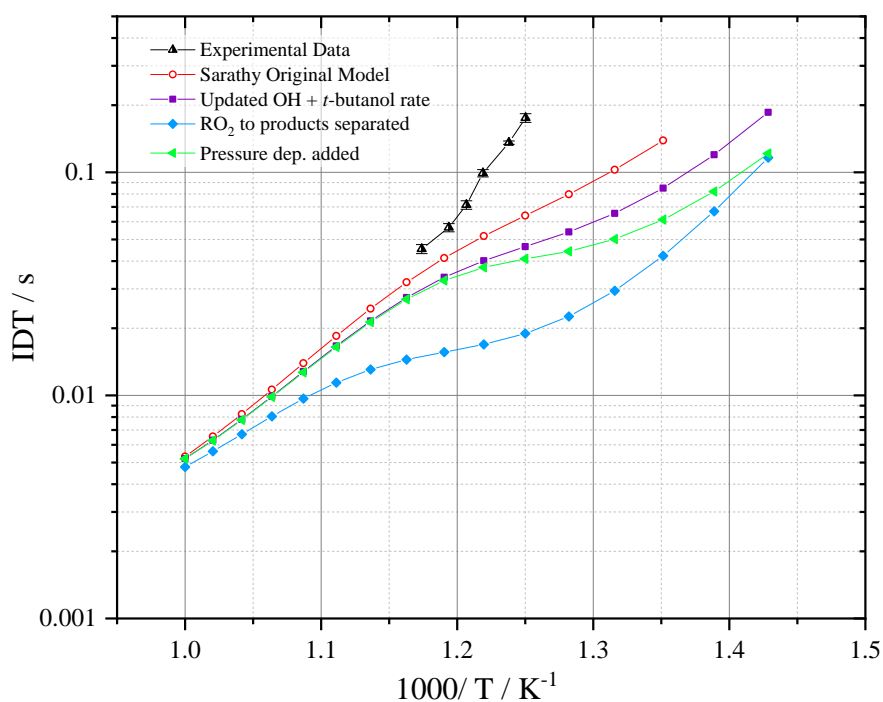


Figure 5-10: Ignition delay time data from Weber and Sung [47] obtained at 15 bar and $\Phi = 1$. Simulations using the Sarathy *et al.* [55] base combustion mechanism shown as red hollow circles, with subsequent updates: Purple squares: Updating total bimolecular OH + *t*-butanol reactivity. Blue diamonds: Separating of $\text{RO}_2 \rightarrow \text{QOOH} \rightarrow \text{Product}$ reactions based on recommended rates of Sun, *et al.* Green triangles: Addition of pressure dependence to RO_2 separated reactions based on recommendations of Sun *et al.*

Following the update to the total bimolecular rate coefficient for the reaction of *t*-butanol with OH, the reaction of the $\beta\text{-RO}_2$ species decomposing straight to OH, formaldehyde and acetone was separated out into the following two reactions, described by reactions R 5-11 – R 5-12, with the recommended rate constants as reported by Sun *et al.* in their work.



Through separating the decomposition into two reaction steps, the ignition delay time is again reduced across all the temperatures simulated, exacerbating the disagreement with the experimentally measured ignition delay times. This however represents another simplification, as it does not account for the pressure dependence of

the reaction that has been reported in the supplementary information of the work by Sun *et al.*, and assumes that both reactions are occurring at their high pressure limit. Adding in the pressure dependence results in simulated ignition delay times represented by the solid green triangles in Figure 5-10. This results in a better agreement with the experimental IDT data, and also introduces a slight negative temperature coefficient (NTC) region. While this isn't necessarily apparent in the experimental data of Weber and Sung [47], the experimental data does not show a simple linear behaviour. Further improvements to the base mechanism of Sarathy *et al.*, including the pressure dependence described by Sun *et al.* for these reactions, may help to explain this curvature in the data.

Comparisons of ignition delay times obtained from Weber and Sung under the other experimental conditions studied (30 bar total pressure, equivalence ratios of 0.5, 1 and 2) are found in Appendix D for interest. Similar trends to those highlighted in Figure 5-10 were observed for the other conditions investigated.

5.4.4 Summary of Modelling Work

From this investigation into the combustion model constructed for *t*-butanol, it can be concluded that the simplification of the $\beta\text{-RO}_2 \rightarrow \text{QOOH} \rightarrow \text{products}$ reaction steps into $\beta\text{-RO}_2 \rightarrow \text{products}$ is likely an oversimplification which requires further exploration. From the ignition delay time simulations conducted, the separating out of these steps and the inclusion of the pressure dependence has a significant effect on the reactivity at low temperatures and pressures, and the original Sarathy *et al.* mechanism may not accurately capture the reactivity of *t*-butanol at temperatures below 1000 K. Whilst the rate constants calculated by Sun *et al.* [152] might not accurately capture the reactivity of the $\beta\text{-RO}_2$ species, this work shows that simplifying their calculated rates into one concerted reaction has a significant effect on the IDT calculated using the Sarathy *et al.* model.

As stated previously, at these temperatures, the reactivity of the system is dependent upon the chemical kinetics of the system, and while simplifying these reaction steps does result in IDT simulations that are closer to the experimental measurements of Weber and Sung, it may not accurately represent the relevant rates of reactions. Further investigation, such as a sensitivity analysis similar to that conducted for *n*-butanol by Agbro *et al.* [60], is required to investigate which reactions in this temperature and pressure regime have the largest effect on modelled parameters such as the IDT.

5.5 *n*-butanol OH Growth Observation and O (³P) Experiments

5.5.1 Observation of OH Signal Growth

As mentioned previously for *t*-butanol in Section 5.4.1 and in Chapter 4, above 480 K, biexponential OH fluorescence traces were obtained following the reaction of the butanol isomer with the OH radical. This was attributed to unimolecular decomposition of the β -radical formed following abstraction at this site, resulting in the reformation of an OH radical and the relevant butene isomer.

For *n*-butanol, at temperatures of 650 K and above, unusual OH growth behaviour was observed in OH fluorescence traces following addition of significant amounts of oxygen, in the same manner as for *t*-butanol described previously. An example series of kinetic traces obtained as a function of oxygen at 650 K and 130 Torr of pressure nitrogen is shown in Figure 5-11, which shows the transition from increasing biexponential behaviour to instant OH signal growth as a function of oxygen.

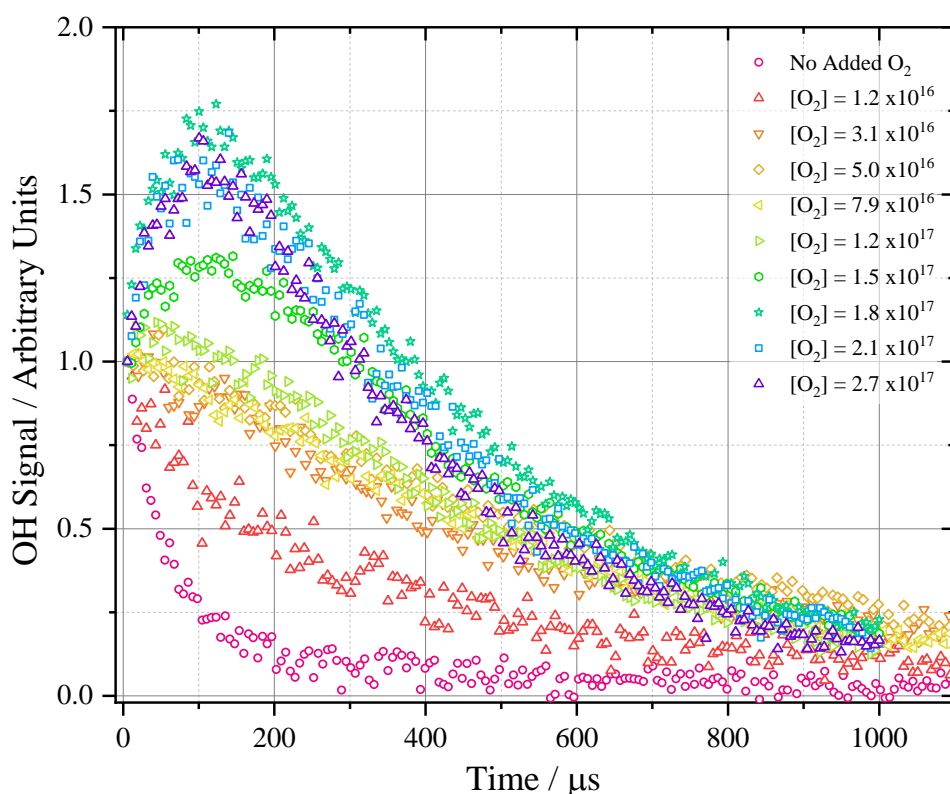


Figure 5-11: An example set of experimental series of traces obtained at high temperatures following addition of oxygen. Traces obtained at 720 K, 130 Torr N_2 , $[n\text{-butanol}] = 1.6 \times 10^{15}$ molecule cm^{-3} , as a function of O_2 . Range of added $[\text{O}_2] = 0 - 2.7 \times 10^{17}$ molecule cm^{-3} .

The observation of OH growth signal was assumed to be some visual representation of the chain branching process, as described for *t*-butanol, as it was an increase in the observation of OH fluorescence dependent on increasing oxygen concentration. Upon further discussion and consideration of the earlier modelling conducted for *t*-butanol, several issues became apparent with this hypothesis. In order to generate a growth in OH signal on the timescale observed here (instantly following the photolysis pulse), simple Kintecus modelling suggests that some reactions, such as isomerisations and the rate of second oxygen addition, would need to be orders of magnitude faster than the current estimates in the combustion models in the literature. Even with this drastic increase in some rate constants, the instant growth in signal could not be recreated at time zero (the simulation of the photolysis pulse), as the R radical required for these chain branching reactions must still be generated prior to any other reactions.

Conversely, if chain branching could explain the rapid growth in OH production, the theory is again questioned by the short timescale of reaction and the subsequent decrease in signal. If chain branching were truly occurring, the branching behaviour would continue until all the fuel has been consumed. Consequently, a series of further experimental tests were designed to test different aspects of the experimental procedure, to examine which experimental factor has the greatest effect on the signal growth observed.

5.5.2 OH Signal Growth Tests

The first experimental test conducted examined the effect of the repetition rate of the photolysis laser on the shape of the OH fluorescence trace. Experiments were conducted at 2, 5 and 10 Hz, the results of which are shown in Figure 5-12.

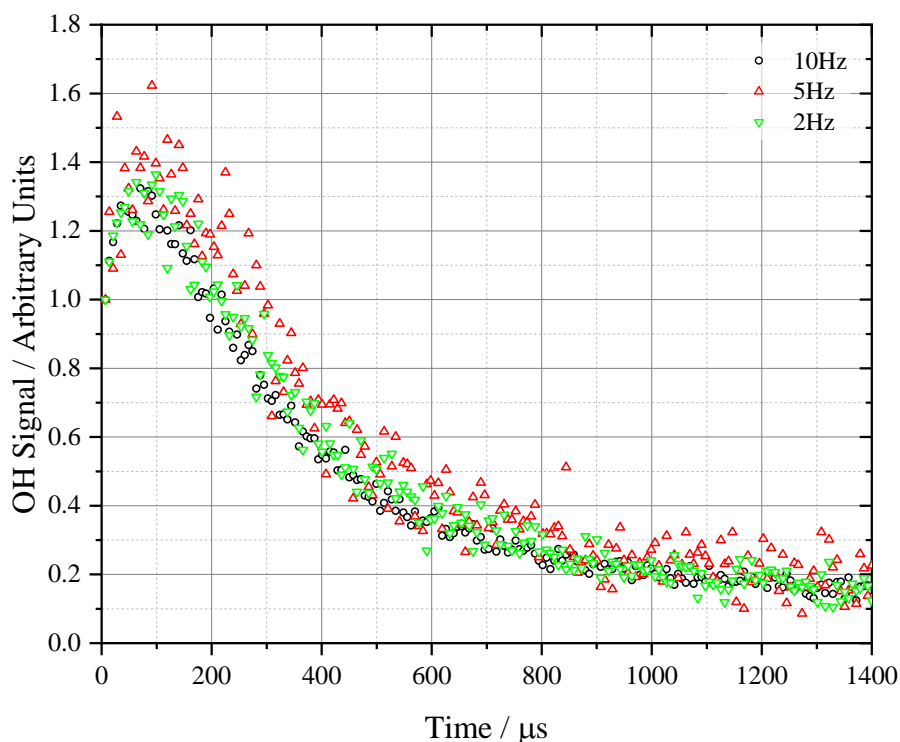


Figure 5-12: OH Fluorescence traces obtained when varying photolysis laser repetition rate. Traces obtained at 760 K, 130 Torr total pressure N_2 , $[n\text{-butanol}] = 2.5 \times 10^{15}$ molecule cm^{-3} and added $[\text{O}_2] = 2.5 \times 10^{16}$ molecule cm^{-3} .

The experimental traces shown in Figure 5-12 confirm that the growth in OH fluorescence observed is not a consequence of secondary chemistry, such as photolysis of products formed from the initial abstraction reaction, as there is no definitive trend observed between the varying repetition rates.

The second experimental test was designed to examine the effect of the hydrogen peroxide precursor on the chemistry occurring in the reactor. Therefore, this test recreated some of the experimental conditions at which OH signal growth is observed, but in the absence of the hydrogen peroxide precursor. The results of this test are shown in Figure 5-13.

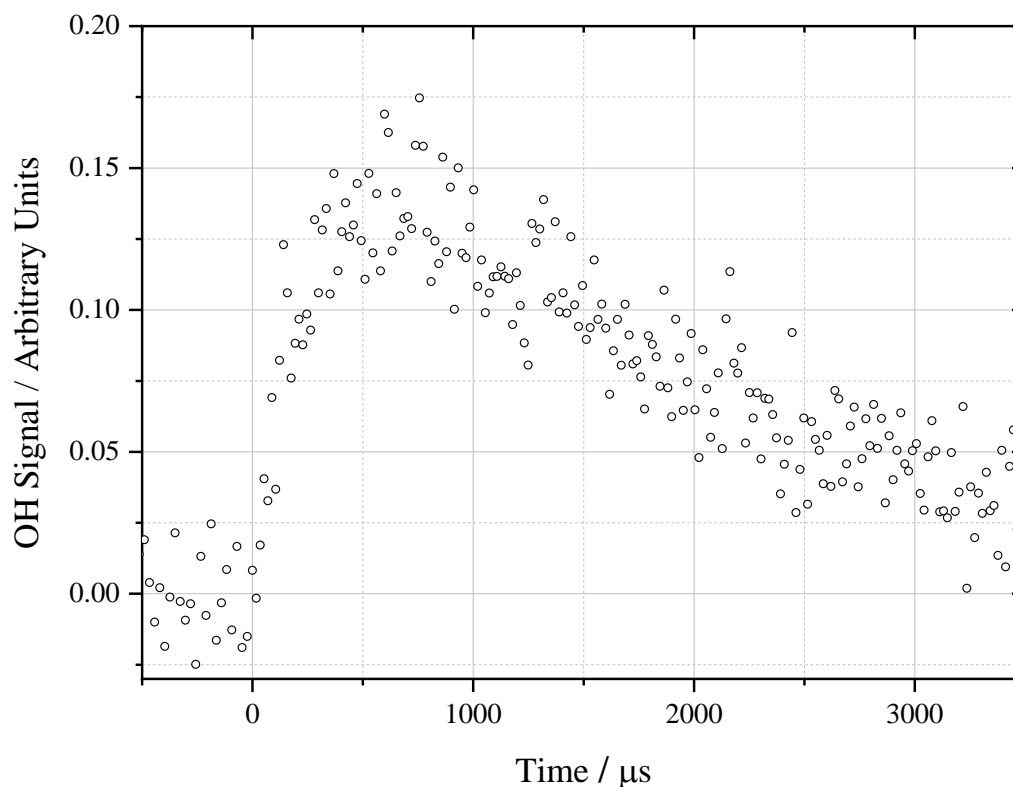


Figure 5-13: Example trace obtained at temperatures above 650 K in the absence of hydrogen peroxide precursor. $[n\text{-butanol}] = 1.86 \times 10^{14}$ molecule cm^{-3} , $[\text{O}_2] = 4.1 \times 10^{16}$ molecule cm^{-3} . Experimental trace was obtained at 682 K, in 35 Torr N_2 .

From the observation of OH fluorescence signal shown in Figure 5-13, it is apparent that OH radicals are still generated in the absence of hydrogen peroxide precursor when oxygen and fuel reagent are present. This confirms that without an OH radical precursor source, a reaction leading to the production of OH radicals is occurring. To examine the effect of the photolysis laser on this OH signal growth, experiments were conducted in the presence and absence of the photolysis laser, to examine if the effect is a result of a photolysis process.

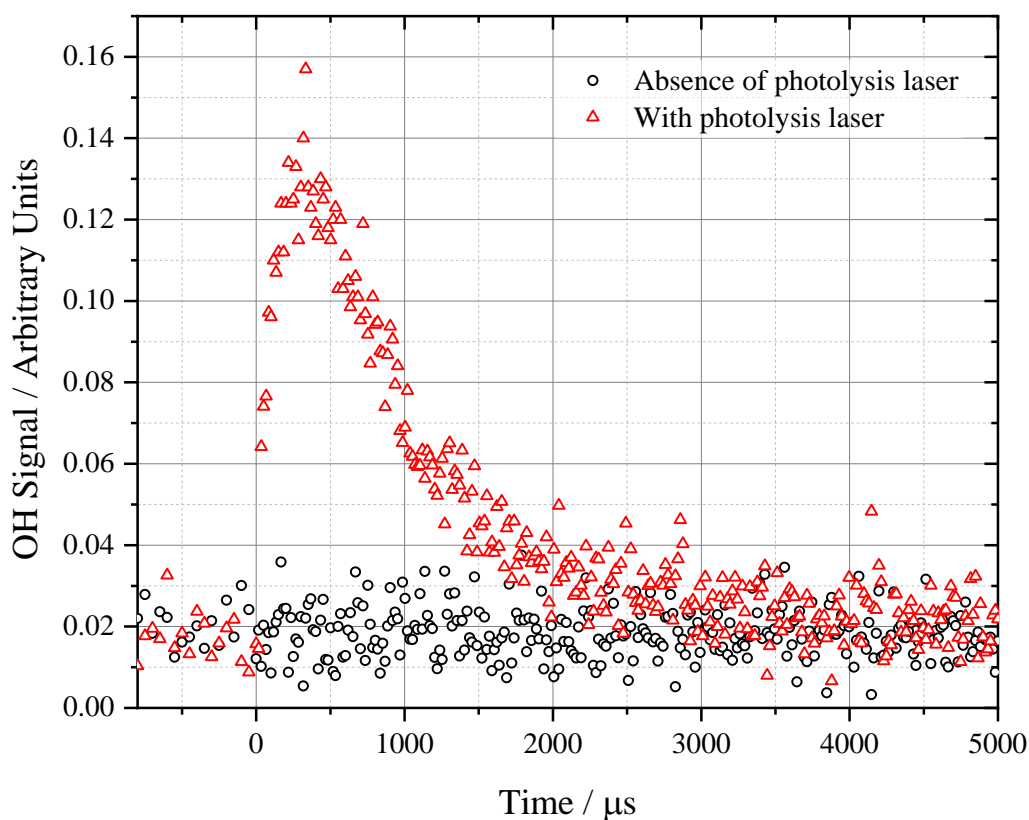


Figure 5-14: Trace obtained in the absence of hydrogen peroxide precursor, with (hollow red triangles) and without (hollow black circles) the photolysis laser. $[n\text{-butanol}] = 7 \times 10^{14}$ molecule cm^{-3} , added $[\text{O}_2] = 8.3 \times 10^{16}$ molecule cm^{-3} . Experimental trace was obtained at 600 K, in 95 Torr N_2 .

The experimental tests represented in Figure 5-14 show that a photolysis laser is also required for an observation of OH fluorescence growth in the absence of hydrogen peroxide precursor, and consequently the photolysis pulse is generating a species capable of producing OH radicals, or producing another radical species able to react and generate OH. A further test designed to examine the source of the OH radicals studies the influence of oxygen present in the system. The results of this test are shown in Figure 5-15.

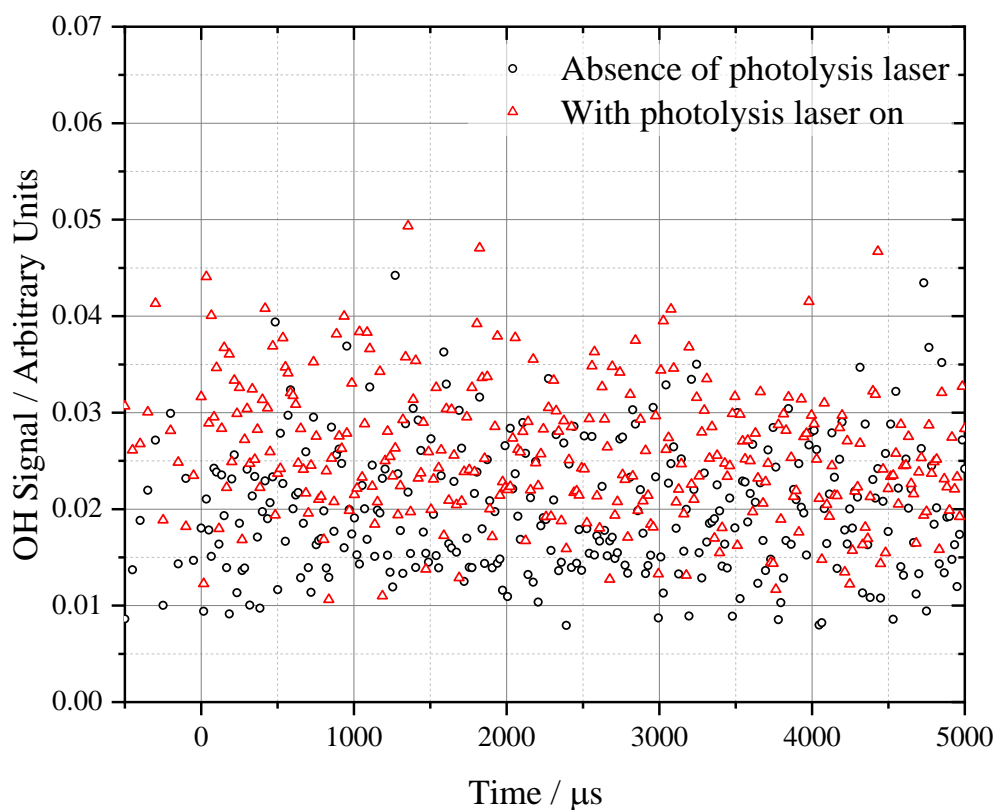


Figure 5-15: Trace obtained in the absence of hydrogen peroxide precursor and oxygen, with (hollow red triangles) and without (hollow black circles) the photolysis laser. $[n\text{-butanol}] = 7 \times 10^{14}$ molecule cm^{-3} . Experimental trace was obtained at 600 K, in 95 Torr N_2 .

Figure 5-15 is a repeat of the conditions from Figure 5-14, however the added oxygen has been removed and replaced with nitrogen to ensure the same total pressure. Figure 5-15 highlights that oxygen is also required in the system for observation of growth in OH fluorescence signal following the photolysis pulse. This confirms that the OH is not produced from direct photolysis of the *n*-butanol reagent. A final test to confirm the presence of oxygen is required for the observation of OH growth was to test the fluorescence signal with the photolysis laser back on, but in the presence and absence of oxygen. The results of this final test are shown in Figure 5-16.

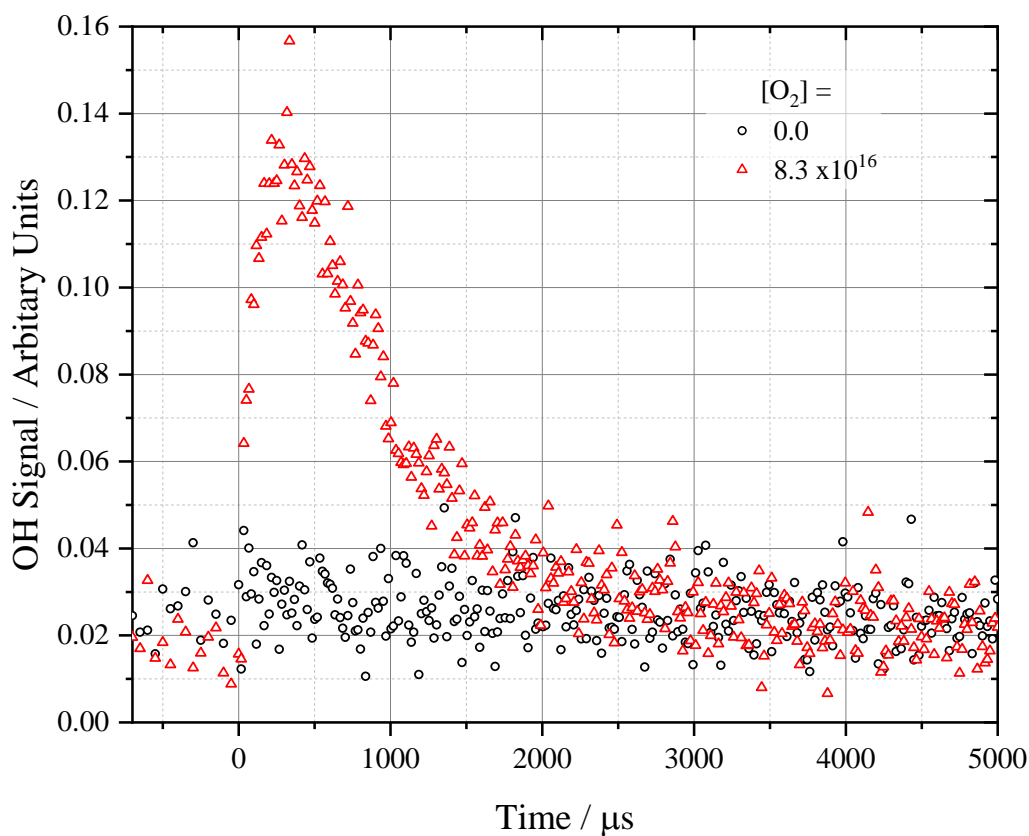


Figure 5-16: Trace obtained in the absence of hydrogen peroxide precursor, with (hollow red triangles) and without (hollow black circles) the addition of 8.3×10^{16} molecule cm^{-3} of oxygen. [*n*-butanol] = 7×10^{14} molecule cm^{-3} . Experimental trace was obtained at 600 K, in 95 Torr N_2 .

Figure 5-15 and Figure 5-16 in conjunction highlight the need for both oxygen and a photolysis laser pulse for observation of OH radical production in the absence of hydrogen peroxide. A summary table of these tests, and if the appearance of OH signal growth was observed is provided in Table 5-2.

Table 5-2: Summary table of the tests conducted to attempt to deduce the source of OH fluorescence growth signal. Key: green filled box indicates present, red filled box indicates absent.

H₂O₂ Precursor	Oxygen	Photolysis Laser	<i>n</i>-butanol	OH Signal observed
				✓
				✓
				X
				X
				X

Several conclusions can be drawn from the tests conducted and outlined in Table 5-2. Firstly, the presence of alcohol reagent, oxygen and the photolysis laser are all required for the appearance of OH signal growth. The requirement of oxygen rules out the possibility of fuel photolysis to directly generate OH, as if this was the case, OH signal would be observed in the absence of oxygen. Following this conclusion, further experimental investigations were conducted to examine the effects of varying the amount of oxygen present in the system on the OH growth signal.

5.5.3 Effects of Varying Oxygen on OH Signal Growth

From the tests conducted in Section 5.5.2, it can be concluded with reasonable certainty that the presence of both oxygen and alcohol reagent in combination with the photolysis laser is required for the observation of the OH growth signal.

At these high temperatures (> 600 K), it is possible that a small fraction of the alcohol reagent is decomposing on the surface of the reactor to produce R radicals of some nature, which is then reacting with the oxygen present in the system to produce RO₂ radicals, as described by reaction R 5-3 in Section 5.2. A series of experimental traces obtained at 600 K for *n*-butanol in the presence of varying amounts of oxygen are shown in Figure 5-17.

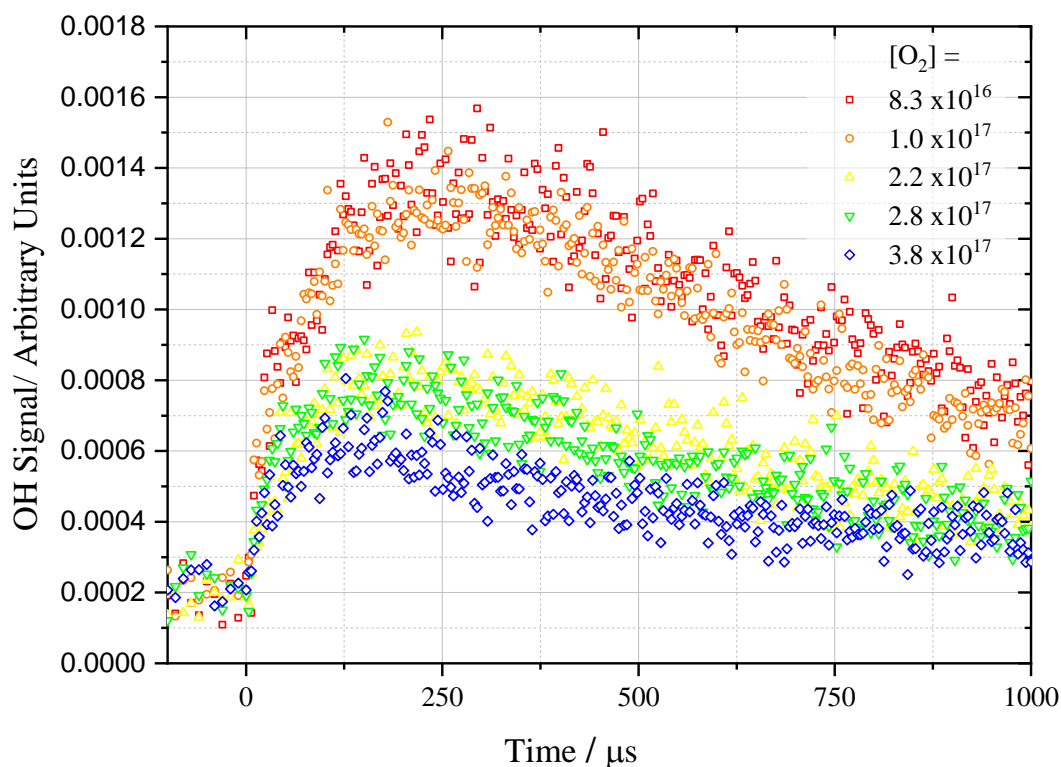


Figure 5-17: Unnormalised OH fluorescence traces for series of *n*-butanol (approximately 7×10^{14} molecule cm^{-3}) in the absence of hydrogen peroxide, as a function of oxygen (varied from $0.8 - 3.8 \times 10^{17}$ molecule cm^{-3}), obtained at 610 K and 94 Torr N_2 .

Figure 5-17 shows the unnormalised (i.e. background OH signal has not been removed) fluorescence signals for a series of *n*-butanol traces obtained as a function of oxygen. On closer examination of the OH fluorescence, it appears that the baseline signal prior to the photolysis laser was increasing as a function of the oxygen in the system. A similar series of experiments was then conducted at a higher temperature, with more data points taken for the pre-photolysis laser pulse and with the oxygen varied in a non-linear fashion to confirm if this was a real observation and not the result of a build-up of radicals in the system. The results of this are shown in Figure 5-18.

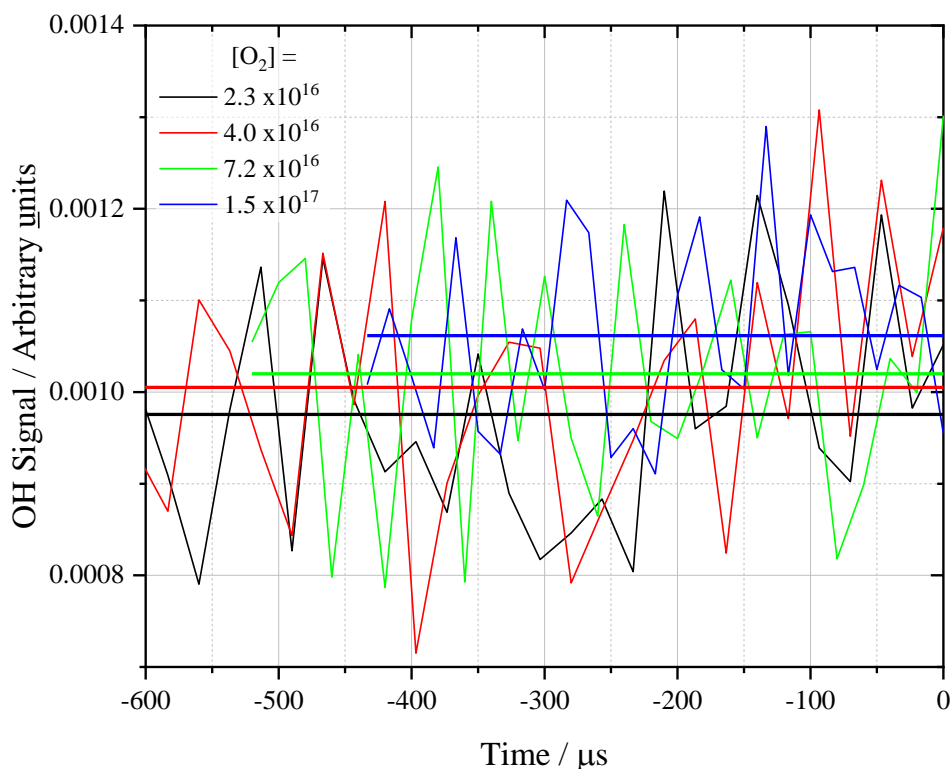


Figure 5-18: Unnormalised OH fluorescence traces for series of *n*-butanol (approximately 7×10^{14} molecule cm^{-3}) experiments in the absence of hydrogen peroxide. Traces obtained as a function of oxygen (varied from $0.8 - 3.8 \times 10^{17}$ molecule cm^{-3}), showing increase in baseline pre-photolysis laser pulse. Traces obtained at 683 K and 94 Torr N_2 . Solid lines are line of best fit with fixed gradient of 0.

Figure 5-18 shows that an increase in the OH fluorescence signal baseline does occur as a function of oxygen. Increasing the amount of oxygen in the system results in quenching of the OH fluorescence, due to oxygen being an effective OH collisional stabiliser. It is therefore likely that the increase in background OH radicals may be more significant than the fluorescence profiles appear, exacerbating this effect. The observation of OH radicals before the photolysis laser pulse potentially suggests the formation of some hydroperoxide species (as described by reactions R 5-4 and R 5-5) and decomposition of this species to produce OH radicals in the absence of a photolysis laser pulse, resulting from some fuel decomposition at these high temperatures.

Further to the suggestion of the presence of hydroperoxides in the system, the addition of significant amounts of oxygen in the system could result in interception of some amount of this QOOH species and result in the formation of an O_2QOOH species (reaction R 5-6). If this species or an RO_2 species present possesses a significant

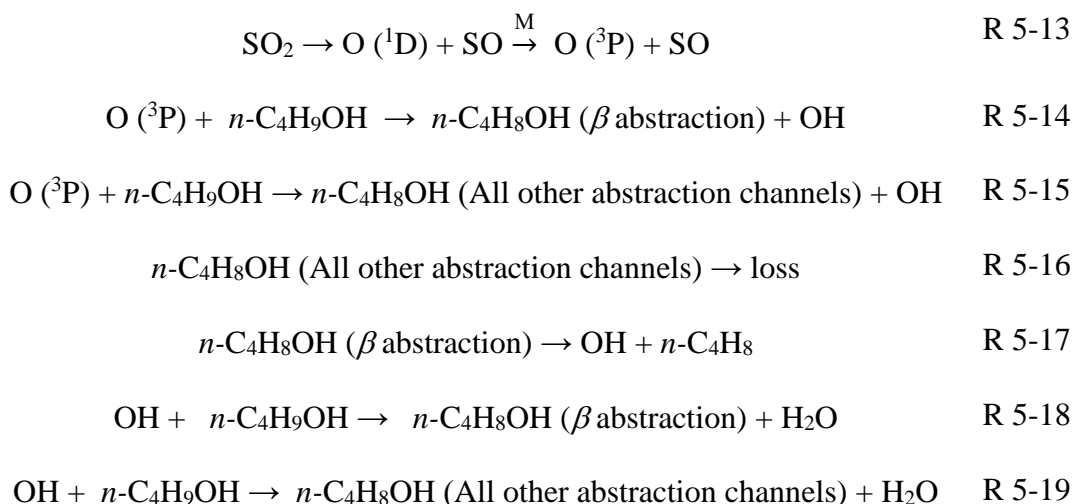
absorption cross-section at 248 nm, photolysis of this radical species could result in formation of a reactive O atom. This in turn could then react with the fuel reagent through abstraction of an H, forming an OH radical which is then detected by fluorescence. The product remaining from this photolysis could then decompose to give a second OH radical and another products species, resulting in the rapid growth of OH signal observed at the shortest timescales following the photolysis pulse.

If some of the unusual OH growth behaviour observed in these kinetic traces is a consequence of O atom chemistry, the ability to constrain this reactivity when attempting to analyse these traces could assist in obtaining meaningful kinetic parameters. Therefore, measurement of the bimolecular rate coefficient for the reaction between O atoms and *n*-butanol would be of use to this work, and will be examined in the next section.

5.5.4 O (³P) + *n*-butanol Measurements

There has been one previous temperature dependent study of the reaction of O (³P) with *n*-butanol, conducted by Roscoe in 1983 [154]. In the work of Roscoe, the discharge flow method was used at pressures around 1 Torr, utilising the production of N atoms by microwave discharge of purified N₂, which were then titrated with NO to produce O (³P) atoms without the interference of O₂. Reaction products from the reaction of O atoms with *n*-butanol were then monitored by gas chromatography. In his work, no products other than water were detected, with suggestion that the products formed would adhere to the glass tubing between the reactors and the cold trap, and thus not be able to be analysed.

In this work, the bimolecular rate coefficient for O (³P) with *n*-butanol has been measured as a function of temperature across the range 490 – 730 K, at pressures between 40 – 55 Torr total pressure of nitrogen bath gas. In order to measure the reaction of O (³P) radicals with *n*-butanol fuel, a suitable oxygen radical precursor is required. In this work, SO₂ was used as a precursor. The reactions involved following photolysis of the SO₂ precursor to oxygen radicals are described below by reactions R 5-13 – R 5-19.



O (³P) reacts with the *n*-butanol alcohol reagent by abstracting H atoms from the potential C–H abstraction sites. As these experiments were all conducted at temperatures above 480 K, abstraction at the β-site resulted in formation of the β-hydroxybutyl radical, which decomposes to give an OH radical and 1-butene (as described in Section 4.6). The full fitting regime required for fitting the experimental traces obtained in these experiments can be found expanded in Appendix E. An example kinetic trace obtained under these conditions is seen in Figure 5-19.

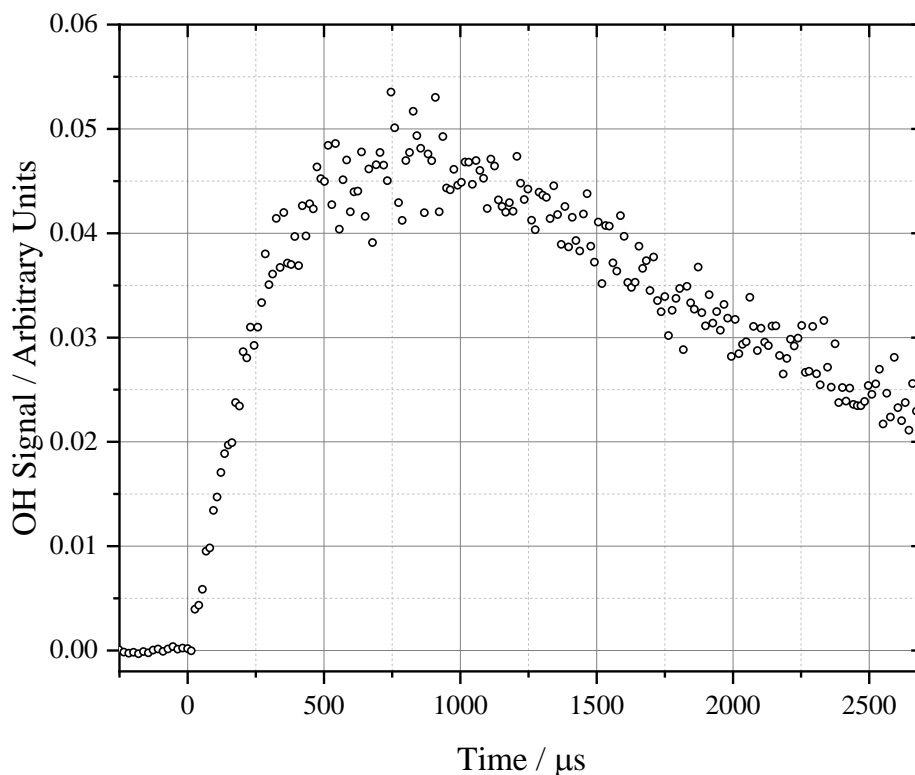


Figure 5-19: Example OH fluorescence kinetic trace obtained for reactions of O (^3P) with *n*-butanol. Experimental trace was obtained at 620 K, in 47 Torr N_2 , with $[n\text{-butanol}] = 2.7 \times 10^{14}$ molecule cm^{-3} .

By varying the concentration of the *n*-butanol reagent, a plot of the pseudo-first-order rate constants for the reaction of O (^3P) with *n*-butanol can be made, the slope of which represents the bimolecular rate coefficient $k_{\text{O}(^3\text{P})+n\text{-butanol}}$. As multiple processes are occurring on the timescale of these experiments, a global fitting regime was employed in the same manner of that used in Chapter 4 for fitting the biexponential recycling traces and for fitting complicated traces that utilised a chlorine radical precursor. An example series of traces fit using this global analysis method is shown in Figure 5-20, with the globally obtained rate parameters summarised in Table 5-3.

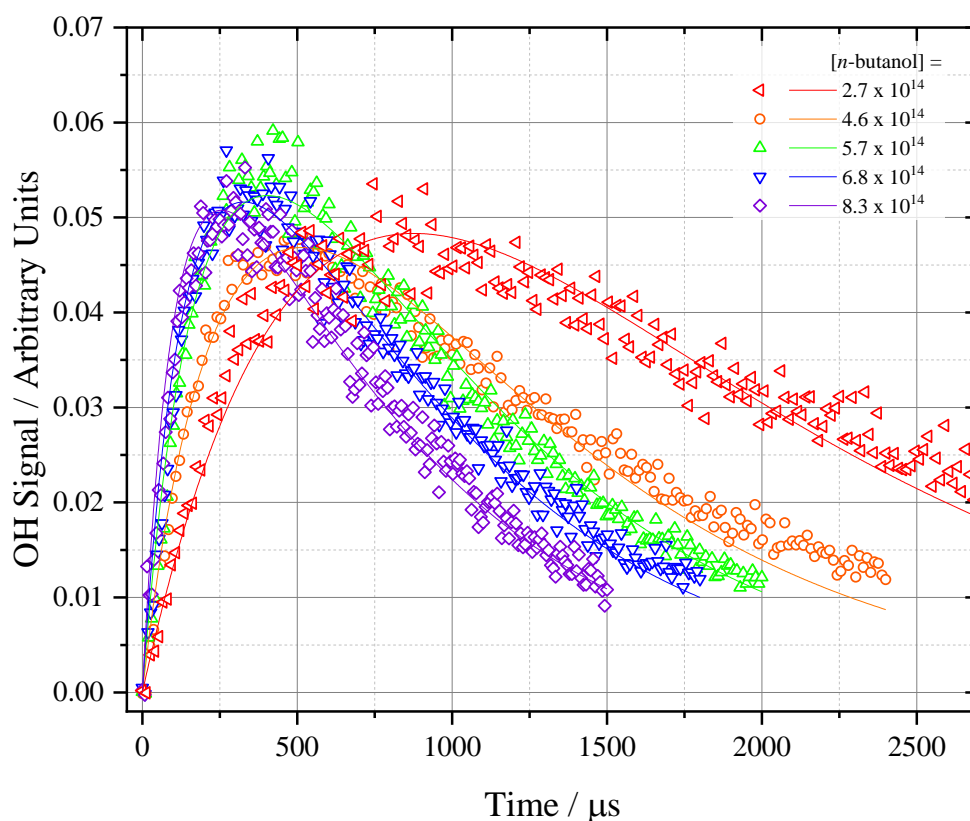


Figure 5-20: Example global fitting results from fitting to multiple OH fluorescence signal traces obtained from reactions of O with *n*-butanol. Traces were obtained at 45 – 48 Torr N₂ and 620 K. Concentration of alcohol reagent: $[n\text{-butanol}] = 2.7 - 8.4 \times 10^{14}$ molecule cm⁻³.

For global analysis of these traces, the recycling parameter k_{recycle} was fixed at an estimate of the value measured previously for a given temperature and pressure, as was the bimolecular rate coefficient $k_{\text{OH}+n\text{-butanol}}$. An estimate of the value for $k_{\text{OH loss}}$ was also made, however varying this value between 50 – 150 s⁻¹ (50 % increase or decrease) did not have a significant effect on the bimolecular rate coefficients obtained (less than 2 %). The parameters obtained when applying a global fitting regime to the traces shown in Figure 5-20 are summarised in Table 5-3, with comments to explain the values employed.

Table 5-3: Parameters obtained from global fitting to series of O (³P) + *n*-butanol traces obtained at 45 – 48 Torr pressure, 620 K, where [*n*-butanol] was varied across the range [*n*-butanol] = 2.7 – 8.4 × 10¹⁴ molecule cm⁻³.

Parameter	Value	Comment
$k_{\text{OH}+n\text{-butanol}} / \text{cm}^3 \text{ molecule}^{-1} \text{ s}^{-1}$	1.1×10^{-11}	Fixed to experimentally measured value from Chapter 3.
$k_{\text{recycle}} / \text{s}^{-1}$	2000	Fixed to estimate of recycling parameter from values obtained in Chapter 4.
$k_{\text{OH loss}} / \text{s}^{-1}$	100	Fixed estimate based on previous experiments, however varying by ± 50 % had no influence on obtained parameters.
$k_{\text{R non-OH}} / \text{s}^{-1}$	380 ± 210	Floated in global fitting, where quoted error is the 1σ error at the statistical level from Origin fitting.
$k_{\text{O(3P)+n-butanol}} / \text{cm}^3 \text{ molecule}^{-1} \text{ s}^{-1}$	$(4.20 \pm 0.42) \times 10^{-11}$	Floated in global fitting, where quoted error is 10 % of obtained bimolecular rate coefficient.

When fitting to these experimental traces, the lowest concentrations of *n*-butanol were excluded from the global fitting analysis, as in these traces, a good analytical fit could not be obtained to the OH fluorescence around and after the peak signal height was observed. According to Roscoe *et al.* [154], this could be a consequence of side reactions such as O (³P) + OH and O (³P) + *n*-butanol abstraction radicals if the alcohol concentration is not kept suitably high. The bimolecular rate coefficients $k_{\text{O(3P)+n-butanol}}$ have been measured as a function of temperature across the range 490 – 730 K, summarised in Figure 5-21.

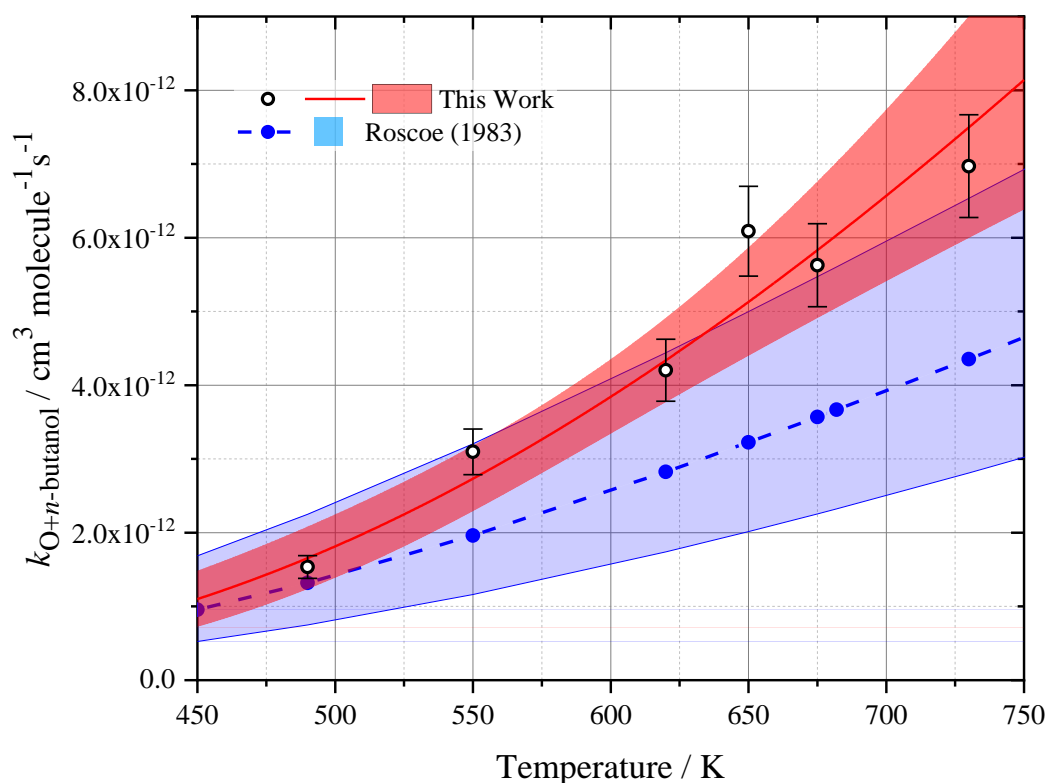


Figure 5-21: All experimentally obtained $k_{\text{O}(^3\text{P})+n\text{-butanol}}$ rate coefficients from this work (hollow black circles with black error bars, representing a 10 % error), with Arrhenius parameterisation and 95 % confidence limits (solid red line, filled red area). Compared with Roscoe *et al.* [154] (blue filled circles calculated from Arrhenius parameterisation fit to data, blue dashed line is Arrhenius parameterisation and filled blue area represents reported errors).

In Figure 5-21, the bimolecular rate coefficients measured in this work for the reaction of O (^3P) atoms are shown, alongside the literature data of Roscoe [154] (described by the Arrhenius parameterisation: $(4.98 \pm 0.80) \times 10^{-11} \times \exp^{(-14800 \pm 1600/RT)}$ $\text{cm}^3 \text{ molecule}^{-1} \text{ s}^{-1}$). The reaction of O (^3P) with *n*-butanol measured in this work displays a positive temperature dependence across the temperatures studied, which is best described by the Arrhenius parameterisation $k_{\text{O}(^3\text{P})+n\text{-butanol}}(490 - 730 \text{ K}) = (1.64 \pm 0.55) \times 10^{-10} \times \exp^{(-18700 \pm 1700/RT)}$ $\text{cm}^3 \text{ molecule}^{-1} \text{ s}^{-1}$. The temperature dependence obtained in this work is consistently higher than the parameterisation of Roscoe, but agrees within the experimental bounds provided up to temperatures of 630 K. However, at temperatures above this, some disagreement is observed, with a deviation of approximately 38 % measured at temperatures around 720 K.

In the literature study of Roscoe *et al.* [154] measured across the temperature range 300 – 600 K, gas chromatography analysis found that the yield of water measured in the experiment was equivalent to the consumption of O (^3P) atoms. This suggests that in their work, no OH recycling from the *n*-butanol was observed. If OH radical recycling had occurred, it would react again with the *n*-butanol reagent present, and this would result in a yield of water higher than the consumption of O (^3P) would suggest. However at the low pressures used in the study of Roscoe, this may be a negligible amount. This could go some way to explaining the discrepancy in the measurements of the bimolecular rate coefficient $k_{\text{O}(^3\text{P})+n\text{-butanol}}$ at temperatures above 500 K.

5.5.5 Fitting of OH Growth Signal Traces

Using the Arrhenius parameterisation obtained in Section 5.5.4 for the reaction of O (^3P) with *n*-butanol, attempts were then made to fit the complicated OH growth signal traces obtained in Section 5.5.3. The full fitting equation derived for fitting these complicated experimental traces can be found in Appendix G. As multiple kinetic parameters relating to these traces could now be fixed, i.e. the bimolecular rate coefficients for the reaction of O (^3P) with *n*-butanol and the reaction of OH with *n*-butanol, this should have in theory helped to constrain the global analysis to allow meaningful analysis of the behaviour observed. This however was not possible, and meaningful values for the other parameters could not be obtained. This is likely due to the highly complicated nature of the chemistry occurring in the reactor, with multiple side reactions at multiple reaction sites not accounted for in the fitting, and the lack of unique solutions to the fitting equation which give apparent ‘good’ fits to the traces obtained.

Whilst the possibility of O atoms reacting with *n*-butanol to produce the OH radicals observed in this work has not been unequivocally proven, it does to some extent provide a reasonable explanation for some of the unusual growth behaviour observed.

5.6 Conclusions

Experimental observations of significant growth of OH radicals in the presence of oxygen have been made at temperatures above 600 K for both *t*-butanol and *n*-butanol. Further experimental investigation into the conditions under which OH radical growth is observed have deduced it is likely the result of some side chemistry initiated by the

decomposition of fuel reagent to produce radicals. Analysis of kinetic traces obtained in this investigation has suggested the formation of some hydroperoxide species, which decomposes to give OH radicals without the influence of the photolysis laser. Decomposition of this hydroperoxide species may also result in formation of a precursor capable of producing O (³P) atoms when photolysed, and capable of decomposing to produce OH following photolysis.

Through the use of SO₂ precursor, experimental measurements of the bimolecular rate coefficient for the reaction of O (³P) with *n*-butanol were made at temperatures of 490 – 730 K, pressure of 40 – 55 Torr, and are described by the Arrhenius parameterisation $k_{\text{O}(^3\text{P})+n\text{-butanol}}(490 - 730 \text{ K}) = (1.64 \pm 0.55) \times 10^{-10} \times \exp^{(-18700 \pm 1700/RT)} \text{ cm}^3 \text{ molecule}^{-1} \text{ s}^{-1}$.

The potential interference of O atoms has been observed for other fuels during experiments conducted at the University of Leeds, such as the experiments conducted on multiple different ethers conducted by Dr D. Potter [155]. Whilst in this work, the interference of side reactions manifested as an obvious growth in reaction signal, it cannot be ruled out that it has occurred for other experimental studies where the effect has been more subtle, for example a slight apparent increase in the recycling parameter k_{recycle} when fitting kinetic traces. This work has thus highlighted the need for more robust experimental investigation for reactions occurring at high temperatures, particularly those involving significant addition of oxygen, to ensure that accurate parameters are obtained for the reaction being studied, unhindered by the interference of side reactions.

Chapter 6 Conclusions

6.1 Summary of This Work

The development of alternative fuels and their use in novel engine technologies such as HCCI engines requires an in-depth understanding of the kinetics governing their reactivity, particularly under low temperature combustion conditions. In this thesis, the reactions of the four butanol isomers, a family of potential biofuels, with the OH radical have been investigated, as well as some of the potential secondary reactions and oxidations following this initiation reaction.

The total bimolecular rate coefficient for the reaction of each butanol isomer with the hydroxyl radical was studied using the laser flash photolysis-laser induced fluorescence method, the results of which have been reported in Chapter 3. This thesis has extended the previous literature high of around 400 K to approximately 715 K for *n*-butanol, 607 K for *i*-butanol, 690 K for *s*-butanol, and 615 K for *t*-butanol. The temperature dependence for the reaction of each isomer with OH can be described by modified Arrhenius parameterisations (all in units of $\text{cm}^3 \text{ molecule}^{-1} \text{ s}^{-1}$):

$$k_{n\text{-butanol+OH}} (298 - 715 \text{ K}) = (1.15 \pm 2.62) \times 10^{-19} \times T^{(2.64 \pm 0.31)} \times \exp\left(\frac{7800 \pm 1100}{R \times T}\right)$$

$$k_{i\text{-butanol+OH}} (298 - 607 \text{ K}) = (2.05 \pm 6.79) \times 10^{-18} \times T^{(2.20 \pm 0.45)} \times \exp\left(\frac{6800 \pm 1600}{R \times T}\right)$$

$$k_{s\text{-butanol+OH}} (298 - 690 \text{ K}) = (1.38 \pm 2.58) \times 10^{-21} \times T^{(3.22 \pm 0.25)} \times \exp\left(\frac{10330 \pm 970}{R \times T}\right)$$

$$k_{t\text{-butanol+OH}} (298 - 614 \text{ K}) = (4.50 \pm 23.7) \times 10^{-21} \times T^{(2.99 \pm 0.71)} \times \exp\left(\frac{5200 \pm 2600}{R \times T}\right)$$

The experimental measurements by McGillen *et al.* [78], also using the LFP-LIF method, provided the previous literature temperature high of approximately 400 K. Their work provided modified Arrhenius temperature dependent parameterisations up to 1200 K through combining their experimental results with other previous high temperature shock tube data by Pang *et al.* [73-75], and the structure-activity parameterisations of Bethel and Atkinson [101]. Good agreement of the experimental data obtained in this work was found with the rate coefficients reported by McGillen *et al.*, and extrapolations of this work to temperatures relevant to low temperature combustion ($> 700 \text{ K}$) are in good agreement with previous high temperature shock tube experimental data.

Through comparison of the structures of the four isomers of butanol, the difference in reactivity was attributed to the bond strengths of the different possible C–H

abstraction environments. The alpha C–H bonds possess the weakest bond strengths due to influence of the neighbouring OH group, and consequently it is expected that this site dominates reactivity at room temperature. The presence of a negative temperature dependent region for all isomers apart from *t*-butanol was attributed to formation of a hydrogen-bonded complex, lowering the activation energy required for abstraction at neighbouring abstraction sites. This negative temperature dependence has been observed previously in the literature, and has also been observed for *t*-butanol at temperatures lower than were studied in this work.

OH fluorescence traces obtained at temperatures above 480 K demonstrated biexponential behaviour, as described in Chapter 4, suggesting OH radicals were being recycled following an initial abstraction reaction. This OH recycling channel was attributed to decomposition of the β -hydroxybutyl radicals formed following reaction of each butanol isomer with the hydroxyl radical, to form a butene molecule and an OH radical. Using the measured OH yield as a proxy for abstraction at the β -site of each isomer, comparisons were also drawn with the initial abstraction branching ratios found in the current literature. Good to excellent agreement was obtained overall with the SAR parameterisations of Atkinson [114] and the branching ratio of McGillen *et al.* [78] for each of the isomers.

The energetic barriers to decomposition for the β -hydroxybutyl radicals of each isomer were calculated at the CCSD/aug-cc-pVTZ//M06-2X/aug-cc-pVTZ level, and for *t*-, *i*- and *n*-butanol, these barriers were optimised using master equation solving in the widely available MESMER package. The energetic barriers, both calculated and optimised, for this decomposition are in good overall agreement with the few previous studies in the literature conducted for *n*-butanol by Zhang, Klippenstein and Law [141], and for *s*-butanol by Antonov *et al.* [142]. The slight differences in the energetic barriers calculated in this work can be rationalised by the groups neighbouring the radical centre. The lowest energetic barrier to decomposition calculated was for the *i*-butanol β -hydroxybutyl radical, as a result of the inductive alkyl groups neighbouring the radical centre. Conversely, the highest energetic barrier calculated was that of the *t*-butanol β -hydroxybutyl radical, which has two hydrogen groups neighbouring the radical centre in place of the methyl groups found in *i*-butanol.

Experiments conducted in Chapter 5 highlighted the observation of unusual OH radical growth behaviour at temperatures above 600 K, initially attributed to potential observation of radical chain branching of butanol fuel. Further experimental investigation

attributed this behaviour to side chemistry initiated by the decomposition of fuel reagent to produce radicals, reacting with oxygen to produce an O atom precursor. Consequently, the reaction of O (³P) atoms with *n*-butanol was investigated as a function of temperature, obtaining the parameterisation: $k_{\text{O}(3\text{P})+n\text{-butanol}}(490 - 730 \text{ K}) = (1.64 \pm 0.55) \times 10^{-10} \times \exp^{(-18700 \pm 1700/RT)} \text{ cm}^3 \text{ molecule}^{-1} \text{ s}^{-1}$, in reasonable agreement with previous literature obtained by Roscoe [154].

Some investigation into the combustion model of Sarathy *et al.* [55] produced for *t*-butanol low temperature combustion highlighted that the consolidating of reaction rate constants, such as that of the RO₂ species' decomposition straight to products rather than through the isomerisation step first, may be an oversimplification at low temperatures. Simulations of the ignition delay times obtained when separating out these steps using the rate constants calculated by Sun, Bozzelli and Law [152] were compared to experimental data of Weber and Sung [47], and found that at the lowest temperatures and pressure studied, this separating of rate constants can decrease the predicted IDT by approximately 37 % at 700 K and 15 bar, in worse agreement with experimental data. This demonstrates the need for further investigation into the low temperature reaction classes described in the combustion model of Sarathy *et al.*, and the lumping together of reactions.

6.2 Future Work

Using the total bimolecular rate coefficients and modified Arrhenius parameterisations obtained in Chapter 3, future work could investigate the branching ratios of the different potential abstraction sites for the four isomers of butanol. As this work has provided constraints on the total bimolecular rate coefficient for each isomer's reaction with the OH radical, the measured total rates could be used in conjunction with structure-activity type parameterisations that compare reactivity using potential abstraction site environments. Future experiments could also make use of isotopically labelled sites to deduce site specific reactivity, such as deuterated C–H bonds or the use of ¹⁸O in the alcohol group of each isomer, similar to the work conducted by Carr *et al.* [100] for ethanol and Stranic *et al.* [76] for *t*-butanol.

From the method used in Chapter 4 for measuring unimolecular decomposition kinetics of β -hydroxybutyl radicals, future work investigating the same potential β -scission route for other alcohols that possess this β -site could be conducted. For the butanol isomers, future work investigating the pressure dependence of the decomposition

should be conducted and parameterised, to allow this decomposition to be accurately represented in combustion modelling. Sensitivity analysis similar to the study by Agbro *et al.* [60] for *n*-butanol should be conducted on models that include this pressure-dependent decomposition channel to examine the effect of this OH reproduction on low temperature combustion modelling.

The unusual OH signal growth behaviour observed in Chapter 5 highlights another area which requires further investigation. Through investigation of the *t*-butanol combustion mechanism, this work has suggested that the combining of several reaction steps from formation of the peroxy radical through to products is an oversimplification, and the reactions should be separated into their individual steps, and parameterised including the pressure dependence calculated by Sun, Bozzelli and Law [152]. Whilst the simplification of direct formation of products may be a reasonable assumption at high temperatures (> 900 K), simulations of the ignition delay times suggest this is not a reasonable simplification at temperatures below this. Further investigation *via* a sensitivity analysis of the reactions involved in *t*-butanol low temperature combustion could highlight which of the reactions has the most significant effect on ignition delay time at low pressures and temperatures, and which reactions require further study and calculation.

To the best of our knowledge, the experiments conducted in Chapter 5 represent the first observation of potential formation of an O atom precursor from the presence of fuel and oxygen in a reaction cell, resulting in instant growth of OH signal following the photolysis laser. This work has highlighted the need for more robust experimental investigation of reaction kinetics at high temperatures, as unexpected influence by side reactions may occur unnoticed without thorough testing. A temperature dependent parameterisation of the reaction of O (^3P) atoms with *n*-butanol measured in this work suggests the rate of this reaction is faster than reported in previous literature by Roscoe at temperatures above 500 K, and thus future work should investigate the reactions of the other isomers of butanol with O (^3P) atoms at these temperatures.

References

- [1] Sarathy, S.M., Osswald, P., Hansen, N. and Kohse-Hoinghaus, K. Alcohol combustion chemistry. *Progress in Energy and Combustion Science*. 2014, **44**, pp.40-102.
- [2] Smith, P., Haberl, H., Popp, A., Erb, K.h., Lauk, C., Harper, R., Tubiello, F.N., Siqueira Pinto, A., Jafari, M. and Sohi, S. How much land-based greenhouse gas mitigation can be achieved without compromising food security and environmental goals? *Global Change Biology*. 2013, **19**(8), pp.2285-2302.
- [3] Stocker, T. *Climate change 2013: the physical science basis: Working Group I contribution to the Fifth assessment report of the Intergovernmental Panel on Climate Change*. Cambridge University Press, 2014.
- [4] UNFCCC. Paris Agreement. 2015.
- [5] BP. *BP Statistical Review of World Energy 2019*. 68th ed., 2019.
- [6] Saxena, R.C., Adhikari, D.K. and Goyal, H.B. Biomass-based energy fuel through biochemical routes: A review. *Renewable & Sustainable Energy Reviews*. 2009, **13**(1), pp.167-178.
- [7] Edenhofer, O., R. Pichs-Madruga, Y. Sokona, E. Farahani, S. Kadner, K. Seyboth, A. Adler, I. Baum, S. Brunner, P. Eickemeier, B. Kriemann, J. Savolainen, S. Schlömer, C. von techow, T. Zwickel and J.C. Minx (eds). *IPCC, 2014: Summary for Policymakers*. Cambridge, UK: Cambridge University Press, 2014.
- [8] Department for Transport. *Renewable Fuel Statistics 2019 First Provisional Report*. 2019.
- [9] Office of Energy Efficiency & Renewable Energy. *Hydrogen Storage*. [Online]. 2019. [Accessed 25/11/2019]. Available from: <https://www.energy.gov/eere/fuelcells/hydrogen-storage>.
- [10] Shahsavan, M. and Mack, J.H. Numerical study of a boosted HCCI engine fueled with n-butanol and isobutanol. *Energy conversion and management*. 2018, **157**, pp.28-40.
- [11] Todts, W. *CO₂ Emissions From Cars: The Facts*. European Federation for Transport and Environment AISBL, 2018.
- [12] Jin, C., Yao, M.F., Liu, H.F., Lee, C.F.F. and Ji, J. Progress in the production and application of n-butanol as a biofuel. *Renewable & Sustainable Energy Reviews*. 2011, **15**(8), pp.4080-4106.

- [13] Valentine, J., Clifton-Brown, J., Hastings, A., Robson, P., Allison, G. and Smith, P. Food vs. fuel: the use of land for lignocellulosic next generation' energy crops that minimize competition with primary food production. *Global Change Biology Bioenergy*. 2012, **4**(1), pp.1-19.
- [14] Nigam, P.S. and Singh, A. Production of liquid biofuels from renewable resources. *Progress in Energy and Combustion Science*. 2011, **37**(1), pp.52-68.
- [15] Demirbas, A. Biofuels sources, biofuel policy, biofuel economy and global biofuel projections. *Energy conversion and management*. 2008, **49**(8), pp.2106-2116.
- [16] Mathews, J.A. Carbon-negative biofuels. *Energy Policy*. 2008, **36**(3), pp.940-945.
- [17] Antizar-Ladislao, B. and Turrion-Gomez, J.L. Second-generation biofuels and local bioenergy systems. *Biofuels, Bioproducts and Biorefining*. 2008, **2**(5), pp.455-469.
- [18] Wu, M., Mintz, M., Wang, M. and Arora, S. Water Consumption in the Production of Ethanol and Petroleum Gasoline. *Environmental Management*. 2009, **44**(5), pp.981-997.
- [19] Serrano-Ruiz, J.C. and Dumesic, J.A. Catalytic routes for the conversion of biomass into liquid hydrocarbon transportation fuels. *Energy & Environmental Science*. 2011, **4**(1), pp.83-99.
- [20] Lange, J.P. Lignocellulose conversion: an introduction to chemistry, process and economics. *Biofuels, Bioproducts and Biorefining*. 2007, **1**(1), pp.39-48.
- [21] Alonso, D.M., Bond, J.Q. and Dumesic, J.A. Catalytic conversion of biomass to biofuels. *Green Chemistry*. 2010, **12**(9), pp.1493-1513.
- [22] Ho, D.P., Ngo, H.H. and Guo, W. A mini review on renewable sources for biofuel. *Bioresource Technology*. 2014, **169**, pp.742-749.
- [23] Alonso, D.M., Wettstein, S.G. and Dumesic, J.A. Bimetallic catalysts for upgrading of biomass to fuels and chemicals. *Chemical Society Reviews*. 2012, **41**(24), pp.8075-8098.
- [24] Fargione, J., Hill, J., Tilman, D., Polasky, S. and Hawthorne, P. Land clearing and the biofuel carbon debt. *Science*. 2008, **319**(5867), pp.1235-1238.
- [25] Tilman, D., Socolow, R., Foley, J.A., Hill, J., Larson, E., Lynd, L., Pacala, S., Reilly, J., Searchinger, T., Somerville, C. and Williams, R. Beneficial Biofuels-The Food, Energy, and Environment Trilemma. *Science*. 2009, **325**(5938), pp.270-271.

- [26] Tilman, D., Hill, J. and Lehman, C. Carbon-negative biofuels from low-input high-diversity grassland biomass. *Science*. 2006, **314**(5805), pp.1598-1600.
- [27] Agarwal, A.K. Biofuels (alcohols and biodiesel) applications as fuels for internal combustion engines. *Progress in Energy and Combustion Science*. 2007, **33**(3), pp.233-271.
- [28] Guo, M.X., Song, W.P. and Buhain, J. Bioenergy and biofuels: History, status, and perspective. *Renewable & Sustainable Energy Reviews*. 2015, **42**, pp.712-725.
- [29] Sun, Y. and Cheng, J. Hydrolysis of lignocellulosic materials for ethanol production: a review. *Bioresource Technology*. 2002, **83**(1), pp.1-11.
- [30] Kumar, B.R. and Saravanan, S. Use of higher alcohol biofuels in diesel engines: a review. *Renewable and Sustainable Energy Reviews*. 2016, **60**, pp.84-115.
- [31] Christensen, E., Yanowitz, J., Ratcliff, M. and McCormick, R.L. Renewable Oxygenate Blending Effects on Gasoline Properties. *Energy & Fuels*. 2011, **25**(10), pp.4723-4733.
- [32] Szwaja, S. and Naber, J.D. Combustion of n-butanol in a spark-ignition IC engine. *Fuel*. 2010, **89**(7), pp.1573-1582.
- [33] Wu, M., Wang, M., Liu, J.H. and Huo, H. Assessment of Potential Life-Cycle Energy and Greenhouse Gas Emission Effects from Using Corn-Based Butanol as a Transportation Fuel. *Biotechnology Progress*. 2008, **24**(6), pp.1204-1214.
- [34] Green, E.M. Fermentative production of butanol - the industrial perspective. *Current Opinion in Biotechnology*. 2011, **22**(3), pp.337-343.
- [35] Qureshi, N., Saha, B.C., Dien, B., Hector, R.E. and Cotta, M.A. Production of butanol (a biofuel) from agricultural residues: Part I - Use of barley straw hydrolysate. *Biomass & Bioenergy*. 2010, **34**(4), pp.559-565.
- [36] Lee, S.Y., Park, J.H., Jang, S.H., Nielsen, L.K., Kim, J. and Jung, K.S. Fermentative butanol production by clostridia. *Biotechnology and Bioengineering*. 2008, **101**(2), pp.209-228.
- [37] Abdehagh, N., Tezel, F.H. and Thibault, J. Separation techniques in butanol production: Challenges and developments. *Biomass and Bioenergy*. 2014, **60**, pp.222-246.
- [38] Kohse-Höinghaus, K., Oßwald, P., Cool, T.A., Kasper, T., Hansen, N., Qi, F., Westbrook, C.K. and Westmoreland, P.R. Biofuel combustion chemistry: from ethanol to biodiesel. *Angewandte Chemie International Edition*. 2010, **49**(21), pp.3572-3597.

- [39] Blocquet, M., Schoemaeker, C., Amedro, D., Herbinet, O., Battin-Leclerc, F. and Fittschen, C. Quantification of OH and HO₂ radicals during the low-temperature oxidation of hydrocarbons by Fluorescence Assay by Gas Expansion technique. *Proceedings of the National Academy of Sciences of the United States of America*. 2013, **110**(50), pp.20014-20017.
- [40] Borghi, R., Destriau, M. and De Soete, G. *Combustion and Flames*. Editions OPHRYS.
- [41] Pilling, M.J. and Seakins, P.W. *Reaction kinetics*. Oxford University Press, 1996.
- [42] Jung, D. Autoignition and Chemical-Kinetic Mechanisms of Homogeneous Charge Compression Ignition Combustion for the Fuels with Various Autoignition Reactivity. In: *Advanced Chemical Kinetics*. 2017.
- [43] Mack, J.H., Schuler, D., Butt, R.H. and Dibble, R.W. Experimental investigation of butanol isomer combustion in Homogeneous Charge Compression Ignition (HCCI) engines. *Applied Energy*. 2016, **165**, pp.612-626.
- [44] Westbrook, C.K. Biofuels combustion. *Annual review of physical chemistry*. 2013, **64**, pp.201-219.
- [45] He, B.-Q., Yuan, J., Liu, M.-B. and Zhao, H. Combustion and emission characteristics of a n-butanol HCCI engine. *Fuel*. 2014, **115**, pp.758-764.
- [46] Vranckx, S., Heufer, K.A., Lee, C., Olivier, H., Schill, L., Kopp, W.A., Leonhard, K., Taatjes, C.A. and Fernandes, R.X. Role of peroxy chemistry in the high-pressure ignition of n-butanol – Experiments and detailed kinetic modelling. *Combustion and Flame*. 2011, **158**(8), pp.1444-1455.
- [47] Weber, B.W. and Sung, C.J. Comparative Autoignition Trends in Butanol Isomers at Elevated Pressure. *Energy & Fuels*. 2013, **27**(3), pp.1688-1698.
- [48] Goldsborough, S.S., Hochgreb, S., Vanhove, G., Wooldridge, M.S., Curran, H.J. and Sung, C.-J. Advances in rapid compression machine studies of low- and intermediate-temperature autoignition phenomena. *Progress in Energy and Combustion Science*. 2017, **63**, pp.1-78.
- [49] Griffiths, J.F. and Barnard, J.A. *Flame and combustion*. CRC Press, 1995.
- [50] Lewis, B. and Von Elbe, G. *Combustion, flames and explosions of gases*. Elsevier, 2012.
- [51] Glassman, I., Yetter, R.A. and Glumac, N.G. *Combustion*. Academic press, 2014.
- [52] Zádor, J., Taatjes, C.A. and Fernandes, R.X. Kinetics of elementary reactions in low-temperature autoignition chemistry. *Progress in Energy and Combustion Science*. 2011, **37**(4), pp.371-421.

- [53] Agbro, E., Tomlin, A.S., Zhang, W., Burluka, A., Mauss, F., Pasternak, M., Alfazazi, A. and Sarathy, S.M. Chemical Kinetic Modeling Study on the Influence of n-Butanol Blending on the Combustion, Autoignition, and Knock Properties of Gasoline and Its Surrogate in a Spark-Ignition Engine. *Energy & Fuels*. 2018, **32**(10), pp.10065-10077.
- [54] Tomlin, A.S. The role of sensitivity and uncertainty analysis in combustion modelling. *Proceedings of the Combustion Institute*. 2013, **34**(1), pp.159-176.
- [55] Sarathy, S.M., Vranckx, S., Yasunaga, K., Mehl, M., Oßwald, P., Metcalfe, W.K., Westbrook, C.K., Pitz, W.J., Kohse-Höinghaus, K. and Fernandes, R.X. A comprehensive chemical kinetic combustion model for the four butanol isomers. *Combustion and Flame*. 2012, **159**(6), pp.2028-2055.
- [56] Curran, H.J., Gaffuri, P., Pitz, W.J. and Westbrook, C.K. A comprehensive modeling study of n-heptane oxidation. *Combustion and Flame*. 1998, **114**(1-2), pp.149-177.
- [57] Ó Conaire, M., Curran, H.J., Simmie, J.M., Pitz, W.J. and Westbrook, C.K. A comprehensive modeling study of hydrogen oxidation. 2004, **36**(11), pp.603-622.
- [58] Zhou, C.-W. et al. A comprehensive experimental and modeling study of isobutene oxidation. *Combustion and Flame*. 2016, **167**, pp.353-379.
- [59] Agbro, E.B. *Experimental and chemical kinetic modelling study on the combustion of alternative fuels in fundamental systems and practical engines*. PhD thesis, University of Leeds, 2017.
- [60] Agbro, E. and Tomlin, A.S. Low temperature oxidation of n-butanol: Key uncertainties and constraints in kinetics. *Fuel*. 2017, **207**, pp.776-789.
- [61] Wardle, B. *Principles and applications of photochemistry*. John Wiley & Sons, 2009.
- [62] Hollas, J.M. *Modern Spectroscopy*. Wiley, 2004.
- [63] Hitz, C.B., Ewing, J.J. and Hecht, J. *Introduction to Laser Technology*. Wiley, 2004.
- [64] Andrews, D.L. *Lasers in Chemistry*. Springer Berlin Heidelberg, 2012.
- [65] Li, H.L., Chu, W., Xu, H.L., Cheng, Y., Chin, S.L., Yamanouchi, K. and Sun, H.B. Simultaneous identification of multi-combustion-intermediates of alkanol-air flames by femtosecond filament excitation for combustion sensing. *Scientific Reports*. 2016, **6**, p.7.
- [66] Baeza-Romero, M.T., Glowacki, D.R., Blitz, M.A., Heard, D.E., Pilling, M.J., Rickard, A.R. and Seakins, P.W. A combined experimental and theoretical study

- of the reaction between methylglyoxal and OH/OD radical: OH regeneration. *Physical Chemistry Chemical Physics*. 2007, **9**(31), pp.4114-4128.
- [67] Photonics, H. In: *Photomultiplier Tubes Basics and Applications*. 2007.
- [68] Levitt, B. *Physical Chemistry of Fast Reactions: Volume 1: Gas Phase Reactions of Small Molecules*. Springer US, 2012.
- [69] Percival, C.J., Shallcross, D.E., Canosa-Mas, C.E. and Dyke, J.M. Recent advances in the application of discharge-flow to the determination of gas-phase rate coefficients at pressures and temperatures of relevance to the Earth's atmosphere. *Journal of Photochemistry and Photobiology A: Chemistry*. 2005, **176**(1), pp.250-259.
- [70] Howard, C.J. Kinetic measurements using flow tubes. *Journal of Physical Chemistry*. 1979, **83**(1), pp.3-9.
- [71] Randazzo, J.B. and Tranter, R.S. Note: An improved driver section for a diaphragmless shock tube. 2015, **86**(1), p.016117.
- [72] Tranter, R.S. and Giri, B.R. A diaphragmless shock tube for high temperature kinetic studies. 2008, **79**(9), p.094103.
- [73] Pang, G.A., Hanson, R.K., Golden, D.M. and Bowman, C.T. Rate constant measurements for the overall reaction of OH+ 1-butanol→ products from 900 to 1200 K. *The Journal of Physical Chemistry A*. 2012, **116**(10), pp.2475-2483.
- [74] Pang, G.A., Hanson, R.K., Golden, D.M. and Bowman, C.T. Experimental Determination of the High-Temperature Rate Constant for the Reaction of OH with sec-Butanol. *Journal of Physical Chemistry A*. 2012, **116**(39), pp.9607-9613.
- [75] Pang, G.A., Hanson, R.K., Golden, D.M. and Bowman, C.T. High-Temperature Rate Constant Determination for the Reaction of OH with iso-Butanol. *Journal of Physical Chemistry A*. 2012, **116**(19), pp.4720-4725.
- [76] Stranic, I., Pang, G.A., Hanson, R.K., Golden, D.M. and Bowman, C.T. Shock Tube Measurements of the tert-Butanol plus OH Reaction Rate and the tert-C₄H₈OH Radical β -Scission Branching Ratio Using Isotopic Labeling. *Journal of Physical Chemistry A*. 2013, **117**(23), pp.4777-4784.
- [77] Wallington, T.J. and Kurylo, M.J. The gas phase reactions of hydroxyl radicals with a series of aliphatic alcohols over the temperature range 240–440 K. *International journal of chemical kinetics*. 1987, **19**(11), pp.1015-1023.
- [78] McGillen, M.R., Baasandorj, M. and Burkholder, J.B. Gas-phase rate coefficients for the OH+ n-, i-, s-, and t-butanol reactions measured between 220 and 380 K:

- Non-Arrhenius behavior and site-specific reactivity. *The Journal of Physical Chemistry A*. 2013, **117**(22), pp.4636-4656.
- [79] Swallow, A. Recent Results From Pulse Radiolysis. *Photochemistry and Photobiology*. 1968, **7**(6), pp.683-694.
- [80] Nelson, L., Rattigan, O., Neavyn, R., Sidebottom, H., Treacy, J. and Nielsen, O.J. Absolute and relative rate constants for the reactions of hydroxyl radicals and chlorine atoms with a series of aliphatic alcohols and ethers at 298 K. *International journal of chemical kinetics*. 1990, **22**(11), pp.1111-1126.
- [81] IUPAC. *Compendium of Chemical Terminology, 2nd Edition, 'The Gold Book'*. 2nd ed. Oxford: Blackwell Scientific Publications, 1997.
- [82] Howes, N.U.M., Mir, Z.S., Blitz, M.A., Hardman, S., Lewis, T.R., Stone, D. and Seakins, P.W. Kinetic studies of C1 and C2 Criegee intermediates with SO₂ using laser flash photolysis coupled with photoionization mass spectrometry and time resolved UV absorption spectroscopy. *Physical Chemistry Chemical Physics*. 2018, **20**(34), pp.22218-22227.
- [83] Baeza-Romero, M.T., Blitz, M.A., Goddard, A. and Seakins, P.W. Time-of-flight mass spectrometry for time-resolved measurements: Some developments and applications. 2012, **44**(8), pp.532-545.
- [84] Andersen, V.F., Wallington, T.J. and Nielsen, O.J. Atmospheric chemistry of i-butanol. *The Journal of Physical Chemistry A*. 2010, **114**(47), pp.12462-12469.
- [85] Atkinson, R. Gas-Phase Tropospheric Chemistry of Organic Compounds. *Journal of Physical and Chemical Reference Data*. 1994, pp.R1-&.
- [86] Chew, A.A. and Atkinson, R. OH radical formation yields from the gas-phase reactions of O₃ with alkenes and monoterpenes. *Journal of Geophysical Research: Atmospheres*. 1996, **101**(D22), pp.28649-28653.
- [87] Atkinson, R. Kinetics of the gas-phase reactions of OH radicals with alkanes and cycloalkanes. *Atmospheric Chemistry and Physics*. 2003, **3**, pp.2233-2307.
- [88] Potter, D.G., Blitz, M.A. and Seakins, P.W. A generic method for determining R + O₂ rate parameters via OH regeneration. *Chemical Physics Letters*. 2019, **730**, pp.213-219.
- [89] Atkinson, R., Baulch, D.L., Cox, R.A., Crowley, J.N., Hampson, R.F., Hynes, R.G., Jenkin, M.E., Rossi, M.J. and Troe, J. Evaluated kinetic and photochemical data for atmospheric chemistry: Volume I - gas phase reactions of Ox, HOx, NOx and SOx species. *Atmospheric Chemistry and Physics*. 2004, **4**(6), pp.1461-1738.

- [90] Dortmund Data Bank. *Saturated Vapour Pressure Calculation by Antoine Equation*. [Online]. [Accessed]. Available from: <http://ddbonline.ddbst.com/AntoineCalculation/AntoineCalculationCGI.exe>.
- [91] Kemme, H.R. and Kreps, S.I. Vapor pressure of primary n-alkyl chlorides and alcohols. *Journal of Chemical & Engineering Data*. 1969, **14**(1), pp.98-102.
- [92] Tully, F.P. and Ravishankara, A.R. Flash photolysis-resonance fluorescence kinetic study of the reactions hydroxyl + molecular hydrogen .fwdarw. water + atomic hydrogen and hydroxyl + methane .fwdarw. water + methyl from 298 to 1020 K. *The Journal of Physical Chemistry*. 1980, **84**(23), pp.3126-3130.
- [93] Dunlop, J.R. and Tully, F.P. A kinetic study of hydroxyl radical reactions with methane and perdeuterated methane. *The Journal of Physical Chemistry*. 1993, **97**(43), pp.11148-11150.
- [94] Atkins, P., de Paula, J. and Friedman, R. *Quanta, Matter, and Change: A Molecular Approach to Physical Chemistry*. OUP Oxford, 2009.
- [95] Diaz-Gonzalez, M., Trevino, C. and Prince, J.C. A Reduced Kinetic Mechanism for the Combustion of n-Butanol. *Energy & Fuels*. 2018, **32**(1), pp.867-874.
- [96] Rajesh Kumar, B. and Saravanan, S. Use of higher alcohol biofuels in diesel engines: A review. *Renewable and Sustainable Energy Reviews*. 2016, **60**, pp.84-115.
- [97] Al-Hasan, M. and Momani, M. The effect of iso-butanol-diesel blends on engine performance. *Transport*. 2008, **23**.
- [98] Moss, J.T., Berkowitz, A.M., Oehlschlaeger, M.A., Biet, J., Warth, V., Glaude, P.-A. and Battin-Leclerc, F. An experimental and kinetic modeling study of the oxidation of the four isomers of butanol. *The Journal of Physical Chemistry A*. 2008, **112**(43), pp.10843-10855.
- [99] Black, G., Curran, H.J., Pichon, S., Simmie, J.M. and Zhukov, V. Bio-butanol: Combustion properties and detailed chemical kinetic model. *Combustion and Flame*. 2010, **157**(2), pp.363-373.
- [100] Carr, S.A., Blitz, M.A. and Seakins, P.W. Site-specific rate coefficients for reaction of OH with ethanol from 298 to 900 K. *The Journal of Physical Chemistry A*. 2011, **115**(15), pp.3335-3345.
- [101] Bethel, H.L., Atkinson, R. and Arey, J. Kinetics and products of the reactions of selected diols with the OH radical. *International journal of chemical kinetics*. 2001, **33**(5), pp.310-316.

- [102] Gorbatenko, I., Tomlin, A.S., Lawes, M. and Cracknell, R.F. Experimental and modelling study of the impacts of n-butanol blending on the auto-ignition behaviour of gasoline and its surrogate at low temperatures. *Proceedings of the Combustion Institute*. 2019, **37**(1), pp.501-509.
- [103] Yasunaga, K., Mikajiri, T., Sarathy, S.M., Koike, T., Gillespie, F., Nagy, T., Simmie, J.M. and Curran, H.J. A shock tube and chemical kinetic modeling study of the pyrolysis and oxidation of butanols. *Combustion and Flame*. 2012, **159**(6), pp.2009-2027.
- [104] Atsumi, S., Hanai, T. and Liao, J.C. Non-fermentative pathways for synthesis of branched-chain higher alcohols as biofuels. *Nature*. 2008, **451**(7174), pp.86-89.
- [105] Ezeji, T.C., Qureshi, N. and Blaschek, H.P. Production of acetone butanol (AB) from liquefied corn starch, a commercial substrate, using *Clostridium beijerinckii* coupled with product recovery by gas stripping. *Journal of Industrial Microbiology & Biotechnology*. 2007, **34**(12), pp.771-777.
- [106] Hess, G. BP, DuPont Form Ethanol Venture. *Chemical and Engineering News*. 2007, **85**(27), p.8.
- [107] Hurley, M.D., Wallington, T.J., Lairsen, L., Javadi, M.S., Nielsen, O.J., Yamanaka, T. and Kawasaki, M. Atmospheric Chemistry of n-Butanol: Kinetics, Mechanisms, and Products of Cl Atom and OH Radical Initiated Oxidation in the Presence and Absence of NO_x. *Journal of Physical Chemistry A*. 2009, **113**(25), pp.7011-7020.
- [108] Wu, H., Mu, Y., Zhang, X. and Jiang, G. Relative rate constants for the reactions of hydroxyl radicals and chlorine atoms with a series of aliphatic alcohols. *International journal of chemical kinetics*. 2003, **35**(2), pp.81-87.
- [109] Oh, S. and Andino, J.M. Kinetics of the gas-phase reactions of hydroxyl radicals with C₁–C₆ aliphatic alcohols in the presence of ammonium sulfate aerosols. *International journal of chemical kinetics*. 2001, **33**(7), pp.422-430.
- [110] Cavalli, F., Geiger, H., Barnes, I. and Becker, K.H. FTIR kinetic, product, and modeling study of the OH-initiated oxidation of 1-butanol in air. *Environmental science & technology*. 2002, **36**(6), pp.1263-1270.
- [111] Yujing, M. and Mellouki, A. Temperature dependence for the rate constants of the reaction of OH radicals with selected alcohols. *Chemical Physics Letters*. 2001, **333**(1–2), pp.63-68.

- [112] Zhou, C.W., Simmie, J.M. and Curran, H.J. Rate constants for hydrogen-abstraction by OH from n-butanol. *Combustion and Flame*. 2011, **158**(4), pp.726-731.
- [113] Sarathy, S.M., Thomson, M.J., Togbé, C., Dagaut, P., Halter, F. and Mounaim-Rousselle, C. An experimental and kinetic modeling study of n-butanol combustion. *Combustion and Flame*. 2009, **156**(4), pp.852-864.
- [114] Atkinson, R. A Structure Activity Relationship for the Estimation of Rate Constants for the Gas-Phase Reactions of OH Radicals With Organic-Compounds. *International journal of chemical kinetics*. 1987, **19**(9), pp.799-828.
- [115] Curran, H.J. Rate constant estimation for C1 to C4 alkyl and alkoxy radical decomposition. *International journal of chemical kinetics*. 2006, **38**, pp.250-275.
- [116] R. Kolodziej and Scheib, J. Bio-isobutanol: The next-generation biofuel. *Hydrocarbon Processing*. 2012, pp.79-85.
- [117] Alasfour, F.N. The Effect of Using 30% Iso-Butanol-Gasoline Blend on Hydrocarbon Emissions from a Spark-Ignition Engine. *Energy Sources*. 1999, **21**(5), pp.379-394.
- [118] Togbé, C., Mzé-Ahmed, A. and Dagaut, P. Kinetics of Oxidation of 2-Butanol and Isobutanol in a Jet-Stirred Reactor: Experimental Study and Modeling Investigation. *Energy & Fuels*. 2010, **24**(9), pp.5244-5256.
- [119] Mellouki, A., Oussar, F., Lun, X. and Chakir, A. Kinetics of the reactions of the OH radical with 2-methyl-1-propanol, 3-methyl-1-butanol and 3-methyl-2-butanol between 241 and 373 K. *Physical Chemistry Chemical Physics*. 2004, **6**(11), pp.2951-2955.
- [120] Merchant, S.S., Zanoelo, E.F., Speth, R.L., Harper, M.R., Van Geem, K.M. and Green, W.H. Combustion and pyrolysis of iso-butanol: Experimental and chemical kinetic modeling study. *Combustion and Flame*. 2013, **160**(10), pp.1907-1929.
- [121] Grana, R., Frassoldati, A., Faravelli, T., Niemann, U., Ranzi, E., Seiser, R., Cattolica, R. and Seshadri, K. An experimental and kinetic modeling study of combustion of isomers of butanol. *Combustion and Flame*. 2010, **157**(11), pp.2137-2154.
- [122] Baxley, J.S. and Wells, J. *The hydroxyl radical reaction rate constant and atmospheric transformation products of 2-butanol and 2-pentanol*. DTIC Document, 1998.

- [123] Jiménez, E., Lanza, B., Garzón, A., Ballesteros, B. and Albaladejo, J. Atmospheric Degradation of 2-Butanol, 2-Methyl-2-butanol, and 2,3-Dimethyl-2-butanol: OH Kinetics and UV Absorption Cross Sections. *The Journal of Physical Chemistry A*. 2005, **109**(48), pp.10903-10909.
- [124] Peeters, J., Boullart, W., Pultau, V., Vandenberg, S. and Vereecken, L. Structure–Activity Relationship for the Addition of OH to (Poly)alkenes: Site-Specific and Total Rate Constants. *The Journal of Physical Chemistry A*. 2007, **111**(9), pp.1618-1631.
- [125] Frassoldati, A., Grana, R., Faravelli, T., Ranzi, E., Oßwald, P. and Kohse-Höinghaus, K. Detailed kinetic modeling of the combustion of the four butanol isomers in premixed low-pressure flames. *Combustion and Flame*. 2012, **159**(7), pp.2295-2311.
- [126] Hansen, N., Harper, M.R. and Green, W.H. High-temperature oxidation chemistry of n-butanol - experiments in low-pressure premixed flames and detailed kinetic modeling. *Physical Chemistry Chemical Physics*. 2011, **13**(45), pp.20262-20274.
- [127] Wallington, T.J., Dagaut, P., Liu, R. and Kurylo, M.J. Gas-phase reactions of hydroxyl radicals with the fuel additives methyl tert-butyl ether and tert-butyl alcohol over the temperature range 240-440 K. *Environmental science & technology*. 1988, **22**(7), pp.842-844.
- [128] Teton, S., Mellouki, A., Le Bras, G. and Sidebottom, H. Rate constants for reactions of OH radicals with a series of asymmetrical ethers and tert-Butyl alcohol. *International journal of chemical kinetics*. 1996, **28**(4), pp.291-297.
- [129] Saunders, S., Baulch, D., Cooke, K., Pilling, M. and Smurthwaite, P. Kinetics and mechanisms of the reactions of OH with some oxygenated compounds of importance in tropospheric chemistry. *International journal of chemical kinetics*. 1994, **26**(1), pp.113-130.
- [130] Kwok, E.S.C. and Atkinson, R. Estimation of hydroxyl radical reaction rate constants for gas-phase organic compounds using a structure-reactivity relationship: An update. *Atmospheric Environment*. 1995, **29**(14), pp.1685-1695.
- [131] McGillen, M. *Personal Communication*, 2019.
- [132] Mellouki, A., Le Bras, G. and Sidebottom, H. Kinetics and Mechanisms of the Oxidation of Oxygenated Organic Compounds in the Gas Phase. *Chemical Reviews*. 2003, **103**(12), pp.5077-5096.

- [133] Smith, I.W.M. and Ravishankara, A.R. Role of Hydrogen-Bonded Intermediates in the Bimolecular Reactions of the Hydroxyl Radical. *The Journal of Physical Chemistry A*. 2002, **106**(19), pp.4798-4807.
- [134] Hess, W.P. and Tully, F.P. Catalytic conversion of alcohols to alkenes by OH. *Chemical Physics Letters*. 1988, **152**(2), pp.183-189.
- [135] Dunlop, J.R. and Tully, F.P. Catalytic Dehydration of Alcohols by OH. 2-Propanol: An Intermediate Case. *Journal of Physical Chemistry*. 1993, **97**(24), pp.6457-6464.
- [136] Zádor, J., Jasper, A. and Miller, J. The reaction between propene and hydroxyl. *Physical chemistry chemical physics : PCCP*. 2009, **11**, pp.11040-53.
- [137] Cai, J.H., Zhang, L.D., Yang, J.Z., Li, Y.Y., Zhao, L. and Qi, F. Experimental and kinetic modeling study of tert-butanol combustion at low pressure. *Energy*. 2012, **43**(1), pp.94-102.
- [138] Lefkowitz, J.K., Heyne, J.S., Won, S.H., Dooley, S., Kim, H.H., Haas, F.M., Jahangirian, S., Dryer, F.L. and Ju, Y. A chemical kinetic study of tertiary-butanol in a flow reactor and a counterflow diffusion flame. *Combustion and Flame*. 2012, **159**(3), pp.968-978.
- [139] Welz, O., Zádor, J., Savee, J.D., Sheps, L., Osborn, D.L. and Taatjes, C.A. Low-Temperature Combustion Chemistry of n-Butanol: Principal Oxidation Pathways of Hydroxybutyl Radicals. *The Journal of Physical Chemistry A*. 2013, **117**(46), pp.11983-12001.
- [140] Welz, O., Savee, J.D., Eskola, A.J., Sheps, L., Osborn, D.L. and Taatjes, C.A. Low-temperature combustion chemistry of biofuels: Pathways in the low-temperature (550-700 K) oxidation chemistry of isobutanol and tert-butanol. *Proceedings of the Combustion Institute*. 2013, **34**, pp.493-500.
- [141] Zhang, P., Klippenstein, S.J. and Law, C.K. Ab Initio Kinetics for the Decomposition of Hydroxybutyl and Butoxy Radicals of n-Butanol. *The Journal of Physical Chemistry A*. 2013, **117**(9), pp.1890-1906.
- [142] Antonov, I.O., Kwok, J., Zádor, J. and Sheps, L. A Combined Experimental and Theoretical Study of the Reaction OH + 2-Butene in the 400–800 K Temperature Range. *The Journal of Physical Chemistry A*. 2015, **119**(28), pp.7742-7752.
- [143] Onel, L., Blitz, M., Dryden, M., Thonger, L. and Seakins, P. Branching Ratios in Reactions of OH Radicals with Methylamine, Dimethylamine, and Ethylamine. *Environmental science & technology*. 2014, **48**(16), pp.9935-9942.

- [144] Glowacki, D.R., Liang, C.H., Morley, C., Pilling, M.J. and Robertson, S.H. MESMER: An Open-Source Master Equation Solver for Multi-Energy Well Reactions. *Journal of Physical Chemistry A*. 2012, **116**(38), pp.9545-9560.
- [145] Zhao, Y. and Truhlar, D.G. The M06 suite of density functionals for main group thermochemistry, thermochemical kinetics, noncovalent interactions, excited states, and transition elements: two new functionals and systematic testing of four M06-class functionals and 12 other functionals. *Theoretical Chemistry Accounts*. 2008, **120**(1-3), pp.215-241.
- [146] Frisch, M.J., Trucks, G.W., Schlegel, H.B., Scuseria, G.E., Robb, M.A., Cheeseman, J.R., Scalmani, G., Barone, V., Mennucci, B., Petersson, G.A. and Nakatsuji, H. Gaussian 09, Revision D.01. *Gaussian Inc.* 2013 (Wallingford, CT).
- [147] Raghavachari, K., Trucks, G.W., Pople, J.A. and Headgordon, M. A 5th-Order Perturbation Comparison Of Electron Correlation Theories. *Chemical Physics Letters*. 1989, **157**(6), pp.479-483.
- [148] Helgaker, T., Klopper, W., Koch, H. and Noga, J. Basis-set convergence of correlated calculations on water. *Journal of Chemical Physics*. 1997, **106**(23), pp.9639-9646.
- [149] Eskola, A.J., Carr, S.A., Shannon, R.J., Wang, B., Blitz, M.A., Pilling, M.J., Seakins, P.W. and Robertson, S.H. Analysis of the Kinetics and Yields of OH Radical Production from the CH₃OCH₂ + O₂ Reaction in the Temperature Range 195–650 K: An Experimental and Computational study. *The Journal of Physical Chemistry A*. 2014, **118**(34), pp.6773-6788.
- [150] Kendall, R.A., Dunning Jr., T.H. and Harrison, R.J. Electron affinities of the first-row atoms revisited. Systematic basis sets and wave functions. 1992, **96**(9), pp.6796-6806.
- [151] *Kintecus*. James C. Ianni, 2017.
- [152] Sun, H., Bozzelli, J.W. and Law, C.K. Thermochemical and Kinetic Analysis on the Reactions of O₂ with Products from OH Addition to Isobutene, 2-Hydroxy-1,1-dimethylethyl, and 2-Hydroxy-2-methylpropyl Radicals: HO₂ Formation from Oxidation of Neopentane, Part II. *The Journal of Physical Chemistry A*. 2007, **111**(23), pp.4974-4986.
- [153] David G. Goodwin, R.L.S., Harry K. Moffat, Bryan W. Weber. Cantera: An object-oriented software toolkit for chemical kinetics, thermodynamics, and transport processes. 2018.

- [154] Roscoe, J.M. The reactions of O (3P) with the butanols. *Canadian Journal of Chemistry*. 1983, **61**(12), pp.2716-2720.
- [155] Potter, D. *Kinetic studies of ether low temperature combustion mechanisms using laser photolysis and modelling*. thesis, University of Leeds, 2019.
- [156] Monge-Palacios, M., Grajales-Gonzalez, E. and Sarathy, S.M. Ab Initio, Transition State Theory, and Kinetic Modeling Study of the HO₂-Assisted Keto-Enol Tautomerism Propen-2-ol + HO₂ double left right arrow Acetone + HO₂ under Combustion, Atmospheric, and Interstellar Conditions. *Journal of Physical Chemistry A*. 2018, **122**(51), pp.9792-9805.
- [157] Rosi, M., Skouteris, D., Balucani, N., Nappi, C., Lago, N.F., Pacifici, L., Falcinelli, S. and Stranges, D. An Experimental and Theoretical Investigation of 1-Butanol Pyrolysis. *Frontiers in Chemistry*. 2019, **7**, p.14.

Appendices

Appendix A: Expanded fitting equation for fitting experimental traces utilising chlorine radical precursor

$$A = k_b$$

$$B = -(k_a + k_d)$$

$$C = k_a$$

$$D = -(k_b + k_2)$$

$$F = (B+D)$$

$$G = (D \times B) - (A \times C)$$

$$H = A \times k_{Cl} \times [Cl]_0$$

$$J = -k_{Cl}$$

$$M = \frac{(-F + \sqrt{F^2 - 4 \times G})}{2}$$

$$N = \frac{(-F - \sqrt{F^2 - 4 \times G})}{2}$$

$$P = H / ((-F \times J) + G + J^2)$$

$$C1 = P \times (N - J) / (M - N)$$

$$C2 = - (C1+P)$$

$$y = C1 \times \exp^{(M \times t)} + C2 \times \exp^{(N \times t)} + P \times \exp^{(J \times t)}$$

Appendix B**Table B1:** *t*-butanol experimentally obtained k_{recycle} values, compared with MESMER calculated values at given conditions and at high pressure limit (8000 Torr)

T / K	Pressure / Torr	Experimentally Obtained $k_{\text{recycle}} /$ s^{-1}	MESMER calculated $k_{\text{recycle}} /$ s^{-1}	MESMER calculated (8000 Torr) $k_{\text{recycle}} / \text{s}^{-1}$
517	39	277 ± 21	203	273
531	39	497 ± 22	361	512
549	39	902 ± 32	717	1098
563	40	1330 ± 55	1175	1919
577	40	1975 ± 91	1863	3264
587	42	2716 ± 68	2577	4694
590	38	2675 ± 103	2780	5222
592	88	3523 ± 42	3633	5603
599	88	3963 ± 44	4472	7142
607	87	4684 ± 74	5655	9357
614	89	5136 ± 71	6928	11780

Table B2: *i*-butanol experimentally obtained k_{recycle} values, compared with MESMER calculated values at given conditions and at high pressure limit (8000 Torr)

T / K	Pressure / Torr	Experimentally Obtained $k_{\text{recycle}} / \text{s}^{-1}$	MESMER calculated $k_{\text{recycle}} / \text{s}^{-1}$	MESMER calculated (8000 Torr) $k_{\text{recycle}} / \text{s}^{-1}$
493	36	38 ± 3	25	26
510	81	113 ± 27	53	55
518	37	88 ± 5	72	77
527	37	107 ± 6	103	110
540	81	241 ± 19	175	182
550	37	245 ± 13	241	263
551	81	343 ± 22	261	273
564	81	507 ± 20	409	430
580	38	369 ± 25	648	727
587	82	908 ± 35	851	905
587	81	874 ± 37	851	905
595	82	1006 ± 28	1081	1153
607	82	1732 ± 46	1522	1635
614	82	1746 ± 55	1843	1988
621	82	2656 ± 111	2220	2404

Table B3: *n*-butanol experimentally obtained k_{recycle} values, compared with MESMER calculated values at given conditions and at high pressure limit (8000 Torr)

T / K	Pressure / Torr	Experimentally Obtained k_{recycle} / s^{-1}	MESMER calculated k_{recycle} / s^{-1}	MESMER calculated (8000 Torr) k_{recycle} / s^{-1}
535	34	138 ± 12	38	41
547	35	203 ± 29	62	67
555	134	428 ± 32	90	92
564	35	240 ± 32	118	129
576	35	306 ± 48	181	200
598	132	607 ± 35	407	421
602	35	374 ± 67	424	479
652	128	1573 ± 61	1925	2032


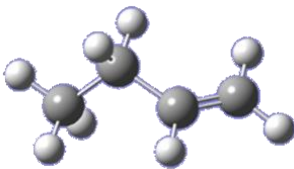
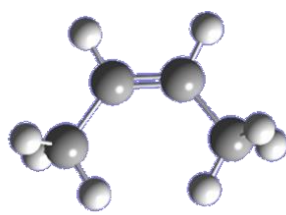
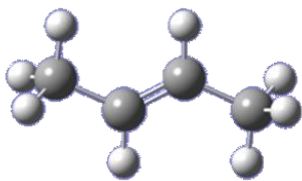
Appendix C: Absolute Energies (including ZPE corrections), Rotational Constants and Vibrational frequencies obtained at the CCSD(T)/aug-cc-pVTZ//M06-2X/aug-cc-pVTZ level for all species in Chapter 4.

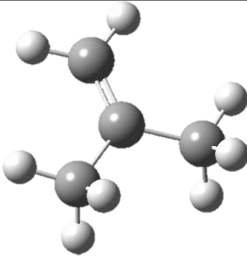
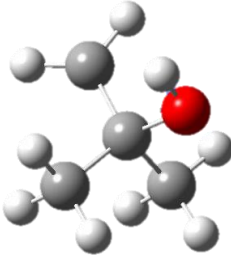
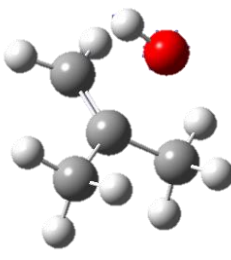
All computational calculations were carried out using the Gaussian 09 programme. The M06-2X suite of functionals were used for optimisations of all structures, based on consensus within the literature [156] of their suitability for calculating main group kinetic studies. The use of the calendar series basis set aug-cc-pVTZ was also chosen based upon its suitability from consensus within the literature [157], as was the computing of the stationary point energies at the CCSD(T) level, using the same basis set. Geometry optimisations were initially obtained at the B3LYP/6-311g level, and subsequently increased to B3LYP/aug-cc-pVDZ, followed by M06-2X/aug-cc-pVTZ, ensuring the convergence criteria highlighted below were always met.

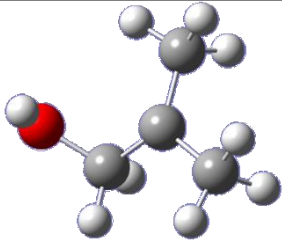
For energy calculations for the stationary points on the potential energy surfaces, CCSD(T) was used (convergence criteria also described below). For t-butanol, CCSD(T)/aug-cc-pVDZ, -pVTZ and -pVQZ were calculated and used to extrapolate to the CBS level (by Dr. D. J. Medeiros). For all other butanol isomers, the highest level calculated was CCSD(T)/aug-cc-pVTZ. The convergence criteria set were the default settings from the Gaussian 09 program, i.e. the maximum displacement threshold was set as 0.001800 Å, the maximum force threshold was set as 0.000450 Ha/Bohr, and the grid size was set as fine.


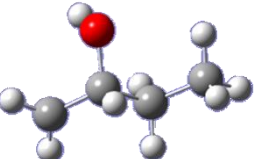
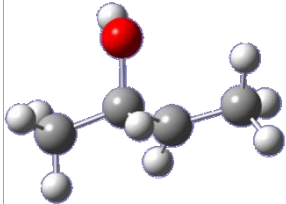
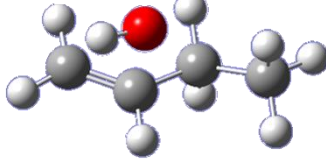
For transition state searches, B3LYP was chosen for the initial location of the transition state structure, as it provided a computationally inexpensive, fast method for searching. Transition state searches were carried out by providing an optimised starting structure for the β -radical and the relevant butene isomer product with OH that would result from the decomposition reaction, and carrying out a QST2 search at the UB3LYP/6-311G level. Once the correct imaginary frequency was visualised within the Gaussview software provided with Gaussian 09, the basis set and calculation method was then increased to UM06-2X/aug-cc-pVDZ, followed by UM06-2X/aug-cc-pVTZ. Stationary point energies were then calculated using CCSD(T) as described above.

As explained in the relevant sections, hindered rotor approximations were used for the rotation of groups such as the methyl group and the OH group. These were carried out by fixing the other bonds in the structure relative to the bond that is to be studied by the hindered rotor approximation, and calculating the energy at 15 ° intervals of rotation around the bond to be studied.

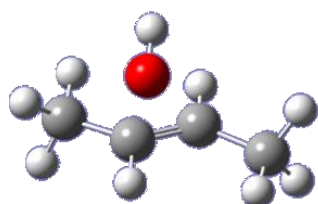
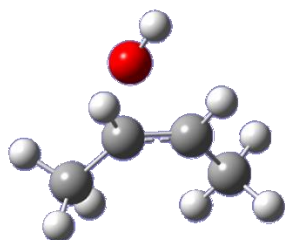
Name and Structure	Energies	Rotational Constants /cm ⁻¹	Vibrational Frequencies /cm ⁻¹			
OH radical 	-75.634	18.865	3751.964			
n-butene 	-156.824	0.750 0.140 0.13	97.63	226.57	317.60	434.32
			662.66	791.68	870.48	966.20
			984.19	1034.33	1048.10	1101.54
			1203.75	1291.25	1320.54	1346.01
			1408.02	1454.78	1485.33	1502.85
			1509.24	1732.46	3044.86	3053.05
			3086.30	3122.65	3136.41	3137.54
			3145.14	3230.60		
Cis-2-butene 	-156.467	0.545 0.171 0.137	115.19	122.32	292.90	397.72
			565.24	695.08	883.76	990.75
			1014.47	1030.90	1066.83	1071.12
			1159.25	1293.70	1391.58	1422.88
			1445.12	1485.26	1491.17	1492.73
			1499.34	1756.17	3053.27	3056.98
			3105.82	3106.20	3125.69	3142.87
			3145.62	3160.64		
Trans-2-butene 	-156.828	1.167 0.125 0.118	162.32	221.58	239.73	282.32
			507.26	754.21	881.80	982.10
			995.90	1063.91	1074.79	1098.10
			1173.25	1326.21	1335.27	1411.30
			1411.55	1480.62	1481.15	1492.77
			1500.79	1774.06	3040.01	3040.11
			3095.14	3095.72	3115.43	3116.28
			3129.58	3134.76		
iso-butene	-156.821	0.307 0.283 0.156	202.29	245.03	383.81	439.75
			445.77	718.19	835.31	950.70
			972.58	996.74	1021.72	1088.73

			1110.05	1309.82	1410.60	1415.37
			1447.61	1480.23	1487.18	1498.81
			1506.13	1744.02	3045.52	3049.05
			3098.73	3100.80	3146.96	3147.82
			3151.09	3235.09		
<i>t</i>-butanol β-hydroxybutyl radical	-232.499	0.165	119.4911	224.3691	274.5406	
		0.160	329.8262	339.9029	362.7135	
		0.157	411.5557	450.1174	473.2267	
			547.617	784.3117	909.9816	
			944.6003	952.059	1004.8374	
			1023.8682	1137.7341	1240.7525	
			1278.5657	1345.8482	1394.9671	
			1409.6472	1447.5037	1477.4271	
			1485.4123	1498.0054	1509.9776	
			3041.6658	3053.8693	3114.1119	
			3129.9779	3138.1819	3147.8467	
			3154.069	3265.2785	3861.8953	
<i>t</i>-butanol β-hydroxybutyl decomposition: Transition state	-232.459	0.162	122.5098	164.8594	191.8175	
		0.139	209.983	269.6707	377.5228	
		0.12	399.2271	438.4714	664.2059	
			707.3739	832.491	914.7288	
			966.4221	986.8271	1014.9735	
			1080.3081	1086.3868	1318.8389	
			1403.8478	1417.3716	1436.7871	
			1467.9942	1482.5236	1487.668	
			1505.5413	1643.2349	3048.2511	
			3054.0533	3119.6553	3121.8658	
			3146.5924	3148.3906	3152.6534	
			3245.928	3803.0329		
			Imaginary frequency: 289.37			
<i>i</i>-butanol β-hydroxybutyl radical	-232.508	0.253	82.37	104.39	157.42	236.79
		0.119	302.13	334.73	362.55	505.88
		0.089	793.48	921.87	940.97	983.51

				1014.42	1060.45	1097.63	1195.41
				1275.88	1315.92	1373.47	1399.21
				1411.60	1427.81	1473.28	1476.97
				1492.85	1500.06	1501.57	2982.83
				2986.26	3014.58	3055.15	3068.74
				3085.09	3115.15	3139.12	
				3864.25			
<i>i</i>-butanol β-hydroxybutyl decomposition: Transition state	-232.470	0.186	90.50	109.38	144.07	196.79	
		0.120	220.09	385.95	435.64	443.67	
		0.102	674.01	774.18	837.09	966.17	
			968.37	996.49	1003.07	1085.53	
			1095.76	1319.02	1406.75	1416.45	
			1438.56	1470.85	1479.95	1490.88	
			1504.27	1667.80	3040.68	3045.07	
			3095.07	3101.73	3144.12	3150.53	
			3165.20	3256.76	3799.89		
							Imaginary frequency: 248.70
<i>n</i>-butanol β-hydroxybutyl radical	-232.501	0.592	84.2166	95.9388	205.482	273.398	
		0.068	317.911	405.032	452.981	507.274	
		0.064	770.894	899.47	952.648	1033.71	
			1072.26	1102.75	1146.1	1161.55	
			1196.75	1276.07	1284.95	1362.15	
			1403.95	1419.29	1451.18	1476.73	
			1501.22	1505.72	1512.28	2981.54	
			3011.27	3035.69	3045.56	3059.54	
			3131.09	3135.17	3181.52		
			3868.52				
<i>n</i>-butanol β-hydroxybutyl decomposition: Transition state	-232.464	0.219	59.89	89.12	163.79	203.70	242.20
		0.108	354.61	443.20	664.10	705.90	
		0.081	791.47	872.33	982.64	986.51	
			1010.25	1041.61	1089.42	1205.63	
			1286.69	1310.92	1333.77	1396.74	
			1454.54	1479.24	1498.41	1510.12	

			1651.80	3033.56	3048.86	3094.18
			3121.33	3136.03	3144.34	3164.29
			3254.59	3792.14		
			Imaginary frequency: 314.33			
s-butanol β-hydroxybutyl radical : C1	-232.504	0.278	124.57	204.78	240.29	254.79
		0.121	309.67	394.19	462.74	496.26
		0.092	581.26	777.09	845.61	942.98
			1003.18	1049.37	1082.21	1150.05
			1189.71	1231.72	1289.05	1332.41
			1390.26	1398.44	1415.59	1462.49
			1481.41	1503.29	1510.74	3014.45
			3038.45	3056.72	3085.09	3124.49
			3146.24	3174.08	3283.47	3849.89
s-butanol β-hydroxybutyl radical : C3	-232.509	0.279	75.38	119.66	228.92	251.27
		0.116	333.28	380.33	401.09	498.17
		0.090	549.59	822.87	924.47	984.38
			1003.37	1059.05	1098.95	1152.11
			1192.32	1250.58	1316.46	1393.69
			1403.99	1407.43	1428.57	1480.40
			1487.47	1492.29	1497.15	3007.80
			3032.84	3045.62	3081.78	3117.54
			3125.74	3138.25	3204.51	3846.96
s-butanol β-hydroxybutyl decomposition: Transition state C1	-232.463	0.219	59.75	100.46	180.64	230.76
		0.120	253.36	326.48	453.38	592.01
		0.087	678.05	779.92	866.94	938.63
			994.11	1006.79	1062.63	1098.33
			1202.25	1293.18	1312.84	1340.15
			1407.79	1455.15	1469.54	1501.33
			1512.09	1642.61	3036.39	3056.99
			3093.60	3123.98	3150.21	3157.47
			3160.88	3245.93	3793.74	
			Imaginary frequency : 290.07			

<i>s</i> -butanol β -	-232.467	0.168	81.43	103.54	119.32	156.46
hydroxybutyl		0.133	235.31	265.78	370.70	579.78
decomposition:		0.097	619.81	713.24	905.81	964.10
Transition state C3 –			1003.09	1029.95	1030.35	1045.16
Cis products			1145.15	1254.82	1354.94	1380.77
			1429.02	1446.11	1456.77	1468.32
			1473.15	1683.54	3054.41	3055.72
			3120.12	3131.01	3152.82	3158.71
			3182.36	3203.36	3778.78	
			Imaginary frequency: 181.83			
<i>s</i> -butanol β -	-232.469	0.203	107.64	134.69	172.58	197.65
hydroxybutyl		0.117	242.64	257.98	296.51	507.11
decomposition:		0.083	683.74	772.13	881.07	985.86
Transition state C3 –			996.21	1051.07	1058.18	1109.53
Trans products			1179.62	1322.91	1326.69	1405.48
			1411.31	1474.97	1480.91	1486.23
			1499.36	1680.91	3043.23	3045.87
			3098.11	3109.98	3124.92	3133.29
			3148.08	3171.22	3802.49	
			Imaginary frequency: 256.84			



Appendix D: Ignition delay time simulations for *t*-butanol at conditions matching those of the experimental data of Weber and Sung, as described in Chapter 5, Section 5.4.3. Different simulations obtained from updating base mechanism of Sarathy *et al.*

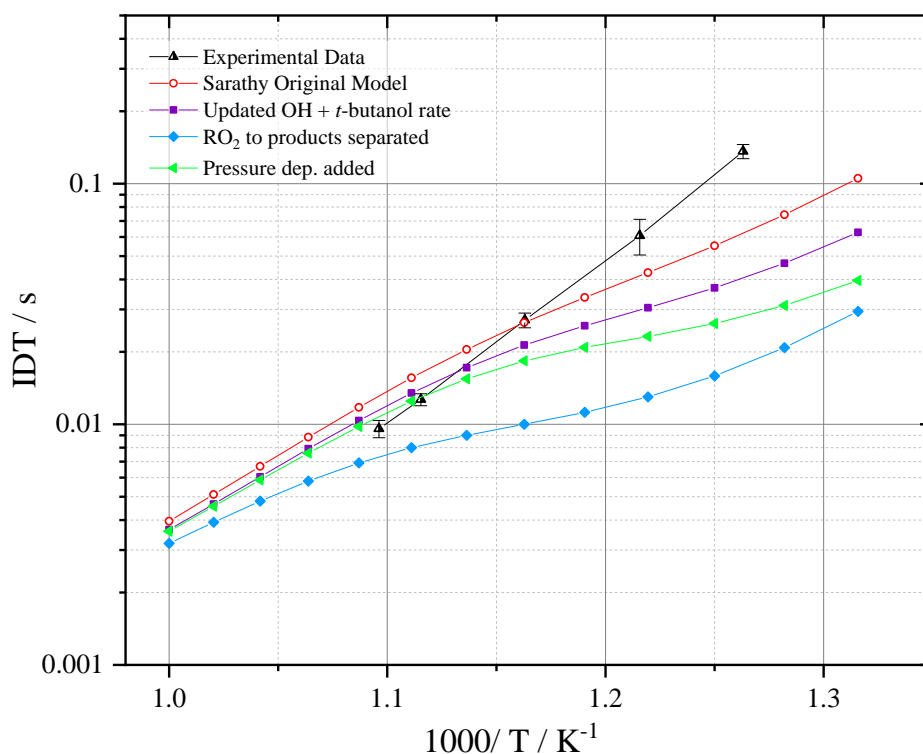


Figure D1: Ignition delay time data from Weber and Sung [47] obtained at 30 Bar and $\Phi = 0.5$, and simulations using the Sarathy *et al.* base combustion mechanism, with varying updates: Solid purple squares: Updating total bimolecular OH+ *t*-butanol reactivity, Solid blue diamonds: Separating of $\text{RO}_2 \rightarrow \text{QOOH} \rightarrow \text{Product}$ reactions based on recommended rates of Sun and Bozzelli, Solid green triangles: Addition of pressure dependence to RO_2 separated reactions based on recommendations of Sun and Bozzelli.

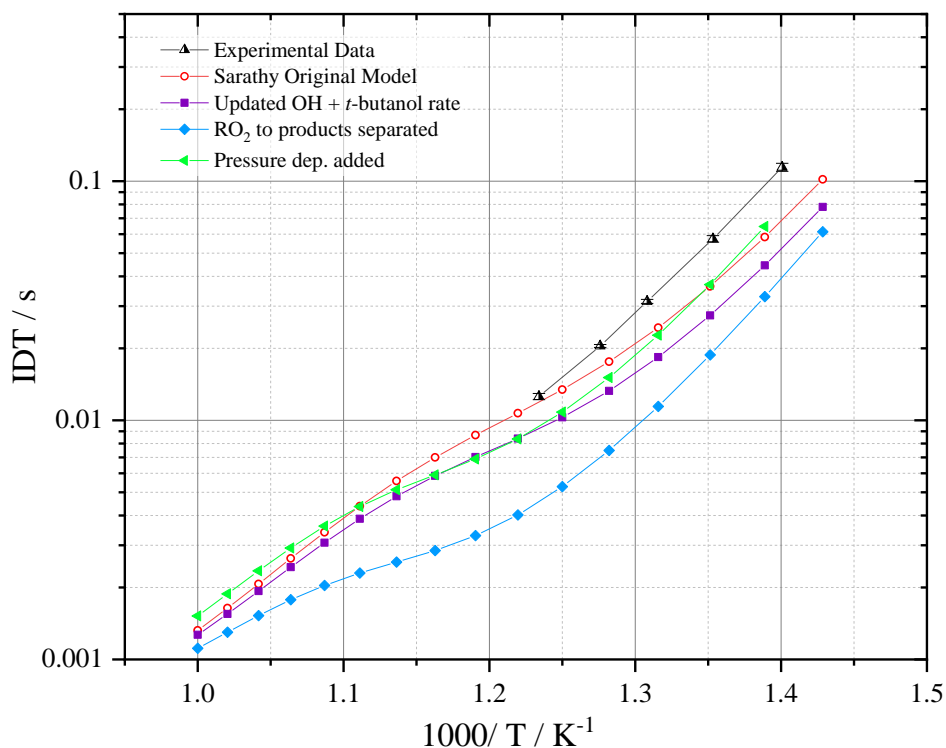


Figure D2: Ignition delay time data from Weber and Sung [47] obtained at 30 Bar and $\Phi = 2$, and simulations using the Sarathy *et al.* base combustion mechanism, with varying updates: Solid purple squares: Updating total bimolecular OH+ *t*-butanol reactivity, Solid blue diamonds: Separating of $\text{RO}_2 \rightarrow \text{QOOH} \rightarrow \text{Product}$ reactions based on recommended rates of Sun and Bozzelli, Solid green triangles: Addition of pressure dependence to RO_2 separated reactions based on recommendations of Sun and Bozzelli.

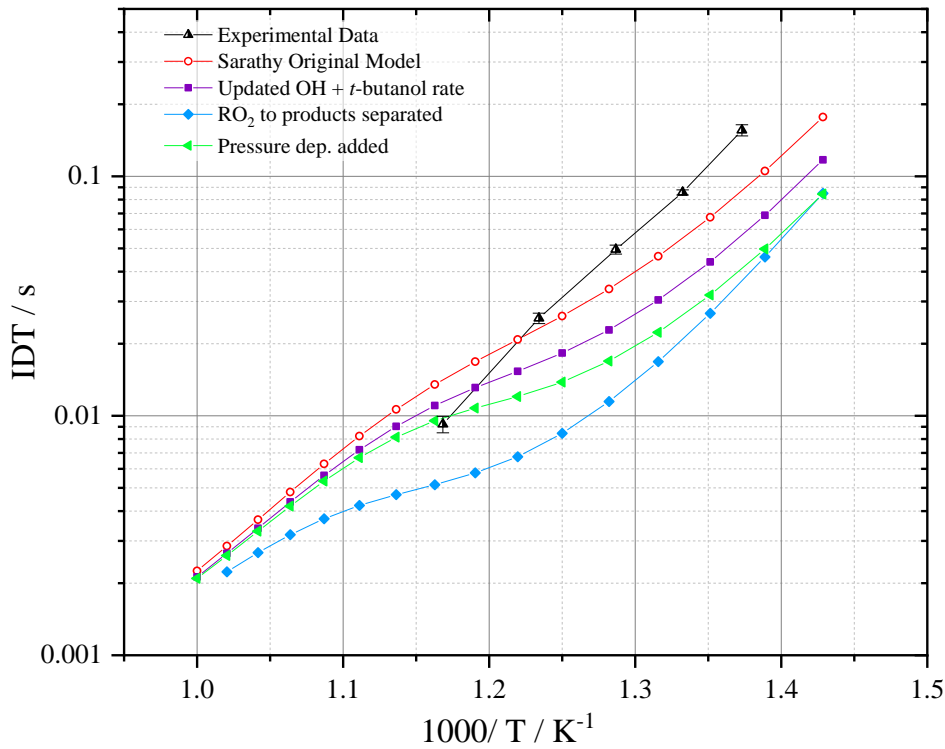


Figure D3: Ignition delay time data from Weber and Sung [47] obtained at 30 Bar and $\Phi = 1$, and simulations using the Sarathy *et al.* base combustion mechanism, with varying updates: Solid purple squares: Updating total bimolecular OH + *t*-butanol reactivity, Solid blue diamonds: Separating of $\text{RO}_2 \rightarrow \text{QOOH} \rightarrow \text{Product}$ reactions based on recommended rates of Sun and Bozzelli, Solid green triangles: Addition of pressure dependence to RO_2 separated reactions based on recommendations of Sun and Bozzelli.

Appendix E: Expanded fitting equation for fitting experimental traces utilising SO₂ radical precursor

$$k_a = k_{\text{OH}+n\text{-butanol}} \times [n\text{-butanol}]$$

$$k_O = k_{\text{O}+n\text{-butanol}} \times [n\text{-butanol}]$$

$$A = -(k_a + k_d)$$

$$B = -(k_b + k_2)$$

$$C = k_O$$

$$D = k_b$$

$$E = k_a$$

$$F = -(A+B)$$

$$G = (A \times B) - (D \times E)$$

$$J = -((B \times C) - (D \times C))$$

$$N = C \times -k_O \times \text{O}(\text{}^3\text{P})_0$$

$$O = J * \text{O}(\text{}^3\text{P})_0$$

$$H = O + N$$

$$M = \frac{(-F + \sqrt{F^2 - 4 \times J})}{2}$$

$$N = \frac{(-F - \sqrt{F^2 - 4 \times J})}{2}$$

$$P = H / ((-F \times C) + J + C^2)$$

$$W = -k_O \times P$$

$$C1 = ((C \times \text{O}(\text{}^3\text{P})_0) + (A \times \text{OH}_0) - W + (M \times P) - (N \times \text{OH})) / (M - N)$$

$$C2 = \text{OH} - C1 - P$$

$$y = C1 \times \exp^{(M \times t)} + C2 \times \exp^{(N \times t)} + P \times \exp^{(-k_O \times t)}$$

Appendix F: O (³P) + *n*-butanol experimental data obtained in this work, compared with calculated bimolecular rate coefficients and upper and lower limits of errors from Arrhenius parameterisations of Roscoe.

Temperature / K	<i>k</i>_{O (3P)+<i>n</i>-butanol} This Work	<i>k</i>_{O(3P)+<i>n</i>-butanol} (Roscoe*)	Upper limit (Roscoe*)	Lower limit (Roscoe*)
490	1.53 ± 0.15	1.32	0.75	2.25
550	3.10 ± 0.31	1.96	1.16	3.2
620	4.20 ± 0.42	2.83	1.74	4.44
650	6.09 ± 0.61	3.23	2.02	5.00
675	5.63 ± 0.56	3.57	2.25	5.47
730	6.97 ± 0.70	3.67	2.32	5.60

* Values calculated from Arrhenius parameterisation and errors.

All bimolecular rate constants in units of / 10⁻¹² cm³ molecule⁻¹ s⁻¹

Appendix G: Full expanded fitting equation for fitting to OH growth profile traces.

$$k_a = k_{\text{OH}+n\text{-butanol}} \times [n\text{-butanol}]$$

$$k_O = k_{\text{O}+n\text{-butanol}} \times [n\text{-butanol}]$$

$$\text{O } (^3\text{P}) \text{ Ratio} = (\text{O1} \cdot \ln([\text{O}_2])) - \text{O2}$$

$$\text{O } (^3\text{P}) = \text{O } (^3\text{P}) \text{ Ratio} \cdot \text{OH}$$

$$A = - (k_a + k_d)$$

$$B = - (k_b + k_2)$$

$$C = k_O$$

$$D = k_b$$

$$E = k_a$$

$$F = - (A+B)$$

$$G = (A \times B) - (D \times E)$$

$$J = - ((B \times C) - (D \times C))$$

$$N = C \times -k_O \times \text{O } (^3\text{P})_0$$

$$O = J \cdot \text{O } (^3\text{P})_0$$

$$H = O + N$$

$$M = \frac{(-F + \sqrt{F^2 - 4 \times J})}{2}$$

$$N = \frac{(-F - \sqrt{F^2 - 4 \times J})}{2}$$

$$P = H / ((-F \times C) + J + C^2)$$

$$W = - k_O \times P$$

$$C1 = ((C \times \text{O } (^3\text{P})_0) + (A \times \text{OH}_0) - W + (M \times P) - (N \times \text{OH})) / (M - N)$$

$$C2 = \text{OH} - C1 - P$$

$$y = C1 \times \exp^{(M \times t)} + C2 \times \exp^{(N \times t)} + P \times \exp^{(-k_O \times t)}$$